UMCS

UNIWERSYTET MARII CURIE-SKŁODOWSKIEJ
W LUBLINIE
Wydział Matematyki Fizyki i Informatyki
Instytut Fizyki

Kierunek: **Fizyka**

Marcin Kurzyna
Nr albumu: 267946

Właściwości elektryczne normalnych i topologicznych łańcuchów atomowych na różnych podłożach

Electrical properties of normal and topological atomic chains on different substrates

Rozprawa doktorska
napisana w Katedrze Fizyki Powierzchni i Nanostruktur
pod kierunkiem dr. hab. Tomasza Kwapińskiego, prof. UMCS

Lublin, Rok 2022

Składam najserdeczniejsze podziękowania mojemu promotorowi, Panu dr. hab. Tomaszowi Kwapińskiemu, prof. UMCS za jego nieocenioną pomoc przy napisaniu niniejszej rozprawy oraz za wsparcie, na jakie zawsze mogłem liczyć jako jego podopieczny.

Spis treści

Streszczenie **7**

Struktura pracy **11**

1 Wstęp **13**

1.1 Motywacje badań 13

1.2 Cele rozprawy doktorskiej 15

1.3 Metody wytwarzania i badania łańcuchów atomowych 16

2 Opis teoretyczny **21**

2.1 Podstawy topologii 21

2.2 Model topologicznego łańcucha atomowego 23

2.2.1 Model Su-Schrieffera-Heegera 23

2.2.2 Fazy topologiczne w modelu SSH 24

2.3 Stacjonarne właściwości elektryczne łańcuchów atomowych 26

2.3.1 Funkcje Greena w opisie układów atomowych 26

2.3.2 Łańcuch atomowy na powierzchni 27

2.3.3 Analityczne rozwiązania dla układów atomowych 30

2.4 Czasowo-zależne właściwości elektryczne układów atomowych 34

2.4.1 Ewolucja układów kwantowych 34

2.4.2 Formalizm operatora ewolucji w opisie układów atomowych 35

3 Nano Modeller **41**

4 Wykaz działalności naukowej **51**

4.1 Wykaz publikacji naukowych 51

4.2 Wykaz konferencji naukowych 67

5 Podsumowanie **69**

Bibliografia **71**

Cykl publikacji naukowych **79**

Streszczenie

Łańcuchy atomowe i struktury niskowymiarowe cieszą się obecnie dużym zainteresowaniem naukowców. Jako najcieńsze możliwe przewodniki prądu [1–3], struktury te mogą znaleźć wiele zastosowań aplikacyjnych w nanoelektronice i optoelektronice [4–6]. Łańcuchy atomowe wykazują istnienie szerokiej gamy zjawisk fizycznych, jak np. oscylacje przewodnictwa, rozseparowanie spinowo-ładunkowe [7], fale ładunkowe [8] i wiele innych [9]. W niniejszej rozprawie zajmuję się teoretycznym opisem właściwości elektrycznych normalnych i topologicznych łańcuchów atomowych umieszczonych na różnych podłożach z uwzględnieniem sprzężenia spin-orbita, odpychania kulombowskiego, poziomu lokalizacji elektronów w podłożu oraz jego geometrii, zależnych od czasu zaburzeń, efektów włączeniowych i innych. W obliczeniach wykorzystuję hamiltonian ciasnego wiązania wraz z formalizmem retardowanych funkcji Greena oraz techniką operatora ewolucji. Właściwości elektryczne badanych łańcuchów analizowane są na podstawie lokalnej gęstości stanów, obsadzeń ładunkowych, przewodności oraz prądów płynących przez łańcuch, zarówno w przypadkach stacjonarnych, jak i niestacjonarnych (zależnych od czasu). Niniejsza rozprawa doktorska oparta jest na cyklu 7 opublikowanych prac naukowych napisanych podczas moich studiów doktoranckich, które zostały opisane w rozdziale 4. Wyniki przedstawione w tych pracach wskazują, iż łańcuchy atomowe są w niewielkim stopniu podatne na zaburzenia zewnętrzne, a także mogą pełnić rolę efektywnych pomp elektronowych. Teoretyczne rozważania przedstawione w tej pracy ujawniają, że topologiczne stany brzegowe w określonych warunkach mogą istnieć poza nietrywialną topologiczną fazą łańcucha atomowego i na dodatek mogą przemieszczać się wzdłuż wewnętrznych węzłów struktury atomowej. Ponadto w niniejszej rozprawie wykazano, iż układ dwóch kropek kwantowych, przejawia w funkcji czasu bardzo regularną strukturę wierzchołków w lokalnej gęstości stanów (tzw. *transient crystal*), która jest odzwierciedleniem gęstości stanów stacjonarnych łańcuchów atomowych. Dodatkowo rozprawa przedstawia narzędzia komputerowe, które pozwalają modelować struktury atomowe na powierzchni, badać ich własności stacjonarne jak i zależne od czasu, oraz wykonywać bardzo szczegółowe wykresy 3D.

Abstract

Atomic chains and low-dimensional systems are of great interest nowadays. As the thinnest electric conductors [1–3], they can found many possible applications in nanoelectronics and optoelectronics [4–6]. Such systems reveal many interesting effects like conductance oscillations, spin-charge separation [7], charge density waves [8] and others [9]. In this dissertation I focus on theoretical description of electrical properties of normal and topological atomic chains on different substrates, taking into account Coulomb repulsion, spin-orbit coupling, electron localization level and geometry of the substrate. In these calculations, I use tight-binding Hamiltonian with Green's functions formalism and evolution operator technique. Electrical properties of atomic chains are determined basing on the calculations of local density of states, charge occupations, conductance and currents in both stationary and non-stationary (time-dependent) cases. This doctoral dissertation is based on a set of 7 scientific papers written and published during my PhD studies, which are described in chapter 4. The results presented in these papers reveal that atomic wires are barely affected by external perturbations and can play a role of an effective electron pump. Additionally, theoretical findings presented in this thesis reveal that topological boundary states in certain conditions can exist outside non-trivial topological phase of atomic chain and travel along internal sites of the structure. Furthermore, there is shown that two quantum-dot system reveals a periodical structure in time domain visible in the local density of states which is related with the stationary long atomic chains density of states (we call these structures transient crystals). Lastly, the dissertation shows computer tools which allow one to model atomic structures on a surface and examine their electrical properties in both stationary and time-dependent cases and perform highly detailed 3D plots.

Struktura pracy

W skład niniejszej rozprawy wchodzi autoreferat, w którym zaprezentowałem cele rozprawy doktorskiej, opisałem wykorzystane metody teoretyczne do zrealizowania postawionych celów, przedstawiłem hipotezy badawcze, a także omówiłem najistotniejsze wyniki opublikowane w cyklu artykułów naukowych stanowiących główną część rozprawy, których kopie zostały załączone do autoreferatu. Niniejsza rozprawa składa się z następujących części:

1. **Wstęp** wprowadzający czytelnika w problematykę rozprawy, w którym zawarte są informacje na temat eksperymentalnych technik wytwarzania łańcuchów atomowych oraz metod pomiaru ich właściwości elektrycznych. W rozdziale tym zostaną omówione również motywacje, które skłoniły mnie do napisania niniejszej rozprawy, a także postawione zostaną cele rozprawy doktorskiej.

2. **Rozdział drugi**, dzięki któremu możemy zapoznać się z pojęciem jednowymiarowego izolatora topologicznego oraz zaznajomić się z modelem Su-Schrieffera-Heegera (SSH), który stanowi popularną realizację tego typu nanostruktury. W części tej opisane są również wykorzystywane przeze mnie teoretyczne metody badań właściwości elektrycznych łańcuchów atomowych- formalizmy retardowanych funkcji Greena oraz operatora ewolucji. Ponadto, w rozdziale tym przedstawione są obliczenia analityczne właściwości elektrycznych regularnych struktur atomowych na powierzchni, które umożliwią czytelnikowi lepsze zrozumienie problematyki rozprawy.

3. **Rozdział trzeci** zawierający opis programu komputerowego *Nano Modeller*, który został napisany do realizacji zadań stanowiących cele rozprawy doktorskiej. Program ten umożliwia modelowanie struktur atomowych na powierzchni, obliczanie ich dynamicznych i statycznych właściwości elektrycznych, sporządzanie zaawansowanych wykresów tychże właściwości, a także zawiera szereg dodatkowych funkcjonalności, które zostaną w tym rozdziale szczegółowo opisane.

4. **Rozdział czwarty** będący sekcją, w której zaprezentowałem szczegółowe cele i hipotezy badawcze pracy doktorskiej, a także omówiłem najważniejsze wyniki badań zawartych w cyklu publikacji naukowych, napisanych w toku studiów doktoranckich. Ponadto w rozdziale tym znajduje się wykaz konferencji naukowych, podczas których miałem możliwość zaprezentowania wyników swoich badań.

5. **Podsumowanie** wieńczące niniejszą rozprawę, w którym uwypuklone są najistotniejsze wnioski płynące z pracy doktorskiej, oraz nakreślone są kierunki dalszych badań.

6. **Cykl publikacji naukowych**- sekcja zawierająca załączone do autoreferatu kopie opublikowanych artykułów naukowych opisanych w rozdziale **4**.

Rozdział 1

Wstęp

1.1 Motywacje badań

Jednym z problemów, z którym borykają się współcześni inżynierowie oraz naukowcy zajmujący się badaniami nad nowoczesnymi urządzeniami elektronicznymi jest zachowanie pełnej ich wydajności, przy jednoczesnym zachowaniu kompaktowych rozmiarów. Śledząc rozwój komputerów na przełomie ostatnich dekad, możemy zauważyć ich ewolucję z monstrualnych machin o niskiej wydajności i dużym zapotrzebowaniu na energię, jak np. ENIAC, który zajmował powierzchnię około 170 m^2 i zużywał 150 kW prądu [10] do kompaktowych i wydajnych urządzeń przenośnych takich jak laptopy, czy telefony komórkowe [11]. Możemy zatem zadać sobie pytanie, czy w kolejnych dekadach znów doświadczymy równie spektakularnego skoku w rozwoju technicznym? Adresatami tego pytania w moim odczuciu powinni być fizycy, którzy dzięki odkryciom praw, jakimi rządzi się świat na skali nano, mogą przyczynić się do kolejnego kroku milowego w tej dziedzinie. Zmniejszając rozmiar przewodników będących komponentami urządzeń, w granicy uzyskamy struktury złożone z pojedynczych atomów. Dlatego też niezwykle pożądane jest zbadanie właściwości elektrycznych jednowymiarowych struktur złożonych z pojedynczych atomów, które mogą okazać się cegiełkami tworzącymi urządzenia przyszłości.

Niezwykle interesującymi materiałami, nad których właściwościami toczą się obecnie intensywne badania naukowe, są izolatory topologiczne, czyli materiały, które posiadają cechy zarówno izolatorów-zawierając przerwę energetyczną, jak i przewodników poprzez obecność stanów metalicznych na krawędziach lub powierzchniach. Przewodnictwo powierzchniowe można zaobserwować w materiałach, w których oddziaływanie spin-orbita odgrywa istotną rolę (np. selenek bizmutu [12, 13]). Kierunek prądów płynących na powierzchni takiego materiału jest silnie skorelowany ze spinem elektronów, przez co dzięki zjawiskom interferencyjnym nośniki prądu napotykają na znikomy opór. Z tego powodu materiały te posiadają duży potencjał aplikacyjny, gdyż mogą one znaleźć zastosowanie jako komponenty komputerów kwantowych jako bezdysypacyjne tranzystory [14], elementy układów optoelektronicznych [15], czy też magnetoelektronicznych [16]. Co ciekawe, takie materiały mogą wykazywać istnienie egzotycznych kwazicząstek, które są z zapałem poszukiwane w ostatnich dekadach przez fizyków, jak np. kwazicząstki Majorany w układach quasi-1D [17, 18], których wykorzystanie w komputerach kwantowych może przełożyć się na znaczny wzrost ich mocy obliczeniowej, ze względu na olbrzymi potencjał kubitów Majorany [19]. Poza majoranami przewidywania teoretyczne sugerują możliwość pojawienia się w izolatorach topologicznych monopoli magnetycznych [20], których istnienie od lat zaprząta głowy naukowców.

Duże zainteresowanie materiałami topologicznymi sprawiło, iż naukowcy zaczęli zastanawiać się, nad tym, czy możliwe jest uzyskanie izolatorów topologicznych w strukturach, w których oddziaływanie spin-orbita nie odgrywa istotnej roli. W 2011 r. pojawiła się praca teoretyczna głosząca, iż powstanie izolatora topologicznego może być zdeterminowane geometrią atomów znajdujących się na powierzchni kryształu, a nie jak do tamtej pory uważano oddziaływaniem spin-orbita [21]. Rozważania te znalazły bardzo szybko eksperymentalne potwierdzenie w postaci kryształów Pb, Sn i Se co zostało dokonane przez polskich naukowców z warszawskiego IF PAN [22], jak również kryształów SnTe [23]- prostego związku, którego topologiczne właściwości były postulowane w roku 2012 [24]. W ostatnich latach właściwości topologicznych doszukuje się też w innych materiałach, jak np. Ca_2As [25], czy też naturalnie występujących minerałach jak Pt_2HgSe_3, czy Pd_2HgSe_3 [26] - co pozwala mieć nadzieję, że w niedalekiej przyszłości materiały topologiczne będą stosowane powszechnie.

Mając na uwadze potencjał aplikacyjny izolatorów topologicznych, a także zważając na postępujący w inżynierii proces miniaturyzacji komponentów elektrycznych, można zadać sobie pytanie, czy istnieje możliwość wytworzenia najcieńszych przewodników prądu, które wykazują właściwości izolatora topologicznego? Odpowiedzi na to pytanie postaram się udzielić w rozdziale drugim, omawiając topologiczne łańcuchy atomowe. Zanim jednak to nastąpi, warto wyjaśnić samo pojęcie łańcucha atomowego. Łańcuchy atomowe to nanostruktury, w których ruch elektronów został ograniczony do tylko jednego kierunku [27, 28]. Zachowanie elektronów poruszających się w jednym wymiarze okazuje się być diametralnie inne od zachowania elektronów mogących poruszać się swobodnie. Modele używane do opisu elektronów w materiałach litych, jak np. model cieczy Fermiego w swej podstawowej formie zawodzi w opisie ruchu ograniczonego do jednego wymiaru [29–31]. Dzieje się tak, ponieważ elektrony nie mogą dłużej unikać siebie nawzajem podczas przemieszczania, co możemy przyrównać do ruchu samochodów przez wąską ulicę jednokierunkową, gdzie auta tracą możliwość wyprzedzania się bocznym pasem jezdni. Funkcje falowe w łańcuchu atomowym stają się wysoce skorelowane, nakładając się na siebie nawzajem [9]. Tak silna interakcja prowadzi do zdumiewających konsekwencji fizycznych, które ujawniają się w postaci mnogości nietypowych faz i zjawisk widocznych w łańcuchach atomowych. Do takich zjawisk możemy zaliczyć m.in. kwantowanie przewodnictwa pojawiające się, gdy dwa rezerwuary elektronów połączone są złączem, którego rozmiary w dwóch wymiarach są mniejsze od średniej drogi swobodnej elektronów [32], rozseparownie spinowo-ładunkowe [33] polegające na tym, że elektrony w jednym wymiarze „rozszczepiają" się na trzy indywidualne kwazicząstki: spinon, orbiton i holon niosące spin, wzbudzenia orbitalne i ładunek elektronu, które niekiedy mogą zachowywać się jak niezależne od siebie cząstki, oraz wiele innych [34, 35]. Wydaje się zatem, że materiały jednowymiarowe stanowią swoistą „kopalnię złota” ze względu na mnogość nowych efektów, których trudno jest się doszukać w materiałach litych.

1.2 Cele rozprawy doktorskiej

Ze względu na bogactwo „nowej fizyki”, jaka pojawia się w materiałach topologicznych, jak i normalnych strukturach jednowymiarowych, za cel niniejszej rozprawy doktorskiej postawiłem sobie dokładne przeanalizowanie właściwości elektrycznych normalnych i topologicznych struktur 1D na różnych powierzchniach (łańcuchów atomowych, bądź łańcuchów złożonych z kropek kwantowych, które nazywane są sztucznymi atomami [36,37] i mają tę zaletę, iż ich parametry, w odróżnieniu od rzeczywistych atomów, można w pełni kontrolować). Zbadam takie właściwości elektryczne jak lokalna gęstość stanów, konduktancja, obsadzenia ładunkowe, czy też płynące w układzie prądy, uwzględniając nie tylko efekty stacjonarne, ale również analizując dynamikę stanów elektronowych w procesach, które są zależne od czasu.

Zwracając uwagę nie tylko na odkrywczy charakter badań, ale również biorąc pod rozwagę aspekt aplikacyjny, należy zauważyć, iż struktury jednowymiarowe jako elementy nowoczesnych urządzeń nie będą mogły stanowić monolitu i być w pełni odizolowane od otoczenia, lecz będą musiały pozostawać w kontakcie z innymi strukturami systemu. Łańcuchy atomowe jako niezwykle cienkie oraz wrażliwe struktury mogą zostać całkowicie zdominowane przez większy o rzędy wielkości rezerwuar elektronów, jakim jest podłoże i z tego powodu elektrony łańcucha mogą np. wniknąć w głąb podłoża, przez co ten zmieni swoje właściwości elektryczne. Dlatego też jednym z celów niniejszej rozprawy jest rozstrzygnięcie, jak bardzo różne podłoża wpływają na właściwości transportowe łańcuchów w stosunku do swobodnych łańcuchów, lub takich, które spoczywają na powierzchniach izolatorowych. Badając wpływ podłoża, stawiam sobie również za cel uwzględnienie jego geometrii, mając w świadomości fakt, iż nie tylko lite materiały mogą stanowić rezerwuar elektronów dla łańcuchów atomowych, ale również materiały dwuwymiarowe takie jak grafen, czy silicen, które cieszą się rosnącym zainteresowaniem grona naukowego ze względu na swoje cenne właściwości.

Kolejnym celem rozprawy jest uwzględnienie zaburzeń, które podobnie jak podłoże mogą mieć znaczący wpływ na właściwości struktur jednowymiarowych. Do zaburzeń, jakie będę rozpatrywał, zaliczają się: adatomy- dodatkowe (najczęściej niepożądane) atomy pojawiające się w procesie tworzenia łańcuchów atomowych, defekty i naruszenia ciągłości łańcucha mogące powstać jako konsekwencja mechanicznej ingerencji w spójność struktury lub wskutek ruchów termalnych, zmiana oddziaływań między stanami elektronowymi atomów łańcucha mogąca powstać w wyniku zmiany stałej sieciowej przy rozciąganiu łańcucha atomowego lub modyfikacji parametrów wiązki laserowej w przypadku sieci optycznych, czy też poprzez obecność pól zewnętrznych. W badaniach zwrócę uwagę na dynamikę zmian stanów elektronowych w normalnych łańcuchach atomowych, a także rozpatrzę dynamikę stanów topologicznych w łańcuchach topologicznych tuż po zainicjowaniu zaburzenia i określę czas niezbędny do tego, by układ był w stanie powrócić do stanu równowagi. Jest to niezwykle istotne z praktycznego punktu widzenia, bowiem pozwala oszacować czas, który musi upłynąć, by układ był ponownie gotowy do dalszego działania.

Mam nadzieję, że moje badania przyczynią się do rozwoju dalszych badań nad strukturami jednowymiarowymi w różnych fazach topologicznych i rzucą nieco światła na fizykę materii skondensowanej.

1.3 Metody wytwarzania i badania łańcuchów atomowych

Poczyniony postęp w dziedzinie fizyki materii skondensowanej i nanotechnologii przyniósł wiele różnorodnych metod otrzymywania łańcuchów atomowych, czy też układów kropek kwantowych [38–41]. Wśród powszechnie stosowanych metod wytwarzania jednowymiarowych układów kwantowych można wyróżnić:

- MCBJ (ang. *Mechanically Controlled Break Junction*),
- metody litograficzne do wytwarzania kropek kwantowych,
- epitaksja z wiązki molekularnej MBE (ang. *Molecular Beam Epitaxy*) na powierzchniach wicynalnych,
- metody optyczne.

MCBJ jest to metoda oparta na wykorzystaniu piezoelektryków oraz metalicznego drutu o zadanej grubości [42]. Piezoelektryki pod wpływem przyłożonego napięcia powodują rozciąganie drutu, co prowadzi do jego stopniowego zwężania, a w konsekwencji sprawia, iż w centralnej części układu dochodzi do powstawania łańcuchów atomowych [43–45], co pokazano na rysunku 1.1. Technika ta pozwala w prosty sposób uzyskiwać struktury jednowymiarowe wprost z materiałów litych. Z punktu widzenia niniejszej rozprawy niewątpliwą zaletą metody MCBJ jest to, iż świetnie nadaje się ona do badania przewodnictwa elektrycznego w funkcji długości łańcucha atomowego, a wadą natomiast jest niedostatecznie długi „czas życia” łańcuchów, spowodowany tym, iż rozciąganie prowadzi ostatecznie do przerwania łańcucha. Z tego powodu wykorzystanie metody MCBJ nie daje możliwości uzyskania stabilnych układów atomowych, co przekłada się na brak możliwości ich obserwacji w dostatecznie długim czasie [46].

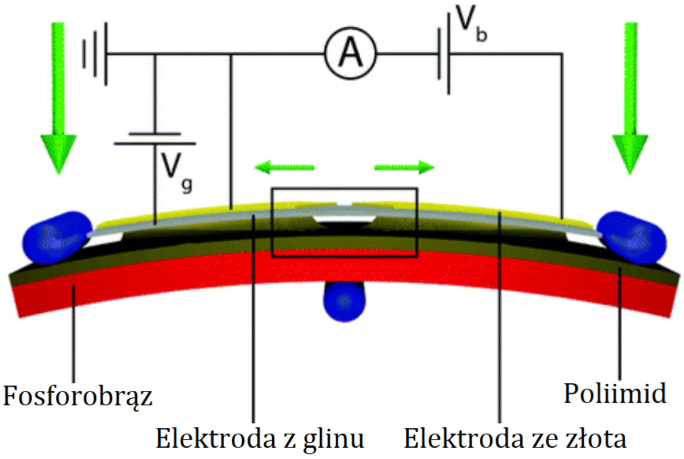

Rysunek 1.1: Schemat przykładowej realizacji techniki MCBJ, w którym przedstawiono makroskopowy drut wykonany ze złota umieszczony na giętkiej płytce fosforobrązowej, oddzielonej od łańcucha warstwą glinu. Źródło rysunku [47].

Inną metodą pozwalającą na uzyskiwanie jednowymiarowych układów kwantowych jest wykorzystanie układów kropek kwantowych, zwanych także sztucznymi atomami. Kropki kwantowe wytwarza się najczęściej metodami trawienia litograficznego [48] (wertykalne kropki kwantowe) lub na dwuwymiarowym gazie elektronowym, poprzez ograniczenie ruchu elektronów specjalnymi elektrodami zewnętrznymi [49, 50], co pokazano na rysunku 1.2. Metoda ta pozwala na modyfikowanie sprzężeń i położeń poziomów energetycznych elektronów układu 1D, które mogą być precyzyjnie kontrolowane poprzez elektrody zewnętrzne. Układy jednowymiarowe wytworzone tą metodą charakteryzują się dużą trwałością, przez co możliwe jest badanie zjawisk stacjonarnych i zależnych od czasu, takich jak efekty włączeniowe (*transient effects*), czy też dynamiczne zaburzenia zewnętrzne, co jest istotne w kontekście niniejszej rozprawy.

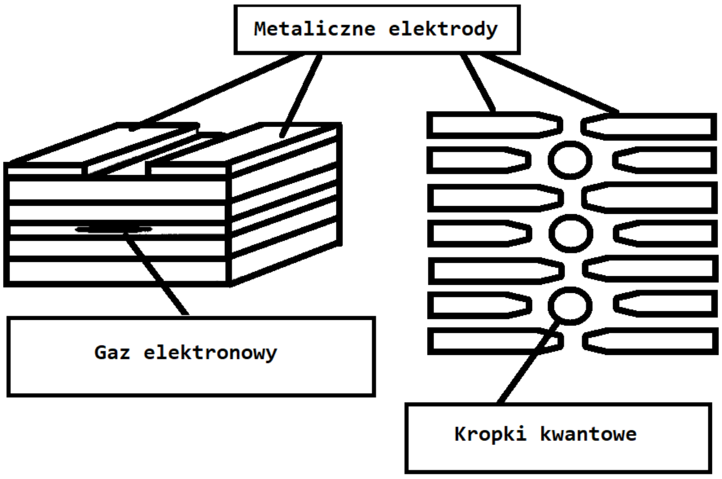

Rysunek 1.2: Jednowymiarowy gaz elektronowy (po lewej) oraz łańcuch złożony z kropek kwantowych (po prawej) wytworzone przez ograniczenie kierunku ruchu elektronów polem elektrycznym bramek (elektrod). Ilustracja na podstawie [49].

Kolejna technika wytwarzania struktur jednowymiarowych polega na wykorzystaniu powierzchni wicynalnych, czyli powierzchni anizotropowych cechujących się występowaniem charakterystycznych powierzchni schodkowych, w których skład wchodzą tarasy o szerokości kilku i wysokości jednego atomu [51], co pokazane zostało na rysunku 1.3. Powierzchnie te można uzyskać poprzez cięcie płaskiej

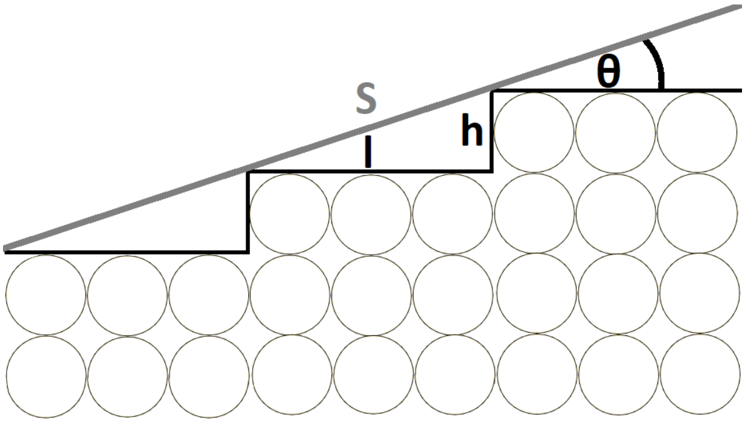

Rysunek 1.3: Schemat kryształu uciętego pod kątem θ z widoczną strukturą tarasową o szerokości $l = 3$ i wysokości $h = 1$ atomów, na której powstała powierzchnia wicynalna S.

próbki pod odpowiednim kątem (np. próbka Si(111) ucięta pod kątem 12,5° tworzy powierzchnię wicynalną Si(553) [52]). Na tak przygotowaną powierzchnię nakłada się atomy przy pomocy epitaksji z wiązki molekularnej w warunkach ultrawysokiej próżni, rzędu 10^{-7} - 10^{-10}Pa. Atomy pochodzące z komórek efuzyjnych [53] osiadają na podłoże, tworząc układy jednowymiarowe, układy quasi-dwuwymiarowe, lub cienkie warstwy.

Następną metodą wytwarzania struktur 1D jest wykorzystanie sieci optycznych, które mogą posłużyć do pułapkowania ultrazimnych atomów za pomocą fal stojących powstałych w wyniku interferencji wiązek laserowych. Tego typu fale tworzą w przestrzeni periodyczny potencjał ograniczający swobodę uwięzionych w nim atomów [54]. Z punktu widzenia niniejszej rozprawy niebywałą zaletą sieci optycznych jest możliwość manipulacji odległością między sąsiednimi komórkami (stałą sieci), która to związana jest z długością fali laserowej. Z tego względu stała sieci może ulec zmianie poprzez zmodyfikowanie długości fali emitowanej przez laser, bądź też w przypadku, gdy zmieniona zostanie faza pomiędzy interferującymi wiązkami [55].

Oprócz wymienionych metod warto również wspomnieć, iż łańcuchy atomowe mogą być wytwarzane przy pomocy skaningowego mikroskopu tunelowego, mającego możliwość manipulowania pojedynczymi atomami na powierzchni. Przy jego pomocy można ułożyć na powierzchni łańcuchy atomowe o dowolnej długości oraz geometrii, jak np. łańcuchy zygzakowate, które są jednym z obiektów zainteresowania niniejszej rozprawy. Dodatkowo aparat ten pozwala na kontrolowane zaburzanie układu jednowymiarowego poprzez umieszczanie na nim adatomów.

Eksperymentalne techniki badań łańcuchów

Istnieje wiele technik pomiaru nanostruktur. Wśród powszechnie stosowanych doświadczalnych metod dających sposobność badania właściwości nanostruktur wytworzonych na różnych powierzchniach znajdują się m.in.

- Odbiciowa dyfrakcja wysokoenergetycznych elektronów- RHEED (ang. *Reflection High Energy Electron Diffraction*) - technika dyfrakcyjna, przy której emitowane są wiązki elektronów o energiach rzędu kilku-kilkudziesięciu keV, które padają na badaną powierzchnię pod niewielkim kątem 0°- 5°. W wyniku odbicia elektronów od powierzchni próbki na ekranie powstaje obraz dyfrakcyjny [56, 57].

- Dyfrakcja elektronów niskoenergetycznych- LEED (ang. *Low-Energy Electron Diffraction*) - metoda badania powierzchni materiałów krystalicznych, polegająca na bombardowaniu powierzchni analizowanej próbki niskoenergetyczną wiązką elektronów (rzędu kilkudziesięciu $4eV$) i obserwacji obrazu dyfrakcyjnego [58, 59].

- Kątowo-rozdzielcza spektroskopia fotoemisji- ARPES (ang. *Angle-Resolved Photoemission*) - metoda pozwalającą na określenie pasmowej struktury elektronowej badanej powierzchni, przy wykorzystaniu zjawiska fotoemisji umożliwiająca określanie energii wiązania i wektora falowego elektronów [60, 61],

- Mikroskopy ze skanującą sondą- SPM (ang. *Scanning Probe Microscopy*) [62, 63]

- Skaningowy mikroskop tunelowy- STM (ang. *Scanning Tunneling Microscope*) - technika wykorzystująca znane z mechaniki kwantowej zjawisko tunelowania. Przyrząd ten daje możliwość uzyskania obrazu topograficznego badanej nanostruktury z rozdzielczością atomową na podstawie analizy prądu tunelowego, którego źródłem są elektrony tunelujące z podłoża do ostrza mikroskopu i na odwrót [64, 65].
- Mikroskop sił atomowych- AFM (ang. *Atomic Force Microscopy*) urządzenie pozwalające na obrazowanie badanych nanostruktur z dużą rozdzielczością sięgającą ułamków nanometrów dzięki pomiarowi siły oddziaływań elektrostatycznych między badaną próbką a ostrzem mikroskopu [66].

W metodach dyfrakcyjnych RHEED i LEED oraz technice ARPES analizie poddawany jest sygnał z obszaru makroskopowego, co wyklucza te metody do badania pojedynczych łańcuchów atomowych. Z drugiej strony metody te znajdują zastosowanie do badania regularnych matryc układów 1D otrzymywanych na powierzchniach wicynalnych.

Najlepszymi technikami spośród wyżej wymienionych są metody SPM. Pomimo wielu podobieństw, jakie łączą mikroskopy STM i AFM istnieją między nimi pewne różnice, które są szczególnie istotnie z punktu widzenia niniejszej pracy doktorskiej. Niewątpliwą zaletą AFM jest fakt, iż mikroskop ten jest w stanie badać zarówno materiały przewodzące, jak i nieprzewodzące prąd, co nie zawsze jest możliwe przy użyciu STM. Kolejną różnicą są wielkości fizyczne badane przez oba mikroskopy. AFM bada siły oddziaływania między próbką a ostrzem, STM natomiast prąd tunelowy między próbką a sondą pomiarową urządzenia. Technika ta świetnie sprawdza się do badania łańcuchów atomowych, ponieważ mikroskopy STM dysponują rozdzielczością atomową rzędu $0{,}1nm$ [64]. Oprócz badania topografii powierzchni, mikroskop STM może pracować w trybie STS (ang. *Scanning Tunneling Spectroscopy*) [67], co pozwala na uzyskanie informacji o przewodnictwie oraz lokalnej gęstości stanów badanych układów ($\frac{dI}{dV} \sim LDOS$), która jest najważniejszą i najczęściej analizowaną wielkością w niniejszej rozprawie. Ostrze mikroskopu STM może zostać potraktowane jako dodatkowa elektroda zewnętrzna w układzie (rezerwuar elektronów) i być uwzględnione w rozważaniach teoretycznych.

Rozdział 2

Opis teoretyczny

W rozdziale tym przedstawione zostaną stosowane przeze mnie techniki obliczeniowe do badania łańcuchów atomowych. Ponieważ w sferze moich zainteresowań oprócz normalnych łańcuchów atomowych, są także jednowymiarowe struktury topologiczne, omówione zostaną tutaj ich najważniejsze cechy.

2.1 Podstawy topologii

By zrozumieć, czym są topologiczne łańcuchy atomowe, najbardziej rozsądnym wydaje się rozpoczęcie od wyjaśnienia terminu topologia. W matematyce jest to dział zajmujący się badaniem takich właściwości obiektów, które nie ulegają zmianie nawet po radykalnym ich zdeformowaniu (figur geometrycznych, brył i obiektów o większej liczbie wymiarów) [68, 69], przy czym przez deformowanie rozumie się tutaj dowolne odkształcanie (zginanie, rozciąganie, skręcanie), ale bez rozrywania i zlepiania różnych części (homeomorfizm) [70]. Właściwości te matematycznie opisuje się za pomocą liczb charakterystycznych dla danej klasy topologicznie równoważnych obiektów, które zwane są niezmiennikami topologicznymi. Proces deformacji najłatwiej wyobrazić sobie przyjmując, że obiekt wykonano

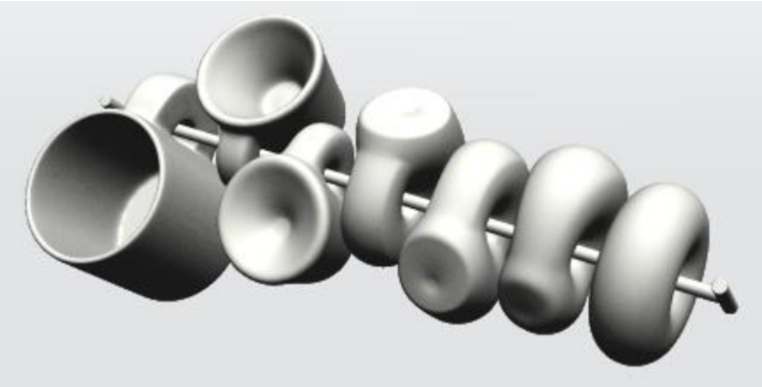

Rysunek 2.1: Wizualizacja obiektów homeomorficznych: kubek (pierwszy z lewej), torus (pierwszy z prawej), oraz niektóre z możliwych form pośrednich powstałych podczas procesu ciągłej deformacji.

z gumy. Rozciągając przedmiot wykonany z gumy, dokonujemy ciągłych deformacji, które zmieniają kształt obiektu. Pomimo przyjmowania różnych form, nasz obiekt pozostaje ciągle tym samym przedmiotem, czyli różne jego formy są sobie topologicznie równoważne. To oznacza, że rozciągając (ściskając) gumę, jesteśmy zdolni przejść od jednego kształtu do innego. Sytuacja zmienia się, gdy wskutek nadmiernego rozciągnięcia nasz przedmiot pęka. Wówczas nie jesteśmy już w stanie ciągłymi transformacjami wrócić do pierwotnej postaci przedmiotu. Mówimy wówczas, że te dwa stany nie są sobie topologicznie równoważne. Innym, najbardziej rozpowszechnionym przykładem jest pokazany na rysunku 2.1 kubek i donut (torus). Obiekty te charakteryzują się istnieniem jednej dziury (środek donuta oraz ucho kubka), co stanowi niezmiennik topologiczny tej klasy obiektów.

Wspomniana liczba dziur nie jest jedynym niezmiennikiem topologicznym charakteryzującym daną klasę równoważnych topologicznie obiektów. Wśród najbardziej popularnych liczb wyróżnia się m.in. charakterystykę Eulera. Charakterystyka ta została początkowo zaproponowana jako niezmiennik wielościanów wypukłych. Z czasem jednak definicja tego niezmiennika została poszerzona o dowolne wielościany (w tym torus). Liczbę tą definiuje się w następujący sposób [71]:

$$\chi = W - K + S, \tag{2.1}$$

gdzie W oznacza liczbę wierzchołków wielościanu, K liczbę krawędzi, natomiast S liczbę ścian. Charakterystyka ta dla wielościanów wypukłych, jak również dla sfery wynosi $\chi = 2$, co oznacza, że bryły te są topologicznie sobie równoważne. W przypadku torusa $\chi = 0$, co sprawia, że bryła ta należy do innej klasy obiektów topologicznych niż sfera i wielościany wypukłe.

Kolejnym przykładem niezmiennika topologicznego jest tzw. *winding number*. Niezmiennik ten określa ile razy skierowana krzywa zamknięta C obiega ustalony punkt P i jest zdefiniowany dla punktów, które nie leżą bezpośrednio na krzywej [72]. Niezmiennik ów przyjmuje wartości całkowite dodatnie (jeśli krzywa obiega punkt w kierunku przeciwnym do wskazówek zegara), ujemne (jeśli krzywa obiega punkt P w kierunku zgodnym z ruchem wskazówek zegara) oraz zero (jeśli punkt P leży na zewnątrz krzywej C), co pokazane zostało na rysunku 2.2.

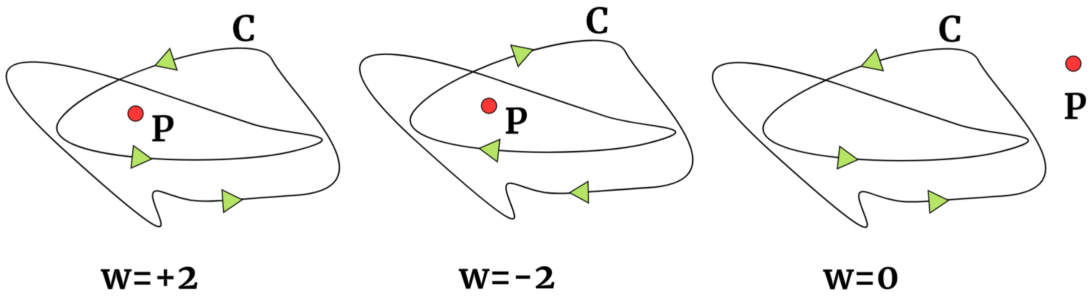

Rysunek 2.2: Winding number w krzywej skierowanej C względem punktu P. Lewa ilustracja odpowiada $w = 2$ - krzywa obiega punkt dwa razy w kierunku przeciwnym do wskazówek zegara. Środkowa grafika odpowiada $w = -2$ - dwa obiegi C wokół P w kierunku zgodnym z ruchem wskazówek zegara. Prawa ilustracja odpowiada $w = 0$, co oznacza, iż punkt P leży poza krzywą.

Poza wymienionymi niezmiennikami występuje szereg innych liczb, które często znajdują zastosowanie do opisu klasy materiałów topologicznych jak m.in. niezmiennik $\mathbb{Z}_2$ [73], faza Berry'ego [74], czy też liczby Cherna [75].

2.2 Model topologicznego łańcucha atomowego

Przełomem w pracach naukowców badających ciała stałe było odkrycie, iż te same zasady, które opisują krzywe, figury geometryczne, czy bryły nadają się do sklasyfikowania hamiltonianów, które pod wpływem ciągłych, powolnych (adiabatycznych) zmian zachowują np. przerwę energetyczną, którą możemy utożsamiać z dziurką w donucie (torusie). Zmiany, pod których wpływem przerwa energetyczna zostaje zamknięta, sprawiają, iż w materiale zachodzi topologiczne przejście fazowe, będące granicą między dwoma różnymi klasami porządku topologicznego.

Materiały topologiczne, jak to zostało wspomniane we wstępie, stanowią obecnie jedną z prężniej rozwijających się dziedzin fizyki materii skondensowanej. Uwaga naukowców nie skupia się tylko wokół materiałów litych, materiałów dwuwymiarowych, takich jak grafen, silicen, antymonen, ale również wokół materiałów takich jak struktury jednowymiarowe (łańcuchy atomowe/ łańcuchy kropek kwantowych). Moim głównym obiektem zainteresowania są obiekty jednowymiarowe, w tym też takie, które wykazują właściwości materiałów topologicznych.

W literaturze spotykamy wiele modeli topologicznych łańcuchów atomowych, wśród których możemy znaleźć łańcuch z niesparowanymi fermionami Majorany- model Kitayeva [76–78], łańcuch z magnetycznymi atomami na nadprzewodniku ze stanami Yu-Shiby-Rusinova [79–81], czy też łańcuch Su-Schrieffera-Heegera, który w niniejszej rozprawie stanowi główny model jednowymiarowego izolatora topologicznego ze względu na swoją prostotę i liczne sposoby eksperymentalnej realizacji [2,3,52,82,83]. Z tego powodu opisowi modelu Su-Schrieffera-Heegera poświęcony zostanie kolejny podrozdział.

2.2.1 Model Su-Schrieffera-Heegera

Łańcuch Su-Schrieffera-Heegera (SSH) jest modelem jednowymiarowego izolatora topologicznego z bazą dwuatomową. Wykazuje on istnienie dwóch faz topologicznych. Fazy te wyróżnia obecność (faza nietrywialna) lub brak (faza trywialna) stanów topologicznych na końcach łańcucha atomowego oraz przerwa energetyczna w jego wnętrzu [84]. Na rysunku 2.3 pokazano łańcuch SSH umieszczony na powierzchni złożony z N atomów, w którym wyodrębniono $N/2$ komórek dwuatomowych (na rysunku $N/2 = 3$). Każdy atom (węzeł) łańcucha atomowego, opisany jest stanem elektronowym o energii ε_l, który może być sprzężony z rezerwuarem elektronów (elektrodą podłoża). Sprzężenie między węzłami a podłożem opisuje parametr $V_{\vec{k}\alpha,l}$. Pomiędzy stanami elektronowymi wzdłuż łańcucha istnieją niezerowe całki przeskoku V_{lm}, które dla sprzężeń międzykomórkowych oznaczamy symbolem w, natomiast w obrębie pojedynczej komórki jako v.

Hamiltonian pojedynczego łańcucha atomowego uwzględnia energie elektronów elektrod- człon $\mathcal{A}$ w równaniu 2.2, energie elektronów na poszczególnych węzłach łańcucha atomowego- człon $\mathcal{B}$, sprzężenia między elektrodą (elektrodami) a łańcuchem- człony $\mathcal{C}, \mathcal{D}$ oraz sprzężenia między stanami

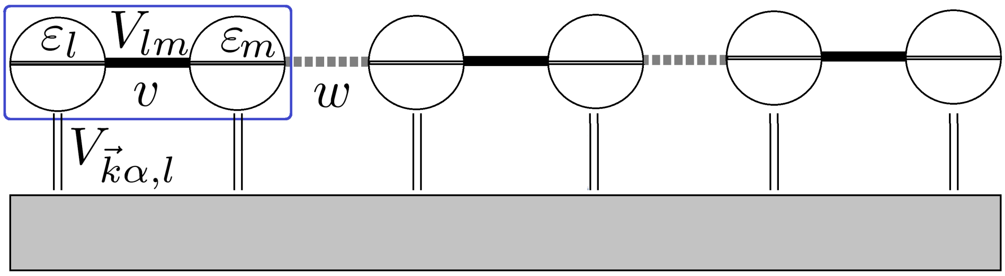

Rysunek 2.3: Model łańcucha SSH z bazą dwuatomową (zaznaczone prostokątną ramką) umieszczonego na podłożu. Sprzężenia między stanami elektronowymi sąsiadujących ze sobą atomów V_{lm} (całki przeskoku) przyjmują dwie wartości: v - całka przeskoku w obrębie komórki, oraz w - całki przeskoku między sąsiednimi komórkami. Poziomy energetyczne stanów elektronowych na poszczególnych węzłach oznaczono symbolami $\varepsilon_l, \varepsilon_m$. Za sprzężenie l-tego węzła z elektrodą α odpowiada parametr $V_{\vec{k}\alpha,l}$.

elektronowymi atomów łańcucha- człon $\mathcal{E}$. W modelu SSH zakładamy, iż wzajemny wpływ mają na siebie jedynie sąsiadujące ze sobą węzły, tzn. $V_{lm} \neq 0 \iff l = m \pm 1$, w przeciwnym wypadku $V_{lm} = 0$. Ponadto V_{lm} przyjmuje jedną z dwóch nieujemnych rzeczywistych wartości: v dla sprzężeń w obrębie tej samej komórki oraz w dla sprzężeń między stanami elektronowymi atomów z sąsiednich komórek [85].

$$\hat{H} = \underbrace{\sum_{\vec{k},\alpha} \varepsilon_{\vec{k}\alpha} \hat{a}^\dagger_{\vec{k}\alpha}\hat{a}_{\vec{k}\alpha}}_{\mathcal{A}} + \sum_{l=1}^{N}\Bigg(\underbrace{\varepsilon_l \hat{a}^\dagger_l \hat{a}_l}_{\mathcal{B}} + \underbrace{\sum_{\vec{k},\alpha} V_{\vec{k}\alpha,l}\hat{a}^\dagger_{\vec{k}\alpha}\hat{a}_l}_{\mathcal{C}} + \underbrace{\sum_{\vec{k},\alpha}\left(V_{\vec{k}\alpha,l}\right)^* \hat{a}^\dagger_l \hat{a}_{\vec{k}\alpha}}_{\mathcal{D}} + \underbrace{\sum_{m=1}^{N} V_{lm}\hat{a}^\dagger_l\hat{a}_m}_{\mathcal{E}}\Bigg). \tag{2.2}$$

W badaniach składających się na niniejszą rozprawę używana była rozszerzona wersja hamiltonianu, która uwzględnia oddziaływania spin-orbita, odpychania kulombowskie, czasowe zależności całek przeskoku, różne geometrie układu i inne efekty związane z podłożem i zaburzeniami zewnętrznymi.

2.2.2 Fazy topologiczne w modelu SSH

Obecność faz topologicznych w strukturach jednowymiarowych jest ściśle związana ze sprzężeniami v oraz w. By dostrzec tę zależność rozpatrzmy łańcuch atomowy odizolowany od podłoża, w którym energie poszczególnych węzłów są sobie równe i wynoszą $\varepsilon_l = 0$. Wówczas jedynym czynnikiem hamiltonianu 2.2, na który musimy skupić uwagę, jest jego część $\mathcal{E}$, która nazywana jest też hamiltonianem przeskoku. Wychodząc z założenia, że w naszym łańcuchu elektrony mogą poruszać się tylko pomiędzy sąsiadującymi stanami, możemy zapisać (przyjmując dla wygody oznaczenia operatorów kreacji/anihilacji w i-tej komórce jako $a_i^{(\dagger)}, b_i^{(\dagger)}$):

$$\mathcal{H} = \sum_{l=1}^{N}\sum_{m=1}^{N} V_{l,m}\hat{a}^\dagger_l\hat{a}_m = v\sum_{i=1}^{\lfloor N/2 \rfloor}\hat{a}^\dagger_i\hat{b}_i + w\sum_{i=1}^{\lceil N/2 \rceil - 1}\hat{b}^\dagger_i\hat{a}_{i+1}. \tag{2.3}$$

Dokonując przejścia do reprezentacji pędowej hamiltonianu przeskoku $\hat{a}_i \to \hat{a}_k$, uwzględniając, że elektrony w łańcuchu mogą poruszać się tylko w jednym kierunku ($\vec{k} \to k$), oraz przyjmując, że stała sieci ma wartość 1 dostajemy [84, 85]:

$$\tilde{\mathcal{H}} = \sum_k v\left(\hat{a}_k^\dagger \hat{b}_k + \hat{b}_k \hat{a}_k^\dagger\right) + w\left(e^{-ik}\hat{b}_k^\dagger \hat{a}_k + e^{ik}\hat{a}_k^\dagger \hat{b}_k\right). \tag{2.4}$$

Wykorzystując tożsamość Eulera, możemy zapisać otrzymany po transformacie Fouriera hamiltonian w postaci kanonicznej:

$$\tilde{\mathcal{H}} = \sum_k (v + w\cos k)\left(\hat{b}_k^\dagger \hat{a}_k + \hat{a}_k^\dagger \hat{b}_k\right) + iw\sin k\left(-\hat{b}_k^\dagger \hat{a}_k + \hat{a}_k^\dagger \hat{b}_k\right). \tag{2.5}$$

Traktując operatory kreacji/anihilacji jako współrzędne wektorów w przestrzeni pędowej, możemy zapisać hamiltonian 2.5 w postaci:

$$\tilde{\mathcal{H}} = \begin{bmatrix} \hat{a}_k^\dagger & \hat{b}_k^\dagger \end{bmatrix} \begin{bmatrix} 0 & (v + w\cos k) + i(w\sin k) \\ (v + w\cos k) - i(w\sin k) & 0 \end{bmatrix} \begin{bmatrix} \hat{a}_k \\ \hat{b}_k \end{bmatrix}. \tag{2.6}$$

Definiując $R_x(k) = v + w\cos k$, $R_y(k) = w\sin k$, $R_z = 0$ oraz wykorzystując macierze Pauliego dostajemy hamiltonian w kompaktowej formie [86]:

$$\tilde{\mathcal{H}} = \begin{bmatrix} \hat{a}_k^\dagger & \hat{b}_k^\dagger \end{bmatrix} \hat{H}_k \begin{bmatrix} \hat{a}_k \\ \hat{b}_k \end{bmatrix}, \tag{2.7}$$

gdzie:

$$\hat{H}_k = R_x(k)\cdot\hat{\sigma}_x + R_y(k)\cdot\hat{\sigma}_y = \mathbf{R}(k)\cdot\hat{\sigma}. \tag{2.8}$$

Wykreślając wektor $\mathbf{R}(k)$ w przestrzeni $\{r_x, r_y\}$, biorąc liczby falowe omiatające pierwszą strefę Brillouin'a $-\pi \rightarrow \pi$, zauważamy, iż zatacza on pewną krzywą zamkniętą, co zostało pokazane na rysunku 2.4. Co ciekawe położenie tej krzywej zależy od wartości sprzężeń v i w. Jak widzimy na lewej ilustracji, która odpowiada sprzężeniom $v > w$ skierowana krzywa zamknięta, którą wyznaczył grot wektora $\mathbf{R}$ ani razu nie obiega punktu O, będącego środkiem układu współrzędnych. Na ilustracji prawej, gdzie $v > w$ skierowana krzywa zamknięta otacza punkt O dokładnie jeden raz. W tym momencie możemy dostrzec podobieństwo tych krzywych do krzywych ukazanych na rysunku 2.2. Jak możemy się domyśleć, nie jest to przypadkowe podobieństwo i na rysunku 2.4 przedstawione są dwie różne fazy topologiczne łańcucha atomowego, które scharakteryzowane są różnymi wartościami niezmiennika *winding number*. Ilustracja lewa odpowiada trywialnej fazie topologicznej łańcucha SSH, dla której wartość niezmiennika wynosi 0. Prawa ilustracja pokazuje nietrywialną fazę topologiczną, której odpowiada *winding number* $= 1$. Należy również wspomnieć, że w przypadku $v = w$ otrzymujemy normalny łańcuch atomowy, dla którego liczba *winding number* jest niezdefiniowana. Jak zatem widzimy narzędzie matematyczne służące pierwotnie do badania obiektów geometrycznych stanowi doskonały „detektor" rozróżniający fazy występujące w łańcuchach atomowych.

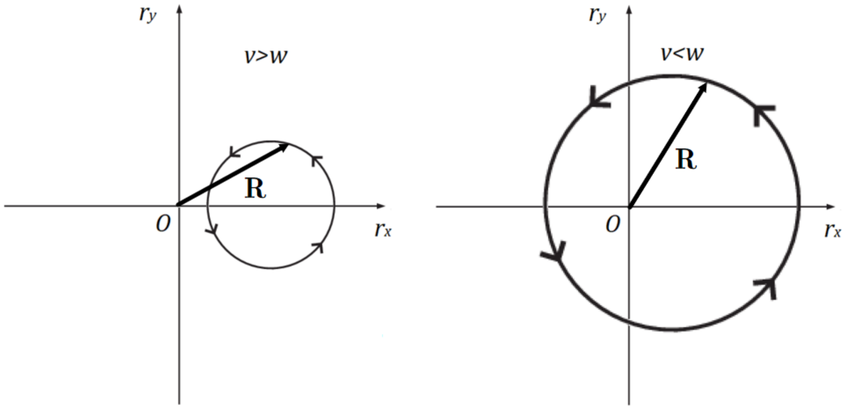

Rysunek 2.4: Skierowane krzywe zamknięte zatoczone przez grot wektora $\mathbf{R}(\mathbf{k})$ powstałe na skutek ciągłej transformacji liczby falowej k omiatającej pierwszą strefę Brillouin'a. Lewa ilustracja odpowiada łańcuchowi SSH w trywialnej fazie topologicznej, prawa zaś nietrywialnej.

2.3 Stacjonarne właściwości elektryczne łańcuchów atomowych

2.3.1 Funkcje Greena w opisie układów atomowych

Funkcje Greena pełnią ważną rolę w fizyce, a w szczególności fizyce kwantowej [87–90]. Funkcje te są powszechnie stosowanym narzędziem do opisu problemów wielociałowych. Niewątpliwą zaletą owych funkcji jest przejrzystość i prostota opisu skomplikowanych systemów mikroskopowych, oraz ich bezpośredni związek z wielkościami mierzonymi eksperymentalnie.

Formalizm funkcji Greena może być stosowany zarówno do opisu układów w stanie równowagi termodynamicznej, w procesach nierównowagowych, jak i do opisu zjawisk niestacjonarnych, zmiennych w czasie (np. w obecności zewnętrznych pól elektromagnetycznych) [91, 92]. W literaturze występuje liczna grupa funkcji Greena, które znajdują zastosowanie do rozwiązywania specyficznych problemów fizycznych. Do grupy tej należą m.in. funkcja Greena Matsubary, przedwczesna, opóźniona, większa, mniejsza, jak i wiele innych, które często są od siebie zależne. W tej rozprawie obliczenia własności elektrycznych łańcuchów atomowych będą oparte o tzw. opóźnioną (retardowaną) funkcję Greena, która dla fermionowych operatorów definiowana jest następująco [93, 94]:

$$G^R_{AB}(t,t') = \ll \hat{A}(t); \hat{B}(t') \gg = -\frac{i}{\hbar}\theta(t,t')\,\langle[\hat{A}(t), \hat{B}(t')]\rangle\,, \tag{2.9}$$

gdzie θ oznacza funkcję schodkową Heavyside'a $\theta\,(t-t') = -\frac{1}{2\pi i}\int_{-\infty}^{\infty} dE\frac{e^{-iE(t-t')}}{E+i\eta}$, w której energia zawiera infinitezymalny czynnik urojony $E^+ = E + i\eta$, który eliminuje nieciągłości mogące występować na rzeczywistej osi energii. Dodatkowo funkcja ta jest związana z funkcją delta Diraca następującą zależnością $\frac{d}{dt}\theta(t,t') = \delta(t,t')$. Zwracając uwagę na fakt, iż ślad macierzy jest wielkością zachowaną przy cyklicznych permutacjach operatorów $\widehat{A}(t)$ i $\widehat{B}\,(t')$:

$$\begin{aligned}
&\mathrm{Tr}\left(\widehat{A}(t)\widehat{B}\,(t')\right) = \mathrm{Tr}\left(e^{i\hat{H}t}\widehat{A}e^{-i\hat{H}t}e^{i\hat{H}t'}\widehat{B}e^{-i\hat{H}t'}\right) = \mathrm{Tr}\left(e^{i\hat{H}t}\widehat{A}e^{-i\hat{H}(t-t')}\widehat{B}e^{-i\hat{H}t'}\right) \\
&= \mathrm{Tr}\left(e^{i\hat{H}(t-t')}\widehat{A}e^{-i\hat{H}(t-t')}\widehat{B}\right) = \mathrm{Tr}\left(\widehat{A}\,(t-t')\,\widehat{B}(0)\right),
\end{aligned} \tag{2.10}$$

możemy zapisać retardowaną funkcję Greena, która fizycznie interpretowana jest jako odpowiedź układu fermionów w czasie t' na zaburzenie występujące w chwili t, jako funkcję jednego parametru czasowego t, kładąc $t' = 0$:

$$G^R_{AB}(t, t' = 0) = G^R_{AB}(t) = \ll \hat{A}(t); \hat{B} \gg = -i\theta(t) \left\langle [\hat{A}(t), \hat{B}] \right\rangle . \tag{2.11}$$

Różniczkując po czasie równanie 2.11, oraz dokonując prostych przekształceń, otrzymujemy równanie ruchu retardowanej funkcji Greena w domenie czasowej [95, 96] :

$$i\frac{d}{dt}G^R_{AB}(t) = \delta(t) \left\langle \left[\hat{A}(t), \hat{B}\right] \right\rangle - i\theta(t) \left\langle \left[\left[\hat{A}(t), \hat{H}\right], \hat{B}\right] \right\rangle , \tag{2.12}$$

które po dokonaniu transformaty Fouriera możemy przedstawić w postaci widmowej (energetycznej):

$$E \left\langle\left\langle \hat{A}; \hat{B} \right\rangle\right\rangle_E = \left\langle \left[\hat{A}, \hat{B}\right] \right\rangle + \left\langle\left\langle \left[\hat{A}, \hat{H}\right]; \hat{B} \right\rangle\right\rangle_E . \tag{2.13}$$

Równanie 2.13, noszące nazwę równania ruchu dla retardowanej funkcji Greena w postaci energetycznej jest niezwykle cennym równaniem, gdyż znajomość tej funkcji Greena pozwala wyznaczyć takie właściwości elektryczne jak [97–99]:

- Lokalna gęstość stanów i-tego stanu łańcucha atomowego:

  $$LDOS_i(E) \equiv \rho_i(E) = -\frac{1}{\pi}\Im(G^R_{i,i}(E^+)). \tag{2.14}$$

- Obsadzenia ładunkowe stanu i:

  $$n_i = \int_{-\infty}^{E_F} LDOS_i(E)dE, \tag{2.15}$$

  gdzie E_F oznaczają energię Fermiego elektrody/podłoża.

- Transmitancja [95, 100]:

  $$T(E) = tr(\hat{\Gamma}_\alpha \hat{G}^R \hat{\Gamma}_\beta \hat{G}^A), \tag{2.16}$$

  gdzie macierze $\hat{\Gamma}_{\alpha,\beta}$ odpowiadają za sprzężenie łańcucha z α-tą i β-tą elektrodą, co zostanie dokładniej opisane w dalszej części rozprawy.

- Prąd między elektrodami o energiach Fermiego E^α_f i E^β_f:

  $$I = \frac{2e}{\hbar}\int_{-\infty}^{+\infty} (f_\alpha - f_\beta)\, T(E)dE = \frac{2e}{\hbar}\int_{E^\beta_f}^{E^\alpha_f} T(E)dE, \tag{2.17}$$

  gdzie $f_{\alpha,\beta}$ to funkcje Fermiego tychże elektrod. Całka po pełnym zakresie energetycznym zastąpiona została do zakresu energii Fermiego między elektrodami w temperaturze $0K$.

2.3.2 Łańcuch atomowy na powierzchni

W tym podrozdziale pokazane zostanie zastosowanie równania ruchu retardowanej funkcji Greena do opisu łańcucha atomowego złożonego z N węzłów, sprzężonego z elektrodami/podłożem. Obliczymy funkcję Greena związaną z węzłami łańcucha, dla których występujące w hamiltonianie fermionowe operatory kreacji i anihilacji i-tego atomu, oznaczone są odpowiednio jako $\hat{a}_i$ oraz $\hat{a}_i^\dagger$. Operatory te spełniają zależności antykomutacyjne: $[\hat{a}_i, \hat{a}_j]_+ = \left[\hat{a}_i^\dagger, \hat{a}_j^\dagger\right]_+ = 0$; $\left[\hat{a}_i, \hat{a}_{\vec{k}\alpha}^\dagger\right]_+ = \left[a_i^\dagger, \hat{a}_{\vec{k}\alpha}\right]_+ = 0$; $\left[\hat{a}_i, \hat{a}_j^\dagger\right]_+ = \delta_{i,j}$; $\left[a_{\vec{k}\alpha}, a_{\vec{k}_2\beta}^\dagger\right]_+ = \delta_{\alpha,\beta}$. Dla operatorów kreacji/anihilacji elektronu w obrębie węzłów łańcucha atomowego równanie ruchu ma postać:

$$EG_{i,j}^R = \langle \left[\hat{a}_i^\dagger, \hat{a}_j\right]_+ \rangle + \langle\langle \left[\hat{a}_i^\dagger, \hat{H}\right]_- ; \hat{a}_j \rangle\rangle_E^R . \tag{2.18}$$

Zapisując komutator operatora anihilacji z hamiltonianem 2.2:

$$\left[\hat{a}_i, \underbrace{\sum_{\vec{k},\alpha} \varepsilon_{\vec{k}\alpha} \hat{a}_{\vec{k}\alpha}^\dagger \hat{a}_{\vec{k}\alpha}}_{\mathcal{A}} + \sum_{l=1}^{N} \left(\underbrace{\varepsilon_l \hat{a}_l^\dagger \hat{a}_l}_{\mathcal{B}} + \underbrace{\sum_{\vec{k},\alpha} V_{\vec{k}\alpha,l} \hat{a}_{\vec{k}\alpha}^\dagger \hat{a}_l}_{\mathcal{C}} + \underbrace{\sum_{\vec{k},\alpha} \left(V_{\vec{k}\alpha,l}\right)^* \hat{a}_l^\dagger \hat{a}_{\vec{k}\alpha}}_{\mathcal{D}} + \underbrace{\sum_{m=1}^{N} V_{l,m} \hat{a}_l^\dagger \hat{a}_m}_{\mathcal{E}} \right)\right], \tag{2.19}$$

dostajemy następujące niezerowe jego elementy:

człon $\mathcal{B}$:

$$\left[\hat{a}_i, \sum_{l=1}^{N} \varepsilon_l \hat{a}_l^\dagger \hat{a}_l\right] = \varepsilon_i \hat{a}_i, \tag{2.20}$$

człon $\mathcal{D}$:

$$\left[\hat{a}_i, \sum_{l=1}^{N} \sum_{\vec{k},\alpha} \left(V_{\vec{k}\alpha,l}\right)^* \hat{a}_l^\dagger a_{\vec{k}\alpha}\right] = \sum_{\vec{k},\alpha} (V_{\vec{k}\alpha,l})^* \hat{a}_{\vec{k}\alpha}, \tag{2.21}$$

człon $\mathcal{E}$:

$$\left[\hat{a}_i, \sum_{l=1}^{N} \sum_{m=1}^{N} V_{m,l} \hat{a}_l^\dagger \hat{a}_m\right] = \sum_{m=1}^{N} V_{i,m} \hat{a}_m . \tag{2.22}$$

Wykorzystując obliczone komutatory i właściwości antykomutacyjne operatorów kreacji/anihilacji możemy zapisać równanie ruchu 2.18 w postaci:

$$EG_{i,j}^R = \delta_{i,j} + \varepsilon_i G_{i,j}^R + \sum_{m=1}^{N} V_{i,m} G_{m,j}^R + \sum_{\vec{k},\alpha} \left(V_{\vec{k}\alpha,l}\right)^* \underline{G_{\vec{k}\alpha,j}^R} . \tag{2.23}$$

Jak widzimy równanie 2.23 zawiera element mieszany $G_{\vec{k}\alpha,j}^R$, który możemy wyznaczyć, korzystając po raz wtóry z równania ruchu dla retardowanej funkcji Greena.

$$EG_{\vec{k}\alpha,j}^R = \langle \left[\hat{a}_{\vec{k}\alpha}, \hat{a}_j^\dagger\right]_+ \rangle + \langle\langle \left[\hat{a}_{\vec{k}\alpha}, \hat{H}\right]_- ; \hat{a}_j^\dagger \rangle\rangle_E^R . \tag{2.24}$$

Podobnie jak w równaniu 2.18 musimy obliczyć komutator operatora anihilacji stanów elektronowych elektrod i hamiltonianu:

$$\left[\hat{a}_{\vec{k}\alpha}, \underbrace{\sum_{\vec{k}_2\beta} \varepsilon_{\vec{k}_2\beta} \hat{a}_{k'\beta}^\dagger \hat{a}_{\vec{k}_2\beta}}_{\mathcal{A}} + \sum_{l=1}^{N} \left(\underbrace{\varepsilon_\varepsilon \hat{a}_l^\dagger \hat{a}_l}_{\mathcal{B}} + \underbrace{\sum_{\vec{k}',\beta} V_{\vec{k}_2\beta,l} \hat{a}_{\vec{k}_2\beta}^\dagger \hat{a}_l}_{\mathcal{C}} + \underbrace{\sum_{\vec{k}',\beta} \left(V_{\vec{k}_2\beta,l}\right)^* \hat{a}_l^\dagger \hat{a}_{\vec{k}_2\beta}}_{\mathcal{D}} + \underbrace{\sum_{m=1}^{N} V_{l,m} \hat{a}_l^\dagger \hat{a}_m}_{\mathcal{E}} \right)\right]. \tag{2.25}$$

W wyniku otrzymujemy dwa niezerowe elementy: pierwszy z członu $\mathcal{A}$: $\left[\hat{a}_{\vec{k}\alpha}, \sum_{\vec{k}_2,\beta} \varepsilon_{\vec{k}_2\beta} \hat{a}_{\vec{k}_2\beta}^\dagger \hat{a}_{\vec{k}_2\beta}\right] = \varepsilon_{\vec{k}\alpha} \hat{a}_{\vec{k}\alpha}$, natomiast drugi z członu $\mathcal{C}$: $\left[\hat{a}_{\vec{k}\alpha}, \sum_{l=1}^{N} \sum_{\vec{k}_2,\beta} V_{\vec{k}_2\beta,l} \hat{a}_{\vec{k}_2\beta}^\dagger \hat{a}_l\right] = \sum_{l=1}^{N} V_{\vec{k}\alpha,l} \hat{a}_l$. Po obliczeniu wszystkich komutatorów możemy przystąpić do zapisania równania ruchu 2.24 w nowej postaci:

$$EG_{\vec{k}\alpha,j}^R = \varepsilon_{\vec{k}\alpha} G_{\vec{k}\alpha,j}^R + \sum_{l=1}^{N} V_{\vec{k}\alpha,l} G_{l,j}^R . \tag{2.26}$$

Dokonując prostych przekształceń równania 2.26, możemy znaleźć, postać mieszanych elementów macierzowych retardowanej funkcji Greena:

$$G^R_{\vec{k}\alpha,j} = \sum_{l=1}^{N} \frac{V_{\vec{k}\alpha,l}}{E - \varepsilon_{\vec{k}\alpha}} G^R_{l,j}. \tag{2.27}$$

Wstawiając otrzymany wynik do równania 2.23, uzyskujemy równanie, w którym pojawia się następująca suma zwana energią własną (*selfenergy*):

$$\sum_{\vec{k},\alpha} \frac{V_{\vec{k}\alpha,l}(V_{\vec{k}\alpha,m})^*}{E - \varepsilon_{\vec{k}\alpha}} = \Sigma_{l,m}(E) = \Lambda_{l,m}(E) + i\frac{\Gamma_{l,m}(E)}{2}. \tag{2.28}$$

Tutaj funkcja $\Gamma_{l,m}(E)$ opisuje efektywne sprzężenie pomiędzy stanami elektronowymi atomów łańcucha a kontinuum stanów elektrody i jest zdefiniowana w następujący sposób:

$$\Gamma_{l,m}(E) = 2\pi \sum_{\vec{k}\alpha} V_{\vec{k}\alpha,l}(V_{\vec{k}\alpha,m})^* \delta\left(E - \varepsilon_{\vec{k}\alpha}\right). \tag{2.29}$$

Funkcja ta jest związana z gęstością stanów elektronowych podłoża i odpowiada za poszerzenie/rozmycie stanów łańcucha spowodowane ich sprzężeniem z kontinuum stanów $\vec{k}$. Funkcja $\Lambda_{l,m}(E)$ natomiast jest transformatą Hilberta funkcji $\Gamma_{l,m}(E)$ [101]:

$$\Lambda_{l,m}(E) = \frac{1}{2\pi} \int_{-\infty}^{+\infty} \frac{\Gamma_{l,m}(E')}{E - E'} dE'. \tag{2.30}$$

Dla powierzchni charakteryzujących się płaską (lub wolnozmienną) gęstością stanów w funkcji energii, bez lokalnych ekstremów, czy też przerw energetycznych (warunki takie są spełnione dla nanostruktur Pb na powierzchni Si(553)-Au [102]) można zastosować tzw. przybliżenie nieskończenie szerokiego pasma- WBL (ang. *Wide-Band Limit*). Zakładając niezależność sprzężeń $V_{\vec{k}\alpha,l}$ od wektora falowego funkcja $\Gamma_{l,m}(E)$ jest stała i niezależna od energii. Oznacza to, że jej transformata Hilberta jest równa zero, tak więc funkcja Σ zachowuje jedynie swą urojoną część [103]. Przybliżenie WBL nie jest spełnione dla powierzchni/elektrod charakteryzujących się nieciągłościami typu van Hove'a w strukturze DOS, jakie pojawiają się w sieciach 2D: prostokątnej lub heksagonalnej, które były przedmiotem moich badań w pracy doktorskiej. W przybliżeniu WBL funkcja spektralna Γ mimo, iż jest niezależna od energii, to może zależeć od położeń poszczególnych atomów układu leżących na wspólnej elektrodzie. Funkcja ta dla $l = m$ opisuje procesy wymiany elektronów pomiędzy danym stanem łańcucha a podłożem, natomiast dla $l \neq m$ dotyczy procesów złożonych wymiany elektronów między stanami na węźle l i węźle m poprzez podłoże. Zakładając, że odległości między sąsiednimi atomami są równe, z równania 2.29 otrzymujemy [103–105]:

$$\Gamma_{l,m} = \Gamma_S \frac{sin\,(k_F a r_{l,m})}{k_F a r_{l,m}}, \tag{2.31}$$

gdzie Γ_S opisuje efektywne sprzężenie między łańcuchem atomowym a podłożem, k_F jest liczbą falową na poziomie Fermiego, a jest stałą sieci, natomiast $r_{l,m}$ jest bezwymiarowym parametrem opisującym odległość między atomami. Iloczyn $k_F a$ odpowiada za lokalizację elektronów w podłożu. W przypadku $k_F a \to 0$ elektrony w podłożu są silnie zdelokalizowane, co sprawia, że elektron, który przetunelował do podłoża może pojawić się na dowolnym węźle łańcucha, co odpowiada podłożom metalicznym. W przypadku bardzo dużych wartości $k_F a \gg 1$ elektrony tracą możliwość przemieszczania się między węzłami łańcucha za pośrednictwem elektrody, co odpowiada podłożom izolatorowym, $\Gamma_{l,m} = \delta_{l,m}\Gamma_S$ i oznacza, że każdy atom łańcucha jest efektywnie sprzężony z osobną elektrodą.

Równanie ruchu retardowanej funkcji Greena dla łańcucha atomowego 2.23 stanowi układ sprzężonych równań algebraicznych i wygodnie jest zapisać go w postaci macierzowej $\hat{A} \cdot \hat{G}^R = \hat{I}$, gdzie $\hat{G}^R$ jest macierzą retardowanych funkcji Greena, $\hat{I}$ macierzą jednostkową, natomiast macierz $\hat{A}$ zdefiniowana jest w następujący sposób:

$$\hat{A} = \begin{bmatrix} E-\varepsilon_1+\Sigma_{1,1}(E) & -V_{1,2}+\Sigma_{1,2}(E) & \Sigma_{1,3}(E) & \dots & \Sigma_{1,N}(E) \\ -V_{2,1}+\Sigma_{2,1}(E) & E-\varepsilon_2+\Sigma_{2,2}(E) & -V_{2,3}+\Sigma_{2,3}(E) & \dots & \Sigma_{2,N}(E) \\ \vdots & \vdots & \vdots & \ddots & \vdots \\ \Sigma_{N,1}(E) & \Sigma_{N,2}(E) & \Sigma_{N,3}(E) & \dots & E-\varepsilon_N+\Sigma_{N,N}(E) \end{bmatrix}. \tag{2.32}$$

Obliczanie funkcji Greena sprowadza się do znalezienia macierzy odwrotnej do $\hat{A}$, co niestety nie zawsze jest zadaniem trywialnym, np. przy uwzględnieniu oddziaływań kulombowskich, czy dla zadanych gęstości stanów elektrody podłoża. Na szczęście dla regularnych łańcuchów atomowych spoczywających na powierzchniach izolatorowych, scharakteryzowanych niezależnym od energii efektywnym sprzężeniem Γ istnieją metody pozwalające wyznaczyć analitycznie retardowane funkcje Greena, co pokazane zostanie w kolejnym podrozdziale.

2.3.3 Analityczne rozwiązania dla układów atomowych

Celem lepszego zaznajomienia się z właściwościami elektrycznymi łańcuchów atomowych, w podrozdziale tym omówione zostaną cechy prostych układów jednowymiarowych umieszczonych na powierzchni, dla których można podać rozwiązania analityczne na retardowane funkcje Greena. Najprostszymi strukturami na powierzchni (pojedyncza elektroda), od których zaczniemy analizę, są: pojedynczy atom oraz układ dwuatomowy, co przedstawione jest na rysunku 2.5.

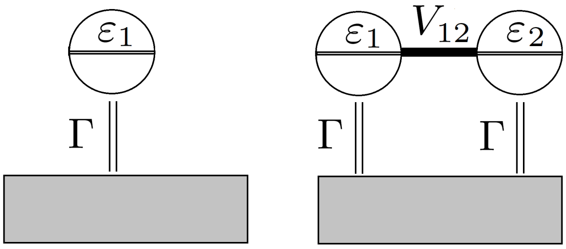

Rysunek 2.5: Proste struktury atomowe: pojedynczy atom (lewy panel) oraz układ dwuatomowy (prawy panel) spoczywające na powierzchni, scharakteryzowanych niezależnym od energii efektywnym sprzężeniem Γ. ε_1, ε_2 oznaczają poziomy energetyczne elektronów na poszczególnych węzłach, natomiast V_{12} oznacza całkę przeskoku między węzłami.

W przypadku pojedynczego atomu znalezienie retardowanej funkcji Greena jest zadaniem trywialnym. Wynosi ona bowiem $\hat{G}^R = \frac{1}{E-\varepsilon_1+i\frac{\Gamma}{2}}$. Znając postać tejże funkcji, możemy policzyć lokalną gęstość stanów związaną z atomem na powierzchni, korzystając z równania 2.14.

$$\rho_1(E) = -\frac{1}{\pi} Im \left[G^R_{11}\right] = -\frac{1}{\pi} Im \left[\frac{1}{E-\varepsilon_1+i\frac{\Gamma}{2}}\right] = \frac{\frac{\Gamma}{2}}{\pi\left[(E-\varepsilon_1)^2+\frac{\Gamma^2}{4}\right]}. \tag{2.33}$$

Gęstość ta przyjmuje postać funkcji typu Lorentza, której maksimum odpowiada energii $E = \varepsilon_1$, natomiast szerokość połówkowa związana jest z wartością efektywnego sprzężenia stanu elektronowego atomu z podłożem, Γ, co przedstawia krzywa fioletowa na rysunku 2.6 (dla $\Gamma \to 0$ otrzymujemy granicę atomową gęstości stanów).

Znając lokalną gęstość stanów, jesteśmy w stanie policzyć prawdopodobieństwo obsadzenia stanu elektronowego atomu, zwane tutaj obsadzeniem ładunkowym lub krócej ładunkiem na atomie.

$$n = \int_{-\infty}^{E_F} \rho_1(E)dE = \frac{1}{\pi}\int_{-\infty}^{E_F} \frac{\frac{\Gamma}{2}}{(E-\varepsilon_1)^2+\frac{\Gamma^2}{4}}dE = \frac{1}{\pi}\,\mathrm{atg}\left(\frac{2(E_F-\varepsilon_1)}{\Gamma}\right)+\frac{1}{2}. \tag{2.34}$$

Jak widzimy, obsadzenie ładunkowe jest bezpośrednio związane z różnicą pomiędzy energią Fermiego elektrody a poziomem energetycznym elektronu na węźle. Przyjmując $\varepsilon_1 = E_F$, stan elektronowy atomu na powierzchni jest obsadzony z prawdopodobieństwem równym $\frac{1}{2}$. Wynika to z faktu, iż lokalna gęstość stanów jest symetryczna względem ε_1 i co za tym idzie, dokładnie połowa gęstości stanów znajduje się poniżej energii Fermiego. W przypadku, gdy $E_F \gg \varepsilon_1$ cała gęstość stanów znajduje się poniżej energii Fermiego i obsadzenie wynosi $n = 1$. W przeciwnym wypadku ($E_F \ll \varepsilon_1$) stan atomu na powierzchni pozostaje nieobsadzony, co pokazuje krzywa fioletowa na rysunku 2.7.

Równanie ruchu dla układu dwuatomowego jest równaniem macierzowym, którego elementami są macierze kwadratowe 2×2 (w przypadku przybliżenia WBL i dla podłoża izolatorowego $\Gamma_{ij} = \delta_{ij}\Gamma$).

$$\begin{bmatrix} E - \varepsilon_1 + i\frac{\Gamma}{2} & -V_{12} \\ -V_{21} & E - \varepsilon_2 + i\frac{\Gamma}{2} \end{bmatrix} \begin{bmatrix} G^R_{11} & G^R_{12} \\ G^R_{21} & G^R_{22} \end{bmatrix} = I. \tag{2.35}$$

Macierz retardowanych funkcji Greena można wyznaczyć w następujący sposób:

$$\hat{G}^R = \frac{\hat{A}^D}{\det(\hat{A})}, \tag{2.36}$$

gdzie $\hat{A}^D$ jest macierzą dopełnień algebraicznych $\hat{A}$, natomiast $\det(\hat{A}) = \left(E - \varepsilon_1 + i\frac{\Gamma}{2}\right)\left(E - \varepsilon_2 + i\frac{\Gamma}{2}\right) - V_{12}^2$. W celu wyznaczenia lokalnej gęstości stanów dla pierwszego i drugiego atomu musimy wyznaczyć elementy diagonalne macierzy $\hat{G}^R$:

$$G^R_{ii} = \frac{1}{\left(E - \varepsilon_i + i\frac{\Gamma}{2}\right) - \frac{V_{12}^2}{\left(E - \varepsilon_{i\pm1} + i\frac{\Gamma}{2}\right)}}, \tag{2.37}$$

co pozwala nam znaleźć lokalną gęstość stanów:

$$\rho_i = -\frac{1}{\pi}\,\mathrm{Im}\left[G^R_{ii}\right] = \frac{1}{\pi}\frac{\frac{\Gamma}{2} + \frac{V_{12}^2\frac{\Gamma}{2}}{\left(E-\varepsilon_{i\pm1}\right)^2 + \frac{\Gamma^2}{4}}}{\left(E - \varepsilon_i - \frac{V_{12}^2\left(E-\varepsilon_{i\pm1}\right)}{\left(E-\varepsilon_{i\pm1}\right)^2 + \frac{\Gamma^2}{4}}\right)^2 + \left(\frac{\Gamma}{2} + \frac{V_{12}^2\frac{\Gamma}{2}}{\left(E-\varepsilon_{i\pm1}\right)^2 + \frac{\Gamma^2}{4}}\right)^2}. \tag{2.38}$$

Wykreślając tak wyznaczone wielkości, widzimy, iż lokalne gęstości stanów opisane równaniem 2.38 przybierają formę krzywej posiadającej dwa lokalne maksima odseparowane od siebie o podwójną wartość całki przeskoku między atomami, $2V_{12}$, co przedstawione zostało jako krzywa zielona na rysunku 2.6. W przypadku, gdy $\varepsilon_1 \neq \varepsilon_2$ wierzchołki te charakteryzują się różną intensywnością, natomiast dla bardzo słabego sprzężenia V_{12} układ dwuatomowy zachowuje się jak para niezależnych atomów, których lokalna gęstość stanów odpowiada krzywej fioletowej.

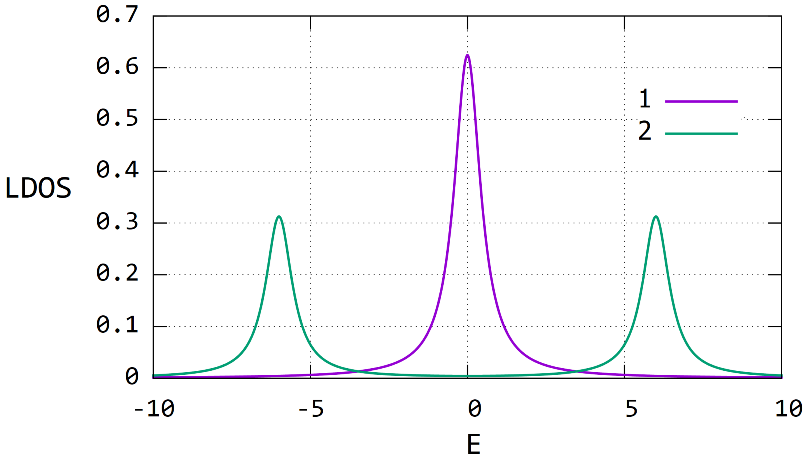

Rysunek 2.6: Lokalna gęstość stanów na pierwszym atomie dla układów atomowych na powierzchni: 1- układ jednoatomowy (krzywa fioletowa), 2- układ dwuatomowy (krzywa zielona). Energie wszystkich atomów wynoszą $\varepsilon_i = 0$, efektywne sprzężenia między atomami a podłożem wynoszą $\Gamma = 1$ (przyjmując za jednostkę energii $0,1eV$ ($\Gamma = 1 \iff \Gamma = 0,1eV$). W przypadku układu dwuatomowego całka przeskoku V_{12} wynosi 6 ($0.6eV$).

Obsadzenia ładunkowe już nawet w przypadku tak prostej struktury, jaką jest układ dwuatomowy, nie są opisane przejrzystymi formułami analitycznymi. Z tego powodu podanie tychże formuł zostanie zaniechane. Na rysunku 2.7 ukazany jest wykres obsadzeń ładunkowych na pierwszym węźle takiego układu (krzywa zielona) zestawiony z obsadzeniami ładunkowymi w układzie jednoatomowym (krzywa fioletowa).

Analizując obsadzenia w układzie dwuatomowym, można zauważyć dwa punkty przegięcia, które występują dla $E_F = \pm V_{12}$. W obszarze wewnątrz dynamika wzrostu obsadzeń jest wyraźnie niższa, co jest bezpośrednio związane z kształtem lokalnej gęstości stanów, która przy dostatecznie dużym sprzężeniu V_{12} charakteryzuje się płaskim minimum w tym zakresie energii (wierzchołki $LDOS(E)$ są od siebie wyraźnie odseparowane).

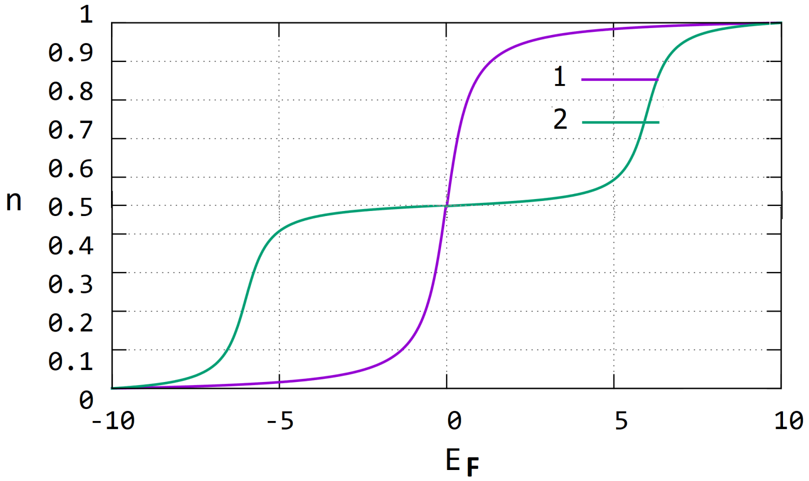

Rysunek 2.7: Obsadzenia ładunkowe na pierwszym atomie jako funkcja energii Fermiego dla układu jedno- i dwuatomowego na powierzchni. Wszystkie parametry układu są identyczne jak na rysunku 2.6.

Dla regularnych łańcuchów atomowych (atomy jednego pierwiastka, o stałych sprzężeniach $V_{ij} = V$, bez adatomów i zewnętrznych zaburzeń), które spoczywają na powierzchniach izolatorowych scharakteryzowanych niezależną od energii funkcją spektralną Γ macierz $\hat{A}$ zdefiniowana w równaniu 2.32 przyjmuje formę trójdiagonalnej macierzy Toeplitza [106]:

$$\hat{A} = \begin{bmatrix} E-\varepsilon_0+i\frac{\Gamma}{2} & -V & 0 & 0 & \dots & 0 \\ -V & E-\varepsilon_0+i\frac{\Gamma}{2} & -V & 0 & \dots & 0 \\ 0 & -V & E-\varepsilon_0+i\frac{\Gamma}{2} & -V & \dots & 0 \\ \vdots & \vdots & \vdots & \vdots & \ddots & \vdots \\ 0 & 0 & 0 & & \dots & E-\varepsilon_0+i\frac{\Gamma}{2} \end{bmatrix}_{N\times N}. \tag{2.39}$$

Dla tego typu macierzy znane są w literaturze formuły na wartości własne mające postać $a + 2\sqrt{bc}\cos\left(\frac{k\pi}{n+1}\right)$, $k = 1, \dots, N$; gdzie $a = E - \varepsilon_0 + i\frac{\Gamma}{2}; b = c = -V$ [107, 108], co umożliwi nam odnalezienie analitycznej postaci retardowanych funkcji Greena, co z kolei pozwoli na wyznaczenie lokalnej gęstości stanów, która zgodnie z definicją 2.14 wymaga od nas znajomości jedynie diagonalnych elementów macierzy $\hat{G}^R$. Korzystając ze wspomnianej właściwości trójdiagonalnych macierzy Toeplitza, możemy przedstawić elementy te w postaci:

$$G^R_{ii} = \frac{detA^{i-1}detA^{N-i}}{detA} = \frac{\prod_{j=1}^{i-1}(E-\varepsilon_0+2V cos\frac{j\pi}{i})\prod_{m=1}^{N-l}(E-\varepsilon_0+2V cos\frac{m\pi}{N+1-i})}{\prod_{l=1}^{N}(E-\varepsilon_0+2V cos\frac{l\pi}{N+1})}. \tag{2.40}$$

Mianownik retardowanej funkcji Greena 2.40 jest iloczynem N wyrażeń, których minima odzwierciedlają energie własne łańcucha atomowego. Każdy wierzchołek $LDOS$ odpowiada energii jednego stanu molekularnego łańcucha. Warto jednak zwrócić uwagę na łańcuchy o długościach takich jak: $N = 3, 5, 7, 8, 9, 11, ...$, dla których część wyrażeń z mianownika G^R_{ii} powiela się w liczniku ułamka, przez co liczba wierzchołków $LDOS$ na wewnętrznych węzłach łańcuchów ulega zmniejszeniu.

Układy jednowymiarowe złożone z kilku atomów spoczywające na powierzchni mogą być rozpatrywane jako molekuły z efektywnymi stanami molekularnymi sprzężonymi z rezerwuarem elektronów. Stany te wyrażane są w postaci kombinacji wszystkich stanów atomowych łańcucha atomowego. Jednakowoż możliwa jest sytuacja, w której stan własny hamiltonianu nie uwzględnia któregoś z węzłów łańcucha i jest nazywany stanem ciemnym. Stany te (opisane po raz pierwszy na gruncie optyki kwantowej [109]), odpowiedzialne są za wstrzymanie przepływu prądu elektrycznego poprzez blokadę ruchu zpułapkowanego elektronu [110]. Stany ciemne były tematem licznych prac naukowych dotyczących układów atomowych w zewnętrznych polach laserowych czy mikrofalowych oraz sprzężonych kropek kwantowych [111, 112], jednak jak dotąd brakowało prac, które badałyby możliwość istnienia stanów ciemnych w stacjonarnych łańcuchach atomowych. Istnienie stanów ciemnych ma bezpośredni związek z wielkościami mierzalnymi eksperymentalnie, gdyż stany te wpływają na wartości prądów tunelowych płynących przez poszczególne węzły łańcucha w badaniach STM. Ostrze mikroskopu tunelowego ma możliwość detekcji stanów, które mieszczą się w ściśle określonym zakresie energetycznym, związanym z napięciem ostrze-próbka i może obejmować stany ciemne, co sprawia, iż w eksperymencie atomy, których lokalna gęstość stanów wykazuje istnienie tychże stanów, nie są widoczne dla zadanej polaryzacji STM.

Badania eksperymentalne oraz teoretyczne nad stanami ciemnymi w odniesieniu do struktur atomowych są efektem wysiłku zespołu naukowców z Katedry Fizyki Powierzchni i Nanostruktur UMCS, do którego ja również należę. Obliczenia teoretyczne znalazły odzwierciedlenie w badaniach eksperymentalnych, a wyniki tychże prac posłużyły do przygotowania manuskryptu pt. *Dark states in atomic chains*, którego autorami są M. Dachniewicz, M. Kurzyna, T. Kwapiński oraz M. Jałochowski. Manuskrypt jest obecnie na etapie finalizacji i niebawem zostanie wysłany do publikacji.

2.4 Czasowo-zależne właściwości elektryczne układów atomowych

Do tej pory omówione zostały właściwości stacjonarnych układów atomowych (niezależnych od czasu), które można było wyznaczyć przy użyciu formalizmu retardowanych funkcji Greena. W tym podrozdziale skupimy się na układach, które ewoluują w czasie i są w stanie nierównowagowym. Pozwoli to nam na zbadanie dynamiki efektów włączeniowych, oraz umożliwi przeanalizowanie wpływu nagle pojawiających się zaburzeń na właściwości elektryczne tychże układów. Formalizm funkcji Greena w procesach nierównowagowych jest dość złożony ze względu na występowanie dwóch argumentów czasowych $G^R(t, t')$. Uwzględnienie w wyrażeniu na energię własną konkretnej gęstości stanów elektrod prowadzi do samozgodnych równań na opóźnioną funkcję Greena z podwójnymi całkami czasowymi. Tak więc zbieżności rozwiązań tych równań należy poszukiwać jednocześnie dla dwóch parametrów czasowych, co nawet dla pojedynczego atomu (czy kropki kwantowej) jest zadaniem dość trudnym [113, 114], a dla układu kropek kwantowych (łańcuchów) komplikacje dodatkowo narastają. Pewne ułatwienie w poszukiwaniu rozwiązań na opóźnione funkcje Greena stanowi przybliżenie WBL [115]. Dla układów wieloatomowych w stanie nierównowagowym znacznie wygodniej jest posłużyć się metodą operatora ewolucji, która jest nieco prostsza w swej konstrukcji. Formalizm ten pozwala opisać ewolucję czasową stanów kwantowych sprzężonych z kontinuum stanów podłoża/elektrod i był z powodzeniem stosowany do opisu rozpraszania atomów na powierzchni czy transportu przez kropkę kwantową lub łańcuch kropek kwantowych wspomagany fotonami [114–117].

2.4.1 Ewolucja układów kwantowych

Stan układu kwantowego jest w pełni opisany przez odpowiadającą mu funkcję falową. Jeżeli założymy, iż funkcja ta ewoluuje w sposób deterministyczny, to należy stwierdzić, iż funkcja falowa w chwili t - $|\psi(t)\rangle$ zależy od swojego stanu początkowego w chwili t_0, $|\psi(t_0)\rangle$, wówczas wywnioskować możemy, iż musi istnieć pewien operator (propagator), zwany operatorem ewolucji, który przeprowadza układ z momentu t_0 do pewnego innego punktu na osi czasu t:

$$|\psi(t)\rangle = U(t, t_0)\, |\psi(t_0)\rangle\,. \tag{2.41}$$

W fizyce występują trzy równoważne sposoby opisu układów kwantowych, czyli tzw. obrazy mechaniki kwantowej. Są nimi obrazy Schrödngera, Heisenberga oraz obraz oddziaływania. W obrazie Schrödingera dynamika układu kryje się w ewolucji funkcji falowej, operatory zaś nie zależą od czasu $|\psi_S(t)\rangle = U\,(t, t_0)\, |\psi_S\,(t_0)\rangle$, $\hat{A}(t) = const$. W obrazie Heisenberga z kolei funkcje falowe są niezmienne w czasie $|\psi_H\,(t)\rangle = |\psi_H\,(t_0)\rangle = |\psi_S\,(t_0)\rangle = |const\rangle$, natomiast to operatory odpowiadają za dynamikę układu, a ich ewolucja opisana jest równaniem Heisenberga:

$$\frac{d}{dt} A_{\mathrm{H}}(t) = \frac{i}{\hbar}\left[H_{\mathrm{H}}, A_{\mathrm{H}}(t)\right] + \left(\frac{\partial A_{\mathrm{S}}}{\partial t}\right)_{\mathrm{H}}\,. \tag{2.42}$$

Obraz oddziaływania łączy ze sobą te dwa różne podejścia do mechaniki kwantowej. W obrazie tym zarówno funkcje falowe:

$$|\psi_I(t)\rangle = U_0^\dagger\,(t, t_0)\,|\psi_S(t)\rangle\,, \tag{2.43}$$

jak i operatory:

$$i\hbar\frac{d}{dt}\hat{A}_I(t) = \left[\hat{A}_I(t), \hat{H}_S^{(0)}\right] + i\hbar U_0^\dagger\,(t, t_0)\left(\frac{\partial}{\partial t}\hat{A}_S(t)\right)U_0\,(t, t_0)\,, \tag{2.44}$$

podlegają ewolucji czasowej. Operator ewolucji w tymże obrazie pełni bardzo ważną rolę, ponieważ znalezienie równań ruchu dla operatora ewolucji pozwala nam na wyznaczenie właściwości badanego systemu kwantowego. W obrazie oddziaływania ewolucja stanów kwantowych, jak i operatorów opisywana jest przez dwie różne części hamiltonianu:

$$\hat{H}(t) = \hat{H}_0 + \hat{V}(t). \tag{2.45}$$

Część $\hat{H}_0$ opisująca ewolucję stanów kwantowych, nazywana jest hamiltonianem swobodnym. Część ta związana jest najczęściej ze stanami elektronowymi, które nie są poddane działaniu sił zależnych od czasu (a więc stacjonarnymi, których rozwiązania równani Schrödingera możemy łatwo wyznaczyć). Druga część, $\hat{V}(t)$, odpowiedzialna za ewolucję układu w czasie opisuje wzajemne oddziaływania między stanami elektronowymi, a także oddziaływania elektronów z zewnętrznymi zaburzeniami zależnymi od czasu. W ogólności część $\hat{H}_0$ może jawnie zależeć od czasu, a operator ewolucji U_0 związany z ewolucją stanów kwantowych opisaną przez $\hat{H}_0$ możemy zapisać jako: $U_0\,(t, t_0) = \mathcal{T}\exp\left[-\frac{i}{\hbar}\int_{t_0}^{t}\hat{H}_0(\tau)d\tau\right]$, gdzie $\mathcal{T}$ oznacza uporządkowanie czasowe wyrażenia. Tak określony operator ewolucji U_0 opisuje ewolucję czasową części perturbacyjnej: $\hat{V}(t) = U_0^\dagger\,(t, t_0)\,\hat{V}U_0\,(t, t_0)$, która posłuży nam do opisu układu sprzężonych stanów elektronowych w łańcuchach atomowych. Równanie ruchu operatora ewolucji dla całego hamiltonianu, $\hat{H}$, w obrazie oddziaływania przyjmuje postać:

$$i\hbar\frac{\partial}{\partial t}U\,(t, t_0) = \hat{V}(t)U\,(t, t_0)\,. \tag{2.46}$$

Równanie to posłuży do obliczenia odpowiednich elementów operatora U i wyznaczenia obsadzeń ładunkowych, prądów i gęstości stanów w łańcuchach atomowych (w naszych obliczeniach przyjmujemy $\hbar = 1$).

2.4.2 Formalizm operatora ewolucji w opisie układów atomowych

W celu znalezienia równań opisujących ewolucję stanów elektronowych pojedynczego łańcucha atomowego w kontakcie z rezerwuarem elektronów podłoża dzielimy hamiltonian 2.2 na część związaną z energiami na poszczególnych węzłach atomowych, $\hat{H}_0$, oraz na część związaną z oddziaływaniami $\hat{V}(t)$.

$$H = \underbrace{\sum_i \varepsilon_i c_i^\dagger c_i + \sum_{\vec{k},\alpha}\varepsilon_{\vec{k}\alpha}c_{\vec{k}\alpha}^\dagger c_{\vec{k}\alpha}}_{\hat{H}_0} + \underbrace{\sum_i\sum_{\vec{k},\alpha}V_{\vec{k}\alpha}(c_{\vec{k}\alpha}^\dagger c_i + c_i^\dagger c_{\vec{k}\alpha}) + \sum_i\sum_j V_{ij}c_i^\dagger c_j}_{\hat{V}(t)}\,. \tag{2.47}$$

Zakładamy, iż do chwili $t = t_0$ układ nie ewoluował w czasie (był odizolowany od rezerwuaru elektronów i wszystkie sprzężenia wynosiły zero). Dla czasu $t > t_0$ włączone zostały nagle wszystkie sprzężenia i funkcje falowe ewoluują w czasie. Bazę funkcyjną naszego układu stanowią funkcje własne hamiltonianu $H_0 : I = \sum_i |i\rangle\langle i| + \sum_{\vec{k},\alpha}|\vec{k}\alpha\rangle\langle\vec{k}\alpha|$.

Jedną z wielkości, która jest szczególnie istotna w prowadzonych przez mnie badaniach jest obsadzenie ładunkowe stanu elektronowego na i-tym węźle łańcucha $n_i(t)$. Wielkość ta równa jest wartości oczekiwanej operatora liczby cząstek $\hat{N}$, czyli $n_i(t) = \langle i(t)| \hat{N} |i(t)\rangle$, gdzie operator liczby cząstek $\hat{N}$ ma postać:

$$\hat{N} = \sum_i \hat{n}_i + \sum_{\vec{k},\alpha} \hat{n}_{\vec{k}\alpha}. \tag{2.48}$$

W równaniu 2.48 pierwszy operator opisuje obsadzenia ładunkowe w obrębie łańcucha, natomiast drugi w obrębie elektrody (elektrod). Mając tak zdefiniowany operator liczby cząstek możemy zapisać równanie na wartość oczekiwaną obsadzeń na i-tym atomie łańcucha:

$$n_i(t) = \langle i| U^\dagger(t) \sum_j \left(\hat{n}_j + \sum_{\vec{k},\alpha} \hat{n}_{\vec{k}\alpha} \right) U(t) |i\rangle = \sum_j \underbrace{\langle i| U^\dagger(t) \hat{n}_j U(t) |i\rangle}_{\mathcal{A}} + \sum_{\vec{k},\alpha} \underbrace{\langle i| U^\dagger(t) \hat{n}_{\vec{k}\alpha} U(t) |i\rangle}_{\mathcal{B}}. \tag{2.49}$$

Wyrażenie to składa się z dwóch części, $\mathcal{A}$ - związanej z atomami w obrębie łańcucha, oraz $\mathcal{B}$ - związanej z rezerwuarem elektronów. Zaczynając od części $\mathcal{A}$ możemy zapisać:

$$\begin{aligned}
&\mathcal{A} = \langle i| U^\dagger(t) \hat{n}_j U(t) |i\rangle = \langle i| U^\dagger(t) I \hat{n}_j I U(t) |i\rangle = \qquad (2.50)\\
&\langle i| U^\dagger(t) \Big(\sum_l |l\rangle \langle l| + \sum_{\vec{k},\alpha} |\vec{k}\alpha\rangle \langle \vec{k}\alpha| \Big) \hat{n}_j \Big(\sum_{l'} |l'\rangle \langle l'| + \sum_{\vec{k}_2,\beta} |\vec{k}_2\beta\rangle \langle \vec{k}_2\beta| \Big) U(t) |i\rangle = \\
&\langle i| U^\dagger(t) \Big(\sum_l |l\rangle \langle l| + \sum_{\vec{k},\alpha} |\vec{k}\alpha\rangle \langle \vec{k}\alpha| \Big) \hat{n}_j \sum_{l'} |l'\rangle \langle l'| U(t) |i\rangle + \\
&\underbrace{+ \langle i| U^\dagger(t) \Big(\sum_l |l\rangle \langle l| + \sum_{\vec{k},\alpha} |\vec{k}\alpha\rangle \langle \vec{k}\alpha| \Big) \hat{n}_j \sum_{\vec{k}_2,\beta} |\vec{k}_2\beta\rangle \langle \vec{k}_2\beta| U(t) |i\rangle =}_{=0}
\end{aligned}$$

$$\begin{aligned}
&\langle i| U^\dagger(t) \sum_l |l\rangle \langle l| \hat{n}_j \sum_{l'} |l'\rangle \langle l'| U(t) |i\rangle + \underbrace{\langle i| U^\dagger(t) \sum_{\vec{k},\alpha} |\vec{k}\alpha\rangle \langle \vec{k}\alpha| \hat{n}_j \sum_{l'} |l'\rangle \langle l'| U(t) |i\rangle}_{=0} = \\
&\sum_{l,l'} \langle i| U^\dagger(t) |l\rangle \underbrace{\langle l| \hat{n}_j |l'\rangle}_{\delta_{lj}\delta_{l,l'}\hat{n}_j} \langle l'| U(t) |i\rangle = \langle i| U^\dagger(t) |j\rangle \langle j| \hat{n}_j |j\rangle \langle j| U(t) |i\rangle = \underline{n_j(t_0)|U_{ij}(t)|^2},
\end{aligned}$$

gdzie $n_j(t_0)$ jest obsadzeniem ładunkowym stanu j dla czasu początkowego t_0. Część elektrodowa wyrażenia 2.49 oznaczona jako $\mathcal{B}$, obliczana jest sposób analogiczny do $\mathcal{A}$ i posiada następującą postać:

$$\mathcal{B} = \langle i| U^\dagger(t) n_{\vec{k}\alpha} U(t) |i\rangle = n_{\vec{k}\alpha}(t_0) |U_{i\vec{k}\alpha}(t)|^2. \tag{2.51}$$

Po wyznaczeniu formuł opisujących człony $\mathcal{A}$ oraz $\mathcal{B}$ możemy zapisać równanie na obsadzenia ładunkowe na i-tym węźle atomowym w następującej formie:

$$n_i(t) = \sum_j n_j(t_0) |U_{ij}(t)|^2 + \sum_{\vec{k},\alpha} n_{\vec{k}\alpha}(t_0) |U_{i\vec{k}\alpha}(t)|^2. \tag{2.52}$$

Zakładając, iż początkowe obsadzenia stanów elektronowych $n_i(t_0) = 0$ możemy sprowadzić równanie 2.52 do postaci:

$$n_i(t) = \sum_{\vec{k},\alpha} n_{\vec{k}\alpha}(t_0) |U_{i\vec{k}\alpha}(t)|^2. \tag{2.53}$$

Sumę po $\vec{k}\alpha$ w powyższym wyrażeniu możemy zastąpić całką po energii z odpowiednią gęstością stanów elektrody α: $D_\alpha(E)$ ($U_{i\vec{k}\alpha}(t) \to U_{i\alpha}(E,t)$). Po uwzględnieniu funkcji Fermiego w temperaturze zerowej pochodzącej od początkowego obsadzania stanów elektrody, $n_{\vec{k}\alpha}(0)$, wyrażenie na obsadzenia ładunkowe przyjmie postać:

$$n_i(t) = \int_{-\infty}^{E_F} \underbrace{\sum_\alpha D_\alpha(E) \left| U_{i\alpha}(E,t) \right|^2}_{LDOS_i(t,\varepsilon)} dE. \tag{2.54}$$

Znajomość odpowiednich elementów macierzowych operatora ewolucji pozwala wyznaczyć nam nie tylko obsadzenia ładunkowe, ale też lokalną gęstość stanów na każdym węźle łańcucha.

Korzystając z równania 2.46 możemy zapisać równanie ruchu dla występujących w równaniu 2.53 operatorów ewolucji $U_{i\vec{k}\alpha}(t)$:

$$i\frac{\partial}{\partial t}\langle i|\,U(t)\,|\vec{k}\alpha\rangle = \langle i|\,\tilde{V}IU(t)\,|\vec{k}\alpha\rangle = \sum_{j}\underbrace{\langle i|\,\tilde{V}\,|j\rangle\,U_{j\vec{k}\alpha}(t)}_{\mathcal{A}} + \sum_{\vec{k}_2,\beta}\underbrace{\langle i|\,\tilde{V}\,|\vec{k}_2\beta\rangle\,U_{\vec{k}_2\beta\vec{k}\alpha}(t)}_{\mathcal{B}}. \tag{2.55}$$

Podobnie jak w równaniu 2.49 prawa strona równania składa się z dwóch członów $\mathcal{A}$ i $\mathcal{B}$, gdzie:

$$\begin{aligned}
&\mathcal{A} = \langle i|\,e^{i\hat{H}_0t}\hat{V}e^{-i\hat{H}_0t}\,|j\rangle\,U_{j\vec{k}\alpha}(t) = \langle i|\,e^{i\hat{H}_0t}I\hat{V}Ie^{-i\hat{H}_0t}\,|j\rangle\,U_{j\vec{k}\alpha}(t) = \\
&\langle i|\,e^{i\hat{H}_0t}\left(\sum_{l}|l\rangle\langle l| + \sum_{\vec{k},\alpha}|\vec{k}\alpha\rangle\langle\vec{k}\alpha|\right)\hat{V}\left(\sum_{l'}|l'\rangle\langle l'| + \sum_{\vec{k}_2,\beta}|\vec{k}_2\beta\rangle\langle\vec{k}_2\beta|\right)e^{-i\hat{H}_0t}\,|j\rangle\,U_{j\vec{k}\alpha}(t).
\end{aligned} \tag{2.56}$$

Elementy macierzowe $\langle i|\,e^{i\hat{H}_0t}\,|\vec{k}\alpha\rangle = 0$, ponieważ hamiltonian H_0 nie opisuje interakcji między stanami elektronowymi atomów łańcucha a elektrodami. Pozwala to zapisać:

$$\begin{aligned}
&\mathcal{A} = \sum_{l,l'}\langle i|\,e^{i\hat{H}_0t}\,|l\rangle\langle l|\,\hat{V}\,|l'\rangle\langle l'|\,e^{-i\hat{H}_0t}\,|j\rangle\,U_{j\vec{k}\alpha}(t) = \\
&\sum_{l,l'}\delta_{i,l}\delta_{j,l'}\,\langle i|\,e^{i\hat{H}_0t}\,|l\rangle\langle l|\,\hat{V}\,|l'\rangle\langle l'|\,e^{-i\hat{H}_0t}\,|j\rangle\,U_{j\vec{k}\alpha}(t) = \langle i|\,e^{i\hat{H}_0t}\,|i\rangle\langle i|\,\hat{V}\,|j\rangle\langle j|\,e^{-i\hat{H}_0t}\,|j\rangle\,U_{j\vec{k}\alpha}(t) = \\
&e^{i\varepsilon_it}V_{ij}e^{-i\varepsilon_jt}U_{j\vec{k}\alpha}(t) = \underline{V_{ij}e^{i(\varepsilon_i-\varepsilon_j)t}U_{j\vec{k}\alpha}(t)}.
\end{aligned} \tag{2.57}$$

Kontynuując obliczenia musimy wyznaczyć również człon $\mathcal{B}$ odpowiedzialny za interakcje pomiędzy stanami łańcucha i elektrody (podłoża):

$$\begin{aligned}
&B = \langle i|\,\tilde{V}\,|\vec{k}_2\beta\rangle\,U_{\vec{k}_2\beta\vec{k}\alpha}(t) = \langle i|\,e^{i\hat{H}_0t}I\hat{V}Ie^{-i\hat{H}_0t}\,|\vec{k}_2\beta\rangle\,U_{\vec{k}_2\beta\vec{k}\alpha}(t) = \\
&\langle i|\,e^{i\hat{H}_0t}\left(\sum_{m}|m\rangle\langle m| + \sum_{\vec{k}_3,\eta}|\vec{k}_3\eta\rangle\langle\vec{k}_3\eta|\right)\hat{V}\left(\sum_{m'}|m'\rangle\langle m'| + \sum_{\vec{k}_4,\chi}|\vec{k}_4\chi\rangle\langle\vec{k}_4\chi|\right)e^{-i\hat{H}_0t}\,|\vec{k}_2\beta\rangle\,U_{\vec{k}_2\beta\vec{k}\alpha}(t) = \\
&\sum_{\vec{k}_4,\chi}\sum_{m}\langle i|\,e^{i\hat{H}_0t}\,|m\rangle\langle m|\,\hat{V}\,|\vec{k}_4\chi\rangle\langle\vec{k}_4\chi|\,e^{-i\hat{H}_0t}\,|\vec{k}_2\beta\rangle\,U_{\vec{k}_2\beta\vec{k}\alpha}(t) = \\
&\sum_{\vec{k}_4,\chi}\sum_{m}\delta_{\vec{k}_2\beta,\vec{k}_4\chi}\delta_{i,m}\,\langle i|\,e^{i\hat{H}_0t}\,|m\rangle\langle m|\,\hat{V}\,|\vec{k}_4\chi\rangle\langle\vec{k}_4\chi|\,e^{-i\hat{H}_0t}\,|\vec{k}_2\beta\rangle\,U_{\vec{k}_2\beta\vec{k}\alpha}(t) = \\
&\langle i|\,e^{i\hat{H}_0t}\,|i\rangle\langle i|\,\hat{V}\,|\vec{k}_2\beta\rangle\langle\vec{k}_2\beta|\,e^{-i\hat{H}_0t}\,|\vec{k}_2\beta\rangle\,U_{\vec{k}_2\beta\vec{k}\alpha}(t) = e^{i\varepsilon_it}V_{i,\vec{k}_2\beta}e^{-i\varepsilon_{\vec{k}_2\beta}t}U_{\vec{k}_2\beta\vec{k}\alpha}(t) = \\
&\underline{e^{i(\varepsilon_i-\varepsilon_{\vec{k}_2\beta})t}V_{i,\vec{k}_2\beta}U_{\vec{k}_2\beta\vec{k}\alpha}(t)}.
\end{aligned} \tag{2.58}$$

Po dokonaniu obliczeń członów $\mathcal{A}$ oraz $\mathcal{B}$, możemy przekształcić równanie ruchu dla operatora ewolucji $U_{i,\vec{k}\alpha}(t)$ 2.55 do następującej postaci:

$$i\frac{\partial}{\partial t}\langle i|\,U(t)\,|\vec{k}\alpha\rangle = \sum_{j}e^{i(\varepsilon_i-\varepsilon_j)t}V_{ij}U_{j\vec{k}\alpha}(t) + \sum_{\vec{k}_2,\beta}e^{i(\varepsilon_i-\varepsilon_{\vec{k}_2\beta})t}V_{i,\vec{k}_2\beta}U_{\vec{k}_2\beta\vec{k}\alpha}(t). \tag{2.59}$$

Jak widzimy równanie to zawiera operator ewolucji $U_{\vec{k}_2\beta\vec{k}\alpha}(t)$, dla którego również należy zapisać osobne równanie ruchu:

$$\begin{aligned}
&i\frac{\partial}{\partial t}\langle\vec{k}\alpha|\,U(t)\,|\vec{k}_2\beta\rangle = \langle\vec{k}\alpha|\,\tilde{V}U\,|\vec{k}_2\beta\rangle = \langle\vec{k}\alpha|\,e^{i\hat{H}_0t}\hat{V}e^{-i\hat{H}_0t}U\,|\vec{k}_2\beta\rangle = \\
&\langle\vec{k}\alpha|\,e^{i\hat{H}_0t}I\hat{V}Ie^{-i\hat{H}_0t}IU\,|\vec{k}_2\beta\rangle = \langle\vec{k}\alpha|\,e^{i\hat{H}_0t}\left(\sum_{m}|m\rangle\langle m| + \sum_{\vec{k}_3,\eta}|\vec{k}_3\eta\rangle\langle\vec{k}_3\eta|\right)\hat{V}\left(\sum_{m'}|m'\rangle\langle m'| +\right. \\
&\left.+\textstyle\sum_{\vec{k}_4,\chi}|\vec{k}_4\chi\rangle\langle\vec{k}_4\chi|\right)e^{-i\hat{H}_0t}\left(\sum_{m''}|m''\rangle\langle m''| + \sum_{\vec{k}_5,\lambda}|\vec{k}_5\lambda\rangle\langle\vec{k}_5\lambda|\right)U\,|\vec{k}_2\beta\rangle\,.
\end{aligned} \tag{2.60}$$

Uwzględniając, że $\langle\vec{k}\alpha| e^{i\hat{H}_0 t} |m\rangle = 0$ oraz $\langle\vec{k}\alpha| \hat{V} |\vec{k}_2\beta\rangle = 0$ otrzymujemy:

$$i\frac{\partial}{\partial t}U_{\vec{k}_2\beta\vec{k}\alpha}(t) = \sum_{\vec{k}_3,\eta} \langle\vec{k}\alpha| e^{i\hat{H}_0 t} |\vec{k}_3\eta\rangle \langle\vec{k}_3\eta| \hat{V}\Bigg(\sum_{m'} |m'\rangle\langle m'| + \tag{2.61}$$

$$+\textstyle\sum_{\vec{k}_4,\chi} |\vec{k}_4\chi\rangle\langle\vec{k}_4\chi| \Bigg) e^{-i\hat{H}_0 t}\Bigg(\sum_{m''} |m''\rangle\langle m''| + \sum_{\vec{k}_5,\lambda} |\vec{k}_5\lambda\rangle\langle\vec{k}_5\lambda|\Bigg) U |\vec{k}_2\beta\rangle$$

$$i\frac{\partial}{\partial t}U_{\vec{k}_2\beta\vec{k}\alpha}(t) = \sum_{m'}\sum_{m''}\sum_{\vec{k}_3,\eta} \langle\vec{k}\alpha| e^{i\hat{H}_0 t} |\vec{k}_3\eta\rangle \langle\vec{k}_3\eta| \hat{V} |m'\rangle \langle m'| e^{-i\hat{H}_0 t} |m''\rangle \langle m''| U |\vec{k}_2\beta\rangle =$$

$$\sum_{m'} e^{i(\varepsilon_{m'}-\varepsilon_{\vec{k}\alpha})t} V_{m',\vec{k}\alpha} U_{m',\vec{k}_2\beta}(t).$$

Formalne rozwiązanie powyższego równania przybiera postać:

$$U_{\vec{k}_2\beta\vec{k}\alpha}(t) = \delta_{\vec{k}_2\beta,\vec{k}\alpha} - i\int_0^t \sum_{m'} e^{i(\varepsilon_{m'}-\varepsilon_{\vec{k}\alpha})t'} V_{m',\vec{k}\alpha} U_{m',\vec{k}_2\beta}(t')dt'. \tag{2.62}$$

Podstawiając wyrażenie na element $U_{\vec{k}_2\beta\vec{k}\alpha}$ do równania 2.59 dostajemy ostatecznie równanie ruchu dla operatora ewolucji $U_{i\vec{k}\alpha}$.

$$i\tfrac{\partial}{\partial t}\langle i| U(t) |\vec{k}\alpha\rangle = \sum_j e^{i(\varepsilon_i-\varepsilon_j)t} V_{ij} U_{j\vec{k}\alpha}(t) + V_{i,\vec{k}\alpha} e^{i(\varepsilon_i-\varepsilon_{\vec{k}\alpha})t} - i|V_{i,\vec{k}\alpha}|^2 \int\limits_0^t D_\alpha(t-t') e^{i\varepsilon_i(t'-t)} U_{i,\vec{k}\alpha}(t')dt'. \tag{2.63}$$

Formuła ta ma postać równania różniczkowo-całkowego Voltery II rodzaju [118–120], w którym $D_\alpha(t)$ jest transformata Fouriera gęstości stanów elektrody α. Dla regularnych struktur atomowych ($V_{ij} = V, \varepsilon_i = \varepsilon_j = \varepsilon_0$) spoczywających na powierzchniach izolatorowych scharakteryzowanych niezależną od energii funkcją spektralną Γ w przybliżeniu WBL powyższe równanie przyjmie postać:

$$i\frac{\partial}{\partial t}\langle i| U(t) |\vec{k}\alpha\rangle = \sum_j e^{i(\varepsilon_i-\varepsilon_j)t} V_{ij} U_{j\vec{k}\alpha}(t) + V_{i,\vec{k}\alpha} e^{i(\varepsilon_i-\varepsilon_{\vec{k}\alpha})t} - i\frac{\Gamma}{2} U_{i\vec{k}\alpha}(t). \tag{2.64}$$

Równanie to w istocie stanowi układ sprzężonych ze sobą równań różniczkowych na elementy U zapisanych dla każdego węzła i oraz dla każdego wektora falowego $\vec{k}$ (czyli energii) każdej elektrody w układzie. Zakładając istnienie tylko dwóch elektrod opisywanych przez 500 wektorów $\vec{k}$ oraz łańcucha atomowego złożonego z $N = 20$ węzłów, otrzymujemy do rozwiązania $2 \times 500 \times 20 = 20000$ równań różniczkowych dla jednego tylko parametru czasu t, zatem niezwykle ważne jest poszukiwanie rozwiązań analitycznych dla rozpatrywanych układów. W przypadku omówionych powyżej założeń możliwe jest rozwiązanie równania 2.64 przy użyciu transformaty Laplace'a:

$$sF_i(s) = -i\sum_j VF_j(s) - \frac{iV_{i,\vec{k}\alpha}}{s - i(\varepsilon_i - \varepsilon_{\vec{k}\alpha})} - \frac{\Gamma}{2}F_i(s), \tag{2.65}$$

gdzie $F_i(s) = \mathcal{L}\left\{U_{i\vec{k}\alpha}(t)\right\}$. Jak można zauważyć transformata Laplace'a pozwala zapisać układ równań różniczkowych 2.64 w postaci układu równań algebraicznych. W tym przypadku możemy zapisać równanie 2.65 w postaci następującego równania macierzowego:

$$\begin{bmatrix} s+\frac{\Gamma}{2} & iV & \cdots & 0 \\ iV & s+\frac{\Gamma}{2} & \cdots & 0 \\ \vdots & \vdots & \vdots & \vdots \\ 0 & 0 & \cdots & s+\frac{\Gamma}{2} \end{bmatrix} \begin{bmatrix} F_1(s) \\ F_2(s) \\ \vdots \\ F_n(s) \end{bmatrix} = \begin{bmatrix} -\frac{iV_{1,\vec{k}\alpha}}{s-i(\varepsilon_0-\varepsilon_{\vec{k}\alpha})} \\ -\frac{iV_{2,\vec{k}\alpha}}{s-i(\varepsilon_0-\varepsilon_{\vec{k}\alpha})} \\ \vdots \\ -\frac{iV_{n,\vec{k}\alpha}}{s-i(\varepsilon_0-\varepsilon_{\vec{k}\alpha})} \end{bmatrix} \tag{2.66}$$

Podobnie jak w równaniu 2.40 zauważamy obecność trójdiagonalnej macierzy Toeplitza, co pozwala nam analitycznie rozwiązać równanie 2.66. Następnie należy znaleźć transformaty odwrotne do obliczonych funkcji $F_i(s)$, co też nie jest zadaniem trywialnym (i w zależności od czasowego zaburzenia układu nie zawsze jest możliwe). Ostatecznie, analityczne wyrażenia na zależne od czasu elementy operatora ewolucji przyjmują następującą postać:

$$U_{j\vec{k}\alpha}(t) = \frac{(-i)^j V^{j-1} V_{j\vec{k}\alpha} \prod_{l=1}^{N-j} \left(s_0 + \frac{\Gamma}{2} + 2iV \cos\frac{l\pi}{N-j+1}\right)}{\prod_{l=1}^{N} \left(s_0 + \frac{\Gamma}{2} + 2iV \cos\frac{l\pi}{N+1}\right)} e^{i\left(\varepsilon_0 - \varepsilon_{\vec{k}\alpha}\right)t} + \tag{2.67}$$

$$\sum_{m=1}^{N} \frac{(-i)^j V^{j-1} V_{j\vec{k}\alpha} \prod_{l=1}^{N-j} \left(s_m + \frac{\Gamma}{2} + 2iV \cos\frac{l\pi}{N-j+1}\right)}{(s_m - s_0) \prod_{l=1, l\neq m}^{N} \left(s_m + \frac{\Gamma}{2} + 2iV \cos\frac{l\pi}{N+1}\right)} e^{-\frac{\Gamma}{2}t} e^{-2iV \cos\frac{m\pi}{N+1}t},$$

gdzie $s_0 = i(\varepsilon_0 - \varepsilon_{\vec{k}\alpha})$, $s_m = -\frac{\Gamma}{2} - 2iV \cos\frac{m\pi}{N+1}$ dla $m > 0$.

Powyższe rozwiązanie na $U_{j\vec{k}\alpha}(t)$ pozwala obliczyć $LDOS$ na j-tym węźle, obsadzenia ładunkowe jak również prąd przepływający przez dowolną z elektrod $j_\alpha(t) = -e\frac{d}{dt}\sum_{\vec{k}\alpha} n_{\vec{k}\alpha}(t)$. Przedstawiając schemat wyprowadzenia tego równania, chciałem pokazać skalę trudności, jaką napotykamy przy próbach znajdowania zależnych od czasu rozwiązań analitycznych w rozważanych układach. Warto podkreślić, że dla $t \to \infty$ drugi człon równania 2.67 dąży do 0 i pozostaje jedynie człon pierwszy, który zależy od czasu poprzez wyrażenie $e^{i\left(\varepsilon_0 - \varepsilon_{\vec{k}\alpha}\right)t}$, a zatem obliczając moduł kwadrat operatora ewolucji (np. w równaniu 2.52), otrzymujemy wyrażenie niezależne od czasu. Obliczone w ten sposób wyrażenia na lokalną DOS na węźle j-tym, jak również obsadzenia ładunkowe zgadzają się z wynikami otrzymanymi przy pomocy formalizmu retardowanych funkcji Greena.

Warto nadmienić, iż próbując opisać analitycznie łańcuchy atomowe poza przybliżeniem WBL na podłożach, które nie są scharakteryzowane wolnozmienną DOS bez lokalnych maksimów, czy też próbując uwzględnić oddziaływania kulombowskie, napotykamy na trudne do ominięcia przeszkody, dlatego też poza szczególnymi przypadkami równania ruchu nie są możliwe do rozwiązania bez uciekania się do metod numerycznych. Ten wniosek popchnął mnie do tego, by opracować narzędzie informatyczne, którego jedną z funkcjonalności będzie właśnie numeryczne rozwiązywanie równań ruchu, i które opiszę w kolejnym rozdziale.

Rozdział 3

Nano Modeller

Jak pokazały wcześniejsze części rozprawy, formuły analityczne opisujące właściwości elektryczne struktur atomowych są możliwe do wyprowadzenia jedynie w szczególnych przypadkach, tzn. dla regularnych i symetrycznych łańcuchów, złozonych z identycznych atomów. W przypadku bardziej skomplikowanych układów cechujących się nietrywialną geometrią, niejednorodnymi sprzężeniami, czy też różnym rodzajem atomów wchodzących w skład łańcucha, niezbędne było opracowanie metod do numerycznego rozwiązywania równań ruchu. Wszystkie obliczenia numeryczne wykonane w trakcie studiów doktoranckich zostały uzyskane przeze mnie przy pomocy mojego autorskiego programu komputerowemu o nazwie *Nano Modeller*, który został stworzony jako narzędzie do szybkiego i efektywnego realizowania celów rozprawy. Jest to program napisany w języku Java 1.8, który służy do modelowania układów kilkuatomowych, łańcuchów atomowych, jak również bardziej skomplikowanych nanostruktur, oraz wyznaczania ich dynamicznych i statycznych właściwości elektrycznych takich jak: lokalna i całkowita gęstość stanów, obsadzenia ładunkowe, transmitancja, czy prąd płynący przez układ. Program ten został podzielony na dwie warstwy: warstwę użytkownika- GUI (ang. *Graphical User Interface*) [121], oraz warstwę obliczeniową. Warstwy te działają w myśl paradygmatu programowania równoległego i są od siebie niezależne, zatem użytkownik ma możliwość tworzenia/modyfikowania modeli bez konieczności oczekiwania na zakończenie procesu obliczeń, który działa w tle. Warstwy te komunikują się za pomocą standardu XML (ang. *Extensible Markup Language*) [122]. Uwspólniony plik XML, do którego warstwy posiadają dostęp, pełni rolę bazy danych, przechowując wszystkie dane wprowadzone przez użytkownika w trakcie pracy. Zaletą odseparowania warstw od siebie jest możliwość wykorzystania ich niezależenie od siebie np. poprzez zintegrowanie warstwy użytkownika z inną warstwą obliczeniową wspierającą standard XML napisaną w innym języku programowania (np. C++, C, Fortran, Python). Program *Nano Modeller* do poprawnego działania wymaga wcześniejszego zainstalowania na komputerze środowiska Java w wersji 1.8 lub wyższej, a także oprogramowania obsługującego pliki w formacie plt. *Nano Modeller* oferuje wsparcie dla programu Gnuplot [123] obsługującego tego rodzaj plików, poprzez dostarczenie użytkownikowi specjalnych funkcjonalności do intuicyjnego i wygodnego tworzenia wykresów w tym formacie.

Na rynku istnieje wiele zaawansowanych programów komputerowych umożliwiających prowadzenie zaawansowanych obliczeń numerycznych oraz modelowanie nanostruktur, takich jak np. Materials Studio [124], MBN Explorer [125], LAMMPS [126] i wiele innych. Niestety większość tego typu programów wymaga zakupu licencji (często zbyt kosztownej jak na kieszeń doktoranta) i nie zawiera wszystkich funkcjonalności, jakie były mi potrzebne do moich badań, co skłoniło mnie do opracowania własnego programu, który mógłbym dowolnie modyfikować i udoskonalać w zależności od zaistniałych potrzeb.

Na rysunku 3.1 przedstawiony został ekran główny programu *Nano Modeller*, który podzielony został na 7 segmentów A-G, które na rysunku zostały oznaczone różnymi kolorami. Każdy z segmentów grupuje w swoim obrębie różne funkcjonalności programu.

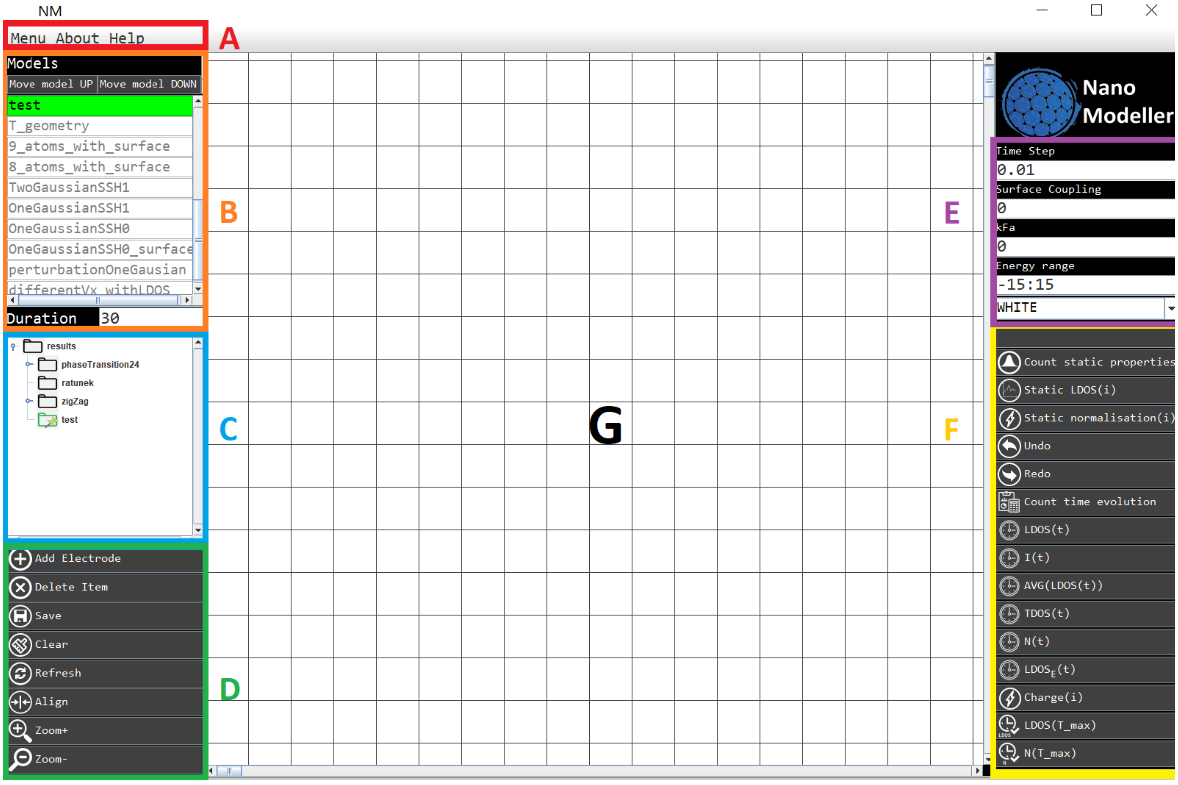
NM
Menu About Help
A
Models
Move model UP
Move model DOWN
test
T_geometry
9_atoms_with_surface
8_atoms_with_surface
TwoGaussianSSH1
OneGaussianSSH1
OneGaussianSSH0
OneGaussianSSH0_surface
perturbationOneGausian
differentVx_withLDOS
B
results
phaseTransition24
ratunek
zigZag
test
C
Add Electrode
Delete Item
Save
Clear
Refresh
Align
Zoom+
Zoom-
D
G
E
F
Nano Modeller
Count static properties
Static LDOS(i)
Static normalisation(i)
Undo
Redo
Count time evolution
LDOS(t)
I(t)
AVG(LDOS(t))
TDOS(t)
N(t)
LDOS_E(t)
Charge(i)
LDOS(T_max)
N(T_max)

Duration 30

Time Step 0.01

Surface Coupling 0

kFa 0

Energy range -15:15

WHITE

Rysunek 3.1: Ekran główny programu *Nano Modeller*. Ekran ten został podzielony na 7 segmentów, które pogrupowane zostały pod względem oferowanych funkcjonalności.

(A) Sekcja Menu - umożliwia dostęp do ustawień programu, zawiera informacje o programie, jak również daje wgląd do jego dokumentacji.

(B) Modele użytkownika, czyli inaczej utworzone projekty struktur atomowych. Program umożliwia przechowywanie projektów wielu struktur, co pozwala na wygodny powrót do stworzonych w przeszłości modeli bez konieczności ponownego wprowadzania danych. Użytkownik ma możliwość aktywacji i dezaktywacji danych projektów. Funkcjonalność ta jest szczególnie przydatna, gdy chcemy wyznaczyć dynamiczne właściwości elektryczne dla wybranych struktur atomowych licząc wiele rzeczy bez konieczności uruchamiania programu dla każdego aktywnego projektu z osobna. Przyciski „UP" and „DOWN" pozwalają na określenie kolejności wykonywania obliczeń dla danych aktywnych modeli. Obliczenia realizowane są od „góry do dołu", więc użytkownik powinien umieszczać najbardziej interesujące go modele na szczycie listy. Pole tekstowe na dole sekcji oznacza czas, przez jaki prowadzone mają być obliczenia dla poszczególnego modelu.

(C) Eksplorator plików - pozwala na wygodne zarządzanie miejscem zapisywania danych dla poszczególnych projektów (modeli) użytkownika.

(D) Sekcja zarządzania projektem, która odpowiada za następujące funkcjonalności:

- dodawanie elektrod (rezerwuarów elektronów),
- usuwanie elementów nanostruktury (atomów, rezerwuarów, sprzężeń),

- zapisywanie projektu,
- czyszczenie sekcji roboczej (segment G), tzn. usunięcie całej nanostruktury (pozwala zacząć projekt od nowa),
- odświeżenie projektu- przywraca model do ostatnio zapisanej postaci,
- wyrównanie elementów do siatki,
- przybliż/oddal- zmiana perspektywy sekcji roboczej, co jest szczególnie przydatne dla długich i złożonych łańcuchów (np. $N = 100$).

(E) Sekcja danych obliczeniowych- umożliwia wprowadzanie danych układu, takich jak m.in. krok czasowy Δt dla obliczeń czasowo-zależnych, krok energii ΔE, sprzężenie z podłożem, poziom zdelokalizowania elektronów w podłożu, zakres energii stosowanej w obliczeniach, styl elementu.

(F) Sekcja obliczeń- ta sekcja odpowiada za odwoływanie się do warstwy obliczeniowej programu. Poszczególne elementy tej sekcji to:

- Wykonaj obliczenia statyczne- wydanie tej komendy spowoduje przesłanie warstwie obliczeniowej polecenia wyznaczenia równania ruchu dla retardowanej funkcji Greena. Program znajduje macierz odwrotną do macierzy 2.32. i na jej podstawie obliczane są stacjonarne właściwości łańcucha, tj. np. lokalna gęstość stanów (równanie 2.14), czy też obsadzenia ładunkowe (równanie 2.15). Wybór wielkości, które mają zostać wyznaczone, może być modyfikowana w ustawieniach programu.
- Pokaż lokalną gęstość stanów. W celu użycia tego przycisku wpierw ukończone muszą zostać obliczenia „zlecone do wykonania" przyciskiem powyżej. Jeśli obliczenia zostały już wykonane, zaznaczamy poprzez kliknięcie myszą interesujący nas węzeł i za pomocą tego przycisku wyświetlamy wykres interesującej nas wielkości.
- Normalizacja- pozwala nam na sprawdzenie, czy obliczona gęstość stanów jest znormalizowana. Jest to przycisk kontrolny, który ułatwia weryfikację dokładności obliczeń dla układu przy zadanych parametrach- szczególnie ważny z punktu widzenia programisty w procesie rozwijania aplikacji i wprowadzania nowych funkcjonalności.
- Przyciski wstecz i powtórz, które umożliwiają cofnięcie. powtórzenie ostatnio wykonanej operacji.
- Obliczanie ewolucji czasowej układu- wciśnięcie tego przycisku spowoduje przesłanie warstwie obliczeniowej polecenia wyznaczenia równania ruchu dla operatora ewolucji i podobnie jak w przypadku statycznym obliczenie interesujących nas dynamicznych właściwości łańcucha, takich jak kolejno widoczne na rysunku:
  - zależna od czasu lokalna gęstość stanów,
  - prąd płynący w układzie,
  - całkowita gęstość stanów,
  - obsadzenia ładunkowe,
  - lokalna gęstość stanów dla określonej w ustawieniach energii (przekrój wykresu 3D),
  - lokalna gęstość stanów dla ustalonego czasu (przekrój wykresu 3D) - może służyć do porównania obliczeń dynamicznych z obliczeniami stacjonarnymi,
  - przekrój wykresu obsadzeń ładunkowych.

(G) Sekcja robocza- główna sekcja interfejsu użytkownika. Na niej tworzone są nanostruktury, dla których obliczane są właściwości elektryczne.

Skupiając się na sekcji roboczej (G), możemy przystąpić do utworzenia interesującej nas struktury atomowej. Dwukrotne kliknięcie myszką w obszarze sekcji roboczej spowoduje dodanie pierwszego atomu, który graficznie reprezentowany jest jako gwiazdka. Klikając przycisk „Add electrode" z sekcji D, bądź używając skrótu Ctrl + podwójne kliknięcie powoduje dodanie elektrody do sekcji roboczej. W celu utworzenia wiązania między dwoma elementami (atom-atom - linia ciągła, atom-elektroda - linia przerywana) należ pojedynczym kliknięciem myszy zaznaczyć pierwszy element, a następnie ze wciśniętym przyciskiem Ctrl kliknąć drugi element. W taki sposób jesteśmy w stanie utworzyć pierwszy model łańcucha atomowego. Przykładowy model dwóch sprzężonych atomów, z których każdy połączony jest z elektrodą przedstawia rysunek 3.2.

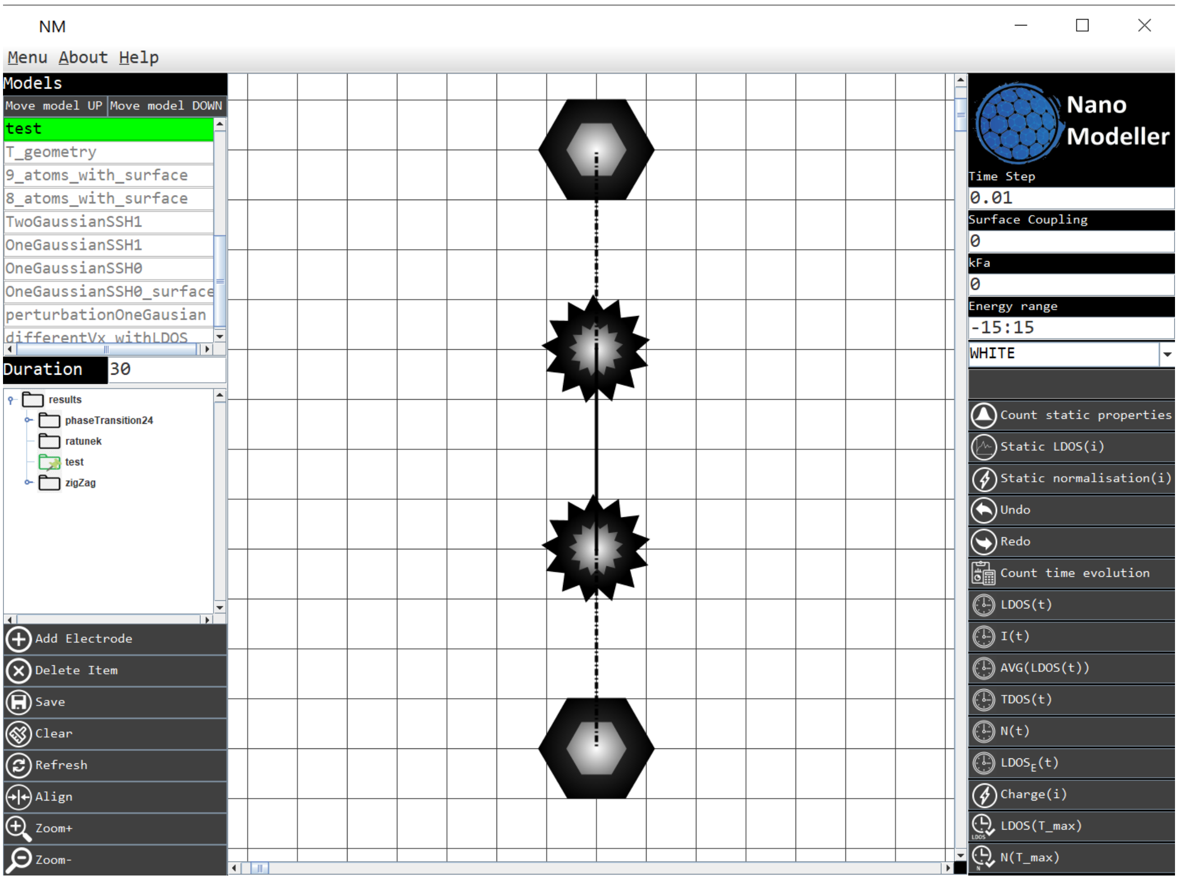
NM
Menu About Help
Models
Move model UP
Move model DOWN
test
T_geometry
9_atoms_with_surface
8_atoms_with_surface
TwoGaussianSSH1
OneGaussianSSH1
OneGaussianSSH0
OneGaussianSSH0_surface
perturbationOneGausian
differentVx_withLDOS
results
phaseTransition24
ratunek
test
zigZag
Add Electrode
Delete Item
Save
Clear
Refresh
Align
Zoom+
Zoom-
Nano
Modeller
Count static properties
Static LDOS(i)
Static normalisation(i)
Undo
Redo
Count time evolution
LDOS(t)
I(t)
AVG(LDOS(t))
TDOS(t)
N(t)
LDOS_E(t)
Charge(i)
LDOS(T_max)
N(T_max)

Duration 30

Time Step 0.01

Surface Coupling 0

kFa 0

Energy range -15:15

WHITE

Rysunek 3.2: Struktura atomowa złożona z dwóch atomów pomiędzy elektrodami wykonana za pomocą programu *Nano Modeller*.

W celu ustalenia innych parametrów naszego układu, należy jednokrotnie kliknąć myszką interesując nas element. W momencie, gdy element ten zostanie podświetlony, sekcja oznaczona literą E na rysunku 3.1 ulega zmianie i umożliwia teraz wprowadzenie parametrów zaznaczonego elementu, tak jak zostało to pokazane na rysunku 3.3. Panel A rysunku 3.3 przedstawia zaznaczoną elektrodę, dla której możemy zmienić skok czasowy dla obliczeń numerycznych, efektywne sprzężenie z łańcuchem atomowym, energię Fermiego, typ elektrody, oraz kolor elementu. „Rodzaj elektrody" jest to etykieta, która umożliwia pogrupowanie elementów, które w zamyśle użytkownika powinny cechować się tymi samymi właściwościami. Uzupełnienie tego pola tym samym napisem dla różnych elektrod umożliwia zaaplikowanie wprowadzonych parametrów od razu dla wszystkich elektrod posiadających tę samą etykietę np. „e1". Jeżeli pole to jest puste, to po kliknięciu przycisku „Zastosuj do wszystkich", wszystkie elektrody z pustą etykietą otrzymają te same parametry. To samo zachowanie dotyczy pozostałych elementów, którymi są energie jednoelektronowe oraz sprzężenia. Panel B przedstawia zaznaczony atom, dla którego możemy zmienić energię stanu elektronowego, wartość sprzężenia spin-flip, początkowe obsadzenie ładunkowe, oraz podobnie jak w przypadku elektrody jego typ i kolor. Oprócz tego możemy zdecydować, czy konieczne jest zapisywanie w pliku danych dla tego atomu. Na panelu C zaprezentowane jest zaznaczone sprzężenie między atomami, dla którego możemy zmienić jego wartość. Zauważmy, że gdy ustawimy dwa różne typy sprzężenia w łańcuchu, to możemy w łatwy sposób otrzymać topologiczny łańcuch SSH. Jeżeli klikniemy sekcję roboczą bez zaznaczania żadnego elementu nasza sekcja E z rysunku 3.1 wróci do pierwotnej postaci, jak widzimy to na panelu D rysunku 3.3. Daje to nam możliwość ustawiania parametrów podłoża, które możemy traktować jako dodatkową elektrodę, którą w zależności od potrzeb możemy uwzględniać w obliczeniach.

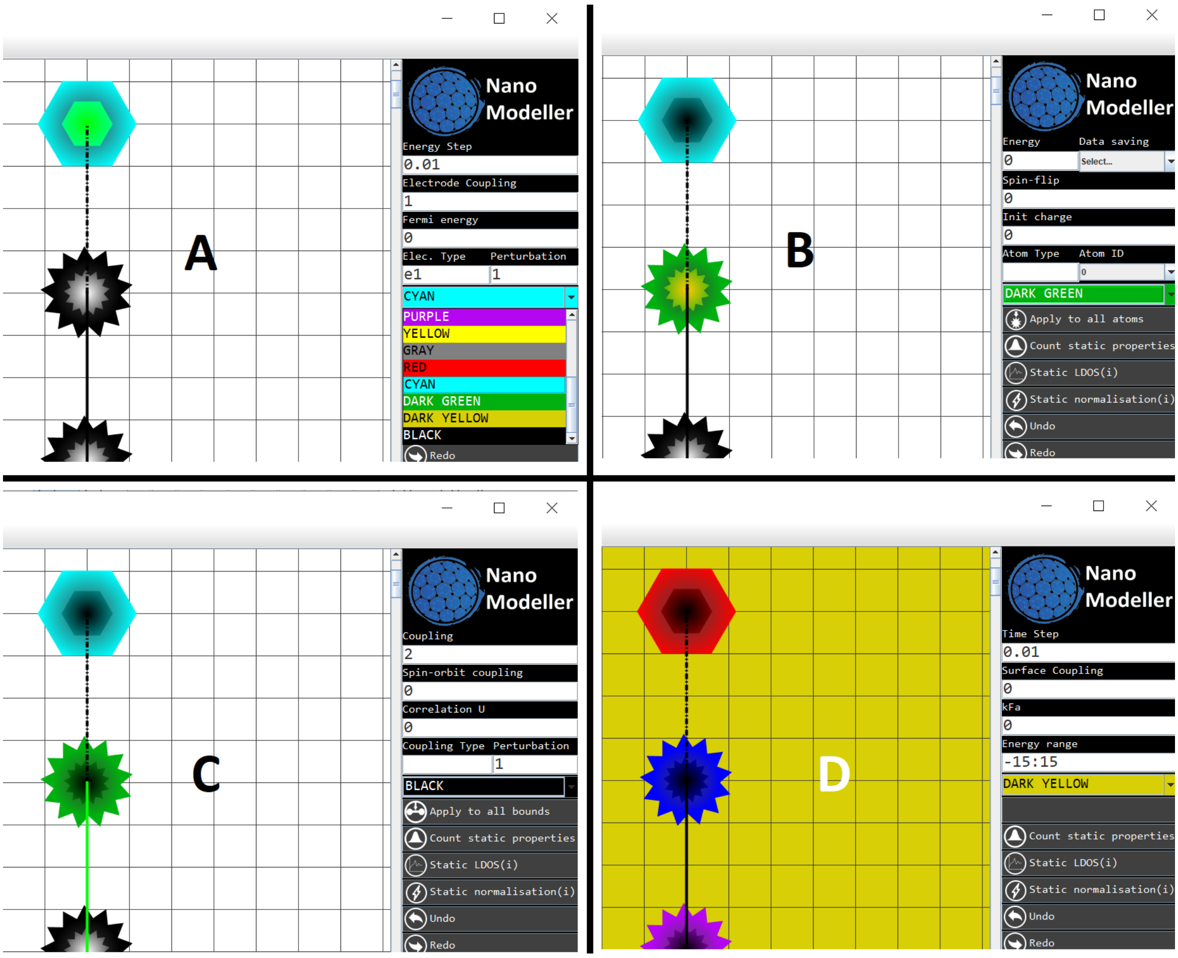
A
Nano Modeller
PURPLE
YELLOW
GRAY
RED
CYAN
DARK GREEN
DARK YELLOW
BLACK
Redo
B
Nano Modeller
Apply to all atoms
Count static properties
Static LDOS(i)
Static normalisation(i)
Undo
Redo
C
Nano Modeller
Apply to all bounds
Count static properties
Static LDOS(i)
Static normalisation(i)
Undo
Redo
D
Nano Modeller
Count static properties
Static LDOS(i)
Static normalisation(i)
Undo
Redo

A
Energy Step
0.01
Electrode Coupling
1
Fermi energy
0
Elec. Type e1
Perturbation 1
CYAN

B
Energy 0
Data saving Select...
Spin-flip
0
Init charge
0
Atom Type
Atom ID 0
DARK GREEN

C
Coupling
2
Spin-orbit coupling
0
Correlation U
0
Coupling Type
Perturbation 1
BLACK

D
Time Step
0.01
Surface Coupling
0
kFa
0
Energy range
-15:15
DARK YELLOW

Rysunek 3.3: Wycinki ekranu głównego programu *Nano Modeller* przedstawiające zaznaczone elementy różnego typu: A) elektroda, B) atom, C) wiązanie między atomami, D) podłoże, dla których użytkownik ma możliwość wprowadzenia żądanych parametrów.

Tworzenie skomplikowanych struktur o dużej ilości elementów jest czasochłonnym zadaniem. Próbując stworzyć model N-atomowego łańcucha, użytkownik musi wykonać N operacji dodawania atomów, oraz co najmniej $N-1$ operacji łączenia atomów (zadawanie sprzężeń pomiędzy stanami atomowymi). W przypadku modelu 100-atomowego łańcucha atomowego daje nam to łączną liczbę 199 operacji do wykonania. Wychodząc naprzeciw utrudnieniom pojawiającym się w procesie projektowania, *Nano Modeller* oferuje funkcjonalność pozwalającą na powielanie prostych struktur (komórek elementarnych) oraz daje możliwość wygodnego ich obracania (odbicie lustrzane w kierunku wertykalnym i horyzontalnym), co pozwala na efektywne zagospodarowanie sekcji roboczej. By powielić, bądź zmienić orientację interesującej nas struktury, należy zaznaczyć ją, trzymając wciśnięty prawy przycisk myszy, a następnie wybrać z menu kontekstowego odpowiedni przycisk, tak jak zostało to pokazane na ilustracji 3.4.

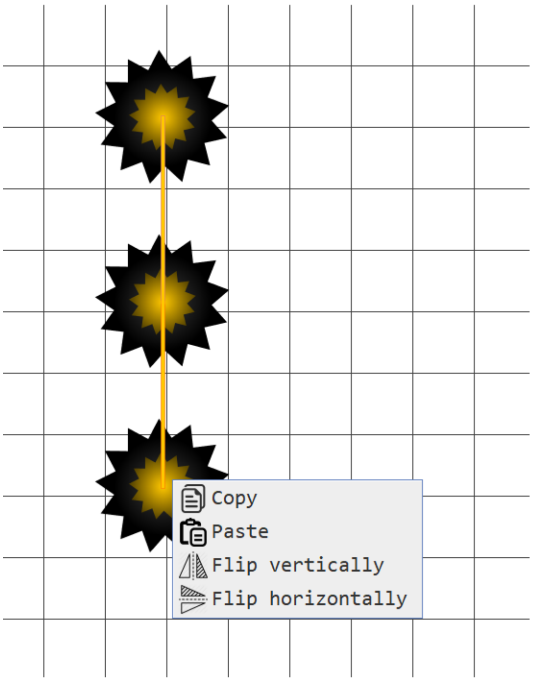

Rysunek 3.4: Zaznaczony układ trzech atomów, który może posłużyć jako komórka elementarna do szybkiego skonstruowania długiego łańcucha atomowego. Kliknięcie prawym przyciskiem myszy powoduje wyświetlenie się menu kontekstowego posiadającego przyciski: kopiuj, wklej, odbij pionowo, odbij poziomo.

Jak zostało wspomniane na początku rozdziału, program *Nano Modeller* dzięki współpracy ze środowiskiem graficznym Gnuplot, daje użytkownikom możliwość tworzenia wykresów funkcji dotyczących właściwości elektrycznych dowolnego atomu, a także całego układu w sposób szybki i intuicyjny. By móc wykreślić interesującą nas zależność, musimy w pierwszej kolejności upewnić się, czy wszystkie niezbędne obliczenia zostały już zainicjalizowane (program posiada ikonę postępu obliczeń, co pomaga użytkownikowi określić niezbędny czas pracy warstwy obliczeniowej). Jeżeli obliczenia są wykonywane, zaznaczamy interesujące nas atomy (możemy wybrać dowolną ich liczbę) i klikamy przycisk „Show <nazwa wielkości>" (program umożliwia dostęp do danych w czasie rzeczywistym, tzn. użytkownik nie musi czekać do zakończenia pracy warstwy obliczeniowej, by móc podejrzeć wyniki), bądź wybieramy sam przycisk jeżeli dana wielkość charakteryzuje cały układ, jak np. całkowita gęstość stanów. *Nano Modeller* w sposób zautomatyzowany dostosuje rodzaj i liczbę wykresów do potrzeb użytkownika, co możemy zauważyć na rysunkach 3.5 i 3.6, gdzie wykreślone zostały lokalne gęstości stanów dla jednego i dwóch atomów odpowiednio dla przypadku niezależnego oraz zależnego od czasu: wykresy funkcji jednej i dwóch zmiennych odpowiednio. Parametry wykresów takie jak np. nazwa osi, zakres danych, kolor wykresu, tytuł i wiele innych mogą być dostosowane do potrzeb użytkownika w ustawieniach programu.

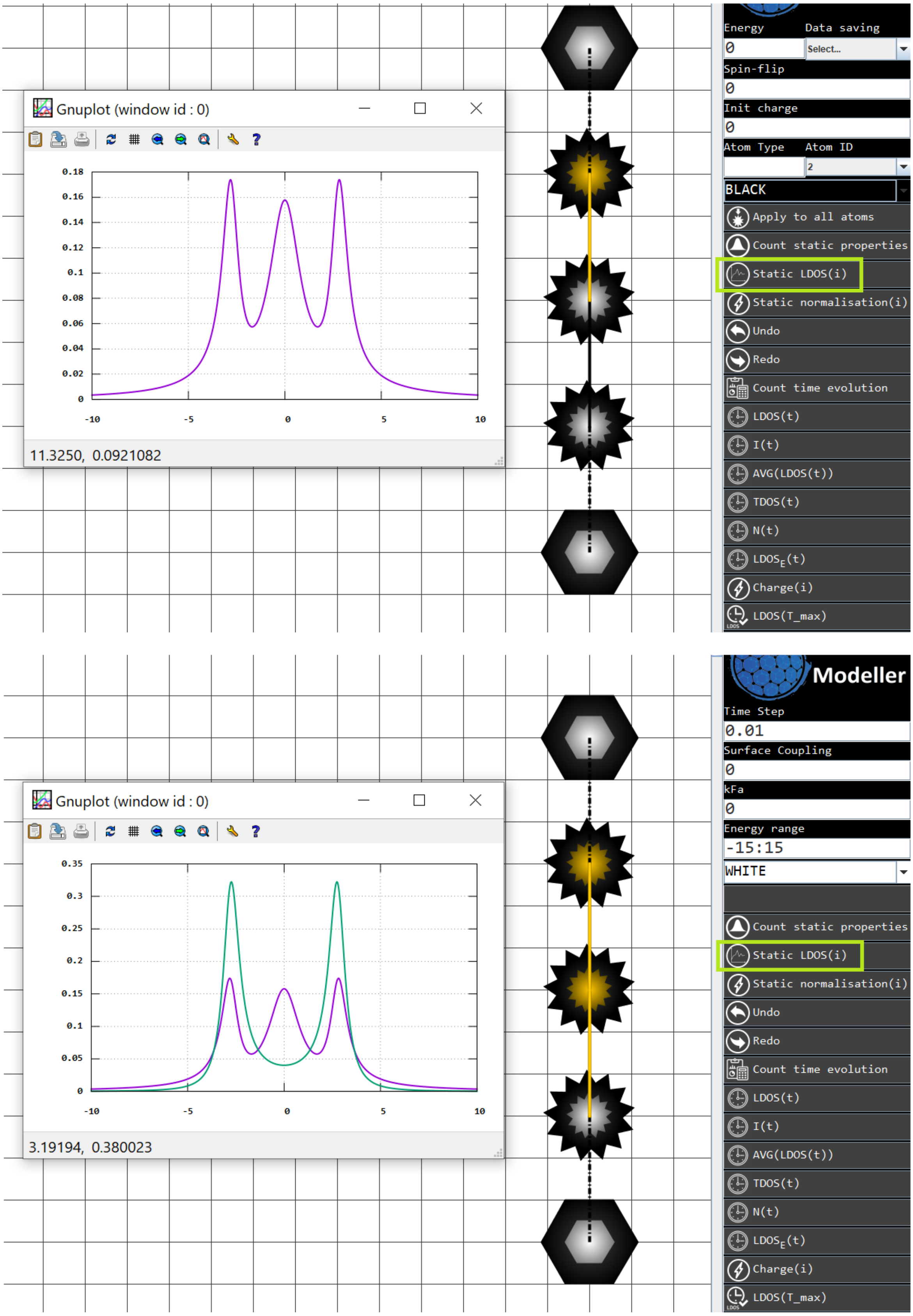

Gnuplot (window id : 0)

11.3250, 0.0921082

Energy: 0

Data saving: Select...

Spin-flip: 0

Init charge: 0

Atom Type:

Atom ID: 2

BLACK

Gnuplot (window id : 0)

3.19194, 0.380023

Time Step: 0.01

Surface Coupling: 0

kFa: 0

Energy range: -15:15

WHITE

0.18
0.16
0.14
0.12
0.1
0.08
0.06
0.04
0.02
0
-10
-5
0
5
10
Apply to all atoms
Count static properties
Static LDOS(i)
Static normalisation(i)
Undo
Redo
Count time evolution
LDOS(t)
I(t)
AVG(LDOS(t))
TDOS(t)
N(t)
LDOS_E(t)
Charge(i)
LDOS(T_max)
Modeller
0.35
0.3
0.25
0.2
0.15
0.1
0.05
0
-10
-5
0
5
10
Count static properties
Static LDOS(i)
Static normalisation(i)
Undo
Redo
Count time evolution
LDOS(t)
I(t)
AVG(LDOS(t))
TDOS(t)
N(t)
LDOS_E(t)
Charge(i)
LDOS(T_max)

Rysunek 3.5: Wyświetlanie wykresów funkcji jednej zmiennej - $LDOS(E)$ jednego, oraz dwóch atomów jednocześnie w programie *Nano Modeller* zintegrowanym ze środowiskiem graficznym Gnuplot.

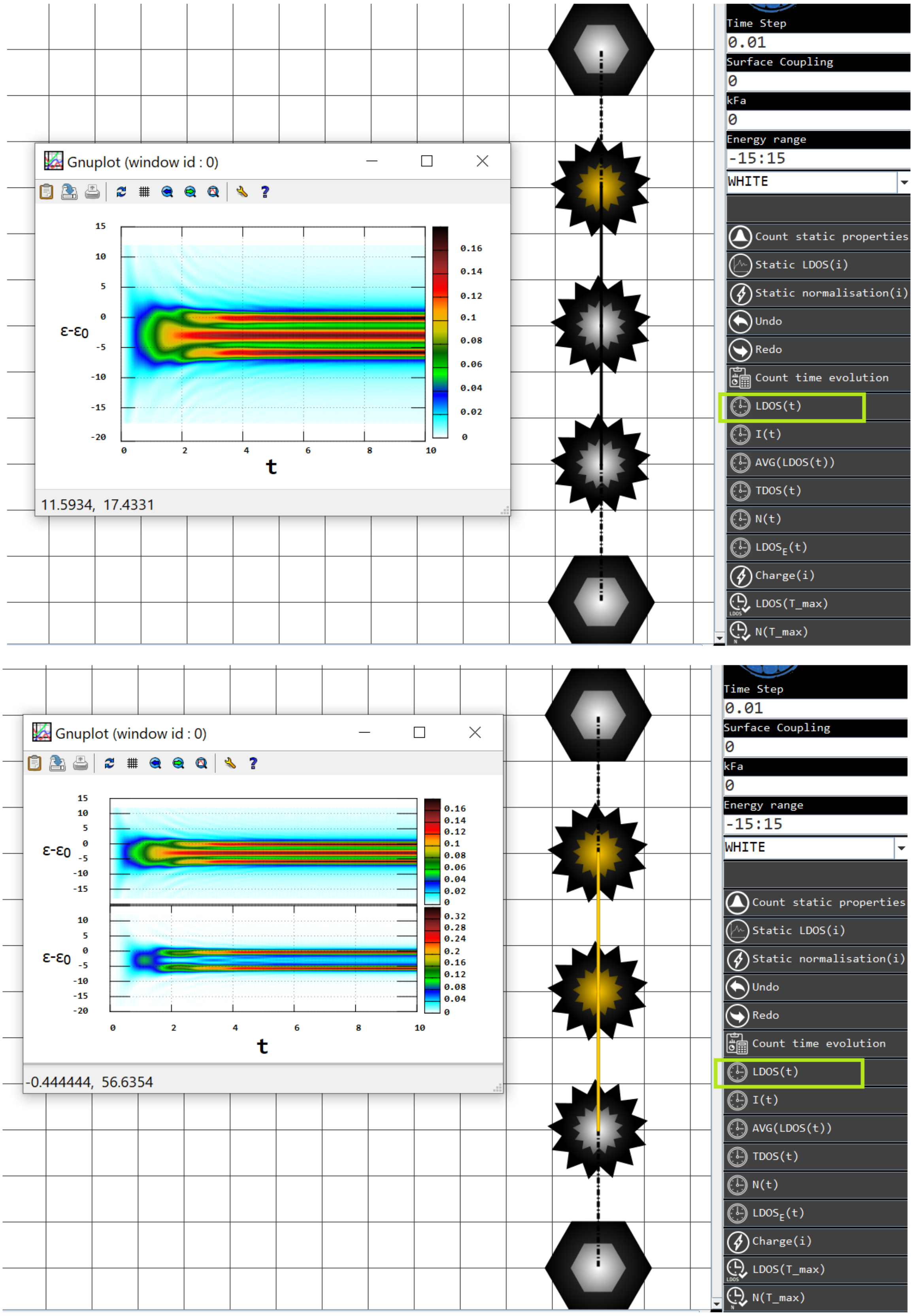
Gnuplot (window id : 0)
ε-ε0
t
15
10
5
0
-5
-10
-15
-20
0
2
4
6
8
10
0.16
0.14
0.12
0.1
0.08
0.06
0.04
0.02
0
Count static properties
Static LDOS(i)
Static normalisation(i)
Undo
Redo
Count time evolution
LDOS(t)
I(t)
AVG(LDOS(t))
TDOS(t)
N(t)
LDOS_E(t)
Charge(i)
LDOS(T_max)
N(T_max)
0.32
0.28
0.24
0.2
0.16
0.12
0.08
0.04

11.5934, 17.4331

Time Step
0.01
Surface Coupling
0
kFa
0
Energy range
-15:15
WHITE

-0.444444, 56.6354

Time Step
0.01
Surface Coupling
0
kFa
0
Energy range
-15:15
WHITE

Rysunek 3.6: Wykresy funkcji zależnej od czasu lokalnej gęstości stanów w postaci map cieplnych dla pojedynczego atomu (panel górny), oraz dwóch atomów (panel dolny) powstałe w programie *Nano Modeller* zintegrowanym ze środowiskiem graficznym Gnuplot.

Zarządzanie parametrami wykresów, jak również sposobem zapisywania danych przez program odbywa się poprzez okno ustawień programu *Nano Modeller*, którego zrzut ekranu został zaprezentowany na rysunku 3.7. Okno opcji programu posiada dwie wydzielone części. Pierwsza z nich pozwala na zarządzanie pamięcią. W tej sekcji możemy ustalić częstotliwość dostępu warstwy obliczeniowej do pamięci komputera poprzez ustalenie interwałów zapisu danych do pliku. W celu zaoszczędzenia miejsca na dysku możemy zmniejszyć rozmiar wynikowego pliku z danymi poprzez zażądanie zapisywania wyników obliczeń z określoną częstotliwością. Dodatkowo możemy ustalić czas, od którego powinno zacząć się zapisywanie danych do pliku. Ta funkcjonalność może przydać się w momencie gdy dynamika dojścia układu do stanu równowagowego nie jest dla nas istotna i początkowe dane zbędnie zajmowałyby miejsce na dysku. Kolejną możliwością oferowaną przez program, są zmienne użytkownika, których okno zaznaczone jest niebieską strzałką na rysunku 3.7. Dzięki nim obsługa programu staje się prostsza, ponieważ możemy zmieniać parametry całego łańcucha w jednym miejscu. Należy też zwrócić uwagę, że niektóre symbole są zarezerwowane i są zmiennymi predefiniowanymi przez program, jak np. zmienna „t" oznaczająca czas. Druga sekcja okna opcji pozwala nam na spersonalizowanie wykresów interesujących nas zależności, takich jak np. rozmiar, styl, położenie tekstu (nazwy osi, tytuł), obecność siatki, zagęszczenie punktów na osiach (rozdzielczość wykresu), zakres osi, czy też ustawienia wyświetlania wykresów wielu zależności jednocześnie. Dodatkowo użytkownik ma możliwość podania własnego skryptu, który powinien zostać wykonany przez program (odpowiednik terminala programu Gnuplot), a także ręcznego wybrania palety barw i odpowiadających tym barwom wartości numerycznych dla wykresów trójwymiarowych.

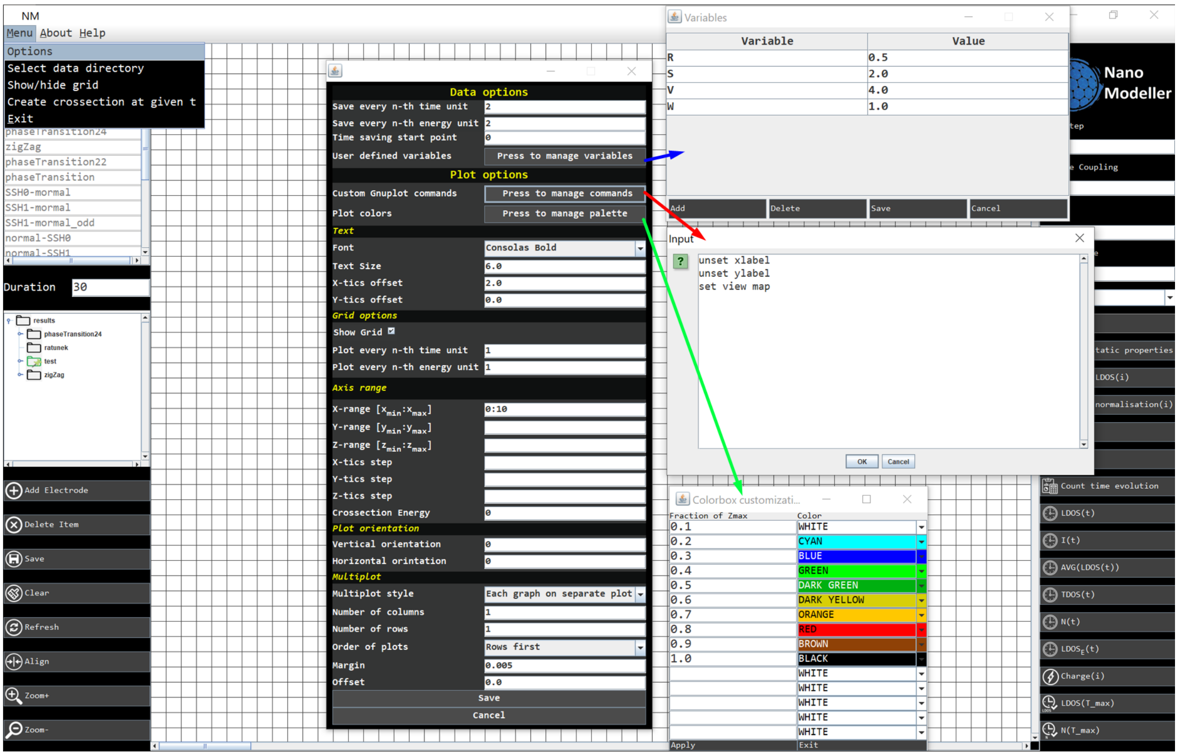
NM
Menu About Help
Options
Select data directory
Show/hide grid
Create crossection at given t
Exit
phaseTransition24
zigZag
phaseTransition22
phaseTransition
SSH0-normal
SSH1-normal
SSH1-normal_odd
normal-SSH0
normal-SSH1
results
phaseTransition24
ratunek
test
zigZag
Add Electrode
Delete Item
Save
Clear
Refresh
Align
Zoom+
Zoom-
Nano Modeller
Coupling
tatic properties
LDOS(i)
normalisation(i)
Count time evolution
LDOS(t)
I(t)
AVG(LDOS(t))
TDOS(t)
N(t)
LDOS$_E$(t)
Charge(i)
LDOS(T_max)
N(T_max)
Variables
Add
Delete
Save
Cancel
Input
OK
Cancel
Colorbox customizati...
Apply
Exit

Duration 30

Data options

Save every n-th time unit	2
Save every n-th energy unit	2
Time saving start point	0
User defined variables	Press to manage variables

Plot options

Custom Gnuplot commands	Press to manage commands
Plot colors	Press to manage palette
Text	
Font	Consolas Bold
Text Size	6.0
X-tics offset	2.0
Y-tics offset	0.0
Grid options	
Show Grid ☑	
Plot every n-th time unit	1
Plot every n-th energy unit	1
Axis range	
X-range [x_{min}:x_{max}]	0:10
Y-range [y_{min}:y_{max}]	
Z-range [z_{min}:z_{max}]	
X-tics step	
Y-tics step	
Z-tics step	
Crossection Energy	0
Plot orientation	
Vertical orientation	0
Horizontal orintation	0
Multiplot	
Multiplot style	Each graph on separate plot
Number of columns	1
Number of rows	1
Order of plots	Rows first
Margin	0.005
Offset	0.0
Save	
Cancel	

Variable	Value
R	0.5
S	2.0
V	4.0
W	1.0

```
unset xlabel
unset ylabel
set view map
```

Fraction of Zmax	Color
0.1	WHITE
0.2	CYAN
0.3	BLUE
0.4	GREEN
0.5	DARK GREEN
0.6	DARK YELLOW
0.7	ORANGE
0.8	RED
0.9	BROWN
1.0	BLACK
	WHITE
	WHITE
	WHITE
	WHITE
	WHITE

Rysunek 3.7: Okno ustawień programu *Nano Modeller*. Pierwsza sekcja „Data Options" pozwala na zarządzanie pamięcią zajmowaną przez wynikowe pliki z obliczeniami, druga zaś „Plot options" pozwala na dostosowanie wykresów do potrzeb użytkownika. Widoczne z prawej strony okna oznaczone kolorowymi strzałkami są opcjami szczegółowymi.

Rozdział 4

Wykaz działalności naukowej

4.1 Wykaz publikacji naukowych

Wyniki badań naukowych, które składają się na niniejszą rozprawę doktorską, ukazały się w postaci 7 artykułów w recenzowanych czasopismach naukowych, których kopie zostały dołączone na końcu autoreferatu. Uczestniczyłem we wszystkich etapach powstawania wymienionych prac, a mój wkład w ich powstanie wynosi 50%. Artykuły te stanowią tematyczny cykl publikacji dotyczących badań normalnych i topologicznych łańcuchów atomowych na różnych powierzchniach, w przypadkach stacjonarnych oraz zależnych od czasu. W niniejszym podrozdziale wymienione zostaną szczegółowe cele i hipotezy badawcze, oraz streszczone wyniki badań zawartych w poszczególnych pracach naukowych. Chciałbym zaznaczyć, że publikacja nr **7**, mimo iż koncentruje się na warstwie informatycznej (związanej z wizualizacją danych), to zawiera również wyniki dotyczące układów jednowymiarowych, a zaproponowana w niej metoda wizualizacji wyników była kluczowa przy odkryciu struktur *transient crystal* opisanych w publikacji nr **4**. Z tego powodu została ona zawarta w cyklu publikacji naukowych.

Poza wymienionymi opublikowanymi artykułami stanowiącymi tematyczny cykl publikacji naukowych wchodzącymi w skład rozprawy doktorskiej jestem również współautorem publikacji dotyczącej teoretycznych i eksperymentalnych badań nad stanami ciemnymi w układach 1D, która obecnie jest przygotowywana do publikacji: *Dark states in atomic chains*, Marek Dachniewicz, Marcin Kurzyna, Tomasz Kwapinski, Mieczysław Jałochowski.

Ponadto jestem współautorem artykułu naukowego z dziedziny inżynierii oprogramowania, w którym zbadany został poziom użyteczności interfejsów użytkownika aplikacji mobilnych: *A comparative analysis of interface quality of mobile access to the services of selected banks*, Marcin Kurzyna, Damian Matysiak, Marek Miłosz, Journal of Computer Science Institute, **5**, 159-166, (2017).

1. *Non-local electron transport through normal and topological ladder-like atomic systems*

Marcin Kurzyna, Tomasz Kwapiński, Journal of Applied Physics **123**(19), 194301 (2018)

Cele badań

Łańcuchy atomowe, jako najcieńsze przewodniki prądu mogą znaleźć wiele zastosowań w urządzeniach elektrycznych przyszłości. Należy zatem zweryfikować, czy ich właściwości elektryczne nie zmieniają się w sposób diametralny w kontakcie z podłożem, czy też przy obecności zaburzeń zewnętrznych, które są nieodzownym elementem realistycznych struktur. Już w samym procesie wytwarzania łańcuchów atomowych np. z wykorzystaniem powierzchni wicynalnych, trudno ustrzec się od nadmiarowych atomów (adatomów) lub defektów stanowiących zaburzenia układu. Ponadto osadzając większą ilość atomów, możemy doprowadzić do wytworzenia podwójnych łańcuchów atomowych (czy nawet potrójnych) [3]. Rozłożenie atomów w takim łańcuchu jest zależne od stałej sieci podłoża oraz rozkładu atomów w łańcuchu sąsiednim. Takie otoczenie może prowadzić do powstania w łańcuchu geometrii SSH, a tym samym pojawienia się fazy topologicznej.

Istotną kwestią jest znalezienie różnic we właściwościach elektrycznych między łańcuchami atomowymi w różnych fazach topologicznych i zweryfikowanie, jaki ma to wpływ na stabilność układów jednowymiarowych.

Hipotezy badawcze

(a) Losowo osadzające się na łańcuchu adatomy zaburzają przewodnictwo elektryczne łańcucha, przez co ich obecność znacznie ogranicza zastosowania aplikacyjne najcieńszych przewodników prądu.

(b) Stany brzegowe łańcuchów atomowych w nietrywialnej fazie topologicznej są stanami chronionymi, zatem nie ulegają one destrukcji pod wpływem zaburzeń adatomami czy też przy kontakcie z podłożem.

(c) Obsadzenia ładunkowe w przypadku topologicznych łańcuchów atomowych nie zmieniają się pod wpływem obecności adatomów.

Wyniki badań

Dokonując obliczeń z wykorzystaniem formalizmu retardowanych funkcji Greena oraz hamiltonianu ciasnego wiązania udało nam się odkryć długookresowe oscylacje konduktancji łańcucha atomowego jako funkcji liczby adatomów. Wynik ten oznacza, iż konduktancja praktycznie nie zmienia się jeżeli w układzie występuje pojedyncze zaburzenie, które w sposób niekontrolowany może pojawić się podczas procesu wzrostu łańcucha. Zmiany są widoczne, dopiero gdy na głównym łańcuchu atomowym osadza się dużo większa ilość dodatkowych atomów. Jednakże pojawienie się takiej ilości adatomów nie jest już zjawiskiem niekontrolowanym, co oznacza, że konduktancja łańcucha atomowego może być w pełni kontrolowana przez operatora eksperymentu, co jest niezwykle istotne z praktycznego punktu widzenia. Otrzymane wyniki spowodowały, iż musieliśmy zweryfikować naszą pierwszą hipotezę badawczą, która w ogólności (na szczęście) okazała się być błędna. Daje to zielone światło przyszłym badaniom, które ukierunkowane są pod kątem zastosowań aplikacyjnych łańcuchów atomowych.

Dodatkowo przeanalizowaliśmy zachowanie łańcuchów atomowych w nietrywialnej fazie topologicznej i zauważyliśmy, iż obecność adatomów, czy też obecność różnego rodzaju podłoży nie wpływa na strukturę stanów topologicznych, co odróżnia stany te od stanów atomowych w zwykłych nietopologicznych łańcuchach atomowych, które to są zauważalnie modyfikowane przez otoczenie. Obecność adatomów (domieszek) w łańcuchu może zatem posłużyć do detekcji brzegowych stanów topologicznych, gdyż ich energie nie zmieniają się pod wpływem zaburzeń. Spostrzeżenia te pozwalają uznać naszą drugą hipotezę badawczą za słuszną.

Ponadto wykazaliśmy, iż struktura obsadzeń ładunkowych zaburzonych topologicznych łańcuchów atomowych różni się znacząco od obsadzeń w idealnych łańcuchach. Normalne łańcuchy atomowe wykazują istnienie fal ładunkowych w obrębie całego łańcucha, zwanych oscylacjami Friedela. Idealne łańcuchy SSH natomiast nie przejawiają żadnych oscylacji ze względu na przerwę energetyczną na wewnętrznych węzłach układu. Sytuacja zmienia się jednak przy obecności adatomów. Wówczas łańcuchy SSH również wykazują oscylacje ładunkowe, ale co ważne, jedynie na tych węzłach, które mają bezpośredni kontakt z dodatkowym łańcuchem zbudowanym z adatomów. Z tego względu musieliśmy odrzucić ostatnią hipotezę badawczą.

2. *Electronic properties of atomic ribbons with spin-orbit couplings on different substrates*

Marcin Kurzyna, Tomasz Kwapiński, Journal of Applied Physics **125**(14), 144301 (2019)

Cele badań

Model SSH jest modelem struktury atomowej z ograniczoną liczbą stopni swobody nie tylko za względu na ograniczenie ruchu elektronów do jednego wymiaru, ale również ze względu na spin. W układach jednowymiarowych ruch elektronów wzdłuż łańcucha atomowego może być spinowo-niezależny.

Aby uwzględnić efekty typu spin-orbita pojawiające się w realnych strukturach jednowymiarowych oraz quasi-jednowymiarowych (łańcuchy, struktury drabiniaste i wstążki atomowe), należy rozszerzyć bazowy hamiltonian sprzężonych łańcuchów SSH o dodatkowe dwa człony:

$$H_{so} = \sum_{\sigma,\sigma'} \left(V_{so}^{||} \sum_{i,j} (\hat{a}_i^{\sigma'})^{\dagger} (i\hat{\sigma}_x)_{\sigma,\sigma'} \hat{a}_j^{\sigma} - V_{so}^{\perp} \sum_{i} (\hat{a}_i^{\sigma'})^{\dagger} \, (i\hat{\sigma}_y)_{\sigma,\sigma'} \, a_i^{\sigma} \right) + \sum_{i,\sigma} V_{sf} (\hat{a}_i^{\sigma})^{\dagger} \hat{a}_i^{-\sigma} + h.c. \tag{4.1}$$

Pierwszy z nich opisuje sprzężenie spin-orbita między węzłami tego samego łańcucha (||, wzdłuż łańcucha), bądź między węzłami z różnych łańcuchów ($\perp$), dla łańcuchów podwójnych, wstążek atomowych lub struktur drabiniastych. Drugi człon odpowiada za odwrócenie spinu na poszczególnych węzłach łańcucha atomowego (sf ang. *spin-flip*). W hamiltonianie 4.1, $\hat{\sigma}_x, \hat{\sigma}_y$ oznaczają macierze Pauliego, $V_{so}^{||}$, $V_{so}^{\perp}$, V_{sf} oznaczają odpowiednio efektywne sprzężenia spin-orbita w dwóch kierunkach, oraz wartość sprzężenia *spin-flip*. Uwzględnienie tego dodatkowego oddziaływania wymaga, by rozszerzyć macierz A 2.32, występującą w równaniu ruchu dla retardowanej funkcji Greena, o człony, które są zależne od spinu elektronu: odpowiednio σ oraz $-\sigma$:

$$\hat{A} \to \hat{C} = \begin{bmatrix} \hat{A}^{\sigma} & \hat{D}^{\sigma,-\sigma} \\ \hat{D}^{-\sigma,\sigma} & \hat{A}^{-\sigma} \end{bmatrix}, \tag{4.2}$$

gdzie elementy macierzy $\hat{D}^{\sigma,-\sigma}$ zdefiniowane są następująco:

$$D_{id,jd'}^{\sigma,-\sigma} = -V_{sf}\delta_{ij}\delta_{dd'} - V_{so}^{||}(\delta_{i,j-1} - \delta_{i,j+1})\delta_{dd'} + \mp i V_{sf}\delta_{d,d'\pm1}\delta_{i,j\pm1} \tag{4.3}$$

Oddziaływanie spin-orbita było uwzględniane w badaniach nad łańcuchami atomowymi, w tym nad łańcuchami topologicznymi [127, 128]. Brakowało nam jednak w literaturze rozważań uwzględniających również wpływ podłoża, na którym te obiekty są tworzone oraz wzajemnego oddziaływania dodatkowych łańcuchów atomowych na właściwości elektryczne sprzężonych łańcuchów atomowych.

Hipotezy badawcze

(a) Źródłem asymetrii lokalnej gęstości stanów jest zarówno delokalizacja elektronów w podłożu, jak i oddziaływanie spin-orbita.

(b) Obsadzenia ładunkowe widoczne na poszczególnych węzłach łańcuchów atomowych mogą być spinowo-spolaryzowane.

(c) Topologiczne łańcuchy atomowe wykazują spinowo-spolaryzowane obsadzenia ładunkowe jedynie na swych brzegach.

Wyniki badań

Korzystając z metody funkcji Greena dla hamiltonianu ciasnego wiązania, wykazaliśmy, iż poziom zlokalizowania elektronów w podłożu ma wpływ na symetrię lokalnej gęstości stanów struktur atomowych umieszczonych na tejże powierzchni. Ukazane zostało, iż podłoża metaliczne, o dużym stopniu delokalizacji elektronów powodują wzrost asymetrii lokalnej gęstości stanów na węzłach łańcucha. Co ciekawe struktury atomowe leżące na podłożach izolatorowych z silnie zlokalizowanymi elektronami również mogą wykazywać asymetrię $LDOS$ ze względu na oddziaływania $spin-flip$ oraz spin-orbita, które oprócz łamania symetrii układu, również rozszczepiają wierzchołki funkcji spektralnej, która na dodatek staje się spinowo-zależna. Tak więc należy przyjąć pierwszą hipotezę badawczą za słuszną. Co ważne, oddziaływania te powodują również rozszczepienie stanów topologicznych nietrywialnych łańcuchów SSH.

Analizując dłuższe łańcuchy atomowe w różnych fazach topologicznych, wykazaliśmy, iż normalne, nietopologiczne łańcuchy atomowe cechują się polaryzacją spinową obsadzeń ładunkowych jedynie na końcowych węzłach łańcucha ze względu na spinowo-niezależną charakterystykę $LDOS$ w środku łańcucha, co było zgodne z drugą hipotezą badawczą. Badając topologiczne łańcuchy SSH, odkryliśmy, iż w przypadku obecności oddziaływań *spin-flip* oraz spin-orbita struktury te wykazują istnienie fal ładunkowych w obrębie całego łańcucha, co zdecydowanie różni się od wyników bez uwzględnienia tych oddziaływań, gdzie oscylacje Friedela nie występują. Z tych względów musieliśmy odrzucić ostatnią hipotezę badawczą.

Dodatkowo badając strukturę lokalnej gęstości stanów wstążek atomowych wzdłuż łańcuchów, odkryliśmy, iż położenia lokalnych ekstremów funkcji spektralnej w poszczególnych łańcuchach wstążki atomowej silnie zależą od oddziaływań *spin-flip* oraz spin-orbita. Jeżeli oddziaływania związane ze spinem są niewielkie, wówczas minima i maksima $LDOS$ są ze sobą w fazie. Zwiększenie wartości tych oddziaływań natomiast prowadzi do odwrotnej sytuacji, gdyż wówczas dla dużych wartości tychże oddziaływań ekstrema te pozostają ze sobą w antyfazie.

3. *Edge-state dynamics in coupled topological chains*

Marcin Kurzyna, Tomasz Kwapiński Physical Review B **102**(19), 195429 (2020)

Cele badań

By łańcuchy atomowe mogły posłużyć w przyszłości jako elementy złożonych systemów nanoelektronicznych, kluczowe jest zbadanie dynamiki ich właściwości elektrycznych w momencie zainicjowania kontaktu tychże struktur z rezerwuarem elektronów (podłożem), a także przeanalizowanie ich zachowania w odpowiedzi na zaburzenia zewnętrzne takie jak np. zmiana oddziaływań między stanami elektronowymi atomów łańcucha, kontakt z innymi łańcuchami atomowymi lub też mechaniczna ingerencja w integralność łańcucha (przerywanie, pękanie, wytrącanie atomów). Badając dynamikę stanów elektronowych łańcuchów atomowych, warto rozważyć różne fazy topologiczne tychże struktur. W szczególności warto zwrócić uwagę na dynamikę formowania się stanów topologicznych w nietrywialnych łańcuchach SSH i określić charakterystyczne skale czasowe tego procesu oraz zrozumieć mechanizmy nim rządzące. Warto również zastanowić się, jaki będzie efekt dynamicznej zmiany parametrów łańcucha atomowego prowadzącej do zaistnienia topologicznego przejścia fazowego w łańcuchu, a także jaki wpływ na siebie będą miały oddziałujące ze sobą łańcuchy atomowe w różnych fazach topologicznych. Istotne jest, by uwzględnić również korelacje elektronowe i zbadać czy rola odpychania kulombowskiego jest tak samo ważna dla normalnych, jak i topologicznych łańcuchów atomowych.

Hipotezy badawcze

(a) Czas potrzebny do uformowania się stabilnej (stacjonarnej) struktury stanów elektronowych łańcucha atomowego, w którym zainicjowano kontakt z rezerwuarem elektronów, bądź poddano zaburzeniom zewnętrznym zależy od poziomu delokalizacji elektronów w podłożu.

(b) Stany topologiczne nietrywialnych łańcuchów atomowych mogą przemieszczania się w czasie między sąsiednimi węzłami łańcucha atomowego, w tym też istnieje możliwość krótkotrwałego wyindukowania stanów topologicznych w łańcuchu atomowym w trywialnej fazie topologicznej.

(c) Kontakt topologicznego łańcucha atomowego z normalnym łańcuchem atomowym nie wpływa na obsadzenia ładunkowe na poszczególnych węzłach łańcucha SSH ze względu na istnienie wzdłuż niego przerwy energetycznej.

Wyniki badań

W badaniach dynamiki układów atomowych skupiliśmy się na zależnych od czasu obsadzeniach ładunkowych, prądach płynących przez łańcuch oraz w głównej mierze na lokalnej gęstości stanów elektronowych. Przeanalizowaliśmy zachowanie układu w przypadku nagłej zmiany oddziaływań stanów elektronowych łańcucha, tak by parametry te odpowiadały dwóm różnym fazom topologicznym łańcucha atomowego. W przypadku nagłego przejścia między zwykłą (nietopologiczną) a nietrywialną fazą topologiczną łańcucha zauważyliśmy, iż obecność stanu topologicznego nie jest widoczna natychmiastowo w lokalnej gęstości stanów, lecz pojawia się on dopiero po pewnym czasie. Dodatkowo sam proces formowania stanu topologicznego jest ściśle uzależniony od obecności, czy też rodzaju podłoża, na którym znajduje się łańcuch atomowy. W przypadku braku podłoża lub dla podłoża izolatorowego układ wykazuje wysoką niestabilność, a proces dochodzenia do stanu równowagi jest rzędy wielkości dłuższy niż w przypadku podłoży metalicznych, co potwierdza naszą pierwszą hipotezę. Ponadto dostrzegliśmy, iż formujący się stan topologiczny w układzie tworzy się wprost ze stanów bocznych charakterystycznych dla zwykłych łańcuchów atomowych, i co za tym idzie przez pewien czas układ jednowymiarowy będący w nietrywialnej fazie topologicznej, zachowuje informacje o swoim poprzednim stanie. Dodatkowo badając reakcję łańcucha atomowego na jego przerwanie, dostrzegliśmy, iż zabieg ten wpływa jedynie na atomy, które były swoimi sąsiadami przed zerwaniem sprzężeń układu, a co zaskakujące praktycznie nie wpływa na pozostałe, bardziej oddalone atomy.

W dalszej części badań skupiliśmy się na wpływie sprzężeń między dwoma łańcuchami atomowymi, mogącymi charakteryzować się różnymi fazami topologicznymi, na lokalną gęstość stanów układu. Zauważyliśmy, iż dynamika zmian stanów brzegowych jest uzależniona od wielu czynników, między innymi od tego czy oddziaływające ze sobą łańcuchy mają zgodne, czy też różne fazy topologiczne. Co zaskakujące najciekawsza fizyka pojawia się w przypadku łańcuchów będących w różnych fazach, gdyż ich wzajemny wpływ na siebie może skutkować migracją stanu topologicznego do łańcucha w fazie trywialnej, a także penetracją tegoż stanu w głąb łańcucha. Kolejnym ważnym czynnikiem jest również parametr sprzężenia między łańcuchami i co ciekawe, kluczowej roli nie odgrywa tutaj sama wartość tegoż sprzężenia, lecz dynamika jego zmiany. Analizując różne tempa łączenia ze sobą łańcuchów zauważyliśmy istotne różnice w lokalnej gęstości stanów między złączeniem, w którym sprzężenie pomiędzy łańcuchami odbywa się adiabatycznie a takim, w którym parametr ten zmienia się skokowo (efekt typu *quench*). Interesujące jest to, iż jedynie dla nagłego połączenia zachodzi migracja w czasie stanu topologicznego do łańcucha w fazie trywialnej oraz jego penetracja na pozostałe węzły łańcucha. Tym samym udało nam się potwierdzić drugą hipotezę badawczą.

Uwzględniając oddziaływania kulombowskie między węzłami łańcuchów oraz dopuszczając możliwość wzajemnego oddziaływania na siebie łańcuchach będących w różnych fazach topologicznych, odkryliśmy, iż odpychanie się elektronów powoduje wytworzenie się oscylacji ładunkowych w topologicznym łańcuchu atomowym, które do tej pory nie były przewidziane w literaturze i co ważne, oscylacje te pozostają w antyfazie z obsadzeniami ładunkowymi zwykłego łańcucha atomowego. Fakt ten skłonił nas do odrzucenia trzeciej hipotezy badawczej.

4. *Nontrivial dynamics of a two-site system: Transient crystals*

Marcin Kurzyna, Tomasz Kwapiński, Physical Review B **102** (24), 245414 (2020)

Cele badań

Analiza efektów włączeniowych i dynamiki dojścia układów do stanu równowagi w nanostrukturach jest zagadnieniem ważnym z punktu widzenia zastosowań tych struktur w nanoelektronice. Większość prac podejmujących tę tematykę skupia się na badaniu charakterystyk prądowych i obsadzeń ładunkowych bez poświęcenia należytej uwagi funkcji gęstości stanów elektronowych ze względu na trudność obliczania tejże funkcji (np. stosując metodę równań ruchu Heisenberga dla operatorów fermionowych, znajdujemy od razu wartości oczekiwane operatora liczby cząstek na węźle, a nie lokalną gęstość stanów [129]). Z tego powodu naszym celem jest dokonanie analizy dynamiki funkcji spektralnej prostych układów atomowych przy uwzględnieniu oddziaływania kulombowskiego oraz kontaktu z różnymi podłożami. Biorąc za obiekt badań krótki łańcuch stanowiący układ dwóch stanów (np. kropek kwantowych) podłączonych nagle do rezerwuaru elektronów, zbadamy dynamikę tworzenia się w czasie struktury $LDOS$ na obu węzłach.

Hipotezy badawcze

(a) Lokalna gęstość stanów układu z dwiema kropkami kwantowymi połączonymi nagle z rezerwuarem elektronów wykazuje efekty interferencyjne (lokalne maksima w $LDOS$), które związane są z „odbijaniem się" fali elektronowej od brzegów łańcucha i które zanikają z czasem.

(b) Układ 2-atomowy w stanie nierównowagowym może stanowić efektywną jednoparametrową pompę elektronową

Wyniki badań

Przy użyciu formalizmu operatora ewolucji, przeanalizowaliśmy dynamikę tworzenia lokalnej gęstość stanów układu złożonego z dwóch sprzężonych kropek kwantowych, który nagle został połączony z zewnętrzną elektrodą. Zauważyliśmy, iż owa funkcja cechuje się dużą regularnością w domenie czasu i co ciekawe tworzy się w niej nietrywialna struktura lokalnych ekstremów $LDOS$. Sprawdziliśmy, że struktura ta odpowiada stacjonarnej gęstości stanów dla układu N-atomowego. Tego rodzaju dynamiczny system stanowi pewną formę kryształów czasowych, nazwanych przez nas *transient crystals*, które charakteryzują się istnieniem regularnie zmieniającej się struktury zanikającej w czasie.

W pracy tej pokazujemy także, że zaobserwowana przez nas struktura periodyczna jest również dobrze widoczna w obecności różnych podłoży oraz przy uwzględnieniu odpychania kulombowskiego między węzłami. Skłania nas to do uznania pierwszej hipotezy badawczej za słuszną, choć dopiero dokładna analiza periodycznej struktury $LDOS$ w domenie czasu (przeprowadzona przy pomocy metod opisanych w publikacji nr **7**) pozwoliła na sformułowanie wniosków dotyczących istnienia w czasie kryształów typu *transient*.

Ponadto w pracy demonstrujemy, iż układy stanowiące takie kryształy mogą pełnić rolę jednoparametrowej pompy elektronowej, w której istnieje możliwość kontrolowania kierunku przepływu prądu przy pomocy napięcia bramki. Jest to niezwykle istotne z aplikacyjnego punktu widzenia, albowiem pompy jednoparametrowe w odróżnieniu od zwykłych pomp elektronowych cechują się kompaktowymi rozmiarami oraz ograniczoną liczbą punktów styczności z rezerwuarami elektronów, co prowadzi do ograniczenia roli procesów dyssypacyjnych [130, 131]. Otrzymane wyniki skłoniły nas do zaakceptowania drugiej postawionej przez nas hipotezy badawczej.

5. *Electron Pumping and Spectral Density Dynamics in Energy-Gapped Topological Chains*

Marcin Kurzyna, Tomasz Kwapiński, Applied Sciences **11**(2), 772 (2021)

Cele badań

Kontynuując badania przedstawione w publikacji nr **4**, gdzie przedstawiliśmy układ dwóch kropek kwantowych pełniący rolę efektywnej, jednoparametrowej pompy elektronowej postaramy się sprawdzić, czy uzyskanie podobnego efektu możliwe jest dla łańcuchów topologicznych. Topologiczne łańcuchy atomowe charakteryzują się istnieniem przerwy energetycznej wzdłuż całego łańcucha, dlatego też można domniemywać, iż struktury te nie są dobrymi przewodnikami prądu. Sytuacja ta może się zmienić w obecności zależnych od czasu pól zewnętrznych. Postaramy się zatem znaleźć warunki, dla których w układach z przerwą energetyczną będzie mógł przepływać prąd elektryczny.

Dodatkowo celem rozszerzenia badań opisanych w publikacji nr **3** zbadamy, czy istnienie stanów topologicznych może być zaobserwowane w łańcuchach scharakteryzowanych trywialną bądź normalną fazą topologiczną poprzez użycie innego mechanizmu wyindukowania stanów topologicznych, niż ten polegający na zainicjowaniu kontaktu dwóch łańcuchów atomowych w różnych fazach topologicznych.

Hipotezy badawcze

(a) Topologiczne łańcuchy atomowe mogą pełnić rolę efektywnych pomp elektronowych pod wpływem zewnętrznych, zależnych od czasu zburzeń zewnętrznych.

(b) Nagła zmiana sprzężeń między stanami elektronowymi węzłów łańcucha (przejście z fazy nietrywialnej do trywialnej) nie prowadzi do natychmiastowego zaniku stanów brzegowych, lecz pozwala na ich egzystencje w fazie trywialnej przez określony czas.

(c) Hipoteza (b) sprawdza się jedynie dla łańcuchów SSH w trywialnej fazie topologicznej i nie może być rozszerzona na łańcuchy nietopologiczne ($v = w$).

Wyniki badań

Korzystając z formalizmu operatora ewolucji oraz hamiltonianu ciasnego wiązania, zbadaliśmy funkcje spektralne, obsadzenia ładunkowe, oraz prądy przepływające przez topologiczne łańcuchy SSH zaburzone zewnętrznymi perturbacjami rozchodzącymi się wzdłuż łańcucha w postaci pulsów gaussowskich (typu *train impulse*). Pokazujemy, iż tak zaburzane łańcuchy topologiczne mogą pełnić rolę efektywnych pomp elektronowych i co ciekawe, najwięcej ładunku przepływa przez łańcuch SSH w trywialnej fazie topologicznej, który scharakteryzowany jest przerwą energetyczną w obrębie całego łańcucha. Ponadto wykazujemy, iż w przeciwieństwie do normalnych układów jednowymiarowych, łańcuchy topologiczne dają możliwość sterowania kierunkiem przepływu prądu za pomocą kontroli przyłożonego napięcia bramki (podłoża), co skłania nas do uznania pierwszej hipotezy badawczej za słuszną.

Dodatkowo zbadaliśmy dynamikę lokalnej gęstości stanów zaburzonego łańcucha atomowego, w którym na skutek zmian sprzężeń międzywęzłowych nastąpiło topologiczne przejście fazowe z fazy nietrywialnej do fazy trywialnej, bądź do fazy nietopologicznej. Wykazaliśmy, iż pod wpływem takiej zmiany stan topologiczny jest w stanie przetrwać w układzie przez pewien czas i na dodatek przemieszcza się on między węzłami łańcucha, powoli zanikając, co z kolei przemawia za prawdziwością postawionej przez nas drugiej hipotezy badawczej. Analizując przejście z nietrywialnej fazy topologicznej do fazy nietopologicznej ($v = w$) dostrzegliśmy, iż w takim przypadku stan topologiczny nie dosyć, że jest w stanie przetrwać w układzie przez pewien czas, to na dodatek czas ten jest zauważalnie dłuższy niż w przypadku przejść z nietrywialnej do trywialnej fazy łańcucha SSH, co skłoniło nas do odrzucenia ostatniej hipotezy badawczej.

6. *Topological Atomic Chains on 2D Hybrid Structure*

Marcin Kurzyna, Tomasz Kwapiński, Materials **14**(12), 3289. (2021)

Cele badań

Struktury dwuwymiarowe takie jak np. grafen, są postrzegane jako materiały przyszłości ze względu na swoje niezwykle pożądane z aplikacyjnego punktu widzenia właściwości (lekkość, elastyczność, wytrzymałość, duża ruchliwość nośników ładunku, przewodnictwo). Istotne jest więc rozważenie różnych struktur dwuwymiarowych jako potencjalnych rezerwuarów elektronów dla normalnych i topologicznych łańcuchów atomowych. Tego typu podłoża 2D scharakteryzowane są nietrywialnymi, zależnymi od energii funkcjami gęstości stanów z charakterystycznymi lokalnymi maksimami, zwanymi nieciągłościami van Hove'a. Istotne jest więc uwzględnienie w obliczeniach podłoży o różnych geometriach (m.in. podłoża o komórce prostokątnej czy heksagonalnej) na właściwości elektryczne struktur jednowymiarowych będących z nimi w kontakcie. Mając na uwadze różne geometrie podłoża, możemy zadać sobie pytanie, czy aspekt geometrii może również dotyczyć samych łańcuchów atomowych. Odpowiedź jest twierdząca, gdyż łańcuchy atomowe mogą występować w postaci charakterystycznych łamanych, zwanych w literaturze geometriami zygzaka oraz krawędzi krzesła (ang. *armchair-edge*), które możemy zaobserwować w łańcuchach uzyskanych z nanowstążek grafenu. Z tego powodu celem naszych badań jest uwzględnienie nie tylko geometrii podłoża, ale również geometrii samych łańcuchów na ich właściwości elektryczne.

Hipotezy badawcze

(a) Topologiczne stany brzegowe w nietrywialnych łańcuchach SSH mogą istnieć w obszarze przerwy energetycznej dwuwymiarowego podłoża.

(b) Stany topologiczne pojawiające się na skrajnych węzłach łańcucha atomowego są topologicznie chronione i nie zależą od struktury gęstości stanów podłoża.

Wyniki badań

Korzystając z formalizmu retardowanych funkcji Greena, pokazujemy, iż dwuwymiarowe elektrody scharakteryzowane wierzchołkami van Hove'a w funkcji spektralnej w sposób istotny modyfikują strukturę energetyczną topologicznego łańcucha atomowego sprzężonego z tą powierzchnią i mogą prowadzić do rozszczepienia stanu topologicznego. Dodatkowo wykazujemy, iż stany topologiczne mogą istnieć poza granicami pasma energetycznego elektrod, co potwierdza pierwszą hipotezę. Ciekawy wynik uzyskaliśmy dla łańcucha SSH, gdzie stan topologiczny zlokalizowany był w pobliżu krawędzi DOS dwuwymiarowego podłoża. Stany końcowe w takich łańcuchach mogą składać się jednocześnie z szerokiego wierzchołka typu Lorentza (wskutek sprzężenia łańcucha atomowego z podłożem) oraz wąskiego, silnie zlokalizowanego wierzchołka (granica atomowa).

Biorąc pod uwagę nietrywialną geometrię topologicznych łańcuchów atomowych, odkryliśmy, iż poprzez połączenie łańcuchów typu zygzak lub *armchair-edge* do elektrod scharakteryzowanych różnymi funkcjami spektralnymi, możliwe jest zbudowanie układu, którego lokalne gęstości stanów wykazują przestrzenną asymetrię, i w którym same stany topologiczne widoczne na skrajnych atomach łańcucha, mogą ulegać rozseparowaniu energetycznemu.

7. *Braid Plot—A Mixed Palette Plotting Method as an Extension of Contour Plot*

Marcin Kurzyna, Tomasz Kwapiński, IEEE Computer Graphics and Applications **42**(01), 95-104 (2022)

Cele badań

Możliwość dokonywania nowych odkryć wymaga nierzadko posiadania odpowiednich narzędzi do tego celu. Trudno sobie wyobrazić współczesną medycynę, biologię, genetykę bez mikroskopów, czy też astronomię bez teleskopów. Narzędzia te pozwoliły naukowcom spojrzeć z zupełnie innej perspektywy na otaczający ich świat i dostrzec nowe zjawiska. W naszej pracy naukowej również stanęliśmy przed podobnym problemem. Dobranie odpowiedniej skali do wizualizacji danych liczbowych, sprawia, iż możemy zauważyć pewne prawidłowości, jakimi rządzi się badane zjawisko lub też kompletnie przeoczyć intrygujące zachowanie układu jeśli zakres osi wykresu jest zbyt mały, lub też przeciwnie zbyt duży, co można odnieść do świata makro- widzianego gołym okiem, oraz świata mikro- widzialnego przy użyciu mikroskopu. Jak się okazało, badanie właściwości elektrycznych łańcuchów atomowych może uwypuklić pewne zjawiska w zależności od skali, z której poziomu interpretujemy to, co widzimy.

Hipoteza badawcza

LDOS układów atomowych przejawia w domenie czasowej subtelne, regularne struktury, które mogą być bez trudu zaobserwowane na wykresie o dowolnie dobranych skalach osi jedynie przy wykorzystaniu nowej metody wizualizacji danych liczbowych polegającej na naprzemiennym wykorzystywaniu dwóch lub więcej kontrastujących ze sobą palet barw.

Wyniki badań

Opracowanie nowej metody wizualizacji danych miało swój początek w dostrzeżeniu głównej wady wykresów trójwymiarowych, na których wartości często reprezentowane są przez kolory (np. wartości ujemne: chłodne kolory- błękitny, niebieski; wartości dodatnie: kolory ciepłe- żółty, czerwony). Im większej dokładności wykresu żądamy, a co za tym idzie większej czułości na subtelne zmiany, tym więcej odcieni poszczególnych barw musimy użyć do jego wykonania. Problem polega na tym, że paleta kolorów przy dużej ich ilości dla ludzkiego oka przyjmuje charakter ciągły i co za tym idzie, kolory mieszają się ze sobą, co z kolei uniemożliwia rozróżnienie drobnych różnic w wykresie badanej zależności. W przypadku klasycznych wykresów, by zmiany były dobrze dostrzegalne, wartości sąsiadujących ze sobą argumentów $(x, y), (x + \Delta x, y + \Delta y)$ muszą znacznie się od siebie różnić, a co za tym idzie, kolory reprezentujące te wartości muszą ze sobą kontrastować. Opierając się na tej obserwacji, doszliśmy do wniosku, iż jeżeli niewielkie zmiany mają być widoczne dla ludzkiego oka, to kolory odpowiadające tym niewiele różniącym się wartościom również muszą ze sobą kontrastować. By tego dokonać, postanowiliśmy użyć nie jednej palety barw, a kilku, w których to paletach każda para kolorów jest od siebie w pełni rozróżnialna przez ludzkie oko. Do sporządzenia wykresu palety barw używane są naprzemiennie z wysoką częstotliwością, w efekcie czego dostajemy bardzo dokładny obraz, w którym to każda drobna zmiana jest zauważalna. Opracowana przez nas metoda nosi nazwę wykresu warkoczowego (ang. *braid plot*), gdyż opiera się ona na przeplataniu ze sobą kolorów. Dzięki tej metodzie udało nam się znaleźć wiele interesujących zjawisk fizycznych m.in. periodyczne struktury na wykresie *LDOS* układów atomowych, które to były niedostrzegalne przy użyciu klasycznych metod wizualizacji i tym samym potwierdzić hipotezę badawczą. Omawiana publikacja była zatem kluczowa dla odkrycia struktur typu *transient crystal* i zawiera przykładowe rysunki prezentujące te struktury, natomiast szczegółowa analiza tychże struktur została zawarta w publikacji nr **4**.

4.2 Wykaz konferencji naukowych

W trakcie studiów doktoranckich brałem czynny udział w krajowych oraz międzynarodowych konferencjach naukowych, na których prezentowałem wyniki swoich badań. Poniżej zaprezentowana jest pełna lista moich wystąpień:

1. **10th Workshop on Applications of Scanning Probe Microscopy – STM/AFM** ,
   Zakopane 28.11. - 02.12 2018
   - (a) *Topological and normal atomic chains with different substrates*- prezentacja ustna
   - (b) *Electron resonant states in clusters and atomic chains*– poster
2. **9th International Workshop on Surface Physics**,
   Trzebnica, 24-28.06 2019, *Dynamic properties of topological atomic chains* - poster
3. **CMD2020GEFES (Condensed Matter Division (CMD) of the European Physical Society (EPS) and the Condensed Matter Physics Division (GEFES) of the Spanish Royal Physics Society (RSEF))**,
   Madryt 31.08.20 - 04.09.20
   - (a) *Dynamic electrical properties of coupled topological chains* – prezentacja ustna
   - (b) *Quench dynamics in two-atom system on a surface*- poster
4. **Sympozjum Młodych Naukowców Wydziału Fizyki Uniwersytetu Warszawskiego**,
   Warszawa 24-28.08.20, *Właściwości elektryczne topologicznych łańcuchów atomowych*– prezentacja ustna
5. **Oxford Instruments Virtual Symposium Quantum Technology, Semiconductors and Power Generation**, Oksford 8-10.06.21, *Electrical properties of topological atomic chains*- prezentacja ustna
6. **Sympozjum Młodych Naukowców Wydziału Fizyki Uniwersytetu Warszawskiego**, Warszawa 30.08-03.09.21
   - (a) *Braid plot- a new method of preparing threedimensional plots*- prezentacja ustna
   - (b) *Atomic chains the thinnest electrical conductors*- poster, praca wyróżniona

Badania naukowe prowadzone przeze mnie podczas studiów doktoranckich zostały częściowo sfinansowane ze środków projektu NCN OPUS 16 nr 2018/31/B/ST3/02370, w którym brałem udział jako doktorant-stypendysta.

Rozdział 5

Podsumowanie

Przeprowadzone badania składające się na niniejszą rozprawę pozwoliły odkryć wiele interesujących właściwości najcieńszych przewodników prądu, jakimi są łańcuchy atomowe. Wykorzystując formalizmy retardowanych funkcji Greena oraz operatora ewolucji, przeanalizowane zostały tutaj układy atomowe w różnych fazach topologicznych w przypadku stacjonarnym, jak i zależnym od czasu, gdzie mogliśmy śledzić dynamikę zmian w czasie (ewolucję) wybranych wielkości fizycznych. W badaniach uwzględnione zostały takie czynniki jak: rodzaj podłoża, na którym znajdują się łańcuchy, oddziaływania kulombowskie, oddziaływania spin-orbita oraz spin-flip, stacjonarne i zależne od czasu zaburzenia zewnętrzne, czy też geometria łańcuchów i elektrod. Do najważniejszych wyników niniejszej rozprawy można zaliczyć:

- Odkrycie długookresowych oscylacji przewodnictwa łańcuchów atomowych zaburzonych adatomami.
- Wykazanie silnego wpływu podłoży metalicznych oraz oddziaływań *spin-flip* i spin-orbita na asymetrię lokalnej gęstości stanów w łańcuchach atomowych.
- Znalezienie indukowanych stanów topologicznych w łańcuchach niebędących w nietrywialnej fazie topologicznej i zbadanie ich dynamiki czasowej (propagacji) w różnych układach atomowych.
- Odkrycie nietrywialnej periodycznej struktury *LDOS* w układzie dwóch sprzężonych kropek kwantowych, nazywanej *transient cristal*.
- Wykazanie, że topologiczne łańcuchy atomowe mogą pełnić rolę efektywnych pomp elektronowych.
- Wykazanie asymetrii energetycznej stanów topologicznych na dwóch końcach nietrywialnego łańcucha atomowego pod wpływem kontaktu z dwuwymiarowymi elektrodami

Uważam, że cele pracy zostały osiągnięte, a postawione hipotezy badawcze zostały zweryfikowane. Uzyskane w tej rozprawie rezultaty mogą być zweryfikowane eksperymentalnie przy użyciu skaningowego mikroskopu tunelowego, gdyż mierzalny prąd tunelowy bezpośrednio zależy od lokalnej gęstości stanów elektronowych, która była główną wielkością analizowaną w tej rozprawie. Ponadto w toku rozprawy udało się opracować narzędzie informatyczne umożliwiające modelowanie nanostruktur oraz prowadzenie obliczeń numerycznych ich właściwości elektrycznych- *Nano Modeller*. Dodatkowo opracowana została nowa technika wizualizacji danych, nazywana wykresem warkoczowym, która umożliwiają wizualizację niewielkich perturbacji na tle dużych zmian.

W przyszłości planuję rozszerzyć zakres swoich badań o analizę właściwości elektrycznych normalnych i topologicznych łańcuchów atomowych w kontakcie z nadprzewodnikami, a także uwzględnić rozszerzony model SSH oraz cząstki Majorany. Planuję również dalej rozwijać program *Nano Modeller* wzbogacając go o nowe funkcjonalności (np. uwzględnianie rzeczywistych atomów z wieloma orbitalami) oraz udoskonalając efektywność jego działania.

Mam nadzieję, że uzyskane w tej rozprawie wyniki wnoszą pewien wkład do fizyki materii skondensowanej, w tym fizyki izolatorów topologicznych i fizyki układów niskowymiarowych, oraz umożliwią wykorzystanie normalnych i topologicznych łańcuchów atomowych do celów aplikacyjnych w nowoczesnych urządzeniach elektronicznych.

Bibliografia

[1] M. Kopciuszyński, P. Dyniec, M. Krawiec, P. Łukasik, M. Jałochowski, and R. Zdyb, "Pb nanoribbons on the Si(553) surface," *Physical Review B*, vol. 88, p. 155431, 2013.

[2] A. Baski, K. Saoud, and K. Jones, "1-D nanostructures grown on the Si(5 5 12) surface," *Appl. Surf. Sci.*, vol. 182, pp. 216–222, 2001.

[3] M. Jałochowski, T. Kwapinski, P. Łukasik, P. Nita, and M. Kopciuszyński, "Correlation between morphology, electron band structure, and resistivity of Pb atomic chains on the Si(553)-Au surface," *J. Phys. Condens. Matter*, vol. 28, p. 284003, 2016.

[4] A. Zhang, G. Zheng, and C. M. Lieber, *Nanowires: Building blocks for nanoscience and nanotechnology.* Springer, 2017.

[5] A. Jorio, G. Dresselhaus, and M. S. Dresselhaus, *Carbon nanotubes: advanced topics in the synthesis, structure, properties and applications*, vol. 111. Springer, 2008.

[6] B. Wei and X. Han, "Telluride Te_2I: Electronic properties of one-dimensional atomic chains structure," in *E3S Web of Conferences*, vol. 236, p. 01028, EDP Sciences, 2021.

[7] O. M. Auslaender, H. Steinberg, A. Yacoby, Y. Tserkovnyak, B. I. Halperin, K. W. Baldwin, L. N. Pfeiffer, and K. W. West, "Spin-Charge Separation and Localization in One Dimension," *Science*, vol. 308, no. 5718, pp. 88–92, 2005.

[8] J. S. Shin, K.-D. Ryang, and H. W. Yeom, "Finite-length charge-density waves on terminated atomic wires," *Physical Review B*, vol. 85, p. 073401, 2012.

[9] N. Oncel, "Atomic chains on surfaces," *Journal of Physics: Condensed Matter*, vol. 20, no. 39, p. 393001, 2008.

[10] M. H. Weik, "Ballistic research laboratories report no971—a survey of domestic electronic digital computing systems," *S Department of Commerce, Tech. Rep*, 1955.

[11] R. Rojas and U. Hashagen, *The first computers: History and architectures.* MIT press, 2002.

[12] H. Zhang, C.-X. Liu, X.-L. Qi, X. Dai, Z. Fang, and S.-C. Zhang, "Topological insulators in Bi_2Se_3, Bi_2Te_3 and Sb_2Te_3 with a single Dirac cone on the surface," *Nature physics*, vol. 5, no. 6, pp. 438–442, 2009.

[13] P. Orgiani, C. Bigi, P. Kumar Das, J. Fujii, R. Ciancio, B. Gobaut, A. Galdi, C. Sacco, L. Maritato, P. Torelli, *et al.*, "Structural and electronic properties of Bi_2Se_3 topological insulator thin films grown by pulsed laser deposition," *Applied Physics Letters*, vol. 110, no. 17, p. 171601, 2017.

[14] M. Konig, S. Wiedmann, C. Brune, A. Roth, H. Buhmann, L. W. Molenkamp, X.-L. Qi, and S.-C. Zhang, "Quantum spin Hall insulator state in HgTe quantum wells," *Science*, vol. 318, no. 5851, pp. 766–770, 2007.

[15] Z. Yue, G. Xue, J. Liu, Y. Wang, and M. Gu, “Nanometric holograms based on a topological insulator material,” *Nature Communications*, vol. 8, no. 1, pp. 1–5, 2017.

[16] Z. Yue, B. Cai, L. Wang, X. Wang, and M. Gu, “Intrinsically core-shell plasmonic dielectric nanostructures with ultrahigh refractive index,” *Science advances*, vol. 2, no. 3, p. e1501536, 2016.

[17] J. Klinovaja, A. Yacoby, and D. Loss, “Kramers pairs of Majorana fermions and parafermions in fractional topological insulators,” *Physical Review B*, vol. 90, p. 155447, 2014.

[18] J. Alicea, “New directions in the pursuit of Majorana fermions in solid state systems,” *Reports on progress in physics*, vol. 75, no. 7, p. 076501, 2012.

[19] R. Aguado and L. P. Kouwenhoven, “Majorana qubits for topological quantum computing,” *Physics Today*, vol. 73, no. 6, pp. 44–50, 2020.

[20] X.-L. Qi, R. Li, J. Zang, and S.-C. Zhang, “Inducing a magnetic monopole with topological surface states,” *Science*, vol. 323, no. 5918, pp. 1184–1187, 2009.

[21] L. Fu, “Topological Crystalline Insulators,” *Physical Review Letters*, vol. 106, p. 106802, 2011.

[22] B. M. Wojek, R. Buczko, S. Safaei, P. Dziawa, B. J. Kowalski, M. H. Berntsen, T. Balasubramanian, M. Leandersson, A. Szczerbakow, P. Kacman, T. Story, and O. Tjernberg, “Spin-polarized (001) surface states of the topological crystalline insulator $Pb_{0.73}Sn_{0.27}Se$,” *Physical Review B*, vol. 87, p. 115106, 2013.

[23] M. Safdar, Q. Wang, M. Mirza, Z. Wang, K. Xu, and J. He, “Topological surface transport properties of single-crystalline SnTe nanowire,” *Nano letters*, vol. 13, no. 11, pp. 5344–5349, 2013.

[24] T. H. Hsieh, H. Lin, J. Liu, W. Duan, A. Bansil, and L. Fu, “Topological crystalline insulators in the SnTe material class,” *Nature communications*, vol. 3, no. 1, pp. 1–7, 2012.

[25] X. Zhou, C.-H. Hsu, T.-R. Chang, H.-J. Tien, Q. Ma, P. Jarillo-Herrero, N. Gedik, A. Bansil, V. M. Pereira, S.-Y. Xu, H. Lin, and L. Fu, “Topological crystalline insulator states in the $\mathrm{ca_2As}$ family,” *Physical Review B*, vol. 98, p. 241104, 2018.

[26] J. I. Facio, S. K. Das, Y. Zhang, K. Koepernik, J. van den Brink, and I. C. Fulga, “Dual topology in jacutingaite $\mathrm{pt_2hgse_3}$,” *Physical Reviev Materials*, vol. 3, p. 074202, 2019.

[27] J. Appenzeller, J. Knoch, M. T. Bjork, H. Riel, H. Schmid, and W. Riess, “Toward Nanowire Electronics,” *IEEE Transactions on Electron Devices*, vol. 55, no. 11, pp. 2827–2845, 2008.

[28] S. Datta, *Electronic transport in mesoscopic systems.* Cambridge university press, 1997.

[29] J. Luttinger, “An exactly soluble model of a many-fermion system,” *Journal of mathematical physics*, vol. 4, no. 9, pp. 1154–1162, 1963.

[30] V. Mastropietro, *Luttinger Model: The First 50 Years and Some New Directions*, vol. 20. World Scientific, 2014.

[31] J. Sólyom, “The fermi gas model of one-dimensional conductors,” *Advances in Physics*, vol. 28, no. 2, pp. 201–303, 1979.

[32] H. van Houten and C. Beenakker, “Quantum Point Contacts,” *Physics Today*, vol. 49, no. 7, p. 22–27, 1996.

[33] S.-i. Tomonaga, “Remarks on Bloch’s method of sound waves applied to many-fermion problems,” *Progress of Theoretical Physics*, vol. 5, no. 4, pp. 544–569, 1950.

[34] P. Tien and J. Gordon, “Multiphoton process observed in the interaction of microwave fields with the tunneling between superconductor films,” *Physical Review*, vol. 129, no. 2, p. 647, 1963.

[35] D. Averin and K. Likharev, “Coulomb blockade of single-electron tunneling, and coherent oscillations in small tunnel junctions,” *Journal of low temperature physics*, vol. 62, no. 3, pp. 345–373, 1986.

[36] T. Chakraborty, “Physics of the artificial atoms: Quantum dots in a magnetic field,” *Comments Cond. Mat. Phys*, vol. 16, pp. 35–68, 1992.

[37] R. J. Silbey, R. A. Alberty, and M. G. Bawendi, *Physical chemistry.* Wiley, 2005.

[38] M. J. Kelly, “Intrinsic top-down unmanufacturability,” *Nanotechnology*, vol. 22, no. 24, p. 245303, 2011.

[39] H. W. Yang, S. F. Horng, and H. L. Hwang, “Fabrication of quantum wires by wet etching techniques,” *MRS Proceedings*, vol. 325, p. 85, 1993.

[40] Y. Arakawa, “Fabrication of quantum wires and dots and nanostructure characterization,” in *Low Dimensional Structures Prepared by Epitaxial Growth or Regrowth on Patterned Substrates*, pp. 197–205, Springer, 1995.

[41] D. Scheiner, Y. Hanein, and M. Heiblum, “Fabrication of quantum wires in thermally etched V-grooves by molecular beam epitaxy,” *Semiconductor science and technology*, vol. 12, no. 8, p. 1046, 1997.

[42] C. Martin, R. Smit, R. Egmond, H. Zant, and J. van Ruitenbeek, “A versatile low-temperature setup for the electrical characterization of single-molecule junctions,” *The Review of scientific instruments*, vol. 82, p. 053907, 2011.

[43] J. Moreland and J. Ekin, “Electron tunneling experiments using Nb-Sn “break”junctions,” *Journal of applied physics*, vol. 58, no. 10, pp. 3888–3895, 1985.

[44] C. Muller, J. Van Ruitenbeek, and L. De Jongh, “Conductance and supercurrent discontinuities in atomic-scale metallic constrictions of variable width,” *Physical Review Letters*, vol. 69, no. 1, p. 140, 1992.

[45] C. Muller, J. Van Ruitenbeek, and L. De Jongh, “Experimental observation of the transition from weak link to tunnel junction,” *Physica C: Superconductivity*, vol. 191, no. 3-4, pp. 485–504, 1992.

[46] N. Agraït, “Quantum properties of atomic-sized conductors,” *Physics Reports*, vol. 377, no. 2, pp. 81–279, 2003.

[47] M. L. Perrin, E. Galán, R. Eelkema, J. M. Thijssen, F. Grozema, and H. S. van der Zant, “A gate-tunable single-molecule diode,” *Nanoscale*, vol. 8, no. 16, pp. 8919–8923, 2016.

[48] B. Legrand, D. Deresmes, and D. Stievenard, “Silicon nanowires with sub 10 nm lateral dimensions: From atomic force microscope lithography based fabrication to electrical measurements,” *Journal of Vacuum Science & Technology B: Microelectronics and Nanometer Structures Processing, Measurement, and Phenomena*, vol. 20, no. 3, pp. 862–870, 2002.

[49] Á. I. Csurgay, W. Porod, and C. S. Lent, “Signal processing with near-neighbor-coupled time-varying quantum-dot arrays,” *IEEE Transactions on Circuits and Systems I: Fundamental Theory and Applications*, vol. 47, no. 8, pp. 1212–1223, 2000.

[50] R. Zak, B. Röthlisberger, S. Chesi, and D. Loss, “Quantum Computing with Electron Spins in Quantum Dots,” *Rivista del Nuovo Cimento*, vol. 33, 2009.

[51] F. Leroy, P. Müller, J. Metois, and O. Pierre-Louis, “Vicinal silicon surfaces: from step density wave to faceting,” *Physical Review B*, vol. 76, no. 4, p. 045402, 2007.

[52] J. Crain, J. McChesney, F. Zheng, M. Gallagher, P. Snijders, M. Bissen, C. Gundelach, S. C. Erwin, and F. Himpsel, “Chains of gold atoms with tailored electronic states,” *Physical Review B*, vol. 69, no. 12, p. 125401, 2004.

[53] M. B. Panish, “Molecular beam epitaxy,” *Science*, vol. 208, no. 4446, pp. 916–922, 1980.

[54] I. Bloch, “Ultracold quantum gases in optical lattices,” *Nature physics*, vol. 1, no. 1, pp. 23–30, 2005.

[55] L. Fallani, C. Fort, J. E. Lye, and M. Inguscio, “Bose-Einstein condensate in an optical lattice with tunable spacing: transport and static properties,” *Optics Express*, vol. 13, no. 11, p. 4303, 2005.

[56] Y. Horio, Y. Hashimoto, and A. Ichimiya, “A new type of RHEED apparatus equipped with an energy filter,” *Applied Surface Science*, vol. 100-101, pp. 292–296, 1996.

[57] A. Ichimiya, P. I. Cohen, and P. I. Cohen, *Reflection high-energy electron diffraction.* Cambridge University Press, 2004.

[58] M. Prutton, “Low energy electron diffraction. The theory and its application to determination of surface structure,” *Acta Crystallographica Section A: Crystal Physics, Diffraction, Theoretical and General Crystallography*, vol. 31, no. 4, pp. 526–527, 1975.

[59] M. A. VanHove, W. H. Weinberg, and C.-M. Chan, *Low-energy electron diffraction: experiment, theory and surface structure determination*, vol. 6. Springer Science & Business Media, 2012.

[60] A. Damascelli, Z. Hussain, and Z.-X. Shen, “Angle-resolved photoemission studies of the cuprate superconductors,” *Reviews of Modern Physics*, vol. 75, no. 2, p. 473–541, 2003.

[61] S. Hüfner, *Very high resolution photoelectron spectroscopy*, vol. 715. Springer, 2007.

[62] G. Binnig, C. F. Quate, and C. Gerber, “Atomic Force Microscope,” *Physical Review Letters*, vol. 56, pp. 930–933, 1986.

[63] S. M. Salapaka and M. V. Salapaka, “Scanning Probe Microscopy,” *IEEE Control Systems Magazine*, vol. 28, no. 2, pp. 65–83, 2008.

[64] C. Bai, *Scanning tunneling microscopy and its application*, vol. 32. Springer Science & Business Media, 2000.

[65] J. Chen, *Introduction to Scanning Tunneling Microscopy Third Edition*, vol. 69. Oxford University Press, USA, 2021.

[66] S. H. Cohen, M. L. Lightbody, and M. T. Bray, *Atomic force microscopy/scanning tunneling microscopy.* Springer, 1997.

[67] R. J. Hamers and D. F. Padowitz, “Methods of tunneling spectroscopy with the STM,” *Scanning Probe Microscopy and Spectroscopy: Theory, Techniques, and Applications*, vol. 2, 2001.

[68] B. Broda, “Fizyka i topologia,” *Physics and Topology*, vol. 55, no. 3, pp. 120–122, 2004.

[69] A. S. Schwarz, *Topology for physicists*, vol. 308. Springer Science & Business Media, 2013.

[70] S. Willard, *General topology.* Courier Corporation, 2012.

[71] S. R. David, “Euler’s gem: the polyhedron formula and the birth of topology,” *Princeton University Press*, 2012.

[72] J. W. Alexander, “Topological invariants of knots and links,” *Transactions of the American Mathematical Society*, vol. 30, no. 2, pp. 275–306, 1928.

[73] C. Kane, “Topological Band Theory and the $_2$ Invariant,” in *Topological Insulators* (M. Franz and L. Molenkamp, eds.), vol. 6 of *Contemporary Concepts of Condensed Matter Science*, pp. 3–34, Elsevier, 2013.

[74] M. V. Berry, “Quantal phase factors accompanying adiabatic changes,” *Proceedings of the Royal Society of London. A. Mathematical and Physical Sciences*, vol. 392, no. 1802, pp. 45–57, 1984.

[75] R. Bott, L. W. Tu, *et al.*, *Differential forms in algebraic topology*, vol. 82. Springer, 1982.

[76] A. Y. Kitaev, “Unpaired Majorana fermions in quantum wires,” *Physics-Uspekhi*, vol. 44, no. 10S, pp. 131–136, 2001.

[77] C. Li, X. Zhang, G. Zhang, and Z. Song, “Topological phases in a Kitaev chain with imbalanced pairing,” *Physical Review B*, vol. 97, no. 11, p. 115436, 2018.

[78] D. Vodola, L. Lepori, E. Ercolessi, A. V. Gorshkov, and G. Pupillo, “Kitaev chains with long-range pairing,” *Physical Review Letters*, vol. 113, no. 15, p. 156402, 2014.

[79] P. M. R. Brydon, S. Das Sarma, H.-Y. Hui, and J. D. Sau, “Topological Yu-Shiba-Rusinov chain from spin-orbit coupling,” *Physical Review B*, vol. 91, no. 6, p. 064505, 2015.

[80] J. F. Steiner, C. Mora, K. J. Franke, and F. von Oppen, “Quantum magnetism and topological superconductivity in Yu-Shiba-Rusinov chains,” *Physical Review Letters*, vol. 128, no. 3, p. 036801, 2022.

[81] J. Zhang and V. Aji, “Topological Yu-Shiba-Rusinov chain in monolayer transition-metal dichalcogenide superconductors,” *Physical Review B*, vol. 94, no. 6, p. 060501, 2016.

[82] M. Krawiec, T. Kwapiński, and M. Jałochowski, “Double nonequivalent chain structure on a vicinal Si (557)-Au surface,” *Physical Review B*, vol. 73, no. 7, p. 075415, 2006.

[83] P. St-Jean, V. Goblot, E. Galopin, A. Lemaître, T. Ozawa, L. Le Gratiet, I. Sagnes, J. Bloch, and A. Amo, “Lasing in topological edge states of a one-dimensional lattice,” *Nature Photonics*, vol. 11, no. 10, pp. 651–656, 2017.

[84] N. Batra and G. Sheet, “Physics with Coffee and Doughnuts,” *Resonance*, vol. 25, no. 6, p. 765–786, 2020.

[85] J. K. Asbóth, L. Oroszlány, and A. Pályi, “A short course on topological insulators,” *Lecture notes in physics*, vol. 919, p. 166, 2016.

[86] R. Shankar, “Topological Insulators–A review,” *arXiv preprint arXiv:1804.06471*, 2018.

[87] K. M. Urwin, “Mathematical methods in science and engineering,” *The Mathematical Gazette*, vol. 48, no. 366, pp. 479–480, 1964.

[88] V. Bonch-Bruevich and S. Tyablikov, *The Green function method in statistical mechanics.* Courier Dover Publications, 2015.

[89] M. M. Odashima, B. G. Prado, and E. Vernek, “Pedagogical introduction to equilibrium Green’s functions: condensed-matter examples with numerical implementations,” *Revista Brasileira de Ensino de Física*, vol. 39, no. 1, 2017.

[90] G. Rickayzen, *Green’s functions and condensed matter.* Courier Corporation, 2013.

[91] L. P. Kadanoff and G. Baym, *Quantum statistical mechanics: Green’s function methods in equilibrium and nonequilibrium problems.* CRC Press, 2018.

[92] A. Abrikosov, L. Gorkov, and I. Dzyaloshinski, *Methods of quantum field theory in statistical physics.* Courier Corporation, 2012.

[93] N. Bogolyubov and S. Tyablikov, “Retarded and advanced Green functions in statistical physics,” in *Soviet Physics Doklady*, vol. 4, p. 589, 1959.

[94] D. Zubarev, “Double-time Green functions in statistical physics,” *Soviet Physics Uspekhi*, vol. 3, no. 3, p. 320, 1960.

[95] S. Datta, “Nanoscale device modeling: the Green’s function method,” *Superlattices and microstructures*, vol. 28, no. 4, pp. 253–278, 2000.

[96] W. Hänsch and G. D. Mahan, “Transport equations for many-particle systems,” *Physical Review B*, vol. 28, pp. 1902–1922, 1983.

[97] J. C. Delaney, *Local density of states for one dimensional aperiodic binary sequences using local Green’s function method.* Citeseer, 1996.

[98] E. N. Economou, *Green’s functions in quantum physics*, vol. 7. Springer Science & Business Media, 2006.

[99] T. Kramer, E. J. Heller, and R. E. Parrott, “An efficient and accurate method to obtain the energy-dependent Green function for general potentials,” in *Journal of Physics: Conference Series*, vol. 99, p. 012010, IOP Publishing, 2008.

[100] D. K. Ferry, *An Introduction to Quantum Transport in Semiconductors.* Jenny Stanford Publishing, 2017.

[101] M. Desjonqueres and D. Spanjaard, *Concepts in Surface Physics: 2eme édition*, vol. 30. Springer Science & Business Media, 1996.

[102] P. Nita, M. Jałochowski, M. Krawiec, and A. Stpniak, “One-dimensional diffusion of Pb atoms on the Si (553)-Au surface,” *Physical Review Letters*, vol. 107, no. 2, p. 026101, 2011.

[103] T. Kwapiński, S. Kohler, and P. Hänggi, “Electron transport across a quantum wire in the presence of electron leakage to a substrate,” *The European Physical Journal B*, vol. 78, no. 1, pp. 75–81, 2010.

[104] D. Newns and N. Read, “Mean-field theory of intermediate valence/heavy fermion systems,” *Advances in Physics*, vol. 36, no. 6, pp. 799–849, 1987.

[105] T. Kwapiński, S. Kohler, and P. Hänggi, “Electron transport across a quantum wire in the presence of electron leakage to a substrate,” *The European Physical Journal B*, vol. 78, no. 1, pp. 75–81, 2010.

[106] A. Böttcher and S. M. Grudsky, *Toeplitz matrices, asymptotic linear algebra and functional analysis*, vol. 67. Springer, 2000.

[107] S. Noschese, L. Pasquini, and L. Reichel, “Tridiagonal Toeplitz matrices: properties and novel applications,” *Numerical linear algebra with applications*, vol. 20, no. 2, pp. 302–326, 2013.

[108] D. Kulkarni, D. Schmidt, and S.-K. Tsui, “Eigenvalues of tridiagonal pseudo-Toeplitz matrices,” *Linear Algebra and its Applications*, vol. 297, pp. 63–80, 1999.

[109] T. Brandes, “Coherent and collective quantum optical effects in mesoscopic systems,” *Physics Reports*, vol. 408, no. 5-6, pp. 315–474, 2005.

[110] K. Wrześniewski and I. Weymann, “Influence of magnetic field on dark states in transport through triple quantum dots,” *Acta Physica Polonica A*, vol. 132, no. 1, pp. 108–111, 2017.

[111] I. Weymann, B. R. Bułka, and J. Barnaś, “Dark states in transport through triple quantum dots: The role of cotunneling,” *Physical Review B*, vol. 83, p. 195302, 2011.

[112] C. Emary, “Dark states in the magnetotransport through triple quantum dots,” *Physical Review B*, vol. 76, p. 245319, 2007.

[113] J. Maciejko, J. Wang, and H. Guo, “Time-dependent quantum transport far from equilibrium: An exact nonlinear response theory,” *Physical Review B*, vol. 74, p. 085324, 2006.

[114] T. Kwapiński, R. Taranko, and E. Taranko, “Band structure effects in time-dependent electron transport through the quantum dot,” *Physical Review B*, vol. 66, p. 035315, 2002.

[115] A.-P. Jauho, N. S. Wingreen, and Y. Meir, “Time-dependent transport in interacting and noninteracting resonant-tunneling systems,” *Physical Review B*, vol. 50, pp. 5528–5544, 1994.

[116] T. Grimley, V. J. Bhasu, and K. Sebastian, “Electron transfer in the reflection of atoms from metal surfaces,” *Surface Science*, vol. 124, no. 1, pp. 305–319, 1983.

[117] T. Kwapiński, “Time-dependent electron transport through a quantum wire,” *Physical Review B*, vol. 69, p. 153303, 2004.

[118] G. B. Arfken and H. J. Weber, *Mathematical methods for physicists.* American Association of Physics Teachers, 1999.

[119] P. Linz, *Analytical and numerical methods for Volterra equations.* SIAM, 1985.

[120] C. T. Baker, “A perspective on the numerical treatment of Volterra equations,” *Journal of computational and applied mathematics*, vol. 125, no. 1-2, pp. 217–249, 2000.

[121] W. L. Martinez, “Graphical user interfaces,” *WIREs Computational Statistics*, vol. 3, no. 2, pp. 119–133, 2011.

[122] M. Murata, S. S. Laurent, and D. Kohn, “Xml media types,” *RFC3023*, 2001.

[123] P. K. Janert, *Gnuplot in action: understanding data with graphs.* Simon and Schuster, 2016.

[124] S. Sharma, P. Kumar, R. Chandra, S. Singh, A. Mandal, and R. Dondapati, “Overview of BIOVIA materials studio, LAMMPS, and GROMACS,” *Molecular Dynamics Simulation of Nanocomposites using BIOVIA Materials Studio, Lammps and Gromacs, Amsterdam, Netherlands: Elsevier*, pp. 39–100, 2019.

[125] I. A. Solov’yov, A. V. Korol, and A. V. Solov’yov, *Multiscale modeling of complex molecular structure and dynamics with MBN explorer.* Springer, 2017.

[126] M. M. P. Simulator, “Lammps,” *Theater*, vol. 2012, 2012.

[127] M. Bahari and M. V. Hosseini, “Zeeman-field-induced nontrivial topological phases in a one-dimensional spin-orbit-coupled dimerized lattice,” *Physical Review B*, vol. 94, no. 12, p. 125119, 2016.

[128] H. Li, M. Zhou, S. Wu, and X. Liang, “Research of spin-orbit interaction in organic conjugated polymers,” in *IOP Conference Series: Materials Science and Engineering*, vol. 213, p. 012005, IOP Publishing, 2017.

[129] R. Taranko and T. Kwapiński, “Charge and current beats in T-shaped qubit–detector systems,” *Physica E: Low-dimensional Systems and Nanostructures*, vol. 70, pp. 217–224, 2015.

[130] L. P. Kouwenhoven, N. C. Van der Vaart, A. Johnson, W. Kool, C. Harmans, J. Williamson, A. Staring, and C. Foxon, “Single electron charging effects in semiconductor quantum dots,” *Zeitschrift für Physik B Condensed Matter*, vol. 85, no. 3, pp. 367–373, 1991.

[131] S. K. Watson, R. M. Potok, C. M. Marcus, and V. Umansky, “Experimental realization of a quantum spin pump,” *Physical Review Letters*, vol. 91, p. 258301, 2003.

JOURNAL OF APPLIED PHYSICS **123**, 194301 (2018)

Non-local electron transport through normal and topological ladder-like atomic systems

Marcin Kurzyna and Tomasz Kwapiński[a)]
Institute of Physics, M. Curie-Skłodowska University, Pl. M. Curie-Skłodowskiej 1, 20-031 Lublin, Poland

(Received 12 March 2018; accepted 30 April 2018; published online 21 May 2018)

We propose a locally protected ladder-like atomic system (nanoconductor) on a substrate that is insensitive to external perturbations. The system corresponds to coupled atomic chains fabricated on different surfaces. Electron transport properties of such conductors are studied theoretically using the model tight-binding Su-Schriffer-Hegger (SSH) Hamiltonian and Green's function formalism. We have found that the conductance of the system is almost insensitive to single adatoms and oscillates as a function of the side chain length with very large periods. Non-local character of the electron transport was observed also for topological SSH chains where nontrivial end states survive in the presence of disturbances as well as for different substrates. We have found that the careful inspection of the density of states or charge waves can provide the information about the atom energy levels and hopping amplitudes. Moreover, the ladder-like geometry allows one to distinguish between normal and topological zero-energy states. It is important that topological chains do not reveal Friedel oscillations which are observed in non-topological chains. *Published by AIP Publishing.* https://doi.org/10.1063/1.5028571

I. INTRODUCTION

Considerable progress in the fabrication of atomically thick regular chains has been achieved recently. Very long chains of various species of atoms e.g., Pb, Au, and Sb have been investigated experimentally on different reconstructed surfaces like Si(335), Si(557), Ge(001), or others.[1–5] The electronic properties of such one-dimension systems are of great interest due to their prospective applications in nanoelectronics as they are the thinnest possible electric wires. Atomic chains can be also used in spintronic devices.[6] These systems reveal many interesting effects like conductance quantization,[7,8] conductance oscillations,[9,10] spin-charge separation,[11] charge density waves,[12,13] spinless topological states,[14,15] Majorana zero modes,[16,17] or others which often do not appear in bulk materials.

Electrical properties of low-dimensional systems are strongly determined by the geometrical configurations of atoms. Regular atomic chains are characterized by the peaked density of states (DOS) structure with no energy gaps. On the other hand, a chain with different tunneling amplitudes can reveal a topological phase with protected states. One of the simplest 1D models with both trivial and non-trivial phases is the Su-Schriffer-Hegger (SSH) model describing spinless fermions hopping on an atomic lattice with stagger hopping integrals.[14,18–21] It exhibits rich physical phenomena and can be exactly resolved giving two different phases which are topologically distinct in the open boundary condition. These phases are distinguished by the presence or absence of topological nontrivial states at the chain ends and the energy gap inside the chain. The SSH model with topological states can be realized experimentally in the form of photonic quantum walks, optical lattices, and recently also in the form of a vacancy lattice in a chlorine monolayer on a Cu(100) surface.[15,22,23]

There are some nontrivial problems concerning atomic chains and their possible applications. Low-dimensional structures are sensitive to external disturbances. The conductance of thin films (or atomic ribbons) depends on the surface scattering centers and thus, even a very low number of external atoms on a surface can significantly change the transport properties.[24] Also short atomic chains are sensitive to impurities and in the presence of a single side-attached atom or cluster of atoms the spectral density function or the conductance can drastically change.[25–29] Moreover, the one-atom thick chain stands for a single path for electrons but it can be easily broken due to e.g., thermal effects and it cannot be too strongly coupled with the surface because electrons are willing to leakage from the chain. Thus, there is a great challenge to find 1D stable systems which are locally protected against disturbances and which overcome the above problems i.e., which ensure respectable control of the electrical properties.

In the present paper, we propose quasi-one-dimensional chains which are locally protected against disturbances i.e., which are insensitive (or almost insensitive) to single external perturbations. The system consists of two coupled atomic chains of different lengths in normal and topological phases between two electron reservoirs and coupled with the substrate electrode, which is schematically shown in Fig. 1. It stands for a kind of ladder-like atomic cluster. The electrical properties of the system are controlled by the length of the second (shorter) chain which we called additional or side chain. This unusual system reveals interesting transport properties, different from those of a straight chain of atoms. Moreover, the ladder-like geometry allows one to distinguish between normal and topological zero-energy states and determines the electron energies and

---

[a)] Electronic mail: tomasz.kwapinski@umcs.pl

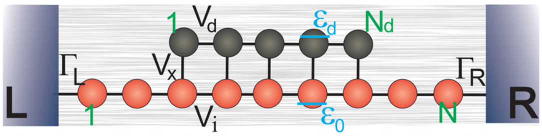

FIG. 1. Schematic view of the system under consideration: N-site linear chain (red circles) on a surface between the left (L) and right (R) electrodes and coupled with adatoms which form the second atomic chain of the length N_d (black circles). The parameters Γ_L, Γ_R, V_i, V_x, and V_d describe the couplings (electron hopping integrals) between appropriate electron states and ε_0, ε_d are the on-site electron energies in the main chain or in the additional chain, respectively.

coupling parameters of the system. Note that freely suspended chains like molecular break junction (MBJ) chains[9,30,31] are almost unpractical for potential applications. Here, we consider a relatively stable ladder-like structure of atoms on various substrates. The system can be realized experimentally on vicianl (stepped) surfaces e.g., on modified perfectly ordered Si(553)/Au or Si(557)/Au substrates with multiple Pb or Sb chains fabricated on each vicinal terrace.[4,32,33] On such surfaces, Pb atoms self-assemble into chains growing in the sequential way.[4] Formation of perfectly ordered chains is governed by the atomic diffusion and for small Pb coverage, only one complete atomic chain is observed. Next, for larger coverages the second chain is formed in the middle of each terrace which grows in a specific way, i.e., randomly deposited Pb atoms join together to form short chains which grow and grow (along the first chain). Finally, two Pb atomic chains appear at each vicinal terrace. This process corresponds to the model considered in this paper where we analyze the electrical properties of the system during the process of growing of the second atomic chain. It is important that the process described above relies on the epitaxial growth of atoms (which can be precisely controlled) and concerns the whole macroscopic surface.

To describe theoretically the conductance, electron occupancies, and the local DOS along the ladder-like normal and topological atomic systems the model tight-binding Hamiltonian and Green's function formalism are used.[26,34,35] In this paper, we analyze also half-widths of the conductance peaks to find the non-local character of the conductance in non-trivial chains which is crucial from the practical point of view. Moreover, the local DOS and charge occupation waves along both normal and topological chains are investigated as they give some insight into the physical mechanism of the transport properties.[36–39] Note that stable atomic chains need a background substrate underneath. Our substrate model assumes local tunnel couplings i.e., the spatial separation of the chain atoms is considered which allows one to investigate localized and delocalized electrons in the substrate. These two regimes may be interpreted as an insulating or a conducting substrate, respectively.

The paper is organized as follows. Section II is devoted to the theoretical model, formalism, and analytical calculations. In Sec. III, the main results of the paper are discussed: large-period conductance oscillations (Sec. III A), local DOS along normal and topological chains (Sec. III B), interference effects between both chains (Sec. III C), charge waves along a ladder-like atomic system (Sec. III D), and electron localization effect in the substrate (Sec. III E). Section IV stands for a short summary.

II. THEORETICAL MODEL, FORMALISM, AND ANALYTICAL CALCULATIONS

We consider the system which is schematically shown in Fig. 1—it consists of a linear atomic chain of N sites in a normal or SSH configuration (red balls) coupled with two metallic leads (L and R) and a further substrate electrode (S). This chain is disturbed by additional atoms (disturbances, adatoms) which can form a regular shorter chain (black balls) coupled with the main one. In our investigations, we study various lengths of this additional chain, from a single adatom up to N_d sites. The system can represent e.g., one vicinal terrace of the Si(553) surface with Pb chains.[4] The tight-binding model Hamiltonian for this system, in the standard second-quantized notation, can be written in the following form: $H = H_0 + H_{coup} + H_{surf}$, where

$$H_0 = \sum_{i=1}^{N} \varepsilon_i a_i^{+} a_i + \sum_{i_d=1}^{N_d} \varepsilon_{i_d} a_{i_d}^{+} a_{i_d} + \sum_{\vec{k}\alpha=L,R,S} \varepsilon_{\vec{k}\alpha} a_{\vec{k}\alpha}^{+} a_{\vec{k}\alpha} \qquad (1)$$

describes the on-site electron energies in the main chain, ε_i, in the additional chain, ε_{i_d}, or in the leads, $\varepsilon_{\vec{k}\alpha}$ with the wave vectors $\vec{k}$. The operators $a_{i/i_d}(a_{i/i_d}^{+})$ annihilate and create an electron at site $i = 1, \ldots, N$ or $i_d = 1, \ldots, N_d$, and $a_{\vec{k}\alpha}(a_{\vec{k}\alpha}^{+})$ are the according lead operators. It is assumed that the electron-electron interactions do not play an important role in the system which is reasonably well satisfied e.g., for Au or Pb chains on vicinal silicon surfaces and can be captured by an effective shift of the onsite energies.[4,33,41] Thus, both spin directions are independent of each other and the spin index in the Hamiltonian is suppressed. The coupling Hamiltonian describes the transitions between electron sites in both chains and between the main chain and the left and right leads, and can be written as follows:

$$\begin{aligned} H_{coup} = {} & \sum_{\vec{k}\alpha=L(R)} V_{\vec{k}\alpha} a_{\vec{k}\alpha}^{+} a_{1(N)} + \sum_{i=1}^{N-1} V_{i,i+1} a_i^{+} a_{i+1} \\ & + \sum_{i_d=1}^{N_d-1} V_{i_d,i_d+1} a_{i_d}^{+} a_{i_d+1} + \sum_{i_d=1}^{N_d} V_x a_{i_d}^{+} a_{i'} + \text{h.c.}, \qquad (2) \end{aligned}$$

where i' corresponds to such atomic sites in the main chain, i, which are coupled with additional atoms, i.e., $i' = r_1, r_2, \ldots, r_{N_d}$, and in Fig. 1 we have $r_1 = 3$, $r_{N_d} = 7$. The tunnel matrix elements $V_{i,i+1}$ and V_{i_d,i_d+1} describe the couplings between the neighboring sites in both chains and V_x is the chain-chain hopping integral—here, this parameter is site-independent, which means that all additional atoms are equally coupled with the main chain. Note that for different every second couplings in the chain $V_{i,i+1}$ ($V_{even,even+1} \neq V_{odd,odd+1}$) the system corresponds to the topological chain[14,19,21] and for equally coupled sites ($V_{i,i+1} = V$) the system is in the normal (non-topological) state. Electron transitions between the first and the last sites of the chain and the left and right leads are established by $V_{\vec{k}L(R)}$ matrix elements. The last part of the main Hamiltonian, H_{surf}, describes the chain-substrate coupling and will be specified later in the text. We assume the substrate as a further weakly coupled electrode (electron reservoir) and for an insulator surface we put $H_{surf}=0$, which is considered in our analytical calculations.

We are interested in the electron transport properties of the ladder-like system and obtain the conductance, density of states, and charge occupations of electron states in both chains. The linear conductance at zero temperature is given by the Landauer formula

$$G = \frac{2e^2}{h}\Gamma_L\Gamma_R|G^r_{1N}(E_F)|^2\,, \tag{3}$$

where $G^r_{1N}(E_F)$ is the Fourier transform of the time-dependent retarded Green's function, $G^r_{ij}(t) \equiv \langle\langle a_i(t); a_j^+(0)\rangle\rangle = i\theta(t)\langle[a_i(t), a_j^+(0)]_+\rangle$, obtained for the Fermi energy and for $i=1$ and $j=N$. In the energy space, the retarded Green function satisfies the following equation of motion:[35]

$$\varepsilon G^r_{ij}(\varepsilon) = \langle[a_i, a_j^+]_+\rangle + \langle\langle[a_i, H]_-; a_j^+\rangle\rangle_\varepsilon, \tag{4}$$

where the bracket $\langle\langle\ldots\rangle\rangle_\varepsilon$ corresponds to the new energy-dependent Green's function which in general includes $\vec{k}\alpha$ states (they appear due to the total Hamiltonian in the anticommutator). Fortunately, in the wide-band limit (WBL) approximation, these states are captured via the energy-independent Γ_α parameter, $\Gamma_{L/R} = 2\pi\sum_{\vec{k}}|V_{\vec{k}L/R}|^2\delta(\varepsilon-\varepsilon_{\vec{k}L/R})$, which is the spectral density of the chain-lead coupling. Thus, the total Green's function depends only on i and i_d states and one obtains $(N+N_d)$ linear dependent equations which can be written in the matrix notation: $\hat{G}^r\cdot\hat{C} = I$, where I is the identity matrix. The matrix $\hat{G}^r = G^r_{\beta_1\beta_2}$ stands for the $(N+N_d)\times(N+N_d)$ array of the appropriate Greens' functions, β describes all i and i_d states, and $\hat{C}$ is a square $(N+N_d)\times(N+N_d)$ complex array which takes the following form:

$$\hat{C} = \begin{bmatrix} \hat{A}^{N\times N}_{i,j}(\varepsilon) & \hat{B}^{N\times N_d}_{i,i_d} \\ \hat{B}^{N_d\times N}_{i_d,i} & \hat{D}^{N_d\times N_d}_{i_d,j_d}(\varepsilon) \end{bmatrix}_{(N+N_d)\times(N+N_d)}\,. \tag{5}$$

The on-diagonal matrix in the above relation, $\hat{A}^{N\times N}$ (dimension $N\times N$), concerns the electron states in the main chain and is composed of the following elements:

$$\hat{A}^{N\times N}_{i,j}(\varepsilon) = (\varepsilon-\varepsilon_i)\delta_{i,j} - V_{i,j+1}(\delta_{i,j+1}+\delta_{i+1,j}) + i\frac{\Gamma_L}{2}\delta_{i,1}\delta_{1,j} + i\frac{\Gamma_R}{2}\delta_{i,N}\delta_{N,j}, \tag{6}$$

and the second on-diagonal square array is related to the chain of additional atoms

$$\hat{D}^{N_d\times N_d}_{i_d,j_d}(\varepsilon) = (\varepsilon-\varepsilon_{i_d})\delta_{i_d,j_d} - V_{i_d,j_d+1}(\delta_{i_d,j_d+1}+\delta_{i_d+1,j_d}). \tag{7}$$

The off-diagonal rectangular matrixes in Eq. (5) consist of the chain-chain coupling elements, $\hat{B}^{N\times N_d}_{i,i_d} = -V_x\delta_{i,i_d+r_1-1}$ and $\hat{B}^{N_d\times N} = (\hat{B}^{N\times N_d})^T$. To obtain the conductance, one has to find the retarded Green's function which is expressed by the inverse of $\hat{C}$, Eq. (5), i.e.,

$$G^r_{1N}(\varepsilon) = (\hat{C}^{-1})_{1N} = \frac{\mathrm{cof}\hat{C}_{N1}}{\det\hat{C}}\,. \tag{8}$$

Here, $\mathrm{cof}\hat{C}_{N1}$ is the $(N,1)$ cofactor of the matrix $\hat{C}$, i.e., $(N,1)$ minor of $\hat{C}$ multiplied by $(-1)^{N+1}$. After some algebra, one can obtain

$$\mathrm{cof}\hat{C}_{N1} = \det\hat{D}^{N_d\times N_d}\times\det\Big(\hat{A}^{(N-1)\times(N-1)} - \hat{B}^{(N-1)\times N_d}(\hat{D}^{N_d\times N_d})^{-1}\hat{B}^{N_d\times(N-1)}\Big)_{N1}\,, \tag{9}$$

where the determinant $\det(\ldots)_{N1}$ concerns $\hat{A}$ and $\hat{B}$ matrixes which are formed by deleting the N-th row and 1-th column of the main matrix $\hat{C}$. Further analytical calculations of the Green's function need some assumptions which are satisfied for regular non-topological chains i.e., we consider symmetrical and uniform parameters of the system: $\varepsilon_i=\varepsilon_0$, $\varepsilon_{i_d}=\varepsilon_d$, $V_{i,i+1}=V$, $\Gamma_L=\Gamma_R=\Gamma$ (all symbols are consistent with Fig. 1) and assume $V_{i_d,i_d+1}=V_d=0$ (additional atoms are not coupled between themselves). Now we can find that $\det\hat{D}^{N_d\times N_d} = (\varepsilon-\varepsilon_d)^{N_d}$, and the matrix product in Eq. (9) can be obtained exactly

$$\hat{B}^{(N-1)\times N_d}(\hat{D}^{N_d\times N_d})^{-1}\hat{B}^{N_d\times(N-1)} = \frac{V_x^2}{\varepsilon-\varepsilon_d}\hat{R}^{(N-1)\times(N-1)}, \tag{10}$$

where $\hat{R}$ is the $(N-1)\times(N-1)$ dimension matrix with the following elements:

$$\hat{R}^{(N-1)\times(N-1)}_{ij} = \begin{cases} \delta_{i,j+1} & \mathit{for}\ 2<i<N-1 \\ 0 & \mathit{elsewhere}. \end{cases} \tag{11}$$

Thus, the cofactor, Eq. (9), reads $\mathrm{cof}\hat{C}_{N1} = V^{N-1}(\varepsilon-\varepsilon_d)^{N_d}$. Similar calculations can be performed for $\det\hat{C}$ in the denominator in Eq. (8). After some tedious matrix algebra, we can write the retarded Green's function in the following form:

$$G^r_{1N}(\varepsilon) = \frac{V^{N-1}}{\det\tilde{A}_0^N + i\Gamma\det\tilde{A}_0^{N-1} - \left(\frac{\Gamma}{2}\right)^2\det\tilde{A}_0^{N-2}}\,. \tag{12}$$

Here, $\tilde{A}_0^N$ corresponds to the $\hat{A}^{N\times N}$ matrix, Eq. (6), for $\Gamma_L=\Gamma_R=0$ (chain decoupled from the leads) and for the following substitution of the diagonal matrix elements: $\varepsilon-\varepsilon_0 \to \varepsilon-\varepsilon_0-\frac{V_x^2}{\varepsilon-\varepsilon_d}$ for $r_1\le i\le r_{N_d}$. For arbitrary r_1 and r_{N_d} the determinant $\det\tilde{A}_0^N$ has no short analytical form. However, for $r_1=1$ and $r_{N_d}=N$ (which corresponds to $N_d=N$) this determinant has the solution: $\det\tilde{A}_0^N = \frac{\sin(N+1)\phi}{\sin\phi}$, where ϕ plays the role of the Bloch phase and satisfies the following relation: $\cos\phi = \left(\varepsilon-\varepsilon_0-\frac{V_x^2}{\varepsilon-\varepsilon_d}\right)/2V$. It is worth noting that for decoupled chains, $V_x=0$, the matrix $\hat{C}$ is a tri-diagonal array and its inverse (Green function) can be computed analytically.[40] In this case, the determinant of $\hat{C}$ can be expressed by the Chebyshev polynomial of the second kind with the Bloch phase $\phi = \arccos\frac{\varepsilon-\varepsilon_0}{2V}$. Writing the conductance in terms of the Green's function, one can find the condition on the conductance oscillations $\cos\frac{\pi l}{m} = \frac{E_F-\varepsilon_{eff}}{2V}$, where ε_{eff} is the effective value of the on-site electron energy in the chain ($\varepsilon_{eff} = \varepsilon_0$ for $V_x = 0$), $l = 0, 1, \dots, m-1$ and m is the atomic period of the conductance.

The charge localized at the i-th site can be obtained by integrating the local density of states, $\rho_i(\varepsilon) = DOS_i$, up to the Fermi energy

$$n_i = \int_{-\infty}^{E_F} d\varepsilon \rho_i(\varepsilon) = -\frac{1}{\pi}\int_{-\infty}^{E_F} d\varepsilon \Im G^r_{ii}(\varepsilon) \ , \qquad (13)$$

where $G^r_{ii}(\varepsilon)$ is the retarded Green's function which is obtained together with other elements of the matrix $\hat{G}^r$.

III. RESULTS AND DISCUSSION

In our calculations, we will always assume that the left and right leads couple equally strong to the chain, $\Gamma_L = \Gamma_R = \Gamma$ and assume Γ as the unit energy. If it is not directly stated, we consider no substrate electrode (which is equivalent to an insulator surface). The Fermi energy of the unbiased leads stands for the energy reference point, $E_F = 0$, and the temperature $T = 0$ K. Moreover, in our numerical calculations we consider only regular chains i.e., the on-site electron energies are position independent, $\varepsilon_i = \varepsilon_0$, $\varepsilon_{id} = \varepsilon_d$, and for a normal chain the intra-chain hopping integrals are the same for all i and $V_{ij} = V$, and $V_{i_d, j_d} = V_d$. These assumptions are quite reasonable for chains consisting of one atom species in an equidistant arrangement on the surface. For the SSH chain, we assume $V_{odd,odd+1} = V_1$ and $V_{even,even+1} = V_2$ which corresponds to a chain with two atoms in the unit cell. The conductance is expressed in units of $\frac{2e^2}{h}$, and the parameters have been chosen in order to satisfy the realistic situation in many experiments, e.g., assuming $\Gamma = 0.25$ eV, the hopping integral along the chain is $V = 4 = 1$ eV or between chains is $V_x = 2 = 0.5$ eV.[26,33,41]

A. Large-period conductance oscillations

In the beginning of our studies, we analyze the conductance along a normal (non-topological) chain as a function of the second chain length, N_d. Both chains are coupled via V_x parameter as is schematically shown in Fig. 1 and the main chain length is $N = 100$. In the MBJ geometry with a single atomic chain between electron reservoirs, the conductance drastically changes with N and oscillates as a function of the chain length (even-odd conductance oscillations).[6,8,9,31,42–44] In our studies in Fig. 2, we set the value of ε_0 in the main chain such that it satisfies the condition for the period $m = 2$ ($\varepsilon_0 = 0$), $m = 3$ ($\varepsilon_0 = -V$) or $m = 4$ ($\varepsilon_0 = -\sqrt{2}V$)—red, green, and blue curves respectively, and change the number of atoms in the additional chain. This adatom chain starts to grow from site $r_1 = 10$ ($N_d = 1$) up to $r_{N_d} = 90$ ($N_d = 81$) and we expect to observe the same oscillation period of G. As one can see, the conductance of the non-disturbed chain ($N_d = 0$) is relatively small due to the even chain length, N. However, it is surprising that in the presence of additional atoms the conductance oscillates with very large periods, here $m = 44$, 39 or 32 for $\varepsilon_0 = 0, -V$ or $-\sqrt{2}V$, respectively. These large oscillation periods can be explained from the condition on the conductance oscillations: $m = \frac{\pi l}{\arccos\left(\frac{-\varepsilon_{eff}}{2V}\right)}$, where the effective on-site energy corresponds to the renormalized system energy $\varepsilon_{eff} = \varepsilon_0 + \frac{V_x^2}{\varepsilon-\varepsilon_d}$, and $0 < l < m$. One can easily find that nearly integer numbers of the oscillation period, m, appear (i) for $l = 23$ ($m = 43.98$ - red curve), (ii) for $l = 14$ ($m = 38.97$ - green curve), and (iii) for $l = 9$ ($m = 32.02$ - blue curve). Alternatively, these periods can be explained assuming a linear chain of atomic double-site cells composed of two states with energies: ε_0 and ε_d, and which are coupled together via the V_x parameter. In such a case, the cell is characterized by two molecular states which stand for effective energies of the ladder-like chain

$$\varepsilon_\pm = \frac{\varepsilon_0 + \varepsilon_d}{2} \pm \sqrt{\left(\frac{\varepsilon_0 + \varepsilon_d}{2}\right)^2 + V_x^2}. \qquad (14)$$

The conductance oscillation periods obtained from the above energies, Eq. (14), are in good agreement with the results shown in Fig. 2. Note that the minimal value of G observed for $N_d \simeq 40$ in Fig. 2 is not a general result because, depending on the system parameters (and using the relation on the conductance oscillations), one can find other large periods of the conductance such that the maximum of G can appear for different N_d.

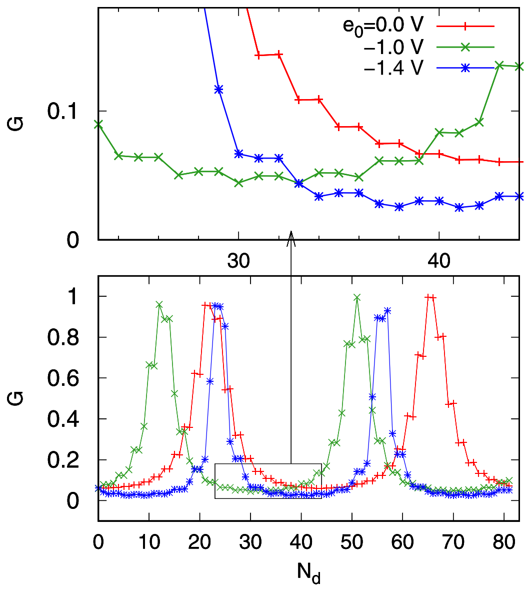

FIG. 2. The conductance through the atomic chain composed of $N = 100$ linear sites as a function of the second chain length, N_d, for $\varepsilon_0 = 0$ (red curve), $\varepsilon_0 = -V$ (green curve), and $\varepsilon_0 = -\sqrt{2}V$ (blue curve) and for $\varepsilon_d = -\sqrt{3}V$, $V = 4$, $V_x = 2$, $V_d = 0$, $\Gamma_L = \Gamma_R = \Gamma = 1$ (energy unit). The atoms of the second chain are placed from $r_1 = 10$ up to $r_{N_d} = 90$ sites of the main chain ($N_d = 81$). The upper panel is a zoom of the indicated area from the bottom one. The lines serve as a guide to the eye.

The second crucial result relating to Fig. 2 concerns the amount of adatoms and their role in the conductance modifications. We have found that small changes of the additional-chain length, N_d, or single side-attached atoms do not modify significantly the conductance through the main chain. This non-local behavior of the conductance is in contrast to the even-odd conductance oscillations where small variations of N change significantly the conductance. As one can see, the half-widths of the conductance peaks are relatively wide. Moreover, to change the conductance from minimal to maximal value one needs tens of atoms. These features make the considered system almost insensitive to inadvertent external perturbations (adatoms) which allows one to precisely control the electron transport through the chain.

It is interesting that also small-period oscillations of the conductance are visible in the curves in Fig. 2, upper panel (zoom of the area indicated by the black rectangle). These oscillations correspond to the condition on the conductance oscillations in the main atomic chain, i.e., $\varepsilon_0 = 0, -V$ or $-\sqrt{2}V$. As one can see, the period of two, three, and four atoms appears on the conductance—red, blue, and green curves, respectively. Thus, the system under consideration reveals both small and large periods of the conductance oscillations. Note that small-period oscillations can provide the information about the electron levels in the non-disturbed chain, ε_0, while large-period oscillations are related to the effective energies of the ladder-like system, ε_{eff}.

The results shown in Fig. 2 were obtained for adatoms placed one after other from sites $r_1 = 10$ up to $r_{N_d} = 90$—it stands for only one possible distribution of additional atoms. However, in real experiments such chains can grow differently e.g., the second Pb chain on Si(557) starts to growth from the so-called "nucleation points" to the left and right sides.[4] We have verified that our results slightly depend on distributions of adatoms coupled with the main chain and thus, henceforth we consider only the atom-by-atom growth from r_1 to r_{N_d} sites. Moreover, we have checked that the conductance periods are the same for both even and odd chain lengths, N. Note that the large-period conductance oscillations are not observed in the SSH chain due to an energy gap inside the system which will be analyzed below. However, in the limit of large bias voltages the electron current can flow through the side-band (non-topological) states of the SSH chain.[18]

B. Local DOS along normal and topological chains

For atomic objects on a surface, the local density of states at the Fermi level is strongly related to the current measured e.g., in STM experiments. Thus, it could be very desirable to analyze the local DOS structure along ladder-like atomic chains. In doing so, we consider both normal and SSH chains as we expect to observe crucial differences between these two systems, Fig. 3 upper and bottom panel, respectively. Here, the local DOS at the Fermi level (plotted for all chain sites, i) is analyzed as a function of additional chain length, N_d. For a normal chain composed of an even number of sites (upper panel) and not disturbed by adatoms, $N_d = 0$, the local DOS along the whole chain is minimal (for $1 \leq i \leq 100$); thus, the conductance is also very small, cf. Fig. 2 for $N_d = 0$. However, for specific lengths N_d, one observes that the local DOS oscillates along the whole chain and e.g., for $N_d = 22$ (adatoms are coupled only to the sites between $r_1 = 10$ and $r_{N_d} = 31$) non-vanishing DOS oscillations appear for all i. It is the reason that the conductance along the chain in this case is maximal.[31,34] The situation drastically changes for the SSH chain being in non-trivial topological phase, $V_1 = 2, V_2 = 4$, bottom panel. As one can see, the local DOS along the chain is nonzero only at both chain ends where topological states appear. It is worth noting that the local DOS values do not depend on the adatom chain length and are the same for the non-disturbed chain, $N_d = 0$, as well as for the disturbed chain, $N_d = 81$. It confirms the non-local character of the topological states in the SSH chain.

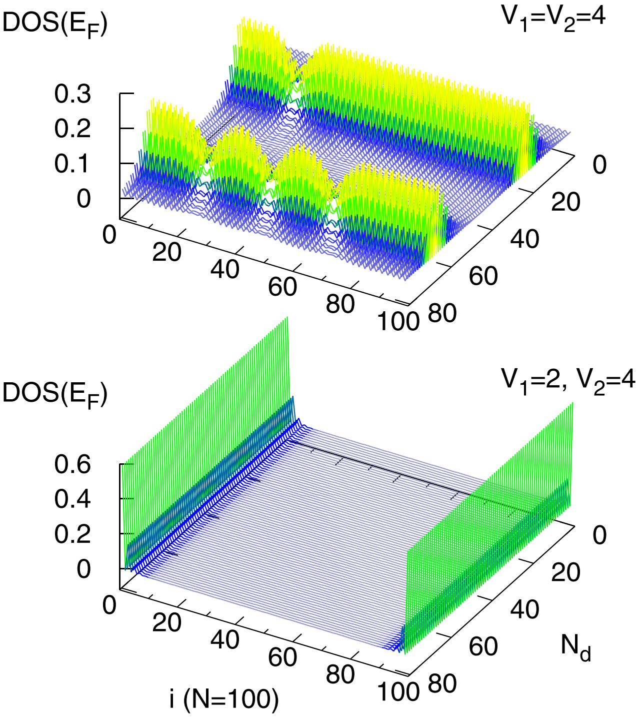

FIG. 3. Local DOS at the Fermi level along the chain as a function of the second chain length, N_d. The upper (bottom) panel corresponds to the normal chain, $V_1 = V_2 = V = 4$, (topological SSH chain, $V_1 = 2, V_2 = 4$). The other parameters are the same as those in Fig. 2, $\varepsilon_d = -\sqrt{3}V$.

In order to further study the influence of topological phases on the local DOS along the chain, we consider the SSH setup with different couplings V_1 and V_2 for the non-disturbed chain, $N_d = 0$ (upper panel, Fig. 4), and for small amount of adatoms, $N_d = 22$ (bottom panel). The SSH chain in the trivial phase ($V_2 < V_1$) is characterized by an energy gap in the structure of DOS; thus, in this case the local DOS along the chain is minimal for all atomic sites. On the other hand, for the chain in the non-trivial phase ($V_1 < V_2$) the chain possesses topological states at both ends and thus finite nonzero values of the local DOS appear in this case, cf. also Fig. 3. As one can see the trivial and nontrivial phases of the SSH chain hardly depend on the amount of adatoms in the second chain (non-local property). The only difference between both phases is observed for the mixed-value region

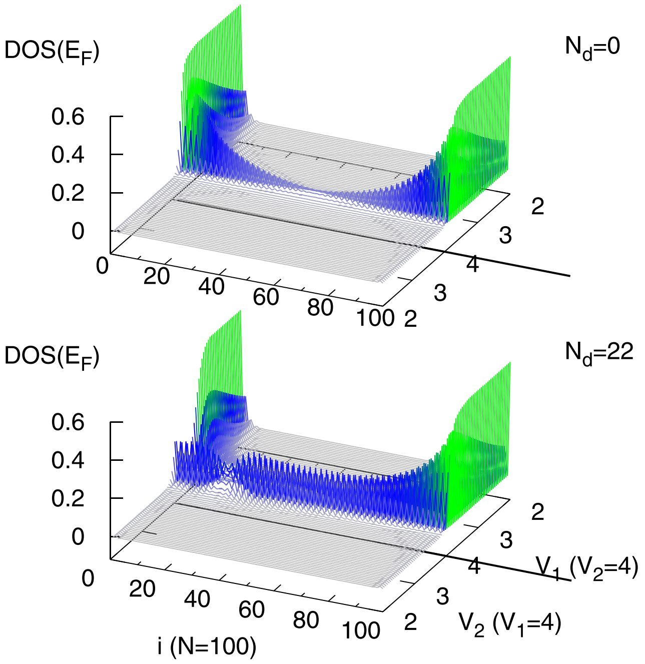

FIG. 4. Local DOS at the Fermi level along the chain for various configurations of the coupling strengths V_1 and V_2. The black solid lines indicate the case $V_1 = V_2 = V = 4$ (normal chain) and the left and right regions correspond to the SSH chain being in the trivial ($V_2 < V_1 = 4$) or non-trivial phase ($V_1 < V_2 = 4$). The upper panel is plotted for the non-disturbed chain ($N_d = 0$) and the bottom one for $N_d = 22$ adatoms, and the other parameters are the same as those in Fig. 2, $\varepsilon_d = -\sqrt{3}V$.

i.e., for $V_1 \simeq V_2$ indicated by the black lines at both panels. In this case, the chain becomes normal and for the non-disturbed case (upper panel), the values of the local DOS strongly decrease from the outer atoms towards the middle of the chain and the conductance is also minimal. However, in the presence of a small number of adatoms (bottom panel), the local DOS oscillates along the whole 100-atom chain which leads to a large value of the conductance in this case.

We have shown that single disturbances almost do not change the conductance which is a manifestation of the non-local character of G. Moreover, topological states of the SSH chain are insensitive to external disturbances. In this context, it is interesting to analyze the role of adatoms in the energetic structure of DOS in the SSH and normal chains. In Fig. 5, we show the local DOS at the first atomic site as a function of the energy for the normal (upper panel) and topological SSH chains (bottom panel) and for $N_d = 81$ adatoms. In the SSH chain, a very wide topological state is visible in the energy gap region which is insensitive to the adatom energy, ε_d. However, the left and right energy bands change in the presence of disturbed adatoms and some modifications of the DOS structure are visible for the energy related to the value of ε_d, cf. the curve for $\varepsilon_d = 3$. This effect provides asymmetry in the local DOS of the SSH chain which can change the electron occupations along the chain—this problem will be studied later. On the other hand, the local DOS of the normal chain at the first atom is also characterized by a zero-energy peak for $\varepsilon_d = 0$ (upper panel). However, this peak comes from adatoms coupled with the normal chain and is not locally protected. It is confirmed by the structure of the local DOS obtained for other values of the adatom energy—we observe local peaks in DOS for $\varepsilon \simeq \varepsilon_d$. Such behavior of the zero-energy peaks can be used to verify experimentally topological and normal states localized at both chain ends as the former are insensitive to external perturbations and the latter change their positions in the presence of adatoms. Moreover, it is possible to determine the adatom energy, ε_d, analyzing the structure of DOS of the ladder-like chains.

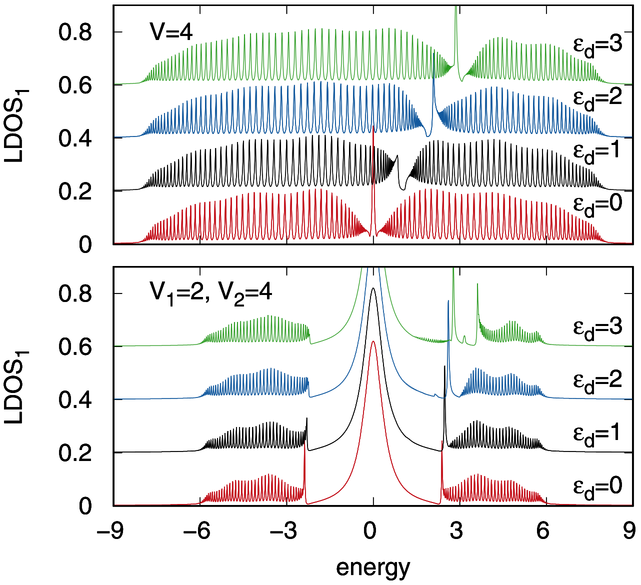

FIG. 5. Energy dependent local DOS at the first atomic site in the normal chain ($V_1 = V_2 = V = 4$, upper panel) and in the SSH chain ($V_1 = 2$, $V_2 = 4$, bottom panel) for various energies of adatoms, $\varepsilon_d = 0, 1, 2, 3$ and for $V_x = 1$, $N_d = 81$. The other parameters are the same as those in Fig. 2. The curves for $\varepsilon_d > 0$ are shifted by 0.2, 0.4, or 0.6 for better visualization.

C. Coupled adatoms—Interference effects

In this subsection we investigate the conductance through N-atom chain coupled with additional atoms which are nearest-neighbor coupled to each other via the V_d parameter. This coupling is responsible for new paths for electrons in the system and therefore, interference effects play here an important role. As the conductance along the SSH chain is not sensitive to adatoms, here we consider the non-topological chain which reveals the non-local character of G.

First, we analyze the conductance vs. the additional chain length, N_d, for two specific values of the electron energies i.e., $\varepsilon_d = E_f = 0$ and $\varepsilon_d = -\sqrt{3}V$, see Fig. 6, upper panel. These positions of ε_d correspond to the conductance oscillation effect in linear chains with periods $m = 2$ or $m = 6$ atoms, respectively. However, in the presence of nonzero hopping integrals in the coupled chain, V_d, the maxima of G appear for even N_d (the so-called odd-even conductance oscillations), red curve in Fig. 6, (contrary to the even-odd oscillations where maxima of G are observed for odd N[31,42,43]) These oscillations are also visible in the middle panel in Fig. 6 where the odd-even conductance oscillations are analyzed for a wide spectrum of V_d. For very small V_d, the conductance is suppressed (black field in the middle panel). For larger values of V_d, one observes maximal

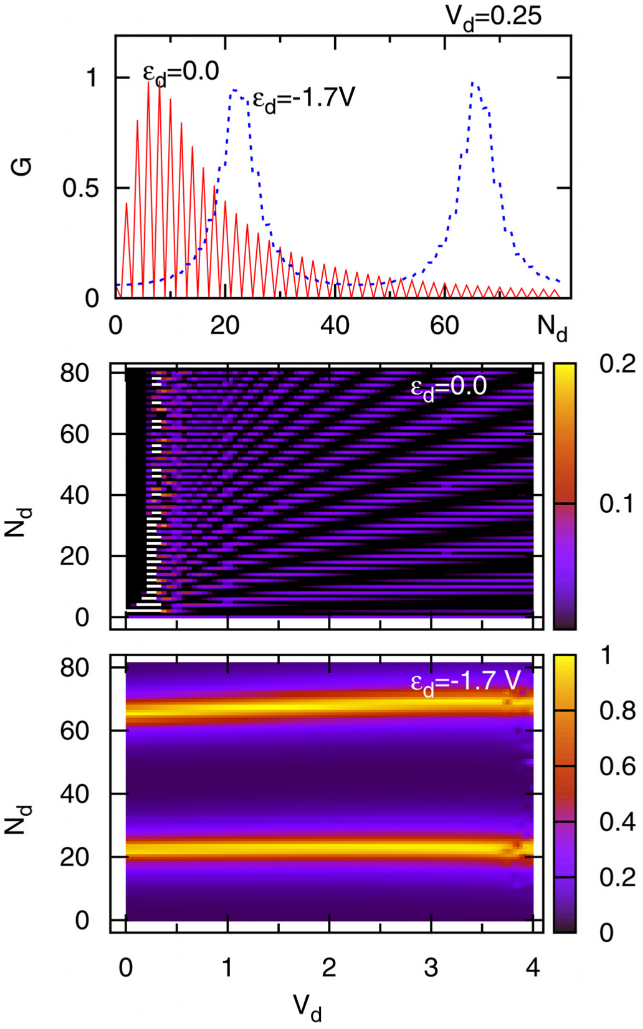

FIG. 6. The conductance through $N = 100$ atomic chain as a function of the second chain length, N_d, and the coupling between additional atoms, V_d, for $\varepsilon_d = 0$ (middle panel) and $\varepsilon_d = -\sqrt{3}V$ (bottom panel). The upper panel corresponds to the conductance from the middle (red curve) and bottom (blue curve) panels obtained for $V_d = 0.25$. The others parameters are the same as those in Fig. 2, $\varepsilon_0 = 0$.

oscillation amplitude of G, and for even larger V_d, the amplitude decreases but the odd-even oscillations are still visible. The situation changes for nonzero on-site electron energies in the second chain, $\varepsilon_d \neq 0$, (blue curve in the upper panel, Fig. 6). Now, instead of the odd-even oscillations of G one expects (from the condition for the G oscillations for $\varepsilon_d = -\sqrt{3}V$) the oscillation period of $m = 6$ atoms. However, we observe here large-period conductance oscillations. This period can be explained by the renormalized effective energies in the chain. It is interesting that in the non-resonant case ($\varepsilon_d \neq 0$) the conductance oscillations slightly depend on the coupling parameter, V_d, which is analyzed in the bottom panel in Fig. 6. Here, the oscillation period as well as oscillation amplitude does not change significantly with V_d. Thus for the non-resonant case (which is satisfied e.g., for different atom species), the system is almost insensitive to the couplings between neighboring sites in the additional chain.

D. Charge waves along atomic chains

Charge distribution along atomic chains is often characterized by an oscillatory (in space) function known as charge waves.[34,36–39,45] These waves are closely related to the conductance oscillation effect and the periods of both effects are exactly the same. However, for a ladder-like system due to external adatoms charge waves should be modified in normal as well as in topological chains which is analyzed in this subsection.

In the upper panel in Fig. 7, we show the charge occupations, n_i, along the linear non-topological chain composed of $N = 100$ sites, free of adatoms (blue curve) and with only one side-attached atom coupled with $i = 50$ site (red crosses). As one can see, the site occupations of the perfect chain, n_i, are equal to 0.5 and are site-independent (here, $\varepsilon_0 = E_F = 0$). In the presence of only one adatom, the Friedel oscillations are well visible with the oscillation period equals to 2 (which is the same as the conductance oscillation period for $\varepsilon_0 = 0$) and exponentially decreasing amplitude.[34,36,38] The situation changes for a larger number of adatoms (middle and bottom panels). For $N_d = 70$ (additional atoms are coupled to the main chain between $r_1 = 11$ and $r_{N_d} = 80$ sites), the occupations n_i are characterized by two separate regions with different periods. For the chain sites which are non-disturbed by

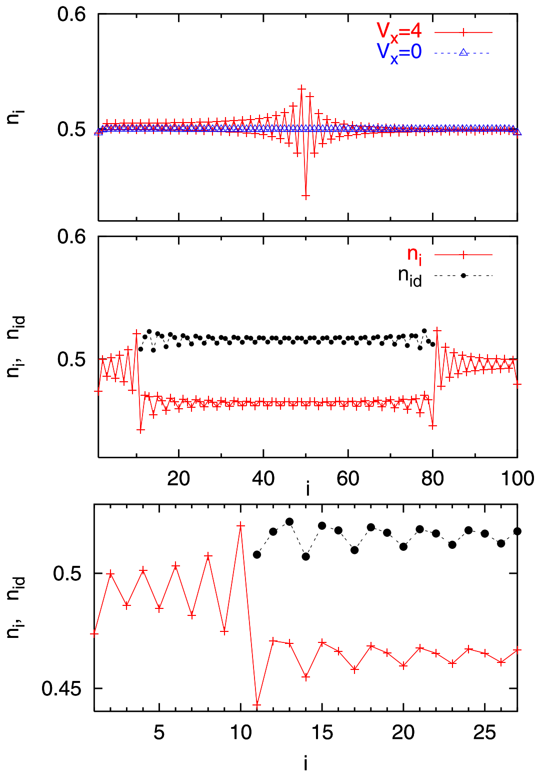

FIG. 7. Charge occupations along the chain composed of $N = 100$ sites with a single side-attached atom at $i = 50$ and for $V_x = 4$ (red crosses, upper panel) and $V_x = 0$ (blue triangles, upper panel). The middle panel corresponds to $N_d = 70$ atoms coupled to the chain from $r_1 = 11$ to $r_{N_d} = 80$ sites with $V_x = 4$ where n_i (n_{id}) stands for the main chain (adatoms) charges – red crosses and black circles, respectively. The bottom panel is an enlarged part of the middle one for $i = 1, \ldots, 27$. The black circles are shifted down by 0.35 for better visualization and the others parameters are the same as those in Fig. 2, $\varepsilon_0 = 0$, $\varepsilon_d = -4$.

adatoms ($i<11$ and $i>80$), the even-odd Friedel oscillations appear with decreasing amplitude towards the chain ends (red crosses), similarly to the case shown in the upper panel. However, for the chain sites which are coupled with additional atoms one observes lower occupations of the main chain, and more important, the oscillation period of n_i changes which is better visible in the bottom panel (zoom of the middle one). This period is related to the V_x parameter and here from the relation $\frac{\pi l}{m} = \arccos\left(\frac{-\varepsilon_d}{2V_x}\right)$, one obtains that $\frac{\pi l}{m} = \frac{\pi}{3}$ and the period is $m=3$ (for $l=1$). Thus, the information about the adatom parameters (ε_d, V_x) can be easily extracted on closer inspection of the Friedel oscillations. It is interesting that the occupancies of additional atoms reflect perfectly the same periodicity as in the main chain. Moreover, the maxima of n_i correspond to the maxima of n_{id}, so there is no phase difference between the waves along both chains.

Our former studies showed that the SSH topological chain is insensitive to external distributions. However, in the presence of adatoms the local DOS at atomic sites in the SSH chain can be non-symmetrical, cf. Fig. 5. Thus, it is desirable to analyze in more detail the structure of charge waves along such chains. In Fig. 8, we investigate the electron occupations, n_i, inside the main chain as a function of the coupling between chains, V_x, for the normal chain (upper panel) and for the SSH chain with topological end-states (bottom panel). As one can see in both cases for $V_x=0$, all sites are half occupied. The situation changes in the presence of adatoms (as before the adatom chain is coupled with the main chain from $r_1=11$ up to $r_{N_d}=80$ sites). For the normal chain (upper panel), the charge occupation smoothly decreases with V_x for $r_1<i<r_{N_d}$ and the Friedel oscillations are observed inside the whole chain, especially the even-odd Friedel oscillations for the non-disturbed chain region ($i<11$ and $i>80$). However, it is surprising that for the SSH chain (bottom panel) the electron occupations also depend on adatoms but there are two important differences: (i) the occupations n_i is almost constant for small V_x, with no oscillations and starts to decrease for $V_x > |\varepsilon_d|$ and (ii) there are no Friedel oscillations at both chain ends. The absence of Friedel oscillations in topological SSH chains allows one to distinguish experimentally between normal or topological systems.

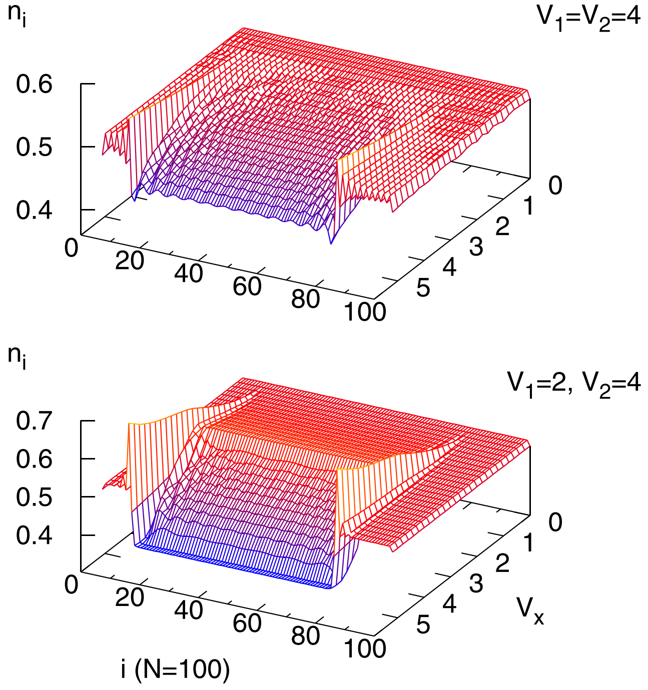

FIG. 8. Charge occupations along the normal chain ($V_1=V_2=V=4$, upper panel) and SSH chain ($V_1=2, V_2=4$, bottom panel) as a function of V_x. The other parameters are the same as those in Fig. 7.

To conclude, for non-trivial topological chains the electron occupancies change in the presence of adatoms (they are not protected against disturbances). It results from the modifications of DOS sidebands due to adatoms. However, the main zero-energy topological state is still insensitive to such disturbances. Although the occupancies of the SSH chain change due to external atoms we do not observe Friedel oscillations in topological chains in contrast to the normal chains.

E. Ladder-like chain on different surfaces

In this subsection, we consider a more realistic case and study the influence of the chain-substrate coupling on the electronic properties along the ladder-like chain. We introduce the wire-surface tunneling Hamiltonian in the form $H_{surf} = \sum_{\vec{k}S} V_{j\vec{k}S} a^{+}_{\vec{k}S} a_j + h.c.$ The tunnel matrix element $V_{j\vec{k}S}$ depends on the position of the j-th chain atom, R_j, at the substrate: $V_{j\vec{k}S} = V_{\vec{k}S} \exp(ikR_j)$[41,46] i.e., the spatial separation of the chain atoms is considered. In our investigations, we assume equal distances between atoms in both chains, a, and moreover, only the substrate electrons with Fermi wavelength play an important role in the electron transport. Thus, one obtains the spectral density function

$$\Gamma^S_{ij} = \Gamma_S \frac{\sin(k_F a r_{ij})}{k_F a r_{ij}}, \tag{15}$$

where Γ_S stands for the effective chain-substrate coupling strength, $\Gamma_S = 2\pi \sum_{\vec{k}S} |V_{\vec{k}S}|^2 \delta(\varepsilon - \varepsilon_{\vec{k}S})$ which in the wide band limit is energy independent and r_{ij} is the distance between i-th and j-th sites expressed in a units. Thus, the chain-substrate coupling modifies all matrix elements in Eq. (5) by additional complex term $i\frac{\Gamma^S_{ij}}{2}$. Note that for a very small $k_F a$ parameter the Γ^S_{ij} function is independent of the atom positions i.e., $\Gamma^S_{ij} = \Gamma_S$ which corresponds to delocalized electron states in the substrate as in the case of metallic-like surfaces. In the opposite limit i.e., for a very large value of $k_F a$ one finds $\Gamma^S_{ij} = \Gamma_S \delta_{ij}$ (each chain site is coupled to an individual additional electrode). This limit describes localized electrons with very short mean-free path as in semiconductor or insulator substrates.

In Fig. 9, we analyze the conductance oscillations through a normal chain in the presence of a weakly coupled substrate, $\Gamma_S = 0.1$, and different values of $k_F a$. Note that the results obtained in the absence of the substrate, i.e., for $\Gamma_S = 0$, are shown in Fig. 2, red curve. Let us first consider almost delocalized electrons in the substrate (small $k_F a$). As one can see, the oscillation period and the oscillation

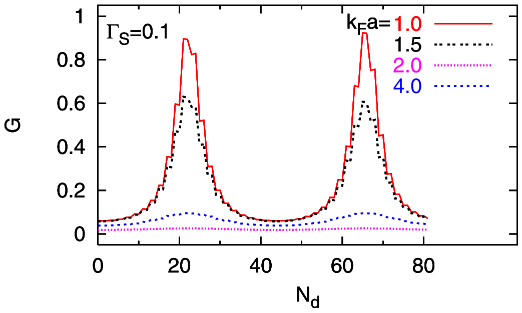

FIG. 9. The conductance through a normal chain as a function of N_d for the same parameters as in Fig. 2 for $\varepsilon_0 = 0$, $\Gamma_S = 0.1$ and for various values of $k_F a$ indicated in the legend.

amplitude are practically not influenced by the substrate in this case, cf. the red curves in Figs. 2 and 9. For the intermediate case of $k_F a$ we observe smaller oscillations of G, and the conductance almost vanishes for $k_F a = 2$. However, for larger $k_F a$ the oscillation amplitude of G increases due to oscillations of the Γ^S_{ij} function, Eq. (15), and e.g., for $k_F a = 4$ large period conductance oscillations are again clearly visible. Thus, we can conclude that the surface leaves the oscillation period unchanged but it influences the oscillation amplitude especially for strongly localized electrons in the substrate. Note that the oscillation amplitude of G as well as the amplitude of charge waves also decreases with increasing Γ_S.

The conductance of a normal chain is sensitive to the surface below the chain which should be also reflected in the structure of the local DOS. For topological chains with protected states, such dependence is not obvious. Thus in our last studies, in Fig. 10, we compare the local DOS structures of the normal and SSH chains (upper and bottom panel, respectively) disturbed by adatoms. For a normal chain with no surface, $\Gamma_S = 0$, the local DOS is characterized by an oscillating structure with zero-energy peak which comes from the disturbances, $\varepsilon_d = 0$ (cf. also Fig. 5). In the presence of the surface, the oscillations of DOS disappear and the structure becomes relatively flat. Moreover, the central peak significantly decreases due to the chain-surface coupling, see the curve for $\Gamma_S = 0.5$. The results for the topological chain are shown in the bottom panel—the protected state slightly depends on the substrate (it becomes somewhat wider and smaller); however, both sideband DOS structures are smoother and smoother as the coupling increases. Thus, the substrate influences mainly the sideband structures of DOS but the protected states are not destroyed by the surface. It means that topological states in one-dimensional ladder-like structures coupled with various surfaces can be observed experimentally even in the case of side-attached disturbances.

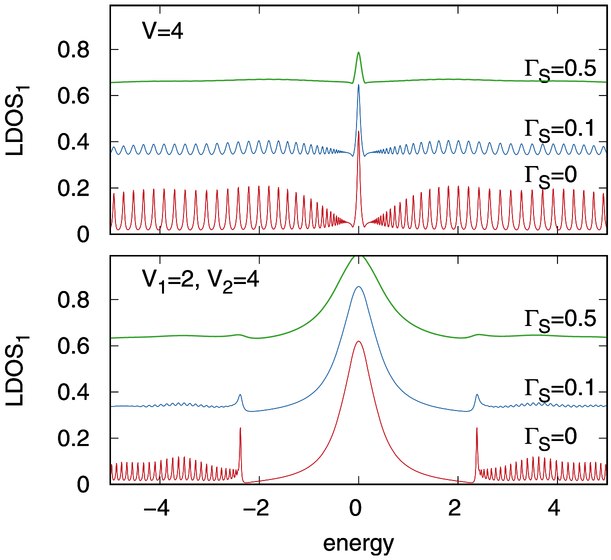

FIG. 10. Local DOS at the first atomic site for normal chain (upper panel) and for the SSH chain in nontrivial phase (bottom panel) for different chain-substrate coupling strength, $\Gamma_S = 0, 0.1$ and 0.5. The other parameters are the same parameters as those in Fig. 2, $k_{Fa} = 4$. The curves for $\Gamma_S = 0.1$ and 0.5 are shifted by 0.3 and 0.6, respectively.

IV. CONCLUSIONS

We have studied the electron transport through a ladder-like atomic system composed of normal or topological chains on different substrates. The tight-binding Hamiltonian and the Green's function approach were used to obtain the conductance, local DOS structure, and the electron occupancies of all chain sites. Our studies showed that the ladder-like systems have an advantage over straight atomic chains which is crucial for potential applications of these systems.

We have found that the conductance oscillates as a function of the additional chain length with very large periods, tens of atoms (not reported in the literature before). This interesting effect allows one to control the conductance by the length of the side chain i.e., by the amount of atoms which can be precisely deposited at the surface using epitaxy methods. The conductance oscillations were confirmed by our analytical calculations. We have also found that single external atoms do not change significantly the electrical properties of the ladder-like system (non-local character of the conductance). Moreover, we have observed modified periods of the charge waves inside the normal chain directly coupled with adatoms.

We have also shown that topological states in the SSH chain are insensitive to external disturbances (adatoms) and they survive for different substrates coupled with the ladder-like system. However, external atoms leave their fingerprints on the local DOS structure of the SSH chain – the electron occupancies along the chain decrease in the presence of adatoms. Note, however, that the Friedel oscillations do not appear in the topological chain. It allows us to distinguish experimentally normal and topological ladder-like systems. We have shown that careful inspection of the local DOS structure as well as charge waves can provide the information about the electron energy levels and coupling integrals.

The results discussed in this paper give some insight into the physical mechanism of the transport properties through the ladder-like one-dimensional normal and topological structures. These systems are locally protected against external impurities and can be precisely controlled; thus, they can be applied in nanoelectronics.

ACKNOWLEDGMENTS

This work was partially supported by the National Science Centre, Poland, under Grant No. 2014/13/B/ST5/04442.

[1] R. Zdyb, M. Stróżak, and M. Jałochowski, Vacuum **63**, 107 (2001).

[2] J. N. Crain, J. L. McChesney, F. Zheng, M. C. Gallagher, P. C. Snijders, M. Bissen, C. Gundelach, S. C. Erwin, and F. J. Himpsel, Phys. Rev. B **69**, 125401 (2004).

[3] A. A. Baski, K. M. Saoud, and K. M. Jones, Appl. Surf. Sci. **182**, 216 (2001).

[4] M. Jałochowski, T. Kwapiński, P. Łukasik, P. Nita, and M. Kopciuszyński, J. Phys.: Condens. Matter **28**, 284003 (2016).

[5] N. Oncel, A. van Houselt, J. Huijben, A.-S. Hallback, O. Gurlu, H. J. W. Zandvliet, and B. Poelsema, Phys. Rev. Lett. **95**, 116801 (2005).

[6] J. Zeng and K.-K. Chen, J. Mater. Chem. C **3**, 5697 (2015).

[7] H. Ohnishi, Y. Kondo, and K. Takayanagi, Nature **395**, 780 (1998).

[8] A. I. Yanson, G. R. Bollinger, H. E. van den Brom, N. Agrait, and J. M. van Ruitenbeek, Nature **395**, 783 (1998).

[9] R. H. M. Smit, C. Untiedt, G. Rubio-Bollinger, R. C. Segers, and J. M. van Ruitenbeek, Phys. Rev. Lett. **91**, 076805 (2003).

[10] N. Agrait, A. L. Yeyati, and J. M. van Ruitenbeek, Phys. Rep. **377**, 81 (2003).

[11] O. M. Auslaender, H. Steinberg, A. Yacoby, Y. Tserkovnyak, B. I. Halperin, K. W. Baldwin, L. N. Pfeiffer, and K. W. West, Science **308**, 88 (2005).

[12] G. Gruner, Rev. Mod. Phys. **60**, 1129 (1998).

[13] H. W. Yeom, S. Takeda, E. Rotenberg, I. Matsuda, K. Horikoshi, J. Schaefer, C. M. Lee, S. D. Kevan, T. Ohta, T. Nagao, and S. Hasegawa, Phys. Rev. Lett. **82**, 4898 (1999).

[14] J. K. Asboth, L. Oroszlany, and A. Palyi, *A Short Course on Topological Insulators* (Springer, Switzerland, 2016).

[15] R. Drost, T. Ojanen, A. Harjuv, and P. Liljeroth, Nat. Phys. **13**, 668 (2017).

[16] A. Y. Kitaev, Phys. Usp. **44**, 131 (2001).

[17] M. Maśka, A. Gorczyca-Goral, J. Tworzydło, and T. Domański, Phys. Rev. B **95**, 045429 (2017).

[18] M. Benito, M. Niklas, G. Platero, and S. Kohler, Phys. Rev. B **93**, 115432 (2016).

[19] L. Linhu, C. Yang, and S. Chen, Europhys. Lett. **112**, 10004 (2015).

[20] W. Su, J. Schrieffer, and A. Heeger, Phys. Rev. Lett. **42**, 1698 (1979).

[21] L. Linhu, X. Zhihao, and S. Chen, Phys. Rev. B **89**, 085111 (2014).

[22] T. Kitagawa, M. Broome, A. Fedrizzi, M. Rudner, E. Berg, I. Kassal, A. Guzik, E. Demler, and A. White, Nat. Commun. **3**, 882 (2012).

[23] E. Meier, F. A. Anc, and B. Gadway, Nat. Commun. **7**, 13986 (2016).

[24] Z. Korczak and T. Kwapiński, Surf. Sci. **601**, 3324 (2007).

[25] T. Kwapiński, J. Phys.: Condens. Matter **19**, 176218 (2007).

[26] T. Kwapiński, M. Krawiec, and M. Jałochowski, Phys. Lett. A **372**, 154 (2008).

[27] P. A. Orellana, F. Dominguez-Adame, I. Gomez, and M. L. Ladron de Guevara, Phys. Rev. B **67**, 085321 (2003).

[28] T. Kwapiński, Vacuum **74**, 201 (2004).

[29] B. Jiang, Y.-H. Zhou, C.-Y. Chen, and K.-Q. Chen, Org. Electron. **23**, 133 (2015).

[30] K. S. Thygesen and K. W. Jacobsen, Phys. Rev. Lett. **91**, 146801 (2003).

[31] T. Kwapiński, J. Phys.: Condens. Matter **17**, 5849 (2005); *ibid.* **22**, 295303 (2010).

[32] H. Okino, I. Matsuda, S. Yamazaki, R. Hobara, and S. Hasegawa, Phys. Rev. B **76**, 035424 (2007).

[33] M. Krawiec, T. Kwapiński, and M. Jałochowski, Phys. Rev. B **73**, 075415 (2006).

[34] T. Kwapiński, J. Phys.: Condens. Matter **18**, 7313 (2006).

[35] S. Datta, *Electronic Transport in Mesoscopic Systems* (Cambridge University Press, Cambridge, 1995).

[36] J. S. Shin, K.-D. Ryang, and H. W. Yeom, Phys. Rev. B **85**, 073401 (2012).

[37] D. F. Urban, C. A. Stafford, and H. Grabert, Phys. Rev. B **75**, 205428 (2007).

[38] A. Gorczyca, M. M. Maska, and M. Mierzejewski, Phys. Rev. B **76**, 165419 (2007).

[39] Y. Weiss, M. Goldstein, and R. Berkovits, Phys. Rev. B **75**, 064209 (2007).

[40] C. M. Fonseca and J. Petronilho, Linear Algebra Appl. **325**, 7 (2001).

[41] T. Kwapiński, S. Kohler, and P. Hänggi, Eur. Phys. J. B **78**, 75 (2010).

[42] T.-S. Kim and H. Hershfield, Phys. Rev. B **65**, 214526 (2002).

[43] Z. Y. Zeng and F. Claro, Phys. Rev. B **65**, 193405 (2002).

[44] Z. Q. Fan, Z. Zhang, X. Deng, G. Tang, C. Yang, L. Sun, and H. L. Ahu, Carbon **98**, 179 (2016).

[45] M. Mierzejewski and M. M. Maśka, Phys. Rev. B **73**, 205103 (2006).

[46] D. M. Newns and N. Read, Adv. Phys. **36**, 799 (1987).

Journal of
Applied Physics

Electronic properties of atomic ribbons with spin-orbit couplings on different substrates

Cite as: J. Appl. Phys. **125**, 144301 (2019); https://doi.org/10.1063/1.5080651
Submitted: 10 November 2018 . Accepted: 15 March 2019 . Published Online: 08 April 2019

Marcin Kurzyna, and Tomasz Kwapiński

View Online Export Citation CrossMark

ARTICLES YOU MAY BE INTERESTED IN

Non-orthogonal tight-binding models: Problems and possible remedies for realistic nano-scale devices
Journal of Applied Physics **125**, 144302 (2019); https://doi.org/10.1063/1.5056178

Terahertz waveform considerations for nonlinearly driving lattice vibrations
Journal of Applied Physics **125**, 144101 (2019); https://doi.org/10.1063/1.5052638

Microwave-assisted reversal of a single electron spin
Journal of Applied Physics **125**, 142801 (2019); https://doi.org/10.1063/1.5064593

Applied Physics Reviews
Now accepting original research
2017 Journal Impact Factor:
12.894

AIP Publishing

© 2019 Author(s).

Journal of Applied Physics ARTICLE scitation.org/journal/jap

Electronic properties of atomic ribbons with spin-orbit couplings on different substrates

Cite as: J. Appl. Phys. **125**, 144301 (2019); doi: 10.1063/1.5080651
Submitted: 10 November 2018 · Accepted: 15 March 2019 ·
Published Online: 8 April 2019

Marcin Kurzyna and Tomasz Kwapiński[a)]

AFFILIATIONS

Institute of Physics, M. Curie-Skłodowska University, Pl. M. Curie-Skłodowskiej 1, 20-031 Lublin, Poland

[a)] **Author to whom correspondence should be addressed:** tomasz.kwapinski@umcs.pl

ABSTRACT

Atomic ribbons and monoatomic chains on different substrates are proposed as spin-dependent electrical conductors with asymmetrical local density of states (DOS) and ferromagnetic occupancies along the chains. The tight-binding Hamiltonian and Green's function techniques were used to analyze the electrical properties of both normal and topological systems with spin-orbit scattering. To make the system more realistic, electron leakage from atomic chains to various types of substrates is considered. We have shown that delocalized electrons in the substrate and spin-orbit interactions are responsible for asymmetry in the local DOS. The structure of DOS for spin-orbit nontopological chains is spin-dependent at both chain edges; however, in the middle of the chain, only paramagnetic solutions are observed. Additionally, we have found different periods of the local DOS oscillations along the chain in the presence of spin-flip and spin-orbit couplings. For topological chains, the edge nontrivial states split in the presence of spin-orbit scattering and spin-dependent Friedel oscillations appear along the whole topological chain. We have also found out-of-phase Friedel oscillations between neighboring chains along the atomic ribbon.

Published under license by AIP Publishing. https://doi.org/10.1063/1.5080651

I. INTRODUCTION

The electron transport properties of atomic chains have been the subject of many theoretical and experimental papers mainly due to their potential applications in nanoelectronics and quantum computing. Modern experimental techniques make it possible to fabricate one-atom thick ribbons or atomic chains, which are the thinnest possible electric wires.[1–4] Semiconductor nanochains are good candidates for application in electronic nanodevices like logic gates or field effect transistors.[5,6] Such quasi-one-dimensional systems reveal many interesting effects like conductance quantization,[7,8] conductance oscillations,[9,10] photon-assisted tunneling,[11,12] Friedel oscillations and charge density waves,[13,14] spin-charge separation,[15] and others. Chains with spin-orbit interactions coupled with the superconductor electrode can reveal nontrivial topological phases with Majorana zero modes[16–18] at both chain ends. Similarly, spinless topological states were predicted in the Su-Schriffer-Hegger (SSH) model describing an atomic lattice with stagger hopping integrals.[19–22] The SSH system is characterized by two different phases (with or without topological end states), which are topologically distinct. These states are protected against external disturbances.[23] The experimental realization of the SSH model is based on optical lattices or on the real atomic lattice (with vacancies) in a chlorine monolayer surface.[20,24]

Freely suspended chains of metallic atoms fabricated, e.g., in the mechanically break junction method[9,25] are relatively short and can easily break, which make these structures useless from the practical point of view. On the other hand, very stable atomic chains can be grown epitaxially on reconstructed silicon surfaces [like Si(335), Si (557), or others].[1–4,26] Such single atomic chains or atomic ribbons are coupled with the surface leading to electron leakage to the substrate states and asymmetry in the density of states (DOS).[27,28] Thus, electron localization in the substrate can significantly modify electronic properties of atomic ribbons. Particularly interesting are low-dimensional conductors with spin–orbit coupling,[29–32] where spin-polarized currents can appear (local asymmetric confinement of electrons leads to spin–orbit coupling of Rashba type[33,34]). The asymmetrical potential produces the precession of electron spins, which is responsible for spin-flip scattering between neighboring sites in the ribbon. Phonon interactions, magnetic impurities, or nuclear spins can lead to the on-site spin-flip processes.[35] Although there are many papers on the spin-orbit systems, very little attention has been paid to investigate the role of the substrate coupled with spin-orbit chains, where the electron localization effects can be very important. It makes the model more realistic and interesting as the chain-substrate systems reveal new physical properties (superradiant states, asymmetry in DOS, and ferromagnetic occupancies). They can be useful in spintronics, e.g., as spin–orbit qubits, spin pumps, or basic elements of spin transistors.[30,36] The spin-orbit coupling strength can be experimentally tuned by external gates and can lead to oscillatory behavior of the ballistic spin conductance.[32,37]

In this paper, we are focusing on the electrical properties of normal and topological atomic chains (ribbons) on different substrates taking into account the spin-orbit scattering. Electron localization in the substrate introduces asymmetry in DOS (Dicke-like effect) but does not mix spin states. On the other hand, the spin-orbit interactions break spin symmetry in the system and thus, it is a great challenge to investigate electrical properties of atomic ribbons in the presence of both surface scattering and spin-orbit couplings. They together can lead to paramagnetic or ferromagnetic solutions with nonsymmetrical spin-dependent DOS and asymmetrical (or irregular) electron occupancies along the atomic ribbon. In our calculations, we consider the spatial separation of atoms and use the substrate model, which allows us to consider the insulator (strongly localized electrons in the substrate), the semiconductor, as well as metallic surfaces (delocalized electrons in the substrate).[27,38] We analyze the asymmetry in the local DOS, DOS at the Fermi level, and the electron occupancies along the system for normal and SSH topological chains. The results of this paper give some insight into the physics of end states, charge density waves (CDW), Friedel oscillations, and topological states in quasi-1D systems. The careful inspection of the local DOS (which is possible using spin-polarized STM), topological states, or charge waves can provide useful information about the hopping amplitudes, on-site single-electron energies, and the ribbon geometry. In our studies, we propose long atomic chains on a substrate as a memory storage device fully controlled by the surface and spin-orbit coupling parameters.

The paper is organized as follows. In Sec. II, we describe the theoretical model and the calculation method for the tight-binding Hamiltonian. In Sec. III, the main results of the paper are discussed: for short atomic systems (Sec. III A), for normal and SSH single atomic chain (Secs. III B–III D), and for coupled chains (ribbons), (Sec. III E). Section IV gives a short summary.

II. MODEL AND THEORETICAL DESCRIPTION

The elementary system we consider in this paper is schematically shown in Fig. 1. It consists of M linear atomic chains (each composed of N sites, red balls) coupled with the substrate electrode. The system corresponds to atomic ribbons, which can be fabricated on stepped-like, vicinal surfaces.[1,4] The model tight-binding Hamiltonian for this system includes the spin-flip and spin–orbit couplings and can be written in the following form: $H = H_0 + H_{so}$, where

$$H_0 = \sum_{\sigma} \left(\sum_{i=1}^{N \cdot M} \varepsilon_{i\sigma} a_{i\sigma}^{+} a_{i\sigma} + \sum_{\vec{k}} \varepsilon_{\vec{k}\sigma} c_{\vec{k}\sigma}^{+} c_{\vec{k}\sigma} + \sum_{\langle i,j \rangle} t_{i,j} a_{i\sigma}^{+} a_{j\sigma} + \sum_{\vec{k},i} V_{i\sigma,\vec{k}\sigma} a_{i\sigma}^{+} c_{\vec{k}\sigma} + \text{h.c.} \right), \tag{1}$$

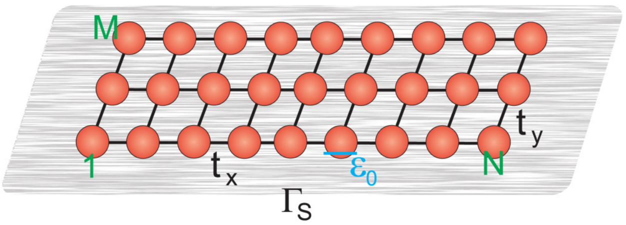

FIG. 1. Schematic view of the system under consideration: M rows of N-site linear chains (red circles) on a surface electrode. The parameters t_x, t_y, Γ_S describe the couplings between appropriate electron states along every chain, between chains, and the hybridization between the ribbon and substrate states, respectively, and ε_0 corresponds to the on-site electron energy.

describes the on-site electron energies in the atomic ribbon, $\varepsilon_{i\sigma}$ ($i = 1, \ldots, N \cdot M$), with spin σ, and the electron energies in the substrate with the wave vectors $\vec{k}$, $\varepsilon_{\vec{k}\sigma}$. The operators $a_{i\sigma}(a_{i\sigma}^{+})$ annihilate and create an electron with spin σ at the i-th site, and $c_{\vec{k}\sigma}(c_{\vec{k}\sigma}^{+})$ are the according substrate operators (related to the substrate Bloch states). Electron transition between neighboring states in the ribbon is described by $t_{i,j}$ elements (here $\langle i, j \rangle$ means the summation over the neighboring sites) and for regular chains, like, e.g., Pb atoms on Si(111) vicinal surfaces, this parameter is spin and position independent and we can write $t_{i,i\pm1} = t_x$ (along each chains) and $t_{i,i\pm N} = t_y$ (between chains). For nonuniform couplings, along the chains, $t_{i,j}$, e.g., for different every second couplings, the system corresponds to the topological SSH chain[19,21] which will be considered later. The last term of H_0 represents electron hybridization of the ribbon states with the substrate Bloch states which in general depends on site positions, R_i (i.e., spatial separation of atoms are considered): $V_{i\sigma,\vec{k}\sigma} = V_{\vec{k}} \exp(ikR_i)$,[27,38] and here is spin-independent. Thus, the spectral density matrix can be written as follows: $(\hat{\Gamma}_S)_{ij} = 2\pi \sum_{\vec{k}} V_{i,\vec{k}} V_{j,\vec{k}}^{*} \delta(E - \varepsilon_{\vec{k}})$. Assuming that only the substrate electrons close to the Fermi surface play an important role and for equal distances between atomic sites in the ribbon, a, one obtains $(\hat{\Gamma}_S)_{ij} = \Gamma_S \frac{\sin(k_F a r_{ij})}{k_F a r_{ij}}$, where $\Gamma_S = (\hat{\Gamma}_S)_{ii} = 2\pi \sum_{\vec{k}} |V_{i,\vec{k}}|^2 \delta(E - \varepsilon_{\vec{k}})$ stands for the effective atom-substrate coupling strength, which in the wide band limit is energy independent. Here, r_{ij} is the distance between two atomic sites in the ribbon, $r_{ij} = |R_j - R_i|$, and is expressed in a units, thus for two sites from the same chain $r_{ij} = |j - i|$, but in general, it should be obtained from the Pythagorean theorem. The parameter $k_F a$ in the above relation is responsible for the electron localization in the substrate. For very small $k_F a$, all elements of the spectral density matrix $\hat{\Gamma}_S$ are position independent and in this case (for $k_F a = 0$), we have $(\hat{\Gamma}_S)_{ij} = \Gamma_S$. In this limit, an electron from the ribbon can flow to the substrate, and then it can appear at the arbitrary site with the same probability. It corresponds to delocalized electron states in the substrate, which is satisfied for metallic-like surfaces. In the opposite limit, for very large value of $k_F a$, the spectral density matrix is diagonal and for $k_F a = \infty$, one finds $(\hat{\Gamma}_S)_{ij} = \Gamma_S \delta_{ij}$. In this case, each ribbon site is coupled effectively to an individual electrode and an electron that tunnels from a particular site to the substrate can re-enter only at the same site. This limit describes localized electrons in the substrate with very short mean-free path, which corresponds to semiconductor or insulator substrates.

The spin–orbit couplings can be effectively modelled by spin-flip hopping terms in a usual tight-binding approach.[17,31,32,34] In this treatment, the spin-orbit Hamiltonian is composed of spin-flip processes at a given site and between neighboring sites and can be written in the following form:

$$\begin{aligned} H_{so} = \sum_{\sigma,\sigma'} \Bigg(& t_{so}^{\parallel} \sum_{\langle i,j\rangle_x} a_{i\sigma'}^{+} (i\hat{\sigma}_x)_{\sigma,\sigma'} a_{j\sigma} \\ & - t_{so}^{\perp} \sum_{\langle i,j\rangle_y}^{N} a_{i\sigma'}^{+} \left(i\hat{\sigma}_y\right)_{\sigma,\sigma'} a_{j\sigma} \Bigg) + \sum_{i,\sigma} t_{sf} a_{i\sigma}^{+} a_{i-\sigma} + \text{h.c.}, \end{aligned} \tag{2}$$

where $\hat{\sigma}_{x/y}$ are the Pauli matrices and $\sum_{\langle i,j\rangle_x}$ corresponds to summation over the neighboring sites within a given atomic chain, and $\sum_{\langle i,j\rangle_y}$ between neighboring sites from different atomic chains.

Here, we consider the system where many-body effects (like the Kondo effect) do not play an important role and they can be omitted in the Hamiltonian. In this sense, the electron-electron interactions is captured by an effective shift of the on-site energies, $\varepsilon_{i\sigma}$, which is reasonably well satisfied for many atoms (like Au, Ag, In, or Pb) on vicinal silicon surfaces.[4,27] In our calculations, we concentrate on the local DOS at a given site, the local DOS at the Fermi level, and the electron occupancies along the ribbon. These quantities can be found from the knowledge of retarded Green functions, $G_{i,j}^{r}$, corresponding to the appropriate ribbon sites. Using the equation of motion for retarded Green's function[39] together with the Hamiltonian one can obtain $2(N \cdot M)$ linear-dependent equations for the retarded Green's function elements, $G_{ij}^{r}(E)$. They can be written in the matrix notation $\hat{G}^r \cdot \hat{C} = \hat{I}$, where $\hat{I}$ is the identity matrix and $\hat{C}$ is a square $(2N \cdot M) \times (2N \cdot M)$ complex array, which inverse stands for the Green's function. This function can be obtained from the relation $\hat{G}^r = \mathtt{cof}\,\hat{C}/\det \hat{C}$, where $(\mathtt{cof}\,\hat{C})_{ij}$ is the (i, j) cofactor of $\hat{C}$ matrix. From the knowledge of retarded Green's function, we obtain the local DOS (LDOS) at the i-th site, $LDOS_i(E) = -\frac{1}{\pi}\Im G_{i,i}^{r}(E)$, and the electron occupancy $n_i = \int_{-\infty}^{E_F} LDOS_i(E)dE$.

Now, we specify $\hat{C}$ matrix corresponding to coupled atomic chains on the substrate. It can be written in the following form:

$$\hat{C} = \begin{bmatrix} \hat{A}^{\sigma}(E) & \hat{D}^{\sigma,-\sigma} \\ \hat{D}^{-\sigma,\sigma} & \hat{A}^{-\sigma}(E) \end{bmatrix}. \tag{3}$$

Each submatrix of $\hat{C}$ has a dimension of $(N \cdot M) \times (N \cdot M)$. Let us first describe diagonal matrices of $\hat{C}$, $\hat{A}^{\pm\sigma}(E)$. They are composed of the following submatrices:

$$\hat{A}^{\sigma}(E) = \begin{bmatrix} \hat{B}_{I,I} & \hat{B}_{I,II} & \hat{B}_{I,III} & \\ \hat{B}_{II,I} & \hat{B}_{II,II} & \hat{B}_{II,III} & \\ & & \ddots & \\ \hat{B}_{M,I} & \hat{B}_{M,II} & & \hat{B}_{M,M} \end{bmatrix}, \tag{4}$$

where $\hat{B}_{\alpha,\beta}$ concerns the square matrix related to all sites from α and β rows $(\alpha, \beta = I, II, \ldots, M)$ with spin σ [or with spin $-\sigma$ for $\hat{A}^{-\sigma}(E)$ matrix]. For $\alpha = \beta$, it takes the following form:

$$\left(\hat{B}_{\alpha,\alpha}\right)_{i,j} = (E - \varepsilon_i)\delta_{i,j} - t_{i,j+1}(\delta_{i,j+1} + \delta_{i+1,j}) + i\frac{(\hat{\Gamma}_S)_{ij}}{2}. \tag{5}$$

For the neighboring α indexes (upper and lower diagonal submatrices of $\hat{A}$), $\hat{B}$ can be written as follows: $\left(\hat{B}_{\alpha,\alpha\pm1}\right)_{i,j} = -t_y\delta_{i,j\pm M} + i\frac{(\hat{\Gamma}_S)_{ij\pm M}}{2}$, and for other indexes: $\left(\hat{B}_{\alpha,\beta}\right)_{i,j} = i\frac{(\hat{\Gamma}_S)_{ij}}{2}$. Now, we describe off-diagonal elements of $\hat{C}$ matrix, which are related with the spin-orbit couplings (electron states with different spins), $\hat{D}^{\sigma,-\sigma}$. In general, this matrix is tri-diagonal and is composed of $\hat{E}$ submatrices

$$\hat{D}^{\sigma,-\sigma} = \begin{bmatrix} \hat{E}_{I,I} & \hat{E}_{I,II} & 0 & \\ \hat{E}_{II,I} & \hat{E}_{II,II} & \hat{E}_{II,III} & \\ & & \ddots & \\ 0 & 0 & & \hat{E}_{M,M} \end{bmatrix}, \tag{6}$$

where the diagonal submatrices describe spin-flip and spin-orbit couplings along the chains and take the form $\left(\hat{E}_{\alpha,\alpha}\right)_{i,j} = -t_{sf}\delta_{ij} - t_{so}^{\parallel}(\delta_{i,j-1} - \delta_{i,j+1})$. The upper and lower diagonal submatrices of the above matrix are related to spin-orbit couplings between chains and are diagonal complex matrices $\left(\hat{E}_{\alpha,\alpha\pm1}\right)_{i,j} = \mp i t_{so}^{\perp}\delta_{i,j\pm1}$. Other elements of $\hat{D}$ are zero. Note that due to complexity of $\hat{A}$, it is difficult to find the short analytical form of $\hat{G}^r$. However, some analytical results exist for the linear geometry of the system (left lead–chain–right lead), where only tri-diagonal matrices appear and their determinates can be expressed by the Chebyshev polynomial of the second kind.[40,41] In this paper, we discuss some analytical calculations for short atomic chains.

III. RESULTS AND DISCUSSION

In our calculations, the temperature is $T = 0$ K, and the energy reference point stands for the Fermi energy of the substrate, $E_F = 0$. It is assumed that each atomic site in the ribbon couples equally strong to the substrate independently on spin, $(\hat{\Gamma}_S)_{ii} = \Gamma_S$, which is the energy unit. Moreover, only regular atomic chains are considered, i.e., the on-site electron energies as well as the intra-chain couplings are position and spin independent, $\varepsilon_{i\sigma} = \varepsilon_0$, $t_{so}^{\parallel} = t_{so}^{\perp} = t_{so}$ and $t_{i,i+1} = t_x$ (between the neighboring sites along each chain) and $t_{i,i+N} = t_y$ (between neighboring sites from different chains). These assumptions are quite reasonable for regular chains consisting of one atom species in an equidistant arrangement on the surface like Pb on the Si(553)/Au substrate. The parameters of the system have been chosen in order to satisfy the realistic situation in many experiments, e.g., assuming $\Gamma_S = 0.25$ eV, the hopping integral along the chain is $t_x = 4 = 1$ eV, between chains is $t_y = 2 = 0.5$ eV, spin-orbit and spin-flip couplings, $t_{so/sf} = 0.1 = 25$ meV, cf. Refs. 4, 27, 32, and 35.

A. Short atomic systems

In this subsection, we analyze the role of the substrate and spin-orbit couplings on the electronic properties of short atomic systems. It allows us to find the main modifications of the local DOS due to spin-orbit couplings and to better understand the properties of larger systems and atomic ribbons.

For a chain composed of two coupled atoms on the substrate, one finds that

$$\hat{A}^{\sigma}(E) = \begin{bmatrix} E - \varepsilon_{1\sigma} + i\frac{\Gamma_{11}}{2} & -t_x + i\frac{\Gamma_{12}}{2} \\ -t_x + i\frac{\Gamma_{21}}{2} & E - \varepsilon_{2\sigma} + i\frac{\Gamma_{22}}{2} \end{bmatrix}, \tag{7}$$

$$\hat{D}^{\sigma,-\sigma} = \begin{bmatrix} -t_{sf} & -t_{so} \\ t_{so} & -t_{sf} \end{bmatrix}, \tag{8}$$

and the determinant of $\hat{C}$ matrix equals $\det\hat{C} = \det\big(\hat{A}^{\sigma} - \hat{D}^{\sigma,-\sigma}(\hat{A}^{-\sigma})^{-1}\hat{D}^{-\sigma,\sigma}\big)\det\hat{A}^{-\sigma}$, where $\det\hat{A}^{\pm\sigma}$ for arbitrary N and no substrate ($\Gamma_S = 0$) can be obtained analytically.[40,41] For $t_{so} = 0$, one can write $\det\hat{C} = \det\Big(\hat{A}^{\sigma} - t_{sf}^2(\hat{A}^{-\sigma})^{-1}\Big)\det\hat{A}^{-\sigma}$. For the case of $t_{sf} = 0$ and $t_{so} \neq 0$, we have $\det\hat{C} = \det\big(\hat{A}^{\sigma} - t_{so}^2\hat{\sigma}_y(\hat{A}^{-\sigma})^{-1}\hat{\sigma}_y\big)\det\hat{A}^{-\sigma}$, and similar relations one can write for the cofactor of $\hat{C}$. Note that for nonzero spin-flip and spin-orbit couplings, one can obtain analytically all Green's function elements but the relations for LDOS or on-site occupancies cannot be written in relatively simple and transparent forms, and thus we skip them in the paper.

In Fig. 2, we consider a two-atom system on a substrate and study the role of the spin-flip and spin-orbit couplings on the local DOS for both spins σ and $-\sigma$ (red solid and blue broken curves, respectively). Such a system for $t_{so} = t_{sf} = 0$ is characterized by two local maxima of LDOS localized exactly at $E = \varepsilon_0 \pm t_x$ (not shown here) and the local DOS is spin-independent in this case. In the presence of the spin-orbit coupling (upper panel), these maxima of LDOS move outside a little and appear at $E = \varepsilon_0 \pm t_x\sqrt{1 + \left(\frac{t_{so}}{t_x}\right)^2}$, but the symmetry of LDOS around $E = \varepsilon_0$ is still visible. For nonzero spin-flip coupling, t_{sf} (and $t_{so} = 0$, middle panel), the structure of LDOS is still spin-independent (red solid and blue broken curves overlap each other) and is symmetrical around $E = \varepsilon_0$, but each maximum of DOS splits into two local peaks separated by $2t_{sf}$. Thus, in this case, one observes four local maxima of LDOS localized at $E = \varepsilon_0 \pm \big(t_x \pm t_{sf}\big)$. Note that for $t_x = t_{sf}$, only three local maxima appear in the structure of LDOS. The situation changes in the presence of both spin-flip and spin-orbit couplings (bottom panel) as in this case, the local DOS at each atomic site depends on spin and in general, $LDOS_{1\sigma}(E) \neq LDOS_{1-\sigma}(E)$. This spin-asymmetry results from the fact that the spin-flip transition between the sites $|1\sigma> \rightarrow |2-\sigma>$ is not the same as for $|1-\sigma> \rightarrow |2\sigma>$ (cf. also $\hat{D}$ matrix). It can also be confirmed analytically: G^r is obtained from the knowledge of $\mathtt{cof}\hat{C}$ and $\det\hat{C}$, here the determinant of $\hat{C}$ is the same for both spins; however, the cofactor of $\hat{C}$ is spin-dependent. For our system, one can obtain that the difference of both cofactors

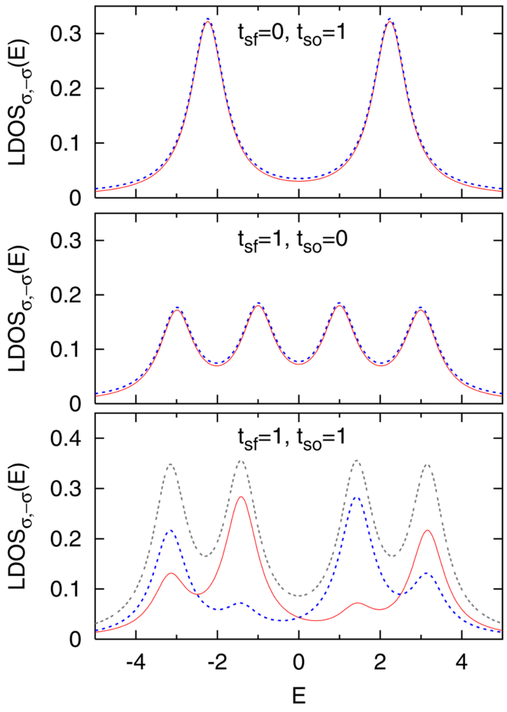

FIG. 2. Local DOS with spin σ and $-\sigma$ (red solid and blue broken lines) at the first atomic site for the system composed of two atoms, $N = 2$, $M = 1$. The upper, middle, and bottom panels correspond to ($t_{sf} = 0$, $t_{so} = 1$), ($t_{sf} = 1$, $t_{so} = 0$), and ($t_{sf} = 1$, $t_{so} = 1$), respectively. The black dotted curve in the bottom panel corresponds to $LDOS_{\sigma}(E) + LDOS_{-\sigma}(E)$. The other parameters are $\varepsilon_0 = 0$, $t_x = 2$, $\Gamma_S = 1$ (energy unit), and $k_F a = 10$.

for spin up and spin down equals

$$\big(\mathtt{cof}\hat{C}\big)_{1\sigma,1\sigma} - \big(\mathtt{cof}\hat{C}\big)_{1-\sigma,1-\sigma} = 4t_{so}t_{sf}\left(t_x + i\frac{\Gamma_{12}}{2}\right). \tag{9}$$

It means that for $t_{sf} = 0$ or $t_{sf} = 0$, there is no difference between both cofactors, and thus the local DOS is spin independent, while for nonzero, both t_{sf} and t_{so}, the cofactor difference leads to spin dependence of LDOS. Note that due to spin-orbit couplings, the local DOS at the second site for a given spin is not the same as at the first site but corresponds to the opposite spin, i.e., $LDOS_{2\sigma}(E) = LDOS_{1-\sigma}(E)$ and $LDOS_{2-\sigma}(E) = LDOS_{1\sigma}(E)$. It is also important that the structure of spin-dependent LDOS is nonsymmetrical vs the Fermi energy, which leads to different occupancies for both spins and will be studied later. However, the total DOS at each atomic site [obtained as $LDOS_{\sigma}(E) + LDOS_{-\sigma}(E)$] is fully symmetrical (black-dotted curve in Fig. 2, bottom panel). The asymmetry in the local DOS structure which appears in the presence of spin-flip and spin-orbit couplings, can be detected using spin-polarized electron leads (e.g., in STM experiments). For a normal STM electrode, where both electron spins are present

Published under license by AIP Publishing.

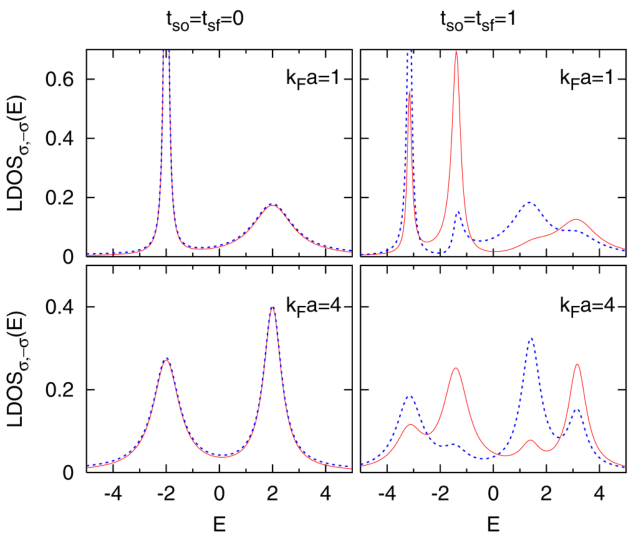

FIG. 3. Local DOS with spin σ and $-\sigma$ (red solid and blue broken lines) at the first atomic site for two-atom system, $N = 2$, $M = 1$, and for $t_{sf} = t_{so} = 0$ (left panels) and $t_{sf} = t_{so} = 1$ (right panels). The upper (bottom) panels correspond to $k_Fa = 1$ ($k_Fa = 4$) and the rest parameters are the same as in Fig. 2.

simultaneously, one cannot distinguish between LDOS signals from each spin and the results are always symmetrical.

Real atomic chains or atomic clusters are often fabricated on different substrates (metallic, semiconductor, or insulator), thus it is desirable to investigate the role of the k_Fa parameter on the local DOS in the presence of spin-flip and spin-orbit couplings. In Fig. 3, we show the local DOS for both spins at the first atomic site for small k_Fa (upper panels) and for larger k_Fa (bottom panels). Additionally, we consider the system with the spin-orbit couplings (right panels) and for $t_{sf} = t_{so} = 0$ (left panels). In the last case, the LDOS curves are spin-independent. As one can see for small value of k_Fa, the structure of LDOS is nonsymmetrical for both $t_{sf} = t_{so} = 0$ and $t_{sf} = t_{so} = 1$. This asymmetry is a hallmark of the Dicke effect predicted in quantum optics and related to the spontaneous emission of two close-lying atoms radiating a photon into the same environment.[42] In our case, both atomic sites are coupled with continuum states of the substrate and the spectral functions of these atoms are characterized by two peaks: a wide Lorentz-like peak and a very narrow Dicke peak, see also Refs. 28 and 43. For $t_{sf} = t_{so} = 0$ (left panels), LDOS asymmetry vanishes with increasing k_Fa. For $k_Fa = 4$, LDOS is still asymmetrical but for fully localized electrons in the substrate, $k_Fa \to \infty$, the structure of LDOS is perfectly symmetrical as in this case $(\hat{\Gamma}_S)_{ij} = \delta_{ij}\Gamma_S$. In the presence of spin-flip and spin-orbit couplings, $t_{sf} = t_{so} = 1$, one observes that each LDOS peak splits (cf. the left and right panels). Moreover, the results are spin-dependent even for larger values of k_Fa (see also Fig. 2, bottom panel obtained for $k_Fa = 10$).

The results analyzed in this subsection indicate that there are two reasons for asymmetry in LDOS for atomic systems: localized electrons in the substrate and spin-orbit couplings. The former is spin-independent, and the latter depends on spins. Thus, it is interesting to consider these effects for larger systems taking into account partially localized substrate electrons in the presence of spin-flip and spin-orbit couplings which we study below.

B. Atomic chains on different substrates

In small atomic systems, in the absence of spin-orbit couplings, we have observed strong asymmetry in LDOS for delocalized electrons in the substrate and almost symmetric LDOS for localized surface electrons. On the other hand, for nonzero spin-orbit couplings, the local DOS curves are always nonsymmetrical for both regimes of the k_Fa parameter. In this subsection, we study how the surface electrons modify the structure of LDOS for regular atomic chains taking into account the system with and without spin-flip and spin-orbit couplings.

In Fig. 4, we analyze the local DOS at the middle site of the atomic chain composed of 50 sites for different values of k_Fa and for $t_{so} = t_{sf} = 0$. For small k_Fa (upper curve), one observes large number of LDOS peaks related to N sites, but the structure of LDOS is nonsymmetrical. For larger, intermediate k_Fa (partially localized electrons), these LDOS peaks are still visible for negative energies, and for positive ones, the LDOS curve is smoother. Finally, the structure of LDOS is characterized by a single Dicke-like peak and a wide smooth background (for $k_Fa = 3$)—such a structure is similar to that one obtained for $N = 2$ (Fig. 3, left upper panel). For larger and larger k_Fa, the Dicke peak vanishes and the local DOS is symmetrical with no localized peaks (bottom curve). The appearance of peaked-like DOS together with the smooth DOS for the intermediate values of k_Fa influences the electron occupations along the chain and will be studied later.

Note that in the absence of spin-orbit couplings, the LDOS curves are spin-independent for all atomic sites in the chain. The situation can change for nonzero t_{so} and t_{sf} parameters. Thus, in Fig. 5, we consider atomic chains with the spin-flip and spin-orbit

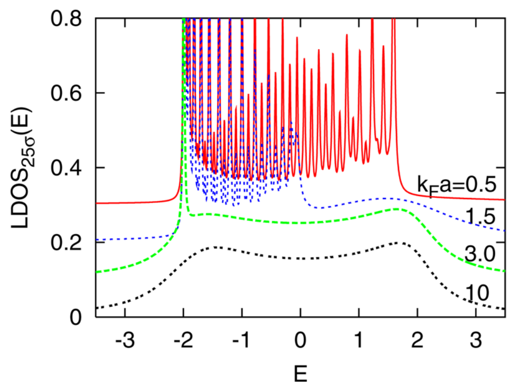

FIG. 4. Local DOS at the middle atomic site $i = 25$ for the chain length $N = 50$ and for different values of k_Fa as is indicated in the legend. The other parameters are $t_{sf} = 0$, $t_{so} = 0$, $t_x = 1$, $\varepsilon_0 = 0$ and the curves for $k_Fa = 3$, 1.5, 0.5 are shifted by 0.1, 0.2, and 0.3, respectively, for better visualization.

Published under license by AIP Publishing.

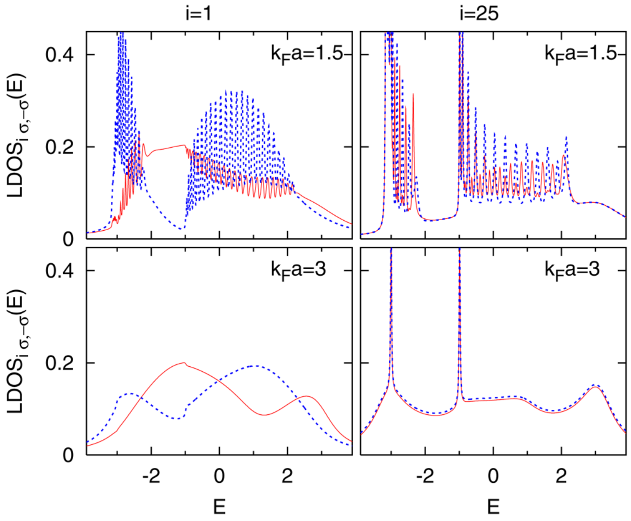

FIG. 5. Local DOS at the chain end, $i = 1$ (left panels) and at the middle atomic site $i = 25$ (right panels) for the chain length $N = 50$ and for $k_Fa = 1.5$ (upper panels) and $k_Fa = 3$ (bottom panels). The solid (red) and broken (blue) lines correspond to LDOS for spin σ and $-\sigma$, respectively. The other parameters are the same as in Fig. 4, $t_{sf} = 1$, $t_{so} = 1$.

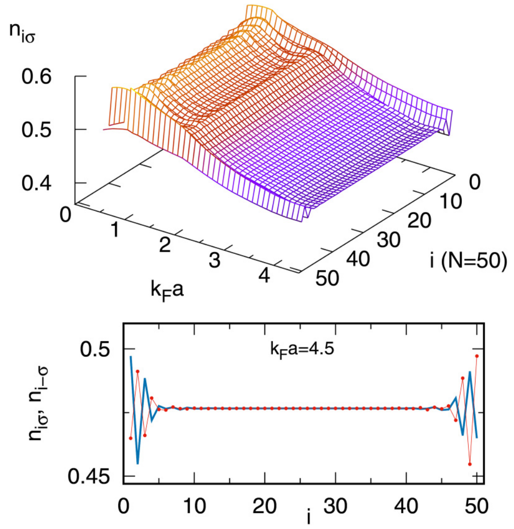

FIG. 6. Charge occupations, $n_{i\sigma}$, along the chain, $N = 50$, as a function of k_Fa parameter and $t_{sf} = t_{so} = 0.5$, $t_x = 1$, $\varepsilon_0 = 0$. The bottom panel shows $n_{i\sigma}$ (solid blue curve) and $n_{i-\sigma}$ (red dots) for $k_Fa = 4.5$.

couplings and investigate the role of electron localization in the substrate on the local DOS. We show the results for $k_Fa = 1.5$ (upper panels) and $k_Fa = 3$ (bottom panel) and analyze the structure of LDOS at the chain end ($i = 1$, left panel) and in the middle of the chain ($i = 25$, right panels). As one can see the structure of the local DOS is asymmetrical and splits, leading to a wider energy region of nonzero LDOS with two spin-degenerate Dicke peaks for intermediate k_Fa parameter (separated by $2t_{sf}$), right bottom panel. More important, the local DOS is almost spin-independent, blue and red curves overlap (right panels). It is in contrast to our previous results from Fig. 3 for the two-atom system and nonzero t_{so} and t_{sf}. To study this problem in a wider context, we also plot the local DOS at the first chain site for both spins (left panels) and find that at both chain ends, the electron spectral function depends on spin. Moreover, this function does not reveal Dicke peaks and is nonsymmetrical. Thus, we have found that in the presence of the spin-flip and spin-orbit couplings, both chain ends show spin-dependent DOS characteristics, whereas in the middle of the chain, only paramagnetic solutions are realized with almost spin-independent local DOS. This feature of linear atomic chains on a substrate has a strong influence on their electrical properties and suggests that the nonmagnetic chain can be spin polarized. However, spin-memory cells can be localized only at both chain ends.

C. Charge distribution and LDOS oscillations

The structure of LDOS analyzed in Sec. III B is crucial for electron occupations of atomic sites, which are related to spin-polarized charges and spin-transport properties.[41,44] To corroborate the existence of spin-dependent occupancies at both chain ends in Fig. 6, we study electron charges along the chain composed of $N = 50$ sites as a function of the electron localization parameter, k_Fa. As one can see for small k_Fa, the occupancies increase because the local DOS peaks move below the Fermi energy, cf. Fig. 4. Then, one observes two local maxima of $n_{i\sigma}$, which are related to the split structure of LDOS showed in Fig. 5, right panels, with two Dicke-like peaks. For larger k_Fa, the local DOS is smoother and smoother and the site occupancies monotonically decrease. Note that the Friedel oscillations with the period of two atoms appear only at both chain ends. These oscillations decrease with k_Fa and are not observed in the middle of the chain, as expected.

It is worth noting that without spin-flip and spin-orbit couplings, charge distribution along the chain is always symmetrical, i.e., $n_{i\sigma} = n_{N-i+1\sigma}$. However, in the presence of the spin-orbit couplings (Fig. 6), the occupancies along the chain are different at both chain ends and $n_{i-\sigma} = n_{N-i+1\sigma}$. This effect is analyzed in the bottom panel, where we show the occupancies for both spins at each atomic site. The asymmetry in $n_{i\sigma}$ along the chain is related to the nonsymmetrical structure of the local DOS in the presence of the spin-flip and spin-orbit couplings. As a main feature of our atomic chain, we have found that the occupancies along the system are spin-dependent only at both chain ends, where spin-dependent Friedel oscillations appear. In the middle of the chain, the occupancies are spin-independent and only paramagnetic solutions are observed, $n_{i\sigma} = n_{i-\sigma}$. Thus, only chain ends can store spin-dependent information.

The oscillations of occupancies along the chain should be also reflected in the structure of the local DOS at the Fermi level, which is often measured in the STM experiments. Thus, in Fig. 7, we study the local DOS along the atomic chain composed of $N = 50$ linear sites for different spin-flip and spin-orbit parameters. In the

Published under license by AIP Publishing.

upper panel, we consider $t_{sf} = 0$ and show the results for $t_{so} = 0.1$ and 1. The local DOS is characterized by a relatively flat structure with even-odd Friedel oscillations at both chain ends, which are more evident for larger t_{so} (broken curve). The situation changes in the presence of nonzero spin-flip parameter, t_{sf} (and for $t_{so} = 0$), middle panel. Note that the t_{sf} parameter is responsible for splitting of the local DOS peaks, which can effectively change the positions of the on-site energies, ε_0. Thus, for small t_{sf}, the modified even-odd oscillations are visible along the chain (middle panel, lower curve). For larger t_{sf}, the positions of split LDOS peaks move and they can satisfy the condition for the conductance oscillations.[44] The period of these oscillations is determined by the relative position of the effective on-site energy levels, ε_{eff}, the Fermi energy, E_F, and the coupling parameters: $\cos\left(\frac{\pi l}{m}\right) = \frac{E_F - \varepsilon_{eff}}{2t_x}$, where m is the oscillation period and $l = 1, \ldots, m-1$. Here, for $t_{sf} = 1$, regular nonvanishing DOS oscillations with the three-atom period are observed as in this case, a single atomic site is characterized by two LDOS peaks at $E = \pm t_{sf}$, and for $t_{sf} = t_x$, it corresponds to the condition for the conductance oscillations with the period of 3 atoms ($\varepsilon_{eff} = \pm t_x$). For larger t_{sf}, the oscillation amplitude changes and LDOS oscillations become irregular. In the presence of both spin-flip and spin orbit couplings (bottom panel), one observes slightly even-odd oscillations for small t_{so}, t_{sf} (solid red curve), and regular oscillations of LDOS with the period of about 6 atoms for larger couplings (broken blue curve). This period comes from a superposition of the even-odd period (upper panel, $m = 2$) and the three-atom period (middle panel, $m = 3$) indicated by the blue-dotted curves. Note that all curves from the upper and middle panels are fully symmetrical along the chain, but for nonzero spin-orbit and spin-flip couplings (bottom panel), the local DOS along the chain depends on the electron spin and is non-symmetrical, which is especially visible at both chain ends (cf. also the asymmetry in Fig. 2 for the two-atom system). For strongly localized electrons in the substrate, $k_F a \to \infty$, the local DOS oscillations along the chain vanish leading to only small even-odd oscillations at both chain ends. The above results show that the spin-orbit and spin-flip scattering can effectively modify charge distribution (periods and amplitudes) along the chain.

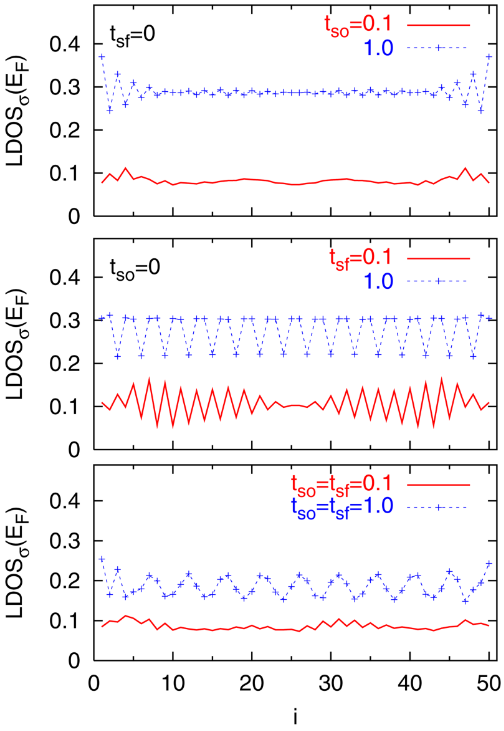

FIG. 7. Local DOS at the Fermi level along the atomic chain composed of $N = 50$ sites for ($t_{sf} = 0$ and $t_{so} = 0.1$, 1.0—upper panel), ($t_{so} = 0$ and $t_{sf} = 0.1$, 1.0—middle panel) and ($t_{sf} = t_{so} = 0.1$ and 1.0 —bottom panel), solid red and broken blue lines, respectively. The other parameters are the same as in Fig. 4, $k_F a = 1$. The upper curves in all panels (broken blue) were shifted by 0.2 (upper and middle panels) and 0.1 (bottom panel) for better visualization.

D. SSH spin-orbit chains

In this subsection, we consider the SSH chain in the topological phase with the spin-orbit and spin-flip couplings. We expect that paramagnetic occupancies inside the chain as well as charge distribution along the chain will be enhanced in the presence of topological end states. Topological states in the SSH model appear at both chain ends for different (but regular) couplings along the chain—here, we set $t_{i,i+1} = 2$ (for odd i) and $t_{i,i+1} = 4$ (for even i), which in the short form can be written as $t_x = (2, 4)$. It leads to the energy gap inside the chain for the energy region $E = \varepsilon_0 \pm 2$.

In Fig. 8, we analyze the local DOS at the first atomic site of the chain and compare these results with the corresponding ones for the middle site of the chain, left and right panels, respectively. As one can see for no spin-flip and spin-orbit couplings, the chain is characterized by a topological state at the first atomic site which is spin-independent (left upper panel, solid red and broken blue curves) or by an energy gap in the local DOS inside the chain (right upper panel). It is worth mentioning that in the literature, the SSH chain is mostly considered in the linear geometry (the chain is coupled with the left electrode via the first atomic site and with the right one via the last site). In such a configuration, the local DOS exhibits strong oscillating (peaked) structure —see the broken black curves in the upper panels, but the topological state at $i = 1$ as well as the energy gap inside the chain appear for the same energies. For the geometry considered in this paper, each atomic site of the chain is coupled with the surface and their spectral functions are more smoother than for the mentioned linear geometry. Note very symmetrical structures of LDOS around $E = \varepsilon_0$ for both configurations as we consider here almost localized electrons in the substrate.

In the presence of the spin-flip and spin-orbit couplings in the SSH chain, bottom panels, the local DOS is spin-dependent (the solid red and broken blue curves do not cover each other) and the symmetry of the local DOS is broken. One should notice that the topological state at the first atomic site (which appears in the middle of the energy gap region) splits leading to asymmetry in LDOS and two local maxima are observed (left bottom panel). Thus, one should observe ferromagnetic occupancies at both ends of the SSH chain.

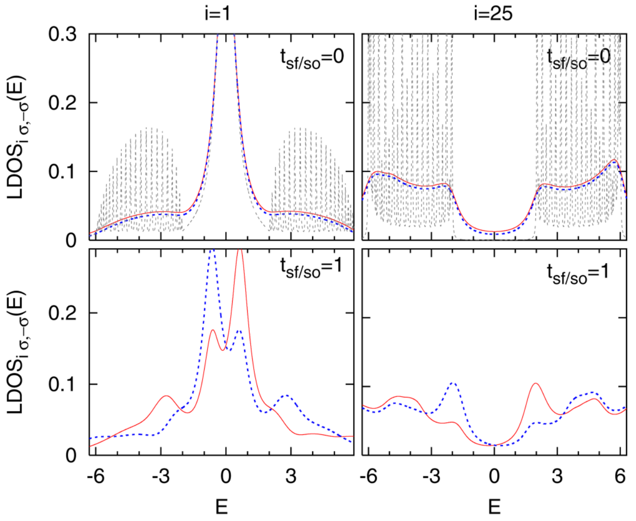

FIG. 8. Local DOS at the chain end, $i = 1$ (left panels) and at the middle atomic site $i = 25$ (right panels) for the chain length $N = 50$ and for $t_{sf} = t_{so} = 0$ (upper panels) and $t_{sf} = t_{so} = 1$ (bottom panels). The couplings are site-dependent and $t_{i,i+1} = 2$ (for odd i) and $t_{i,i+1} = 4$ (for even i), $k_F a = 10$, $\varepsilon_0 = 0$. Spin σ $(-\sigma)$ is represented by the solid red (broken blue) lines and the black broken curves in the upper panels correspond to the system geometry with the chain coupled only with the left and right electrodes (via the first and the last site, respectively).

However, for the SSH chain, all sites are characterized by nonsymmetrical LDOS (cf. right bottom panel for $i = 25$), which leads to spin-polarized solutions inside the chain.

To corroborate this effect, we obtain the electron occupancies along the SSH chain (bottom panel in Fig. 9) and compare them with the occupancies for the normal chain (upper panel). Note that for no spin-flip and spin-orbit couplings, the occupancies do not depend on spin (only paramagnetic solutions are realized) and do not depend on the chain topology (see the blue-dotted curve in the bottom panel obtained for the SSH chain for $t_{sf} = t_{so} = 0$). In the presence of the spin-orbit terms, spin-polarized occupancies are possible. However, in normal chains (upper panel), paramagnetic occupancies dominate inside the chain and only both chain ends are spin-polarized. The situation changes for topological SSH chains, where we observe oscillations of the electron occupancies along the whole chain (bottom panel). It is very important in the context of the Friedel oscillations, which are strongly dumped in the SSH chains due to an energy gap at the Fermi level.[23] However, in our case, for spin-orbit SSH chains, we have found spin-dependent (and nondumped) oscillations of $n_{i\sigma}$. These oscillations are very regular inside the chain with some disturbances at both chain ends, where topological states are localized. Moreover, the occupancies are spin-polarized along the whole SSH chain, which was not observed for normal chains, and they are asymmetrical, $n_{i\sigma} = n_{(N-i+1)-\sigma}$. It is interesting that although we observe oscillations of $n_{i\sigma}$ and $n_{i-\sigma}$ along the chain the average electron occupancies at each site, $(n_{i\sigma} + n_{i-\sigma})/2$,

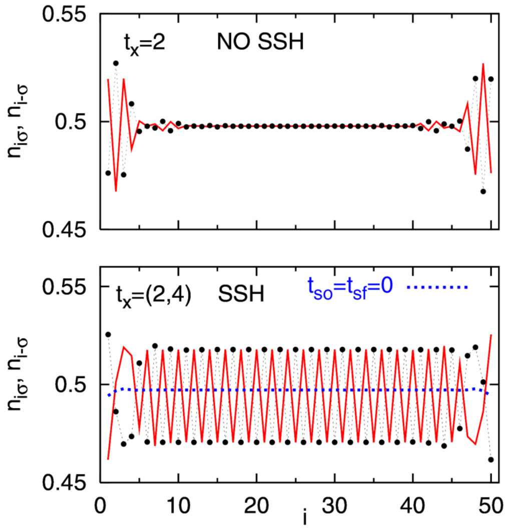

FIG. 9. Spin-dependent occupancies, $n_{i\sigma}$ (red solid curves) and $n_{i-\sigma}$ (black broken curves with circles), obtained for nontopological chain ($t_x = 2$, upper panel) and for the SSH chain [$t_x = (2, 4)$, bottom panel]. The other parameters are $t_{sf} = t_{so} = 1$, $k_F a = 10$, $\varepsilon_0 = 0$, $N = 50$. The dotted blue curve in the bottom panel corresponds to $t_{sf} = t_{so} = 0$.

do not oscillate at all and overlap with the blue line for $t_{sf} = t_{so} = 0$ in the bottom panel. It means that spin-dependent Friedel oscillations in the SSH chain can be detected using spin-polarized external electrodes. The results described above allow one to control chain polarization by means of spin-orbit parameters or by means of topology parameters (the coupling strengths). In this sense, we can use such SSH chains to store and control quantum information in 1D atomic systems.

E. Atomic ribbons

Single atomic chains are the thinnest possible electric wires but are prone to external perturbations or defects and can be unstable. More solid structures on the substrate are coupled atomic chains. In this section, we analyze LDOS oscillations along atomic ribbons on different surfaces with the spin-orbit and spin-flip couplings. First, we consider two-chain ribbon for $t_{sf} = t_{so} = 0$ (upper panel in Fig. 10). As one can see, for decoupled chains in the ribbon, $t_y = 0$, the Friedel even-odd oscillations of LDOS are visible at both chain ends; however, for coupled chains, $t_y = 1$, the local DOS oscillates with the period of three sites. In the last case, nonzero couplings between chains lead to renormalization of the on-site energies at atomic sites and if these effective energies satisfy the condition on the conductance oscillations, one observes the oscillations of LDOS along the chain with the same period as the conductance oscillations.[44] Of course, the spin-orbit as well as the spin-flip couplings also change the energy of on-site states and split these states, which can modify the oscillation period of LDOS. Such a case is shown in the middle panel for two-chain ribbon in the presence of spin-flip coupling (blue broken curve with crosses)

Published under license by AIP Publishing.

or in the presence of spin-orbit coupling (pink-dotted curve with rectangles). In the former case ($t_{sf} \neq 0$, $t_{so} = 0$), the on-site electron energies are split leading to oscillations of LDOS with the period of 5–6 atomic sites, whereas in the latter case (for $t_{so} \neq 0$, $t_{sf} = 0$), the energies of atomic states move in the energy scale and their new positions generate the oscillations period of 4 sites in the system. The most interesting case is shown in the bottom panel in Fig. 10, where we analyze the local DOS along the double-chain ribbon in the presence of both spin-flip and spin-orbit couplings. Now, the oscillation period of LDOS is a combination of the periods from the middle panel and equals about 15 atomic sites. It is worth noting that the local DOS along the ribbon is the nonsymmetrical function only in the last case, i.e., for $t_{sf} \neq 0$, $t_{so} \neq 0$ (bottom panel). For other cases, all LDOS curves are fully symmetrical along the ribbon and are spin-independent. We have shown that the period and the intensity of the LDOS oscillations along the atomic ribbon can be controlled by coupling parameters.

The results shown in Fig. 10 were obtained for only one (intermediate) $k_F a$ parameter. In our further studies, we are going to investigate the role of the electron localization in the substrate on the LDOS oscillations along the atomic ribbon. Thus, in Fig. 11, the local DOS along the double-chain ribbon is shown as a function of the electron localization parameter, $k_F a$, in the presence of both spin-orbit and spin-flip couplings. One can distinguish here two regimes of $k_F a$. For small value of this parameter (delocalized electrons in the substrate) the local DOS changes irregularly with i but for somewhat larger values of $k_F a$, the oscillations become very regular with the period of about 15 sites (cf. also the bottom panel in Fig. 10). The appearance of almost flat and site-independent LDOS(E_F) for larger $k_F a$ is related with modifications of the spectral density function due to the presence of the substrate which was analyzed in Figs. 4 and 5 for a single atomic chain. In that case the corresponding local DOS becomes flat around the Fermi energy, which makes the system less interesting for potential applications.

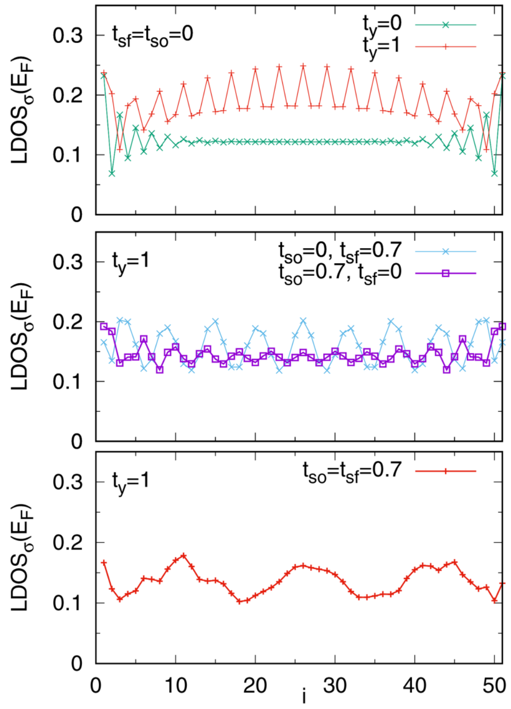

FIG. 10. Local DOS at the Fermi level along coupled atomic chains ($N = 51$, $M = 2$) for $t_{sf} = t_{so} = 0$ (upper panel), and the coupling between chains, $t_y = 0$ (green broken curve) or $t_y = 1$ (red solid curve). The middle and bottom panels correspond to the coupled chains, $t_y = 1$, and different combinations of t_{sf} and t_{so} parameters: 0 or 0.7, as is indicated in the legend, $k_F a = 2$, $t_x = 1$, $\varepsilon_0 = 0$.

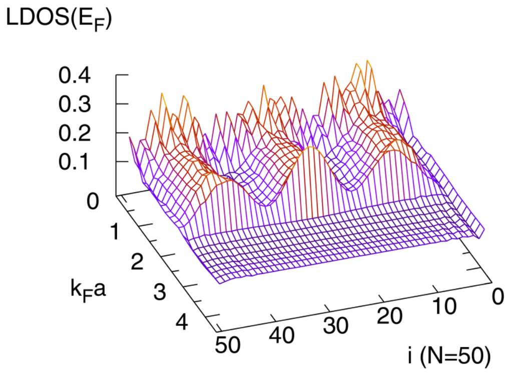

FIG. 11. Local DOS at the Fermi level along two coupled atomic chains ($N = 51$, $M = 2$, $t_y = 1$) as a function of the $k_F a$ parameter for $t_{sf} = t_{so} = 0.7$. The other parameters are the same as in Fig. 10.

In the last studies of this paper, we consider a wider atomic ribbon and analyze three coupled chains on a substrate. For two coupled chains, the results along the first or the second chain were always the same. For wider ribbons, we expect that the results can differ from row to row of atoms. In Fig. 12, we consider a ribbon composed of three coupled chains, $t_y = 1$, for very small spin-orbit coupling, $t_{sf} = t_{so} = 0.1$ (upper panel), and for $t_{sf} = t_{so} = 0.2$ and 0.5 (middle and bottom panels). For the chosen set of parameters, the local DOS oscillates with the period of 4-sites with a relatively large amplitude (upper panel). Moreover, these oscillations are exactly the same for rows I and III (red solid line and black dots) and slightly differ for row II (larger oscillation amplitude). Note that the minima and maxima of the local DOS oscillations are in phase for each atomic row. For somewhat larger spin-orbit couplings (middle panel), the oscillations of LDOS become irregular but still they are in phase for considered rows of atoms. For larger spin-orbit couplings (bottom panel), the oscillation amplitudes decrease and regular oscillations are still visible, but more important, the results for the middle chain and for both side chains are out of phase, i.e., the minima of LDOS for row II correspond to maxima of I and III chains. Additionally, asymmetry in the structure of the local DOS appears at both ribbon ends for each atomic row (similarly to the results presented for the two-atom system and the for atomic chain). This effect is better visible for larger spin-orbit couplings and leads to ferromagnetic occupancies of

Published under license by AIP Publishing.

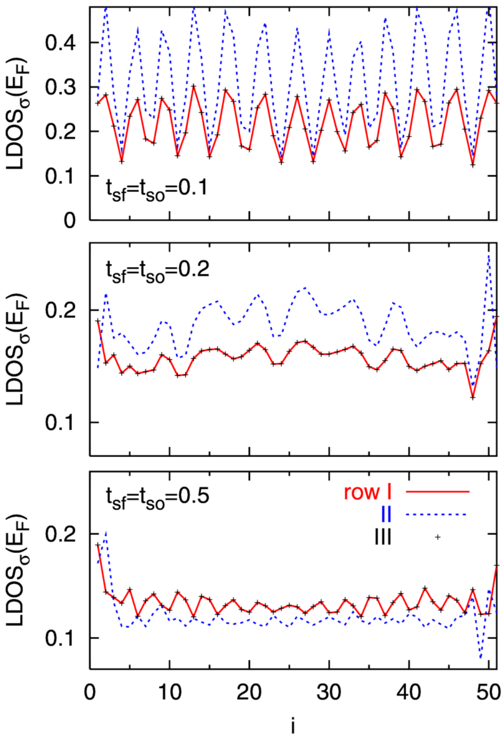

FIG. 12. Local DOS at the Fermi level along three coupled atomic chains (row I of atoms—solid curves, row II—broken curves, and row III—dots) for $t_{sf} = t_{so} =$ 0.1, 0.2 and 0.5 (upper, middle, and bottom panels, respectively). The other parameters are the same as in Fig. 10, $M = 3$, $t_y = 1$, $k_Fa = 2$.

edge sites and paramagnetic ones inside the ribbon. The asymmetry of LDOS in the ribbon and out-of-phase oscillations of the local DOS along different ribbon chains can be confirmed experimentally in the STM experiments.

IV. CONCLUSIONS

We have studied electronic properties of atomic ribbons composed of coupled atomic chains on different substrates using the tight-binding Hamiltonian and Green's function techniques. We have considered the spin-flip and spin-orbit couplings in the ribbon as well as electron leakage from chains to various types of substrates: with delocalized, weakly localized, and perfectly localized substrate electrons, which correspond to metallic, semiconductor, and insulator surfaces, respectively.

We have proposed coupled atomic chains with spin-dependent charge oscillations, where a ferromagnetic phase propagates only at both chain ends (for normal chains) or through the whole system (for topological chains). In particular, we have found strong asymmetry in the structure of the local DOS at atomic sites for short atomic systems due to (i) delocalized electrons in the substrate and (ii) due to spin-flip and spin-orbit couplings. In the former case, LDOS is spin-independent, and for perfectly localized electrons, the asymmetry in LDOS disappears. In the presence of the spin-flip and spin-orbit couplings, the structure of LDOS splits, moreover, is spin-dependent and LDOS asymmetry survives even for perfectly localized electrons in the substrate. These conclusions were verified for longer atomic systems in the presence of both spin-orbit couplings and the substrate electrons. As a main feature, we have found that for nontopological chains, only chain ends show spin-dependent LDOS characteristics, whereas the local DOS in the middle of the chain are spin-independent. As a result, such a chain reveals electron spin polarization only at its edges (ferromagnetic occupancies), but in the middle of the chain, the occupancies are the same for both spins (paramagnetic solutions). We have also investigated SSH spin-orbit chains and found spin-dependent Friedel oscillations along the whole chain. Note that in the SSH chain, without spin-flip and spin-orbit couplings, regular charge oscillations are not observed. The existence of spin-dependent oscillations of the occupancies in the SSH chains is very important for potential applications of these structures in spin-memory devices. Additionally, we have found that the end topological states, which appear in the middle of the energy gap region, split in the presence of spin-flip and spin-orbit couplings and the appropriate local DOS structures are nonsymmetrical around the Fermi energy.

We have also found different periods of the local DOS oscillations (obtained for the Fermi energy at each atomic site) along the normal chain in the presence of spin-flip and spin-orbit couplings. These parameters renormalize the on-site electron energies in the system leading to the Friedel oscillations. The oscillations in coupled atomic chains (atomic ribbon) on a surface were investigated along the ribbon and we have found that minima and maxima of local DOS oscillations (between neighboring chains) are in phase for small spin-orbit parameters, but for larger couplings, these oscillations are out of phase. Of course, for larger spin-orbit couplings, strong asymmetry in the structure of the local DOS appears at both ribbon ends.

It is believed that our results can be verified experimentally using a spin-polarized STM tip for normal or SSH chains localized at different substrates which are the thinnest possible electric wires. Considered here atomic chains can be widely applied in nanoelectronics as their physical parameters can be precisely controlled using external fields or electrodes.

ACKNOWLEDGMENTS

This work was partially supported by National Science Centre, Poland, under Grant No. 2018/31/B/ST3/02370.

REFERENCES

[1] M. Kopciuszyński, P. Dyniec, M. Krawiec, P. Łukasik, M. Jałochowski, and R. Zdyb, Phys. Rev. B **88**, 155431 (2013).

[2] J. N. Crain, J. L. McChesney, F Zheng, M. C. Gallagher, P. C. Snijders, M Bissen, C Gundelach, S. C. Erwin, and F. J. Himpsel, Phys. Rev. B **69**, 125401 (2004).

[3] A. A. Baski, K. M. Saoud, and K. M. Jones, Appl. Surf. Sci. **182**, 216 (2001).

[4] M. Jałochowski, T. Kwapiński, P. Łukasik, P. Nita, and M. Kopciuszyński, J. Phys. Condens. Matter **28**, 284003 (2016).

[5] S. Chuang, Q. Gao, R. Kapadia, A. C. Ford, and J. Guo, Nano Lett. **13**, 555 (2013); J. Zeng and K.-K. Chen, J. Mater. Chem. C **3**, 5697 (2015).

Published under license by AIP Publishing.

[6]M. Masahara, Y. Liu, K. Endo, T. Matsukawa, K. Sakamoto, K. Ishii, S. Ouchi, E. Sugimata, H. Yamauchi, and E. Suzuki, Appl. Phys. Lett. **88**, 072103 (2006).

[7]H. Ohnishi, Y. Kondo, and K. Takayanagi, Nature **395**, 780 (1998).

[8]A. I. Yanson, G. Rubio Bollinger, H. E. van den Brom, N. Agrait, and J. M. van Ruitenbeek, Nature **395**, 783 (1998).

[9]R. H. M Smit, C. Untiedt, G. Rubio-Bollinger, R. C. Segers, and J. M. van Ruitenbeek, Phys. Rev. Lett. **91**, 076805 (2003).

[10]N. Agrait, A. Levy Yeyati, and J. M. van Ruitenbeek, Phys. Rep. **377**, 81 (2003).

[11]W. G. van der Wiel, S. De Franceschi, J. M. Elzerman, T. Fujisawa, S. Tarucha, and L. P. Kouwenhoven, Rev. Mod. Phys. **75**, 1 (2003).

[12]S. Kohler, J. Lehmann, and P. Hanggi, Phys. Rep. **406**, 379 (2005); T. Kwapiński, Phys. Rev. B **69**, 153303 (2004).

[13]G. Gruner, Rev. Mod. Phys. **60**, 1129 (1998).

[14]J. Sung Shin, K.-D. Ryang, and H. Woong Yeom, Phys. Rev. B **85**, 073401 (2012).

[15]O. M. Auslaender, H. Steinberg, A. Yacoby, Y. Tserkovnyak, B. I. Halperin, K. W. Baldwin, L. N. Pfeiffer, and K. W. West, Science **308**, 88 (2005).

[16]A. Y. Kitaev, Phys. Usp. **44**, 131 (2001).

[17]M. Maśka, A. Gorczyca-Goral, J. Tworzydło, and T. Domański, Phys. Rev. B **95**, 045429 (2017).

[18]M. Pawlak, M. Kisiel, J. Klinovaja, T. Meier, S. Kawai, T. Glatzel, D. Loss, and E. Meyer, Quantum Inf. **2**, 16035 (2016); V. Mourik, K. Zuo, S. Frolov, S. Plissard, E. Bakkers, and L. Kouwenhoven, Science **336**, 1003 (2012).

[19]J. K. Asboth, L. Oroszlany, and A. Palyi, *A Short Course on Topological Insulators* (Springer, Switzerland, 2016).

[20]R. Drost, T. Ojanen, A. Harjuv, and P. Liljeroth, Nat. Phys. **13**, 668 (2017).

[21]W. Su, J. Schrieffer, and A. Heeger, Phys. Rev. Lett. **42**, 1698 (1979); L. Linhu, Ch. Yang, S. Chen, Europhys. Lett. **112**, 10004 (2015); L. Linhu, X. Zhihao, S. Chen, Phys. Rev. B **89**, 085111 (2014).

[22]M. Benito, M. Niklas, G. Platero, and S. Kohler, Phys. Rev. B **93**, 115432 (2016); V. Dal Lago, M. Atala, L. E. F. Foa Torres, Phys. Rev. A **92**, 023624 (2015).

[23]M. Kurzyna and T. Kwapiński, J. Appl. Phys. **123**, 194301 (2018).

[24]T. Kitagawa, M. Broome, A. Fedrizzi, M. Rudner, E. Berg, I. Kassal, A. Guzik, E. Demler, and A. White, Nat. Commun. **3**, 882 (2012); E. Meier, F. A. Anc, and B. Gadway, Nat. Commun. **7**, 13986 (2016).

[25]K. S. Thygesen and K. W. Jacobsen, Phys. Rev. Lett. **91**, 146801 (2003).

[26]N. Oncel, A. van Houselt, J. Huijben, A.-S. Hallback, O. Gurlu, H. J. W. Zandvliet, and B. Poelsema, Phys. Rev. Lett. **95**, 116801 (2005).

[27]T. Kwapiński, S. Kohler, and P. Hänggi, Eur. Phys. J. B **78**, 75 (2010).

[28]P. A. Orellana, M. L. Ladron de Guevara, and F. Claro, Phys. Rev. B **70**, 233315 (2004).

[29]A. V. Moroz and C. H. W. Barnes, Phys. Rev. B **60**, 14272 (1999); M. D. Jaffe and J. Singh, Solid State Commun. **62**, 399 (1987).

[30]S. Datta and B. Das, Appl. Phys. Lett. **56**, 665 (1990).

[31]J. E. Birkholz and V. Meden, J. Phys. Condens. Matter **20**, 085226 (2008).

[32]F. Mireles and G. Kirczenow, Phys. Rev. B **64**, 024426 (2001).

[33]Y. A. Bychkov and E. I. Rashba, JETP Lett. **39**, 78 (1984); available at http://www.jetpletters.ac.ru/ps/1264/article_19121.shtml.

[34]L. Peterson and P. Hedegard, Surf. Sci. **459**, 49 (2000); G. Bihlmayer, Y. M. Koroteev, P. M. Echenique, E. V. Chulkov, and S. Blugel, Surf. Sci. **600**, 3888 (2006).

[35]S. I. Erlingsson, Y. V. Nazarov, and V. I. Falko, Phys. Rev. B **64**, 195306 (2001); E. Perfetto, G. Stefanucci, and M. Cini, Phys. Rev. B **78**, 155301 (2008).

[36]S. Nadj-Perge, S. M. Frolov, E. Bakkers, and L. P. Kouwenhoven, Nature **468**, 1084 (2010).

[37]J. Nitta, T. Akasaki, H. Takayanagi, and T. Enoki, Phys. Rev. Lett. **78**, 1335 (1997); D. Liang and X. P. Gao, Nano Lett. **12**, 3263 (2012).

[38]D. M. Newns and N. Read, Adv. Phys. **36**, 799 (1987).

[39]S. Datta, *Electronic Transport in Mesoscopic Systems* (Cambridge University Press, Cambridge, 1995).

[40]G. Y. Hu and R. F. O'Connell, J. Phys. A: Math. Gen. **29**, 1511 (1996); C. M. Fonseca and J. Petronilho, Linear Algebr. Appl. **325**, 7 (2001).

[41]T. Kwapiński, J. Phys. Condens. Matter **18**, 7313 (2006); **25**, 095304 (2017).

[42]R. H. Dicke, Phys. Rev. **89**, 472 (1953).

[43]T. Brandes, Phys. Rep. **408**, 315 (2005).

[44]T. Kwapiński, J. Phys. Condens. Matter **17**, 5849 (2005).

Published under license by AIP Publishing.

PHYSICAL REVIEW B **102**, 195429 (2020)

Edge-state dynamics in coupled topological chains

M. Kurzyna and T. Kwapiński*
Department of Physics, Maria Curie Skłodowska University, 20-031 Lublin, Poland

(Received 30 June 2020; accepted 3 November 2020; published 23 November 2020)

We study time-dependent electrical properties of the Su-Schrieffer-Heeger (SSH) chain and coupled SSH chains on a substrate. Focusing on the midgap edge state dynamics we consider the abrupt transition from the normal to the SSH chain and determine characteristic timescale needed for topological states to develop. We have found that the midgap state is formed from the inside peaks of the normal chain density of states. For a ladderlike system we show that the edge SSH state vanishes in time or oscillates between neighboring sites. Moreover, for nonadiabatical time-dependent perturbations the midgap state can partially leak to other sites leading to induced topological states inside the trivial chain. We also analyze the mean-field correlation effects between the coupled chains revealing the induced Friedel oscillations in nontrivial chains.

DOI: 10.1103/PhysRevB.102.195429

I. INTRODUCTION

Science and engineering in past decades revealed a tendency of making things smaller and smaller. Quantum wires and atomic ribbons are the thinnest possible electric conductors [1–4] and they comprise basic blocks in nanoelectronics. Such low-dimensional systems reveal also many interesting quantum effects, such as conductance oscillations [5,6], spin-charge separation [7], charge-density waves [8], Majorana topological states [9,10], and others.

The study of topological quantum matter is one of the most attractive topic in low-dimensional physics. A Su-Schrieffer-Heeger (SSH) model is a simple tight-binding model in describing band topology in one-dimensional condensed-matter systems [11–17]. The SSH model has time-reversal, particle-hole symmetry, and it supports two distinct topological phases. The manifestation of the topological nontrivial nature in SSH systems is spectrally isolated midgap states localized at the system boundaries. These states are visible in the system density of states (DOS) and they are robust against local perturbations since they are related to the bulk environment (in contrast to conventional defect states which are sensitive to perturbations) [18]. Additional topological physics appear in extended SSH chains with more than two-site periodicity (larger unit cells) [19,20]. For long-range SSH models the site-site tunnelings include also next-nearest-neighbor hoppings or others couplings [11,21–24]. By expanding the standard SSH chain to a double-chain structure in a magnetic field one obtains the Creutz ladder model (cross-linked two-leg ladder system) or modified Harper model [25–27]. In ladderlike systems it is also possible to observe topological Majorana states [28]. Further expansion of a ladder leads to the ribbon SSH geometry or to strictly two-dimensional topological structures [29,30]. In contrast to equilibrium systems topological phases can be also induced by time-dependent external fields, e.g., the Floquet topological insulators [14,31–34]. Also a laser impulse applied to the SSH chain can generate high harmonics which depend on the system topological phase [35]. Moreover coherent destruction of tunneling in one-dimensional (1D) systems can appear as well [31,36,37].

There are a few experimental realizations of 1D topological systems. Very promising materials are stable atomic chains or atomic ribbons which can be grown epitaxially on reconstructed silicon surfaces, such as Si(335), Si(557), or others [1–4]. In such systems the scanning tunneling microscope (STM) measurement of the current-voltage characteristics or the conductance allows one to obtain the local density of states (LDOS) and distinguish different topological phases [38]. Additionally, with state-of-the-art fabrication technology it is possible to prepare 1D chains with gate-defined quantum dot (QD) in two-dimensional electron gas or chains of dopant atoms in silicon with STM [39,40]. In optics, the emerging field of topological photonics aims to fundamentally explore dynamical effects in 1D topological systems [41,42]. Using a photonic realization of the SSH chain it is possible to observe midgap nontrivial states of the SSH chain. Also, the extended SSH model with four-site periodicity were realized in a momentum lattice with ultracold Rb atoms [19]. In such systems topological properties can be estimated from the quench dynamics. Moreover, the Creutz ladder was realized in a driven 1D optical lattice on ultracold fermionic atoms [25]. This technique allows for arbitrary dynamical control over the tunneling phases, tunneling amplitudes or on-site energies [41,43]. Note that also 1D mechanical systems can manifest topological SSH properties [44,45] where the unit cell stands for two acoustic resonates or micromechanical junctions.

Electron transport properties of topological chains have been so far explored mainly in equilibrium (static) cases. Since new experimental techniques allow us to investigate atomic chains under time-dependent perturbations it would be desirable to obtain their time response on quenches and other perturbations. Thus far, such studies have been mostly

---

*tomasz.kwapinski@umcs.pl

2469-9950/2020/102(19)/195429(14)

©2020 American Physical Society

focused on time- or space-dependent probability density of the boundary modes [46–48], whereas the energy-dependent spectral density dynamics of the edge states has been often overlooked. The time evolution of such functions gives deeper insight into the whole on-site energetic structure showing dynamical transitions between the bulk and the topological states. LDOS peaks can be interpreted as the system quasiparticle states and their behavior in time and energy domains is crucial for comprehensive studies of these systems. Similarly, dynamical phenomena of the coupled chains in different topological phases can be analyzed by the spectral density functions at both chains as they contain information about the edge states, gap structure, and normal (bulk) states evolution simultaneously. In this paper we consider such topological hybrid structures and, in particular, we would like to answer the questions: How fast does the edge state respond to an instantaneous or continuously changed perturbations? How is it built or destroyed in time? Moreover, it is desirable to analyze how fast such states could leak/penetrate into nontopological subsystems. In our studies we precisely address these questions and we concentrate on the spectral density function of the SSH chain and analyze its modifications due to the abrupt or adiabatical change in the topological phase. This process takes place when the nearest-neighbor couplings between sites change in time leading to transformation from the normal chain (characterized by uniform couplings) to the topological SSH chain (characterized by different intracell and intercell couplings). For a single atomic chain also other modifications of the couplings are studied, such as the transient effects after breaking the chain where suddenly new edge states appear in the energy gap region. We address the timescale typical for development of the edge states in topological chains. Moreover, we consider different combinations of coupled atomic chains including normal chain—SSH chain or two coupled SSH chains in different topological phases. For the double-chain structures we investigate evolution in time of the edge topological state between both chains and electron occupancy dynamics due to the Coulomb repulsion. Analytic results for such complex systems are hardly available but for some simplifications they are discussed in the paper.

As we are able to analyze full time dynamics of the spectral density function we have shown in the paper that topological edge states are formed directly from the inside peaks of the normal chain DOS and the timescale of this process strongly depends on the surface underneath the chain (which is discussed in Figs. 2–4). More importantly, time dynamics for the coupled chains of the same topological phases shows that the system energy gap is always closed for awhile after the quench (cf. Fig. 6), however, for the hybrid two-chain system composed of different phases the zero-energy state partially leaks to the nontrivial phase and it exists simultaneously at two different sites of this system (Fig. 10). It should be also emphasized the importance of the results discussed in Fig. 11 of this paper. We have found that in the presence of the Coulomb repulsion between both chains the induced Friedel oscillations in the SSH chain can be observed.

The paper is organized as follows. In Sec. II, we describe the theoretical model and the calculation method. In Sec. III, the main results of the paper are discussed for a single SSH chain on a substrate (Sec. III A), coupled chains in different topological phases (Sec. III B), SSH ladderlike chains in the presence of the Coulomb interactions (Sec. III C). Section IV gives a short summary.

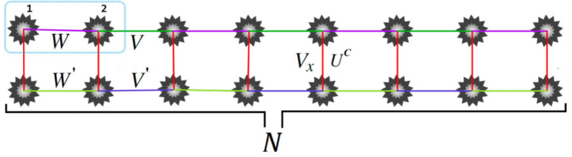

FIG. 1. Model of two coupled atomic chains of the length N that can be in different topological phases with the couplings W, V and W', V', respectively. V_x is the chain-chain coupling, and U^C stands for the Coulomb repulsion between charged sites.

II. MODEL AND THEORETICAL DESCRIPTION

The physical model we consider in this paper consists of a single atomic chain or coupled chains at the substrate as is schematically shown in Fig. 1. Each chain is composed of N single-electron sites with the nearest-neighbor couplings, W, V, W', V', V_x, and the Coulomb interaction U^C (repulsion). All parameters can change in time. The couplings along both chains can by uniform (as in the normal regular chain) or can vary periodically inside and between the primitive cell as in the SSH chain. For intracell couplings greater than intercell couplings we get a topological chain in the nontrivial phase, i.e., with topological midgap states at both chain ends (called here SSH$_1$), otherwise we obtain a chain in the trivial topological phase without end states (SSH$_0$).

The Hamiltonian of the system depends of the chain geometry and, in general, it can be written in the following form:

$$H = \sum_{i=1}^{M} \varepsilon_i a_i^\dagger a_i + \sum_{i=1}^{M} \sum_{\vec{k}_i} \left(\varepsilon_{\vec{k}_i} a_{\vec{k}_i}^\dagger a_{\vec{k}_i} + V_{\vec{k}_i,i} a_{\vec{k}_i}^\dagger a_i + \mathrm{H.c.} \right) + \sum_{i,j}^{M} V_{i,j}(t) a_i^\dagger a_j + \sum_{i,j}^{M} U_{i,j}^C(t) \hat{n}_i \hat{n}_j, \tag{1}$$

where M is the total number of sites in the system, $a^\dagger$, a are the creation and annihilation electron operators at the appropriate sites, $\hat{n}_i = a_i^\dagger a_i$ is the particle number operator, ε_i and $\varepsilon_{\vec{k}}$ stand for the single-electron energies in the chain or in the substrate, respectively (the substrate is considered as M-separate electrodes). Electron transitions between the surface and the sites are established by the couplings $V_{\vec{k},i}$ and $V_{i,j}$ correspond to the nearest-neighbor tunneling between the chain sites (the coupling between chains corresponds to $V_{i,j} = V_x$ and is site independent). The last term in the Hamiltonian $U_{i,j}^C \hat{n}_i \hat{n}_j$ stands for the site-site Coulomb repulsion, and it is assumed that this interaction is captured within the mean-field (Hartree-Fock) approximation which renormalizes the single-electron energies in the Hamiltonian, i.e., $\varepsilon_i \to \varepsilon_i + U_{i,j}^C n_j$, where n_j is the expectation value of $\hat{n}_j$. This approach is justified as the Coulomb interaction in many quantum structures is small [such as in Pb chains on the Si(335) surface], thus, noninteracting eigenstates of the quantum structure are related to those of small U^C. In the opposite limit (large U^C) the energetic structure of the system is split with the Coulomb blockade gap, but if we neglect many-body complex effects, such as the Kondo effect, it is reasonable to focus on a single Coulomb band. Thus, the spin index in our calculations is suppressed as both spin directions are independent.

In order to describe time response of the system on external perturbations the evolution operator method is used in our calculations [49,50]. The charge occupation of the ith site can be expressed in terms of the appropriate matrix elements of the evolution operator (for details see Appendix A),

$$n_i(t) = \sum_{j=1}^{M} n_j(t_0)|U_{i,j}(t,t_0)|^2 + \sum_{j,\vec{k}_j} n_{\vec{k}_j}(t_0)|U_{i,\vec{k}_j}(t,t_0)|^2, \qquad (2)$$

and the current flowing from the surface electrode is obtained from the time derivative of the total number of electrons in this reservoir,

$$j_1(t) = -e\frac{d}{dt}N_1(t) = -e\frac{d}{dt}\sum_{\vec{k}_1} n_{\vec{k}_1}(t), \qquad (3)$$

where $n_{\vec{k}_1}(t)$ is expressed similarly to Eq. (2) and $n_\alpha(t_0)$ is the initial occupancy of state α. In the interaction representation the evolution operator matrix elements satisfy the following equation of motion:

$$i\frac{\partial}{\partial t}U(t,t_0) = \hat{V}(t)U(t,t_0), \qquad (4)$$

where $\hat{V}(t) = U_0(t,t_0)V(t)U_0^\dagger(t,t_0)$, $U_0(t,t_0) = \mathcal{T}\exp\left(i\int_{t_0}^{t} dt' H_0(t')\right)$ and $\mathcal{T}$ is the time-ordering operator. Here $V(t)$ and $H_0(t)$ are the coupling part and the on-site energy part of the total Hamiltonian, respectively ($H_0 = \sum_\alpha \varepsilon_\alpha a_\alpha^\dagger a_\alpha$). In the calculations we put the initial time $t_0 = 0$ (i.e., the couplings are zero for $t < t_0$), and all dynamical effects are analyzed for the system which already reaches its equilibrium state so the initial occupations of the chain sites do not play any role, thus, we assume $n_i(t_0) = 0$. In such a case the chain occupancies can be written as $n_i(t) = \sum_{j,\vec{k}_j} n_{\vec{k}_j}(0)|U_{i,\vec{k}_j}(t)|^2$. The summation over the wave vectors with the initial band fillings $n_{\vec{k}_j}(0)$ is, as usual, replaced by the integral over the energy with the Fermi function $f(\varepsilon)$, i.e., $n_i(t) = \int d\varepsilon \sum_j f(\varepsilon)D_j(\varepsilon)|U_{i,\vec{k}_j}(t)|^2 = \int d\varepsilon\, f(\varepsilon)\mathrm{LDOS}_i(\varepsilon,t)$, where $D_j(\varepsilon)$ is the jth electrode bandwidth and $\mathrm{LDOS}_i(\varepsilon,t)$ is the spectral density function (the local DOS) at the ith site. The evolution operator $U_{i,\vec{k}_j}(t)$ can be found from Eq. (4), and after some algebra (see Appendix A) the differential equation on this function takes the form

$$\begin{aligned} i\frac{\partial U_{i,\vec{k}_j}(t)}{\partial t} = {} & \sum_{i'} V_{ii'}e^{i(\varepsilon_{i'}-\varepsilon_i)t}\exp\left[iU^C\int_0^t dt'\widetilde{n}_{i'}(t') - \widetilde{n}_i(t')\right]U_{i',\vec{k}_j}(t) \\ & - V_{i\vec{k}_j}e^{i(\varepsilon_i-\varepsilon_{\vec{k}_j})t}\exp\left[iU^C\int_0^t dt'\widetilde{n}_i(t')\right] \\ & - |V_{i\vec{k}_j}|^2\int_0^t dt' D(t-t')e^{i\varepsilon_i(t-t')}\exp\left[iU^C\int_{t'}^t dt_1\widetilde{n}_i(t_1)\right]U_{i,\vec{k}_j}(t'), \end{aligned} \qquad (5)$$

where $\widetilde{n}_i(t) = \sum_{j'} n_{j'}$ and j' runs over all neighboring sites (from the ith site) for which there is U^C repulsion between electrons, $U_{ij}^C = U^C$. The time-dependent current, Eq. (3), is also expressed by means of the evolution operator matrix elements, see Eq. (A5), and can be written as follows ($e = 1$):

$$\begin{aligned} j_1(t) = {} & -2\,\mathrm{Im}\left\{\sum_{\vec{k}_1} n_{\vec{k}_1}(0)V_{\vec{k}_1}e^{i(\varepsilon_{\vec{k}_1}-\varepsilon_1)t}\exp\left[-iU^C\int_0^t dt'\widetilde{n}_i(t')\right]U_{1,\vec{k}_1}(t)\right\} - 2\,\mathrm{Re}\left\{\sum_{\vec{k}_i} n_{\vec{k}_i}(0)|V_{\vec{k}_1}|^2U_{1,\vec{k}_i}(t)\right. \\ & \left.\times\int_0^t dt' D_1^*(t-t')e^{i\varepsilon_i(t'-t)}\exp\left[iU^C\int_{t'}^t dt_1\widetilde{n}_i(t_1)\right]U_{1,\vec{k}_i}^*(t')\right\}, \end{aligned} \qquad (6)$$

where $D(t) = \int d\varepsilon\, D(\varepsilon)e^{i\varepsilon t}$ is the time Fourier transform of the lead DOS, $D(\varepsilon)$. Note that the knowledge of $U_{i,\vec{k}_j}(t)$ is necessary to obtain the chain occupancies, spectral density function, or the currents. In general, analytical expressions for these quantities do not exist, and the problem should be resolved numerically. However, some analytical solutions are possible in the wideband approximation as well as for regular and symmetrical chains which will be discussed later in the paper. Assuming the wideband approximation, the influence of the substrate can be captured by the site-dependent spectral density Γ_{ij}, which diagonal elements play the crucial role and are energy independent: $\Gamma_{ii}(\varepsilon) = 2\pi\sum_{\vec{k}}|V_{i\vec{k}}|^2\delta(\varepsilon-\varepsilon_{\vec{k}}) = \Gamma_i$. The off-diagonal terms rapidly vanish with the site-site distance and in the paper are negligible, thus, the surface electrode can be considered as a set of equivalent leads such that each chain site is coupled with its own electrode Γ_i. Within this approach one can obtain the time integral in the last term in Eq. (5) which equals $i\frac{\Gamma_i}{2}U_{i,\vec{k}_j}(t)$. In this case the relation for the current, Eq. (6), can be written as follows:

$$j_1(t) = -2\,\mathrm{Im}\left\{\sum_{\vec{k}_1} n_{\vec{k}_1}(0)V_{\vec{k}_1}e^{i(\varepsilon_{\vec{k}_1}-\varepsilon_1)t}\exp\left[-iU^C\int_0^t dt'\widetilde{n}_i(t')\right]U_{1,\vec{k}_1}(t)\right\} - \Gamma_1 n_1(t). \qquad (7)$$

Note that similar equations for other currents $j_i(t)$ can be derived which should be resolved using the set of differential equations, Eq. (5), together with the relations for $n_i(t)$.

III. RESULTS AND DISCUSSION

Here we analyze electron transport properties of a single chain and coupled atomic chains on a surface focusing on the time evolution of the occupancies, spectral density functions (LDOS), or the currents for different chain geometry. We carry out the quench to the system by suddenly or adiabatically changing some hopping parameters. In our calculations we assume the temperature $T = 0$ K, and the energy reference point stands for the Fermi energy of the surface electrode, which implies $E_F = 0$. Moreover, equal on-site energies for all sites are considered $\varepsilon_i = \varepsilon_0$, and the parameters are chosen to fit the realistic parameters measured in experiments. In our calculations we use the effective chain-lead coupling $\Gamma_i = \Gamma$ as the energy unit, then for $\Gamma = 0.1$ eV, the coupling $V = 4$ corresponds to $V = 0.4$ eV, the time unit is $\hbar/\Gamma \simeq 10^{-15}$ s, and the current unit becomes $2e\Gamma/\hbar \simeq 50\ \mu$A.

A. Single atomic chain

We start by addressing the time-evolution effect of the normal atomic chain which evolves (is transformed) to the topological one and consider a linear chain on a surface for which some analytical expressions can be derived for the uncorrelated case $U^C = 0$. The transition from the normal to topological chain is forced by changing in time the hopping integrals inside the chain.

For a finite 1D system composed of N equal sites in the stationary case one can obtain analytical results, e.g., for the conductance [51]. The Hamiltonian of the SSH chain has chiral symmetry which gives rise to a symmetric energy spectrum and for periodic boundary conditions the results can be also derived analytically [17]. The situation is more complicated for time-dependent transport properties, especially for a chain on a noninsulating substrate. To calculate the time-dependent on-site spectral density function one needs $U_{i,\vec{k}_j}(t)$ matrix elements which can be found using the Laplace transform technique (see Appendix B). After some algebra we find the solution, e.g., for $U_{1,\vec{k}_j}(t)$, which is necessary in the spectral density function $\mathrm{LDOS}_1(\varepsilon)$,

$$U_{1,\vec{k}_j}(t) = \frac{(-i)^j V^{j-1} V_{j,\vec{k}_j} \prod_{j_1=1}^{N-j} \left(s_0 + \frac{\Gamma}{2} + 2iV\ \cos \frac{j_1 \pi}{N-j+1} \right)}{\prod_{j_1=1}^{N} \left(s_0 + \frac{\Gamma}{2} + 2iV\ \cos \frac{j_1 \pi}{N+1} \right)} \exp\left(i(\varepsilon_0 - \varepsilon_{\vec{k}_j}) t \right)$$
$$+ \sum_{j_1=1}^{N} \frac{(-i)^j V^{j-1} V_{j,\vec{k}_j} \prod_{j_2=1}^{N-j} \left(s_{j_1} + \frac{\Gamma}{2} + 2iV \cos \frac{j_2 \pi}{N-j+1} \right)}{[s_{j_1} - i(\varepsilon_0 - \varepsilon_{\vec{k}j})] \prod_{j_2=1,\ j_2 \neq j_1}^{N} \left(s_{j_1} + \frac{\Gamma}{2} + 2iV\ \cos \frac{j_2 \pi}{N+1} \right)} \exp\left(-\frac{\Gamma}{2} t \right) \exp\left(-2\,iV \cos \frac{j_1 \pi}{N+1} t \right), \tag{8}$$

where $s_0 = i(\varepsilon_0 - \varepsilon_{\vec{k}j})$ and $s_j = -\frac{\Gamma}{2} - 2iV\ \cos \frac{j\pi}{N+1}$. Note that the above function oscillates in time (even far from the initial time t_0) and is responsible for time dynamics of the system. The spectral density function is expressed by $|U_{1,\vec{k}_j}(t)|^2$ elements, which also oscillates in time, but for large t (far from the perturbation) it reads

$$|U_{1,\vec{k}_j}(t \to \infty)|^2 = \frac{V^{2(j-1)} V_{j,\vec{k}_j}^2 \prod_{j_1=1}^{N-j} \left[\left(\varepsilon_0 - \varepsilon_{\vec{k}_j} + 2V\ \cos \frac{j_1 \pi}{N-j+1} \right)^2 + \left(\frac{\Gamma}{2} \right)^2 \right]}{\prod_{j_1=1}^{N} \left[\left(\varepsilon_0 - \varepsilon_{k_j} + 2V\ \cos \frac{j_1 \pi}{N+1} \right)^2 + \left(\frac{\Gamma}{2} \right)^2 \right]}, \tag{9}$$

and is time independent. There are N product terms in the denominator of the above relation, which minima determine the spectral density peaks. Note that analytical formulas for the current or site occupancies are possible in this case, but they do not have short transparent form.

To study the time-response effects in our calculations we use Eq. (8) for $U_{i,\vec{k}_j}(t)$ (for regular chains) or resolve numerically the set of differential equations Eq. (5) for arbitrary time-dependent chains. In the beginning we analyze in Fig. 2 the transition effect form the normal chain (described by uniform couplings) to the topological one in the nontrivial phase (SSH_1) for the chain length $N = 8$ placed on the surface. The left, middle, and right panels show the time evolution of the spectral density function at the first, second, and third chain sites, respectively, and the transition takes place at $t = 20$ (i.e., far from the transient effects observed for the initial time). Before this time the chain spectral density is fixed (does not change in time) and for $i = 1$ is expressed by Eq. (9). It is expected that at this site, just after the quench, the energy gap should be opened and simultaneously the midgap state

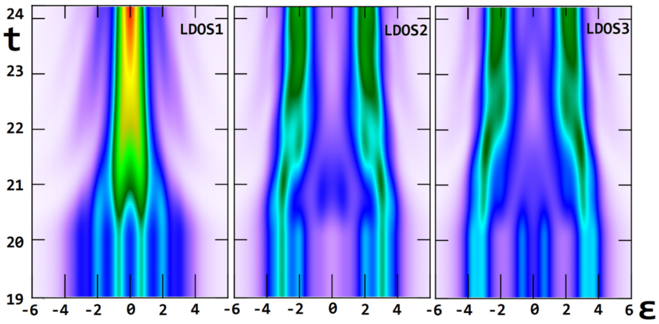

FIG. 2. LDOS time evolution of the normal chain ($V = W = 2$) composed of $N = 8$ sites on the surface for sudden change of the couplings to the SSH parametrization in the nontrivial phase ($W = 0.5,\ V = 2.0$) at $t = 20$. Other parameters are $\varepsilon_0 = 0,\ \Gamma_i = \Gamma = 1,\ U^C = 0$. Red, yellow, green, and blue colors represent the LDOS values equal to 0.6, 0.4, 0.2, and 0.1, respectively.

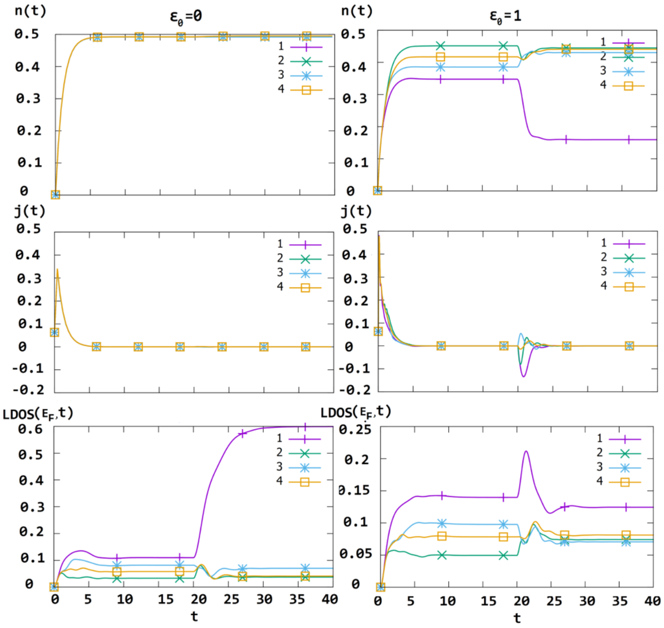

FIG. 3. Time-dependent charge occupancies, currents, and LDOS at the Fermi level (upper, middle, and bottom panels, respectively) for first four sites of the normal chain of length $N = 8$ ($V = W = 2$) switched at $t = 20$ to the SSH$_1$ nontrivial chain with the couplings $W = 0.5,\ V = 2.0$ for different on-site energies $\varepsilon_0 = 0$ (left panels) and $\varepsilon_0 = 1$ (right panels).

should appear. We would like to analyze how this edge state is formed in time: Is it built directly from the normal states, or do these states disappear and then the midgap state arises? To answer this question we have to consider the full time- and space-dependent LDOS because the occupation number or topological invariants cannot resolve this problem. As one can see at $t = 20$ the LDOS at each site is rebuilt in time and the energy gap of the width $\pm 2\eta$ appears along the chain with the midgap topological states at both chain ends (in our case we have $W = 1.25 - \eta$ and $V = 1.25 + \eta$ with $\eta = 0.75$). A careful inspection on the time evolution of LDOS shows that the topological state does not appear just after the quench but it needs few time units to be fixed (about ten time units). More important, during this process the states evolve continuously (without delocalization), and in the first stage the midgap state is built from the central DOS peaks of the normal chain (two peaks join together just after $t = 20$). At the same time two next peaks localized at $\varepsilon = \pm 2$ are bent towards the zero energy (band center) and after some next period of time they reach our topological state. The energy-dependent spectral functions of the interchain sites are characterized by two main sidebands (greenlike regions, Fig. 2, middle and right panels for $t > 20$) with the energy gap between them. However, in contrast to the topological state these bands are formed in a different way: The central LDOS peaks of the normal chain (around the Fermi level) do not support these sidebands, but they vanish very fast after the quench (better visible in the right panel) and the sidebands are smoothly built only from the most outer LDOS peaks.

To study this dynamical process in more detail in Fig. 3 we analyze the charge occupation, currents, and LDOS at the Fermi energy for the first four sites of the system for the same parameters as in Fig. 2. We also compare dynamics of the system for two different values of the on-site energies $\varepsilon_0 = 0$ (symmetrical case) and $\varepsilon_0 = 1$ (asymmetrical case). The transient (turn-on) effects appear in the system only for very small t such that for $t > 10$ the system is in the equilibrium state. For the symmetrical case all sites are half-occupied (upper left panel), and they are almost unaffected by the quench at $t = 20$. It results from the fact that stationary occupancies n_i for the normal and topological chains are exactly the same for $\varepsilon_0 = 0$, and the spectral density changes symmetrically in time for positive and negative energies (as is shown in Fig. 2). It leads to constant occupancies in the chain during the transition. However, even for constant $n_i(t)$, the charge could flow through the system, thus, it is necessary to analyze the electron currents [obtained from Eq. (7)]. It turns out that beyond the initial time the currents do not flow from the substrate to the chain (middle left panel) which confirms that electron charges are localized along the chain and do not flow during the transition. In the bottom panels of Fig. 3 we analyze the spectral density function at the Fermi level. As one can see the LDOS at the first site (with the midgap topological state) grows monotonically just after the quench whereas other middle-chain sites reveal small vanishing in time oscillations. However, the spectral density LDOS$_1$ does not change smoothly but reveals some inflection points which are related to the creation process of the midgap state discussed in Fig. 2. One can note that the spectral density at the first site needs much longer time to reach its equilibrium value (ten units) than the LDOS at other sites. The studies of the reverse process (quench from nontrivial to the trivial phase) leads to very similar results with monotonically decreasing value of the local DOS at the edge sites. However, the midgap state changes just after the quench and is not frozen, cf. Ref. [48] due to the chain-surface coupling which is responsible for the rate of the transition.

For the non-symmetrical case ($\varepsilon_0 \neq E_F$, right panels) the physics of the chain transition is much reacher. Now the occupancies along the normal chain (i.e. before the quench) form a kind of charge waves in the system [8,52]. Next, for

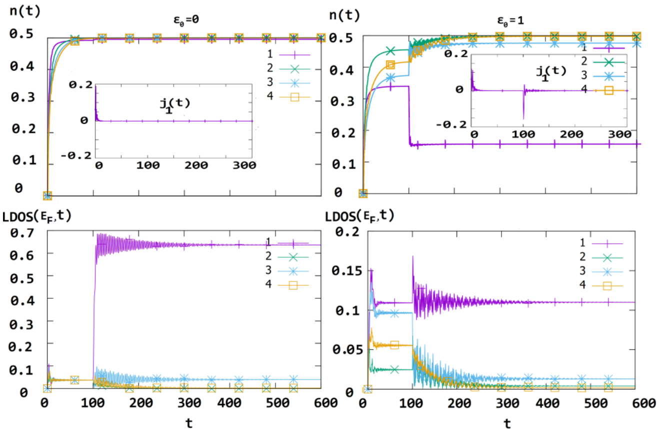

FIG. 4. Electron occupancies (upper panels) and LDOS at the Fermi level (bottom panels) of the first four sites in the normal chain ($V = W = 2$) switched to the nontrivial topological chain ($W = 0.5,\ V = 2.0$) at $t = 100$ for $N = 8,\ \Gamma_1 = \Gamma_N = 1,\ \Gamma_i = 0$ for $\varepsilon_0 = 0$ (left panels) and $\varepsilon_0 = 1$ (right panels). The insets in the upper panels show the left current $j_1(t)$.

$t > 20$ the chain couplings are changed and the occupancies at the middle-chain sites tend to some constant value, common for all sites (almost half-occupied) because the energy gap appears along the chain and the Fermi energy is still in this energy gap region ($\varepsilon_0 = 1,\ E_F = 0$ and the energy gap width is 3). However, the occupancy of the end site rapidly decreases after the quench as now the midgap state is shifted towards ε_0 and there is a relatively low value of LDOS at the Fermi level. The consequence of this asymmetry in the LDOS is the current flowing from the substrate to the chain (middle right panel). The largest quench current appears for the first site because its occupancy rapidly decreases and the excess charge flows out to the surface (the current is negative). Note that other currents $j_i(t)$ oscillate in time and can be positive or negative depending on the occupancy modifications at a given site. All currents flow only for a short period of time after the quench (few time units) and then the system tends to its equilibrium state, thus, the currents vanish. Also the spectral functions at the Fermi level (right bottom panel) show damping oscillations after the quench and tend to the same asymptotic values for all middle sites and to the higher value of the LDOS at the edge site (due to the midgap state).

The transition from the normal to the topological system changes the structure of LDOS along the chain, but the system reaches its steady state relatively fast (almost monotonically or with small damping oscillations). For the chain on a substrate each site is coupled with continuum states in the lead underneath, and the oscillations are strongly suppressed. However, it could be interesting to study the transition effect for a chain on the insulating substrate. Thus, we consider the chain in the L-R geometry, i.e., the chain is coupled only with two (left and right) external electrodes via the edge sites ($\Gamma_1 = \Gamma_N = 1$ and $\Gamma_i = 0$). The results for symmetrical ($\varepsilon_0 = 0$) and nonsymmetrical ($\varepsilon_0 = 1$) spectral density functions are shown in Fig. 4, left and right panels, respectively, and the transition takes place at $t = 100$. In this case the system needs much more time to go beyond the transient effects—the sites are charged up to $t \simeq 80$ (upper panels) whereas for the noninsulating surface this time was ten times smaller. Now lead electrons have to pass through all chain sites to occupy the middle sites. As before, for the symmetrical case the occupancies do not change during the transition and the current does not flow in the system (left upper panel). However, for the nonsymmetrical case the occupancies change their values after the quench (right upper panel) especially at the edge site and oscillate with small damping amplitudes. These oscillations are also visible on the spectral density functions at the Fermi level (bottom panels)—they vary in time with slowly damping oscillations for both symmetrical as well as nonsymmetrical cases. During these oscillations a new spectral density function is formed at each site similar to the noninsulating surface discussed in Fig. 2—the main difference is that for the insulating surface the spectral density does not change smoothly but it oscillates even for hundreds of time units after the quench with slowly vanishing amplitude. However, it is worth noting that the surface coupling Γ_i is responsible for the half-width of the LDOS peaks, thus, the asymptotic occupancies are almost not sensitive to this coupling strength. We have also considered different chain lengths N, and the results remain still valid. However, we have found that the LDOS oscillations can reveal quantum beats which are size dependent (not shown here). It turns out that these beats behave in the same way as the survival probability obtained for 1D Majorana modes [46].

Electrical properties of stationary atomic chains are well known, e.g., topological states of such systems are protected against external perturbations and survive when the chain is coupled with the substrate [18]. However, it is desirable to check if this protection is still present for time-dependent perturbations especially just after the quench. To study this effect we consider the SSH$_1$ chain with the midgap edge states and at a given time $t = 20$ suddenly break the chain into two smaller parts (the chain is broken between the eighth and the ninth sites). This situation is schematically shown in Fig. 5 (upper scheme). The relevant spectral density functions at four chosen sites are shown in the lower panels. One can observe that topological state at the first site is unchanged in time, thus, it is protected against such perturbations. We can also note that internal sites are slightly affected by this destructive process (middle and right panels in Fig. 5) and, e.g., even the last but one site from the perturbation (LDOS$_7$) remains almost unchanged for $t > 20$. Also the occupancies do not change in time in this case because all spectral density functions are symmetrical versus the Fermi energy. What is important, just after the breaking one observes time formation of the topological midgap states at the eighth (bottom panel) and ninth sites in the chain as these sites became new edges for two separated topological chains. These states are smoothly formed from the bulk sidebands of the topological chain. It is worth noting that in this case the perturbation is sharp but the states are not smashed over the energy scale (no decoherence effects) and the LDOS at new edge sites smoothly changes in time by bending the sidebands towards the Fermi energy.

B. Coupled atomic chains

Thus far, we have analyzed midgap state dynamics in a single atomic chain. However, in real systems such a chain

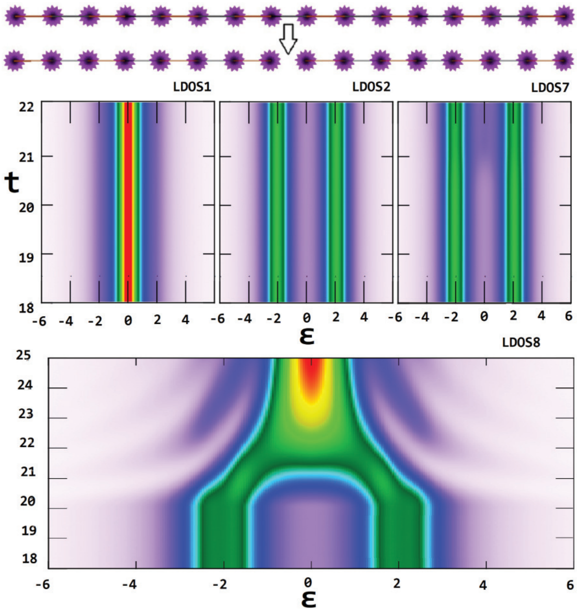

FIG. 5. LDOS time evolution at the first, second, seventh, and eighth sites for the nontrivial chain composed of $N = 16$ sites on the surface ($W = 0.5,\ V = 2.0$) broken at $t = 20$ between the eighth and the ninth sites as is indicated in the upper scheme $\varepsilon_0 = 0$, $\Gamma_i = 1$.

is fabricated in the vicinity of other regular chains, such as on vicinal surfaces Si(335) or Si(557) where two or more parallel chains can be observed at each terrace [1,4]. On the other hand coupled chains are more stable and perspective in nanoelectronics than a single atomic chain which can easily break. In real experiments the site-site hoppings can be modified by changing the distances between atoms (e.g., using the STM technique, varying the substrate temperature, using piezoelectric substrates, or in optical lattices). Alternatively, one can use a linear QD system where all couplings between dots can be fully controlled by external electrodes. Thus, it is desirable to investigate the electronic properties of coupled chains on a surface, in particular, to determine time dynamics of topological states in the presence of neighboring chains being in the same or other topological phase.

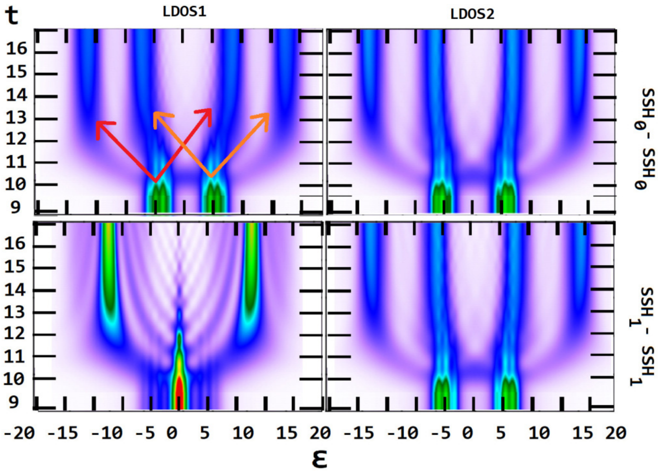

FIG. 6. LDOS time evolution of two first sites LDOS_1, LDOS_2 (left and right panels) for SSH_0-SSH_0 and SSH_1-SSH_1 coupled chains with $V = 2,\ W = 4$ (SSH_0) and $V = 4,\ W = 2$ (SSH_1). The coupling between chains is switched on linearly from zero (at $t = 10$) to $V_x = 10$ (at $t = 11$), $\Gamma_i = 1,\ \varepsilon_0 = 0,\ N = 10$.

First, in Fig. 6 we consider two coupled chains in the same topological phases, i.e., SSH_0-SSH_0 or SSH_1-SSH_1. For such ladderlike systems we analyze the spectral density dynamics for two sites LDOS_1 and LDOS_2 (which are the same for both chains). The coupling V_x changes in time linearly (quenchlike changes) from zero (at $t = 10$) to $V_x = 10$ (at $t = 11$) and before the quench ($t < 10$) both chains are in their initial topological phases, i.e., the trivial phase with the energy gap along the whole chain (SSH_0) or in the nontrivial phase with the midgap edge states (SSH_1). It is interesting that for the SSH_0-SSH_0 system after the quench the sidebands of the LDOS observed for $t < 10$ split in time by the value $\pm V_x$ and they form four separated sidebands (indicated by the arrows). During this process the energy gap is closed for awhile as the sidebands cross together—see the bluelike horizontal stripes around $\varepsilon = 0$ for $t \simeq 10$. Note that for the small value of V_x the splitted sidebands do not cross each other and the energy gap is not closed in that case. This effect is confirmed by the energy spectra calculations shown in the upper panel in Fig. 7 for the SSH_0-SSH_0 system. The spectrum has a reflection symmetry through the Fermi energy in the gap due to the particle-hole symmetry. One can see that for small hopping V_x the energy gap still exists then it is closed for intermediate values of V_x and for larger hoppings it opens again. It is the reason that during the large jump of this parameter the system is not transformed immediately to the energy gap region, but

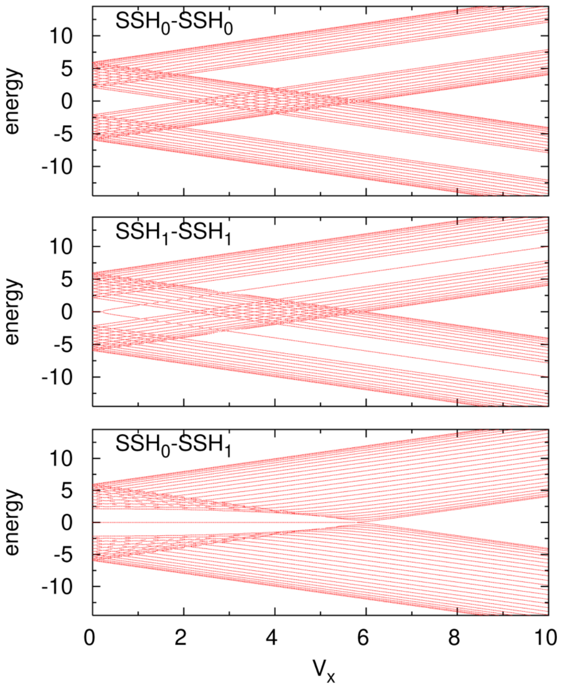

FIG. 7. Quasienergy spectra of two coupled atomic chains as a function of the chain-chain hopping V_x for two SSH_0 chains (upper panel), two SSH_1 chains (middle panel), and for SSH_0-SSH_1 chains of the length $N = 24$. The other parameters as the same as in Fig. 6.

for a moment the energy gap is closed. Note, however, that quasienergy spectra do not give us as wide perspective on the quantum states dynamics as the time- and space-dependent LDOS function. Similar behavior of the LDOS dynamics we observed for all sites in the SSH$_0$-SSH$_0$ system as well as for all intersites of the SSH$_1$-SSH$_1$ system (e.g., right bottom panel in Fig. 6). At these sites there are no topological states at the Fermi level—the energy spectrum for the SSH$_1$-SSH$_1$ geometry is shown in the middle panel in Fig. 7 and the gap existence for large V_x is evident. Note that there are also further gaps in the energy spectra beyond the Fermi level and for the nontrivial phase additional states in the middle of these gaps can exist [38]. The most interesting is the midgap topological state dynamics (left bottom panel in Fig. 6). Here the edge state slowly vanishes and reveals damping oscillations in the energy gap region. Moreover, only two main sidebands are formed at the edge site and these sidebands are accrued from the midgap state by "periodical emission" of the main state towards the sidebands. The emission process takes place when the midgap state reaches maximal values during its oscillations in time. It leads to a nice symmetrical picture with periodical spectral density oscillations in the energy gap region and this effect will be discussed later.

Next we consider two coupled chains that are in different topological phases. The system is composed of the SSH$_1$ (nontrivial phase) and SSH$_0$ (trivial phase) chains. In Fig. 8 we show the LDOS at the first two sites of the SSH$_1$ (left panels) and SSH$_0$ (right panels) topological chains which are coupled at $t = 10$. We consider different time rates of this coupling: It is switched on very slowly [adiabatically, panels (a)], average [panels (b)], and rapidly [fast quench, panels (c)] as is indicated in the upper inset. For adiabatically changed coupling V_x we observe the monotonically vanishing (without oscillations) topological state at the edge site of the nontrivial SSH$_1$ chain [left (a) panel], and for $t \simeq 55$, which corresponds to $V_x \simeq 6$, this state disappears. It is confirmed by the quasienergy spectrum for this system shown in Fig. 7, bottom panel, where the bulk energy gap of the SSH$_0$-SSH$_1$ system with the midgap state closes for $V_x \simeq 6$ and opens again without the appearance of any topological state for larger V_x. Thus, the system changes its topology from the nontrivial phase to the trivial one. Interestingly, that in the trivial chain at the second site, additional midgap state appears in the spectral density for the coupled chains. This state is visible only for a short period of time (which corresponds to $V_x < 6$), and for larger t it smoothly vanishes. The appearance of this induced state in the SSH$_0$ chain is correlated with the intensity of the edge state in the SSH$_1$ chain—one can say that the topological state leaks for a moment to the trivial chain. It is important that this process holds between nondirectly coupled sites in both chains and there is still an energy gap in their neighboring sites at the Fermi level [middle (a) panels]. To confirm this conclusion we analyze in more detail the LDOS at the Fermi energy as a function of time and in Fig. 9(a), one can see that the midgap topological state (purple curve) slowly vanishes for $t > 10$ and at the same time the induced state in the trivial chain appears (orange curve). For a longer time (larger V_x value) the energy gap closes (around $t = 50$) and opens again with the trivial phase without topological states.

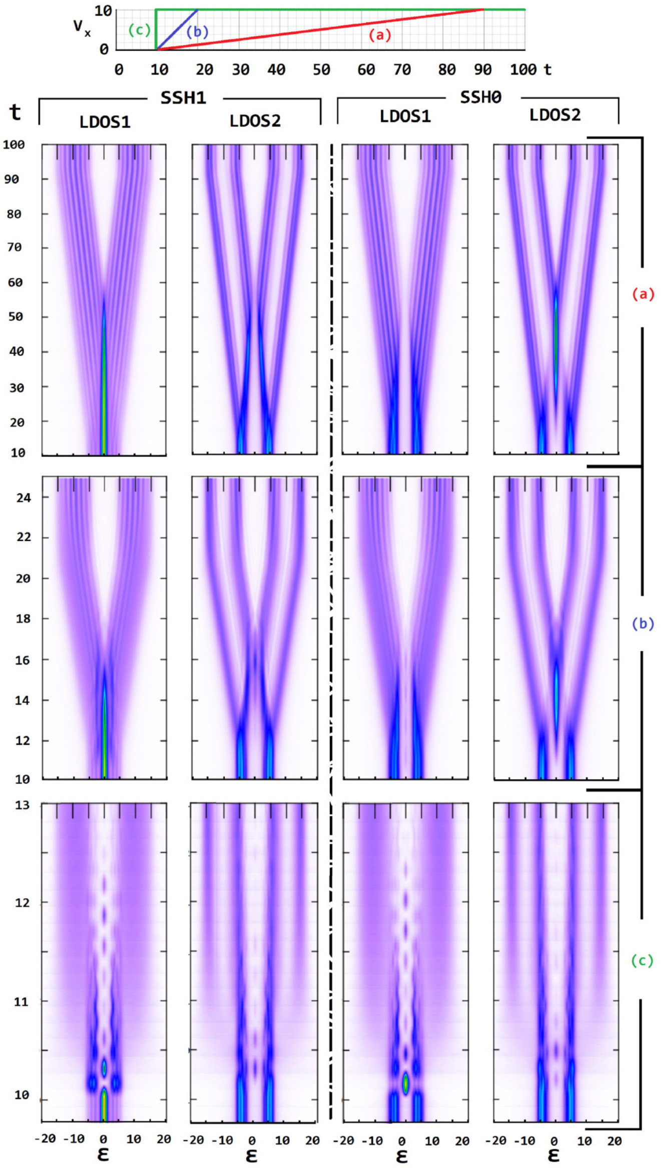

FIG. 8. Time evolution of the LDOS at two sites $i = 1, 2$ of initially decoupled chains of the length $N = 10$ in different topological phases (SSH$_0$ with $V = 2$, $W = 4$ and SSH$_1$ with $V = 4$, $W = 2$). The chains are coupled at $t = 10$ and $V_x(t)$ changes in time as is indicated in the upper inset according to the (a), (b), or (c) curve, respectively.

More interesting physics appears for nonadiabatical perturbations where the chain-chain hopping rapidly change in time [(b) and (c) panels in Fig. 8]. Topological edge states in the SSH$_1$ chain vanish with time [left (b) panel] and the midgap state in the trivial SSH$_0$ chain (at the second site) is observed during the fast linear change of V_x which is shown in the right (b) panel. For this change there is still a short period of time for which V_x corresponds to the nontrivial SSH phase and the induced topological state can appear for a moment. This dynamical process is also visible in Fig. 9, (b) panel where the spectral density functions at the Fermi level are shown for the first two sites of both chains. As before, the topological state vanishes in time (purple curve), but now small oscillations of LDOS are evident. Note that rate-dependent oscillations after

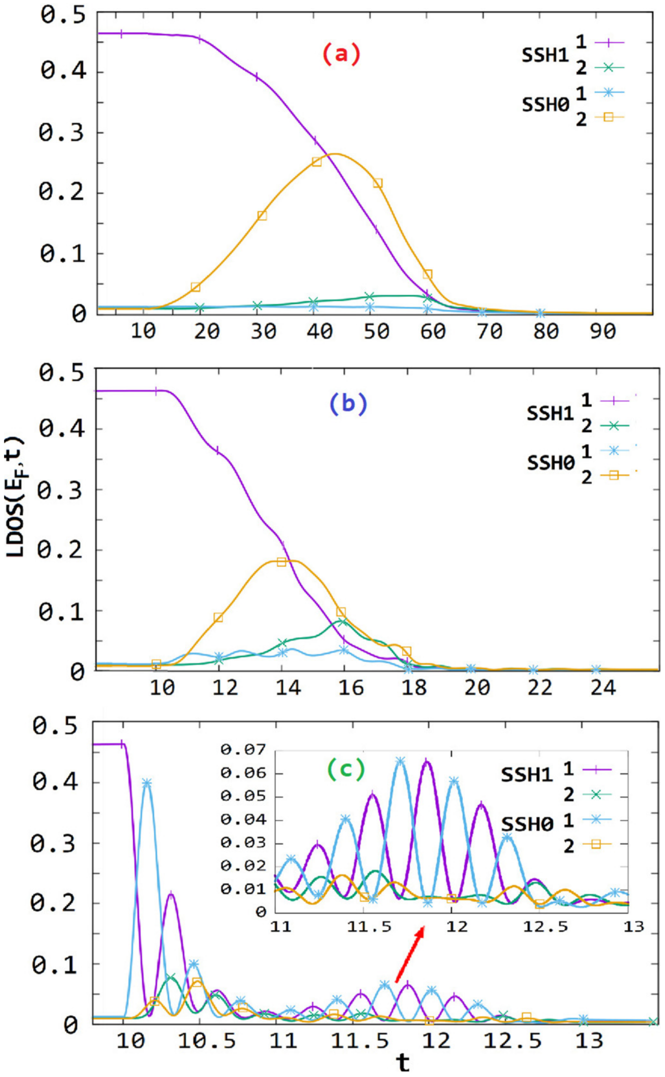

FIG. 9. LDOS at the Fermi energy at two sites ($i = 1$ and $i = 2$) for the same system as in Fig. 8: SSH$_0$-SSH$_1$ chains coupled together at $t = 10$ for different V_x changes (a), (b), and (c), respectively. All parameters are the same as in Fig. 8.

the quench were also observed for the Majorana probability mode where these oscillations increase as the rate of quench becomes larger [47] and for small rates these oscillations are hardly observed. Similarly, the induced midgap state in the SSH$_0$ chain appears for a moment with small oscillations. For larger t the energy gap is open again (trivial phase), and this induced state vanishes in time. Moreover, in this case the LDOS at the neighboring sites (in SSH$_1$—the second site, and in SSH$_0$—the first site) have small nonzero values after the quench and they also oscillate in time. It means that the SSH$_1$ topological state is now transferred also to the neighboring sites. However, for the abrupt change in V_x [sudden change from zero to a finite large value, panel (c) in Fig. 8] the system is transformed directly to the trivial phase and it never takes intermediate values of V_x. Thus, it is not obvious that the topological induced state could appear in the trivial chain during the quench. To answer this intriguing question we study this effect in the (c) panel and find that after the quench the system tends to the trivial phase [as was discussed in (a) and (b) panels], however, we observe that the midgap states appear for a short period of time at the Fermi level in both chains. These induced states do not vanish monotonically, but they reveal oscillations in time. The oscillations are strictly correlated with the vanishing topological state oscillations in the nontrivial SSH$_1$ chain and are analyzed in more details in Fig. 9, (c) panel. As one can see now the oscillations of LDOS(E_F) at the SSH$_0$ sites are in the same phase (blue and orange curves) and in the SSH$_1$ sites are in phase (purple and green curves). However, there are alternating (antiphase) oscillations between sites in both chains, thus, the maximal values of LDOS(E_F) at first SSH chain are correlated with minimal values of LDOS(E_F) at the second chain (Rabi-like oscillations). These vanishing oscillations can be considered as the topological state migration from site to site, which was investigated, e.g., along the Majorana wire [47] after the quench. In our case this effect appear between two sites from different chains (fast oscillations). There are also visible long-period oscillations which are related to the zero-energy state migration along the chain and depend on the energy gap and the sideband energies. These oscillations last relatively long in time, Fig. 8, bottom panels, thus, it makes possible to detect these induced topological states in double-chain structures.

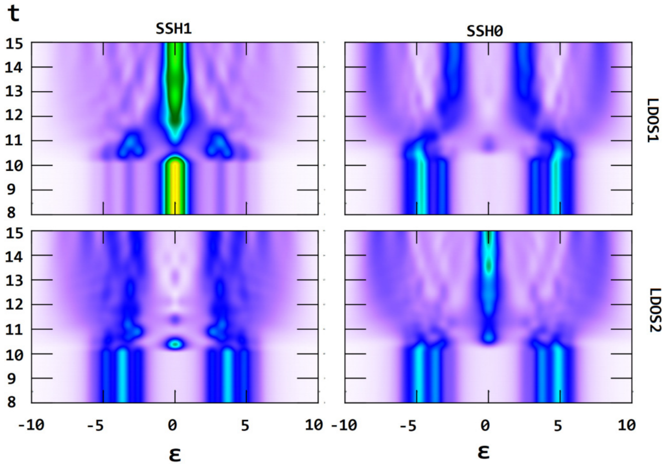

FIG. 10. Time evolution of the LDOS at $i = 1$ and $i = 2$ sites of atomic chains composed of $N = 8$ sites each being in different topological phases (SSH$_0$ and SSH$_1$). At $t = 10$ chains are immediately connected [similarly as in Fig. 8, (c)] $V_x = 3$ and all other parameters are the same as in Fig. 8. Yellow, green, and blue colors represent the LDOS values equal to 0.4, 0.2, and 0.1, respectively.

It is also interesting to analyze the SSH$_0$-SSH$_1$ system for a smaller change in the chain-chain coupling parameter V_x such that after the change the system still remains in the same topological phase. Surprisingly small, but a sudden change leads to unexpected results. In Fig. 10 we show LDOS dynamics at the first two sites of the SSH$_0$ and SSH$_1$ chains for a sudden quench at $t = 10$, and for $V_x = 3$ (thus, for $t > 10$ the system is in the nontrivial phase, cf. the energy spectrum in Fig. 7, bottom panel). In this case the edge midgap state (left upper panel) vanishes for a short period of time just after the quench. During this time zero-energy states appear at the neighboring sites. It is important that through these sites the SSH$_1$ topological state is partially transferred to the SSH$_0$

trivial chain (right bottom panel). For a longer time there are two midgap states in the system: (i) at the edge site in SSH$_1$ and (ii) at the second site in SSH$_0$. The intensity of the SSH$_1$ topological state decreases in comparison with its value before the quench (from a high value represented by a yellowlike color to the lower one—green color) because it leaks to the trivial SSH$_0$ chain. It is also worth noting that the electron occupancies of all sites in both chains do not change in time during this quench as the system is fully symmetrical.

To conclude, we have found that rapid change in V_x in the coupled SSH$_0$-SSH$_1$ system induces topological states in the trivial chain. As a main result we have observed that the SSH topological state can be partially transferred inside the system and exist simultaneously at different sites. It seems reasonable as for the coupled chains the unit cell is not longer the two-site primitive cell (as in the usual SSH chain) but is a four-site cell composed of two sites from the SSH$_0$ and two sites from the SSH$_1$ chains. Thus, the topological state of the coupled chains is still present at the end cell and can leak inside the cell.

C. Coulomb repulsion between atomic chains

Electron charge in a finite-length atomic chain can be distributed uniformly along the chain or can form charge waves called the Friedel oscillations [8,52]. These oscillations are the consequence of asymmetry of the spectral density functions at each site with respect to the Fermi energy. Note that charge oscillations are strongly suppressed in topological chains due to the energy gap in such systems. However, for a double-chain structure the charge waves along a given chain can be reproduced in the second one (in the same phase or in antiphase oscillations) in the presence of the Coulomb repulsion, but it is doubtful if these oscillations can appear in topological chains.

To answer this question in Fig. 11 we analyze the occupancies along two coupled chains (upper panel) obtained for $t \to \infty$ and $U^C = 0$ (thin curves) as well as in the presence of electron-electron repulsion $U^C = 5$ between both chains (thick curves). The charge waves in the normal chain at the substrate satisfy the condition for the period of three sites [52] ($\varepsilon_i = -V,\ U^C = 0$)—upper panel, thin broken green curve. In the vicinity of this chain there is a nontrivial topological chain SSH$_1$ with half-occupied sites (red solid line) and topological edge states. As one can see for nonzero U^C (thick lines) electrons in both chains repeal each other which leads, in general, to decreasing in the occupations in the normal and in the topological chains. However, charge oscillations in the normal chain are still observed, and they induce the Friedel oscillations along the topological chain. This effect is surprising and important for the studies of topological materials as there is an energy gap at the Fermi level in the SSH$_1$ chain. Note that high occupancy values in the normal chain stronger reduce charge values in the topological chain at the corresponding sites leading to the antiphase oscillations in this chain. It is also interesting that electron occupancy at the first site in the topological chain more rapidly decreases in comparison with the other site occupancies. It is a consequence of nontrivial midgap state at this site which in the presence of electron-electron repulsion is renormalized by the value of $U^C n_{1(\mathrm{nor})}$, where $n_{1(\mathrm{nor})}$ is the charge occupancy at the first site in the normal chain. Thus, even for small U^C the spectral density function is shifted towards higher energies and the electron occupancy at the first site drastically decreases whereas at other sites in the chain the changes are smaller due to the energy gap at the Fermi level.

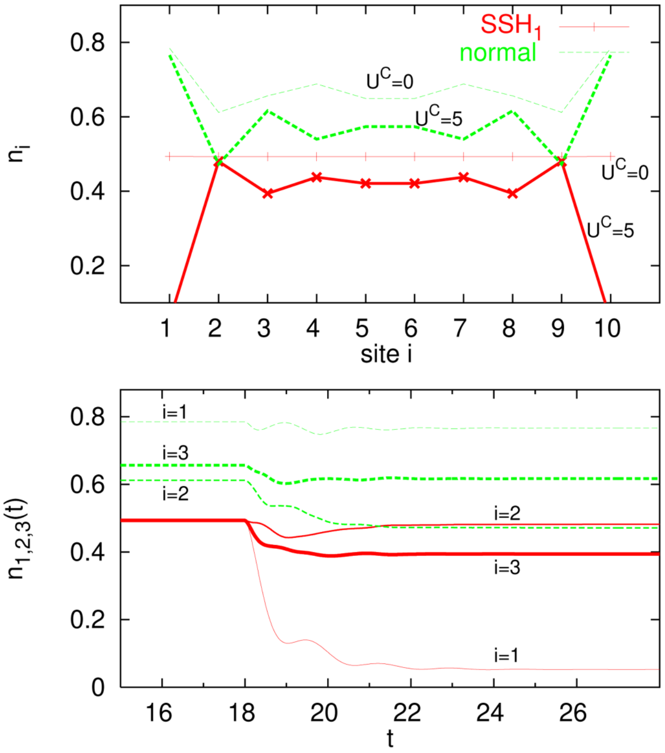

FIG. 11. Electron occupancies along the normal chain (broken green curves) and along the SSH$_1$ chain (solid red curves) of the length $N = 10$ for $U^C = 0$ (thin curves) and $U^C = 5$ (thick curves)—upper panel. The bottom panel shows time-dependent occupancies at $i = 1$–3 sites in both chains for a sudden change of the Coulomb repulsion $U^C = 0$ for $t < 18$ and $U^C = 5$ for $t \geqslant 18$. The other parameters are $V = 4,\ W = 1,\ \varepsilon_i = 0$ (topological chain) and $V,\ W = 4,\ \varepsilon_i = -V$ (normal chain). The lines in the upper panel are plotted for better visualization.

It is also interesting to analyze time evolution of the charge waves which are induced in the coupled chains of different topology. In Fig. 11, bottom panel, we show the occupancies at three sites of the normal chain (green broken curves) and the SSH$_1$ chain (red solid curves) for a sudden change in the Coulomb repulsion at $t = 18$ ($U^C = 5$). Before the Coulomb quench the occupancies are time independent and their values correspond to the steady case for $U^C = 0$. Also for $t \to \infty$ the electron occupancies reach their stationary values, the same as for $U^C = 5$ in the upper panel (thick curves). Just after the perturbation all occupancies change, and the time evolution of n_i shows vanishing oscillations. The period of these oscillations depends on the Coulomb repulsion and equals $T = \frac{2\pi}{U^C n_i}$ (which in our case is $T \simeq 1.6$). Thus, from the knowledge of time-dependent charge oscillations one can estimate the strength of the Coulomb interaction between the sites. It is worth noting that although the occupancies in general decrease in the presence of U^C, it is possible to inverse the occupancies between the neighboring sites in both chains and, e.g., at the second sites $i = 2$ for $U^C = 0$ the charge at the normal chain is larger that in the SSH chain, but for nonzero U^C the opposite relation is satisfied. This process can lead to the electron localization in topological chains due to the Coulomb repulsion.

IV. CONCLUSIONS

We have studied nonequilibrium electrical properties of 1D topological chains and coupled chains on a surface focusing on the energy-dependent spectral density function. For a single chain we have analyzed the transition process from the normal chain to the SSH nontrivial chain where the midgap edge state appears. It turns out that the timescale needed to build this state strongly depends on the surface and for the insulating substrate the system reaches its equilibrium state after hundreds units of time from the quench. Moreover, we have found that the edge state is formed dynamically from the intersidebands of the normal chain (in the first stage after the quench) and then next sidebands support this state after some further period of time. Thus, the midgap state does not appear immediately after the quench and is formed simultaneously with the bulk energy gap. We have also analyzed topological chain which suddenly breaks. In this case the midgap topological state as well as the local DOS at all sites do not change in time except for two sites which comprise new edges of two shorter chains. At these sites, which are characterized by the energy gap, new midgap states are built adiabatically in time from the LDOS sidebands.

We have also considered coupled atomic chains being in the same or in different topological phases (SSH_0 or SSH_1) and studied the time response of the spectral density functions on abruptly or adiabatically changing of the chain-chain couplings V_x. For the SSH_0-SSH_0 geometry the energy gap can be closed (for small V_x) or is still present in the system (for larger V_x), but the midgap topological state does not appear. It is important that for the SSH_1-SSH_1 system the midgap zero-energy state splits adiabatically into two sidebands for small V_x or vanishes for larger V_x—in the last case the energy gap is open in the system. The most interesting case we have observed for different phases of the coupled chains SSH_0-SSH_1. We have found that for larger values of V_x the system changes its phase (from nontrivial to the trivial one) and the midgap topological state vanishes. However, for the adiabatical change in V_x the topological SSH_1 state partially leaks to the trivial SSH_0 chain, and both midgap states exist simultaneously at two different sites. For abruptly changed V_x the topological as well as the induced topological states vanish in time with damping oscillations. These novel conclusions have been obtained from the detail analysis of the full space- and time-dependent LDOS, supported by the quasienergy spectra, which give us a wider perspective on the midgap topological states.

We have also investigated the electron correlation effects between the coupled chains and the induced Friedel oscillations along the SSH chain were found in the vicinity of the normal chain with standard charge waves. The induced out-of-phase Friedel oscillations in topological structures stands for a crucial point of the paper. These oscillations with very low electron occupancy at both end sites can be the essential feature of 1D topology in potential STM experiments.

ACKNOWLEDGMENTS

This work was partially supported by National Science Centre, Poland, under Grant No. 2018/31/B/ST3/02370.

APPENDIX A: EVOLUTION OPERATOR CALCULATIONS

Here we give some details on the charge occupancy and the current obtained within the evolution operator method [49,50]. To derive the time-dependent occupations at a given site $n_i(t)$, one has to find the expectation value of the total particle number operator $\hat{n}_{all}$, taken for the time-dependent state vector related with this site $|\alpha_i\rangle$,

$$n_i(t) = \langle\alpha_i(t)|\, \hat{n}_{all}\, |\alpha_i(t)\rangle\,. \tag{A1}$$

The total particle number of the system can be written as a sum over all electron states $\hat{n}_{all} = \sum_j \hat{n}_j + \sum_{\vec{k},j} \hat{n}_{\vec{k}j}$ and the unitary evolution operator describes time transformation of the state vector from its initial state $|\alpha_i(t_0)\rangle$ such that: $|\alpha_i(t)\rangle = U(t,t_0)\,|\alpha_i(t_0)\rangle$. Now the ith site occupancy can be written in the following form:

$$n_i(t) = \langle\alpha_i(t_0)|\, U^\dagger(t,t_0)| \sum_j \hat{n}_j + \sum_{\vec{k},j} \hat{n}_{\vec{k}j} |U(t,t_0)\,|\alpha_i(t_0)\rangle\,. \tag{A2}$$

Let us consider the first sum in the above equation with $\hat{n}_j$ operators. Using the unit operator for this system which contains all single-particle states at the initial time $\mathbb{1} = \sum_\alpha |\alpha(t_0)\rangle\,\langle\alpha(t_0)|$, one can obtain the formula,

$$\begin{aligned}
&\sum_j \langle\alpha_i(t_0)|\, U^\dagger(t,t_0)|\hat{n}_j|U(t,t_0)\,|\alpha_i(t_0)\rangle \\
&\quad = \sum_j \langle\alpha_i(t_0)|\, U^\dagger(t,t_0)|\mathbb{1}|\hat{n}_j|\mathbb{1}|U(t,t_0)\,|\alpha_i(t_0)\rangle \\
&\quad = \sum_j \sum_\alpha \sum_{\alpha'} \langle\alpha_i(t_0)|\, U^\dagger(t,t_0)\,|\alpha(t_0)\rangle\, \underbrace{\langle\alpha(t_0)|\,\hat{n}_j\,|\alpha'(t_0)\rangle}_{\delta_{\alpha,j}\delta_{\alpha',j}n_j(t_0)} \\
&\qquad \times \langle\alpha'(t_0)|\,U(t,t_0)\,|\alpha_i(t_0)\rangle = \sum_j n_j(t_0)|U_{i,j}(t,t_0)|^2,
\end{aligned} \tag{A3}$$

which stands for the first term of Eq. (2). The second term in Eq. (A2) includes the wave-vector summation $\sum_{\vec{k}j} \langle\alpha_i(t_0)|\,U^\dagger(t,t_0)|\hat{n}_{\vec{k}j}|U(t,t_0)\,|\alpha_i(t_0)\rangle$ and using similar calculations as above one finally obtains the second term in Eq. (2). The electron occupancy of the electrode state $\vec{k}_1$, needed for the current calculations, Eq. (3), can be obtained from the following relation [it can be derived in the same way as Eq. (A3)]:

$$n_{\vec{k}_1}(t) = \sum_{j=1}^{M} n_j(t_0)|U_{\vec{k}_1,j}(t,t_0)|^2 + \sum_{j,\vec{k}_j} n_{\vec{k}_j}(t_0)|U_{\vec{k}_1,\vec{k}_j}(t,t_0)|^2. \tag{A4}$$

Thus, for the initial occupations $n_j(t_0) = 0$, the current flowing, e.g., through the first chain site, Eq. (3), is expressed by the formula,

$$j_1(t) = -e\frac{d}{dt}\sum_{\vec{k}_1}\sum_{j,\vec{k}_j} n_{\vec{k}_j}(t_0)|U_{\vec{k}_1,\vec{k}_j}(t,t_0)|^2$$

$$= \sum_{\vec{k}_1}\sum_{j,\vec{k}_j} 2n_{\vec{k}_j}(t_0)\mathrm{Re}\left(U^*_{\vec{k}_1,\vec{k}_j}(t,t_0)\frac{d}{dt}U_{\vec{k}_1,\vec{k}_j}(t,t_0)\right). \tag{A5}$$

To find the equation for the evolution operator $U_{\alpha,\beta}(t)$ one can use Eq. (4), which can be written as follows: $i\frac{\partial}{\partial t}U_{\alpha,\beta}(t) = \langle\alpha|\,\hat{V}(t)U(t)\,|\beta\rangle$. On the right-hand side we use the unity operator and obtain the coupled set of differential equations,

$$\begin{aligned} i\frac{\partial U_{\alpha,\beta}(t)}{\partial t} &= \langle\alpha|\,\hat{V}(t)|\mathbb{1}|U(t)\,|\beta\rangle \\ &= \sum_{j'}\langle\alpha|\,\hat{V}(t)\,|j'\rangle\,\underbrace{\langle j'|\,U(t)\,|\beta\rangle}_{U_{j',\beta}(t,t_0)} \\ &\quad + \sum_{j',\vec{k}}\langle\alpha|\,\hat{V}(t)\,|\vec{k}_{j'}\rangle\,\underbrace{\langle\vec{k}_{j'}|\,U(t)\,|\beta\rangle}_{U_{\vec{k}_{j'},\beta}(t,t_0)}. \end{aligned} \tag{A6}$$

The terms with $\hat{V}(t)$ are obtained using the Hamiltonian and the relations below Eq. (4), and one can write

$$\begin{aligned} \langle\alpha|\,\hat{V}(t)\,|\beta\rangle &= \langle\alpha|\,U_0(t,t_0)|V(t)|U_0^\dagger(t,t_0)\,|\beta\rangle \\ &= \langle\alpha|\,U_0(t,t_0)|\mathbb{1}|V(t)|\mathbb{1}|U_0^\dagger(t,t_0)\,|\beta\rangle \\ &= (U_0)_{\alpha,\alpha}(t,t_0)(V(t))_{\alpha,\beta}(U_0^\dagger)_{\beta,\beta}(t,t_0), \end{aligned} \tag{A7}$$

where, e.g., $(U_0)_{\alpha,\alpha}(t,t_0) = \exp\left(i\int_0^t dt'\,\langle\alpha|\,H_0(t')\,|\alpha\rangle\right)$. In the same way one can write the differential equations for other evolution operator matrix elements, such as for $U_{\vec{k}_{j'},\beta}(t,t_0)$ and insert their formal solutions into Eq. (A6) which finally gives the integodifferential Volterra equation of the second kind, Eq. (5).

APPENDIX B: LAPLACE TRANSFORM CALCULATIONS

In this Appendix we show some technical aspects for the calculation of Eq. (8) for $U_{i,\vec{k}_j}(t)$ matrix elements. We start from the differential equation, Eq. (5), written for the regular chain of the same sites with vanishing Coulomb interactions and within the wideband approximation, i.e.,

$$i\frac{\partial U_{i,\vec{k}_j}(t)}{\partial t} = \sum_{i'} V_{ii'}U_{i',\vec{k}_j}(t) - V_{i,\vec{k}_j}e^{i(\varepsilon_0-\varepsilon_{\vec{k}_j})t} - i\frac{\Gamma_i}{2}U_{i,\vec{k}_j}(t). \tag{B1}$$

Now we use the Laplace transform technique for this equation, $F_{ij}(s) \equiv \mathcal{L}[U_{i,\vec{k}_j}(t)] = \int_0^{+\infty} U_{i,\vec{k}_j}(t)e^{-st}dt$, and obtain the following set of linear recursive equations on $F_{ij}(s)$ elements,

$$\left(s+\frac{\Gamma_i}{2}\right)F_{ij}(s) + iV_{i,i+1}F_{i+1,j}(s) + iV_{i,i-1}F_{i-1,j}(s)$$

$$= \frac{-iV_{i,\vec{k}_j}}{s-i(\varepsilon_0-\varepsilon_{\vec{k}_j})}\delta_{ij}. \tag{B2}$$

The formal solution of these Laplace transform functions can be written as

$$F_{ij}(s) = \frac{-iV_{i,\vec{k}_j}}{s-i(\varepsilon_0-\varepsilon_{\vec{k}_j})}A^{-1}_{ij}, \tag{B3}$$

where $A_{ij} = (s+\frac{\Gamma_i}{2})\delta_{ij} + iV_{ij}(\delta_{i+1,j}+\delta_{i,j+1})$ is the tridiagonal matrix ($N\times N$ dimension, A^N) for which the determinant can be expressed by the Chebyshev polynomials of the second kind. For the same couplings between sites $V_{ij} = V$ and $\Gamma_i = \Gamma$, the Laplace transform elements take the following form (e.g., for $i = 1$):

$$F_{1j}(s) = \frac{(-i)^jV^{j-1}V_{j,\vec{k}_j}}{s-i(\varepsilon_0-\varepsilon_{\vec{k}_j})}\frac{\det A^{N-j}}{\det A^N}, \tag{B4}$$

where $\det A^N = \prod_{j=1}^N (s+\frac{\Gamma}{2}+2iV\cos\frac{j\pi}{N+1})$. Now, to obtain the solutions in the time domain we have to calculate the inverse Laplace transforms: $U_{i,\vec{k}_j}(t) = \mathcal{L}^{-1}\{F_{ij}(s)\}$, which in our case can be performed analytically as the determinant of (B4) contains only the product terms of s variable. The final result is given by Eq. (8).

---

[1] M. Kopciuszyński, P. Dyniec, M. Krawiec, P. Łukasik, M. Jałochowski, and R. Zdyb, Pb nanoribbons on the si(553) surface, Phys. Rev. B **88**, 155431 (2013).

[2] J. N. Crain, J. L. McChesney, F. Zheng, M. C. Gallagher, P. C. Snijders, M. Bissen, C. Gundelach, S. C. Erwin, and F. J. Himpsel, Chains of gold atoms with tailored electronic states, Phys. Rev. B **69**, 125401 (2004).

[3] A. Baski, K. Saoud, and K. Jones, 1-d nanostructures grown on the si(5 5 12) surface, Appl. Surf. Sci. **182**, 216 (2001).

[4] M. Jałochowski, T. Kwapinski, P. Łukasik, P. Nita, and M. Kopciuszyński, Correlation between morphology, electron band structure, and resistivity of pb atomic chains on the si(553)-au surface, J. Phys.: Condens. Matter **28**, 284003 (2016).

[5] H. Ohnishi, Y. Kondo, and K. Takayanagi, Quantized conductance through individual rows of suspended gold atoms, Nature (London) **395**, 780 (1998).

[6] A. Yanson, G. Rubio-Bollinger, H. E. Brom, N. Agrait, and J. van Ruitenbeek, Formation and manipulation of a metallic wire of single gold atoms, Nature (London) **395**, 783 (1998).

[7] O. M. Auslaender, H. Steinberg, A. Yacoby, Y. Tserkovnyak, B. I. Halperin, K. W. Baldwin, L. N. Pfeiffer, and K. W. West, Spin-charge separation and localization in one dimension, Science **308**, 88 (2005).

[8] J. S. Shin, K.-D. Ryang, and H. W. Yeom, Finite-length charge-density waves on terminated atomic wires, Phys. Rev. B **85**, 073401 (2012).

[9] S. Nadj-Perge, I. K. Drozdov, J. Li, H. Chen, S. Jeon, J. Seo, A. H. MacDonald, B. A. Bernevig, and A. Yazdani, Observation of majorana fermions in ferromagnetic atomic chains on a superconductor, Science **346**, 602 (2014).

[10] R. Pawlak, M. Kisiel, J. Klinovaja, T. Meier, S. Kawai, T. Glatzel, D. Loss, and E. Meyer, Probing atomic structure and majorana wavefunctions in mono-atomic fe chains on superconducting pb surface, npj Quantum Inf. **2**, 16035 (2016).

[11] L. Li, Z. Xu, and S. Chen, Topological phases of generalized Su-Schrieffer-Heeger models, Phys. Rev. B **89**, 085111 (2014).

[12] L. Li, C. Yang, and S. Chen, Winding numbers of phase transition points for one-dimensional topological systems, Europhys. Lett. **112**, 10004 (2015).

[13] M. Benito, M. Niklas, G. Platero, and S. Kohler, Edge-state blockade of transport in quantum dot arrays, Phys. Rev. B **93**, 115432 (2016).

[14] V. Dal Lago, M. Atala, and L. E. F. Foa Torres, Floquet topological transitions in a driven one-dimensional topological insulator, Phys. Rev. A **92**, 023624 (2015).

[15] W. P. Su, J. R. Schrieffer, and A. J. Heeger, Solitons in Polyacetylene, Phys. Rev. Lett. **42**, 1698 (1979).

[16] R. Drost, T. Ojanen, A. Harju, and P. Liljeroth, Topological states in engineered atomic lattices, Nat. Phys. **13**, 668 (2017).

[17] J. K. Asboth, L. Oroszlany, and A. Palyi, *A Short Course on Topological Insulators* (Springer, Cham, Switzerland, 2016).

[18] M. Kurzyna and T. Kwapiński, Non-local electron transport through normal and topological ladder-like atomic systems, J. Appl. Phys. **123**, 194301 (2018).

[19] D. Xie, W. Gou, T. Xiao, B. Gadway, and B. Yan, Topological characterizations of an extended Su-Schrieffer-Heeger model, npj Quantum Inf. **5**, 55 (2019).

[20] V. M. Martinez Alvarez and M. D. Coutinho-Filho, Edge states in trimer lattices, Phys. Rev. A **99**, 013833 (2019).

[21] B. Pérez-González, M. Bello, Á. Gómez-León, and G. Platero, Interplay between long-range hopping and disorder in topological systems, Phys. Rev. B **99**, 035146 (2019).

[22] B. Pérez-González, M. Bello, Álvaro Gómez-León, and G. Platero, SSH model with long-range hoppings: topology, driving and disorder, arXiv:1802.03973.

[23] B.-H. Chen and D.-W. Chiou, An elementary rigorous proof of bulk-boundary correspondence in the generalized Su-Schrieffer-Heeger model, Phys. Lett. A **384**, 126168 (2020).

[24] X.-L. Lü and H. Xie, Topological phases and pumps in the Su-Schrieffer-Heeger model periodically modulated in time, J. Phys.: Condens. Matter **31**, 495401 (2019).

[25] J. H. Kang, J. H. Han, and Y. Shin, Creutz ladder in a resonantly shaken 1d optical lattice, New J. Phys. **22**, 013023 (2020).

[26] N. Sun and L.-K. Lim, Quantum charge pumps with topological phases in a creutz ladder, Phys. Rev. B **96**, 035139 (2017).

[27] J. Zurita, C. E. Creffield, and G. Platero, Topology and interactions in the photonic creutz and creutz-hubbard ladders, Adv. Quantum Technol. **3**, 1900105 (2019).

[28] K. Pöyhönen, A. Westström, J. Röntynen, and T. Ojanen, Majorana states in helical shiba chains and ladders, Phys. Rev. B **89**, 115109 (2014).

[29] D. Obana, F. Liu, and K. Wakabayashi, Topological edge states in the Su-Schrieffer-Heeger model, Phys. Rev. B **100**, 075437 (2019).

[30] J. Arkinstall, M. H. Teimourpour, L. Feng, R. El-Ganainy, and H. Schomerus, Topological tight-binding models from nontrivial square roots, Phys. Rev. B **95**, 165109 (2017).

[31] A. Gómez-León and G. Platero, Floquet-Bloch Theory and Topology in Periodically Driven Lattices, Phys. Rev. Lett. **110**, 200403 (2013).

[32] O. Balabanov and H. Johannesson, Robustness of symmetry-protected topological states against time-periodic perturbations, Phys. Rev. B **96**, 035149 (2017).

[33] T. Kitagawa, E. Berg, M. Rudner, and E. Demler, Topological characterization of periodically driven quantum systems, Phys. Rev. B **82**, 235114 (2010).

[34] T. Ochiai, Su-Schrieffer-Heeger-type Floquet network, arXiv:1811.11984.

[35] C. Jürß and D. Bauer, High-harmonic generation in Su-Schrieffer-Heeger chains, Phys. Rev. B **99**, 195428 (2019).

[36] M. Bello, C. E. Creffield, and G. Platero, Long-range doublon transfer in a dimer chain induced by topology and ac fields, Sci. Rep. **6**, 22562 (2016).

[37] J. Huneke, G. Platero, and S. Kohler, Steady-State Coherent Transfer by Adiabatic Passage, Phys. Rev. Lett. **110**, 036802 (2013).

[38] N. H. Le, A. J. Fisher, N. J. Curson, and E. Ginossar, Topological phases of a dimerized fermi–hubbard model for semiconductor nano-lattices, npj Quantum Inf. **6**, 24 (2020).

[39] T. Hensgens, T. Fujita, L. Janssen, X. Li, C. J. Van Diepen, C. Reichl, W. Wegscheider, S. Das Sarma, and L. M. K. Vandersypen, Quantum simulation of a fermi–hubbard model using a semiconductor quantum dot array, Nature (London) **548**, 70 (2017).

[40] F. A. Zwanenburg, A. S. Dzurak, A. Morello, M. Y. Simmons, L. C. L. Hollenberg, G. Klimeck, S. Rogge, S. N. Coppersmith, and M. A. Eriksson, Silicon quantum electronics, Rev. Mod. Phys. **85**, 961 (2013).

[41] E. J. Meier, F. A. An, and B. Gadway, Observation of the topological soliton state in the Su-Schrieffer-Heeger model, Nat. Commun. **7**, 13986 (2016).

[42] M. Parto, S. Wittek, H. Hodaei, G. Harari, M. A. Bandres, J. Ren, M. C. Rechtsman, M. Segev, D. N. Christodoulides, and M. Khajavikhan, Edge-Mode Lasing in 1d Topological Active Arrays, Phys. Rev. Lett. **120**, 113901 (2018).

[43] E. Taranko, M. Wiertel, and R. Taranko, Transient electron transport properties of multiple quantum dots systems, J. Appl. Phys. **111**, 023711 (2012).

[44] X. Li, Y. Meng, X. Wu, S. Yan, Y. Huang, S. Wang, and W. Wen, Su-Schrieffer-Heeger model inspired acoustic interface states and edge states, Appl. Phys. Lett. **113**, 203501 (2018).

[45] C.-C. Chien, K. A. Velizhanin, Y. Dubi, B. R. Ilic, and M. Zwolak, Topological quantization of energy transport in micromechanical and nanomechanical lattices, Phys. Rev. B **97**, 125425 (2018).

[46] A. Rajak and A. Dutta, Survival probability of an edge majorana in a one-dimensional p-wave superconducting chain under sudden quenching of parameters, Phys. Rev. E **89**, 042125 (2014).

[47] P. D. Sacramento, Fate of majorana fermions and chern numbers after a quantum quench, Phys. Rev. E **90**, 032138 (2014).

[48] C. H. Lee and J. C. W. Song, Quenched topological boundary modes can persist in a trivial system, arXiv:2002.11726.

[49] T. B. Grimley and K. L. Sebastian, Electron transfer in the reflection of atoms from metal surfaces, Surf. Sci. **124**, 305 (1983).

[50] T. Kwapiński, Conductance oscillations and charge waves in zigzag shaped quantum wires, J. Phys.: Condens. Matter **22**, 295303 (2010).

[51] T. Kwapiński, Conductance oscillations of a metallic quantum wire, J. Phys.: Condens. Matter **17**, 5849 (2005).

[52] T. Kwapiński, Charge fluctuations in a perfect and disturbed quantum wire, J. Phys.: Condens. Matter **18**, 7313 (2006).

PHYSICAL REVIEW B **102**, 245414 (2020)

Nontrivial dynamics of a two-site system: Transient crystals

M. Kurzyna and T. Kwapiński[*]
Institute of Physics, M. Curie Skłodowska University, 20-031 Lublin, Poland

(Received 14 August 2020; accepted 19 November 2020; published 14 December 2020)

We analyze theoretically quench dynamics of a two-site system abruptly driven from its equilibrium state focusing on the time dependent spectral density function. In the presence of electron reservoirs this function reveals in time a nontrivial regular pattern of peaks corresponding to the stationary quantum chain structure. Such dynamical system with periodic structure of the spectral density stands for a new transient crystal material. We investigate here the role of the Coulomb repulsion between the sites, nontrivial substrates and different system geometries on the transient crystal pattern which can be measured in the tunneling conductance experiments. We also propose the transient crystal system between unbiased leads as an effective monoparametric pump.

DOI: 10.1103/PhysRevB.102.245414

I. INTRODUCTION

Time response of a quantum system on external perturbations, transient effects, and quench dynamics have attracted considerable attention recently as they can provide much useful information about the system as well as due to potential applications of such structures in spintronics, quantum computing, or metrology. Many interesting effects were found for such systems driven by external forces like the turnstile effect, photon-assisted tunneling, spin and charge quantum pumps [1–5]. Time dependent processes may even lead to the appearance of novel solid state phases like the Floquet topological insulators [6,7] or time crystals [8–10]. In the most general sense time crystals are materials which somehow pulse or have structure behavior in time and their formation is quite analogous to the formation of space crystals [10]. However, in the presence of external periodic perturbation time crystals do not follow the period of the driving force but spontaneously switch to their own time periodicity which was confirmed experimentally [11,12].

Transient effects in atomic systems or quantum dots (QDs) have been intensively studied over recent years focusing on the charge oscillations and current dynamics (see Ref. [13] and references therein). For atomic molecules subjected to sudden perturbations (like the quenches or turnstiles) electronic and vibronic response time lies in the picosecond range like for a single semiconductor quantum dot [14,15] or for a double QD system [16]. On the other hand single-molecule devices work in the microwave regime. This motivates us to extend the molecular device investigations on the transient phenomena as the operation speed of such systems can significantly increase. A number of theoretical works studied the transient effects in different QD geometries as well as for a QD between superconducting leads [13,17,18]. The coherent oscillations and current beats for different types of time-dependent pulses can also provide an insight into the electronic structure of such systems, e.g., from detailed studies of the transient currents one can obtain the spin relaxation time [15] or the parameters defining the system [17].

Thus far theoretical studies on transient/quench effects have been mostly focused on the current (or charge) oscillations while the quench dynamics of the spectral density function related to the quantum system has been often overlooked. The spectral density function corresponds to the local density of states (DOS) at a given site due to its coupling with the continuum electron spectra in the electrode and expresses the possible states for electrons at this site. This function determines many electronic and optical properties of the system and can be experimentally investigated by the scanning tunneling microscope (STM) from the differential conductance characteristics. In this work we concentrate on the dynamical properties of the system composed of two coupled sites on a nontrivial surface focusing on the time dependent spectral density function and its evolution due to quantum quenches or linear perturbations. We expect that such a double-site system just after the quench exchanges information between the sites and can exhibit in time a peaked regular structure of the spectral density function. In this context it is desirable to answer the question *whether a two-atom nonequilibrium system could stand for a kind of time crystal?* Next: *How fast is the structure of the spectral density built in time and then how fast does it vanish after the quench? What is a role of the electron reservoir? Is the spectral density structure periodic or does it change irregularly with time?* We would like also to determine characteristic timescales needed for the spectral density peaks to develop or to disappear. In our studies we precisely address these questions and consider different system geometries and include the Coulomb repulsion between the sites. Moreover, real 2D substrate electrodes characterized by DOS with the van Hove singularities are considered which make the problem nontrivial especially for time dependent Hamiltonian. Note that for flat DOS a wide band limit (WBL) approximation is often used which drastically simplifies mathematical derivations and leads to analytical formulas for stationary as well as for driven

---

[*] tomasz.kwapinski@umcs.pl

©2020 American Physical Society

systems [19–21]. However, for real DOS (beyond the wide band) time dependent calculations need more sophisticated methods [21–24] and, e.g., within the Heisenberg equation of motion it is hardly possible to obtain the time-dependent local DOS. Moreover, nonequilibrium quantum systems (e.g. after the quench) between unbiased leads could be considered as monoparametric pumps. Such systems are of great interest as they involve a reduction of the system size due to a smaller number of contacts which lead to decreasing of dissipation processes in comparison with ordinary two-parameter pumps [2,4,25–34]. Additionally, monoparametric pumps eliminate dipolelike forces which appear in the presence of two or more external time-dependent fields (with a phase shift between them) [35]. Here, we propose the transient crystal system between unbiased electrodes as an effective monoparametric pump. To analyze the pumping currents, electron occupancies, and the spectral density dynamics we use a tight-binding Hamiltonian and the evolution operator technique which was successfully applied for arbitrary time dependence of external perturbations [20,21,24,36]. This method allows us to find some analytical time-dependent formulas for the evolution operator matrix elements within the Laplace transform technique.

The paper is organized as follows. In Sec. II, we describe the theoretical model and the calculation method. In Sec. III, the main results of the paper are discussed for the transient crystal. In Sec. IV the role of the real DOS structure of the electrode is analyzed; in Sec. V different system configurations are discussed. Section VI is devoted to the monoparametric pumping and the Coulomb repulsion between sites is studied in Sec. VII. The last section gives a short summary.

II. MODEL AND THEORETICAL DESCRIPTION

The model under consideration consists of two coupled electron sites (double QD, two-state system, atomic dimer) on the substrate or between external electrodes. We are going to analyze time dynamics of the spectral density related to both sites, the occupancies, and the pumping currents flowing through the system. The total time dependent Hamiltonian can be written in the second quantization notation as follows:

$$H = H_{\text{lead}} + H_0(t) + V(t)\,, \tag{1}$$

where electrons in the leads are described by the term $H_{\text{lead}} = \sum_\alpha \sum_{k\alpha} \varepsilon_{k\alpha} c^\dagger_{k\alpha} c_{k\alpha}$, similarly the Hamiltonian for electrons at the central system takes the form: $H_0(t) = \sum_i \varepsilon_i c^\dagger_i c_i + U^C c^\dagger_1 c_1 c^\dagger_2 c_2$, and the coupling term: $V(t) = V_{12} c^\dagger_1 c_2 + \sum_{i,k\alpha} V_{i,k\alpha}(t) c^\dagger_{k\alpha} c_i + \text{H.c.}$ Here $\alpha = L, R$ concerns the left or the right lead, $i = 1, 2$ describes the central sites (atoms, QDs), and $c_{k\alpha}(c^\dagger_{k\alpha})$, $c_i(c^\dagger_i)$ are the electron annihilation (creation) operators at the appropriate site. The electron transition between atoms is established by V_{12} coupling and between leads and the central system by $V_{i,k\alpha}$ matrix elements. In the above Hamiltonian $\varepsilon_{k\alpha}$ stands for the electron energy spectrum of the αth lead, and ε_i represents the atomic energy levels. For simplicity each site is characterized by a single electron level with the interdot Coulomb interaction between the sites. We investigate the system dynamics due to different time-dependent perturbations like quantum quenches or adiabatically changed coupling parameters.

The time evolution of the dimer spectral density function is described in terms of the evolution operator $U(t, t_0)$ given in the interaction representation by the following equation (we assume $\hbar = 1$):

$$\begin{aligned} i\frac{dU(t,t_0)}{dt} &= \tilde{V}(t,t_0)U(t,t_0) \\ &= U_0(t,t_0)V(t)U_0^\dagger(t,t_0)U(t,t_0)\,, \end{aligned} \tag{2}$$

where $U_0(t, t_0) = T \exp{(i \int_{t_0}^t dt'(H_{\text{lead}}(t') + H_0(t')))}$ and T denotes the time ordering. It is assumed that for $t < t_0$ electron states in the system are decoupled and the couplings are switched on at $t = t_0$ leading to the transient effects. The electron occupation number can be obtained from the knowledge of the appropriate evolution operator matrix elements $\langle i|U|k\alpha\rangle = U_{i,k\alpha}(t, t_0)$:

$$n_i(t) = \sum_{k,\alpha} n_{k\alpha}(t_0)|U_{i,k\alpha}(t,t_0)|^2\,. \tag{3}$$

The spectral density function at each site (also called the local DOS) for the zero temperature can be obtained from the relation:

$$\rho_i(E,t) = \sum_\alpha D_\alpha(E)|U_{i,\alpha}(E,t,t_0)|^2\,, \tag{4}$$

where $D_\alpha(E)$ is the lead's density of states and we use the notation $U_{i,k\alpha}(t, t_0) = U_{i,\alpha}(E, t, t_0)$. In our calculations the Coulomb interdot term is considered in the form of the electrostatically interaction which in the mean field approach takes the form: $U^C c^\dagger_1 c_1 n_2(t) + U^C c^\dagger_2 c_2 n_1(t)$, where $n_i(t)$ is the time dependent expectation value of the appropriate site occupation. In this case the matrix elements $U_{i,k\alpha}(t, t_0)$ for $t_0 = 0$ can be obtained using Eq. (2) from the following integrodifferential Volterra equations of the second kind:

$$\begin{aligned} \frac{dU_{1,kL}(t)}{dt} &= -iV_{12}e^{iU^C(N_2(t)-N_1(t))}U_{2,kL}(t) \\ &\quad - iV_{1,kL}e^{i(\varepsilon_0-\varepsilon_{kL})t}e^{iU^C N_2(t)} - V^2_{1,kL} \\ &\quad \times \int_0^t dt' D_L(t-t')e^{i\varepsilon_0(t-t')}e^{iU^C\int_{t'}^t n_2(\tau)d\tau}U_{1,kL}(t'), \end{aligned} \tag{5}$$

$$\begin{aligned} \frac{dU_{2,kL}(t)}{dt} &= -iV_{12}e^{iU^C(N_1(t)-N_2(t))}U_{1,kL}(t) - V^2_{2,kR} \\ &\quad \times \int_0^t dt' D_R(t-t')e^{i\varepsilon_0(t-t')}e^{iU^C\int_{t'}^t n_1(\tau)d\tau}U_{2,kL}(t'), \end{aligned} \tag{6}$$

where we assume the same onsite electron energies $\varepsilon_1 = \varepsilon_2 = \varepsilon_0$, and $N_i(t) = \int_0^t n_i(t')dt'$. Here $D_\alpha(t-t') = \int d\varepsilon D_\alpha(\varepsilon)\exp(-i\varepsilon(t-t'))$ is the Fourier transform of the electron density of states in the αth electrode. The similar differential relations can be written for $U_{i,kR}(t)$ elements. To find the solution for the evolution operator as a function of time it is necessary to know the charge occupations $n_i(t)$ which are obtained from the knowledge of $U_{i,k\alpha}(t)$ elements. Thus, the problem is not trivial and in general analytical solutions of these equations do not exist. Moreover, the Fourier transforms of the lead DOS, $D(t-t')$, appearing in the right hand side of Eq. (5) and Eq. (6), have no analytical form for arbitrary $D(E)$ (besides some symmetrical DOS functions, like, e.g., the rectangular or Lorentzian DOS). Thus in general we solve the integrodifferential equations [Eqs. (5) and (6)] numerically for a given leads DOS. However, for some specific system parameters, using the Laplace transformation technique, we can obtain some interesting analytical relations and discuss them in the text.

The current flowing from the surface electrode can be obtained from the time derivative of the total number of electrons in this lead:

$$j_L(t) = -e\frac{d}{dt}\sum_{kL} n_{kL}(t)\,, \tag{7}$$

where the electrode occupation, $n_{kL}(t)$, is expressed similarly to Eq. (3) by $U_{k\alpha,k'\alpha'}(t,t_0)$ matrix elements which satisfy the set of integrodifferential equations in the form of Eq. (5) and Eq. (6).

III. 1D TRANSIENT CRYSTAL

In this section we consider a two-site system coupled via the first site with only one (left, L) electrode such that the second site is decoupled from the lead (vertical geometry). For such a case, using Eq. (5) and Eq. (6) and for no Coulomb repulsion, $U^C = 0$, one can write the following set of differential equations for $U_{i,kL}(t)$ elements:

$$\begin{aligned}\frac{dU_{1,kL}(t)}{dt} &= -iV_{12}U_{2,kL}(t) - iV_{1,kL}e^{i(\varepsilon_0-\varepsilon_{kL})t} - \frac{\Gamma}{2}U_{1,kL}(t)\\ \frac{dU_{2,kL}(t)}{dt} &= -iV_{12}U_{1,kL}(t),\end{aligned} \tag{8}$$

where $\Gamma = \Gamma_L = 2\pi\sum_{kL}|V_{1,kL}|^2\delta(E-\varepsilon_{kL})$, i.e., the structureless DOS of the surface electrode is assumed (wide band approximation). The above set of differential equations can be resolved analytically using the Laplace transformation method, $\mathcal{L}\{U_{i,kL}(t)\} = F_i(s)$, which leads to the following solutions for the transformed functions:

$$\begin{aligned}F_1(s) &= \frac{-isV_{1,kL}}{(s-s_0)(s-s_1)(s-s_2)}\\ F_2(s) &= \frac{-VV_{1,kL}}{(s-s_0)(s-s_1)(s-s_2)},\end{aligned} \tag{9}$$

where $s_0 = i(\varepsilon_0 - \varepsilon_{kL})$ and $s_{1/2} = -\frac{\Gamma}{4} \pm \sqrt{\frac{\Gamma^2}{4} - 4V^2}$. In this case the inverse Laplace transformation for $F_i(s)$ can be calculated analytically and after some algebra one obtains time-dependent evolution operator matrix elements:

$$\begin{aligned}U_{1,kL}(t) = {}& \frac{-iV_{1,kL}s_0}{(s_0-s_1)(s_0-s_2)}e^{s_0t} + \frac{-iV_{1,kL}s_1}{(s_1-s_0)(s_1-s_2)}e^{s_1t}\\ &+ \frac{-iV_{1,kL}s_2}{(s_2-s_0)(s_2-s_1)}e^{s_2t}\,,\end{aligned} \tag{10}$$

and similar for $U_{2,kL}(t)$ elements, where one should change $-iV_{1,kL}s_i$ into $-V_{12}V_{1,kL}$ in all nominators in the above equation. It is worth noting that the first part of the above relation oscillates in time while the second and third terms vanish nonmonotonically due to the exponent functions with s_1 and s_2 (which real parts are negative). Analytical solutions for $U_{i,kL}(t)$ evolution operator matrix elements within the WBL allow us to obtain the current form Eq. (7):

$$\begin{aligned}j_L(t) = {}& -2Im\left\{\sum_{kL} n_{kL}(0)V_{kL}e^{i(\varepsilon_{kL}-\varepsilon_0)t}U_{1,kL}(t)\right\}\\ &- \Gamma n_1(t)\,,\end{aligned} \tag{11}$$

where $n_{kL}(0)$ stands for the initial occupation of electron states in the electrode which is related to the Fermi distribution function, and we assume $e = 1$. The relations for $U_{i,kL}(t)$, Eq. (10), have a more transparent form for $\varepsilon_{kL} = \varepsilon_0 = 0$, which can be written as follows (we define $x = \frac{\Gamma}{4V_{12}}$):

$$\begin{aligned}U_{1,kL}(t) &= \frac{-iV_{1,kL}}{V\sqrt{x^2-1}}e^{-\frac{\Gamma}{4}t}\sinh(V_{12}\sqrt{x^2-1}t)\,,\\ U_{2,kL}(t) &= \frac{-V_{1,kL}}{V_{12}} + \frac{-V_{1,kL}}{V_{12}}e^{-\frac{\Gamma}{4}t}\\ &\quad\times\left\{\cosh(V_{12}\sqrt{x^2-1}t)\right.\\ &\quad\left.+\frac{x}{\sqrt{x^2-1}}\sinh(V_{12}\sqrt{x^2-1}t)\right\}.\end{aligned} \tag{12}$$

These analytical relations for $U_{i,kL}(t)$ allow us to analyze time dynamics of the spectral density functions at both sites. In our calculations all energies are expressed in the units of $\Gamma_L = \Gamma \equiv 1$, time in $\hbar/\Gamma$ units (which for $\Gamma = 1$ meV equals 0.6 ps), and the energy reference point is the left electrode Fermi energy, $E_F = 0$, moreover a shortened notation of the site-site coupling $V_{12} = V$ is used.

In the beginning we analyze dynamical formation in time of the spectral density function for $\Gamma_L = 1$, $\Gamma_R = 0$ (vertical geometry). In Fig. 1 we show the local DOS dynamics related to the second site, $\rho_2(E,t)$, for different values of the site-site coupling parameter, $V = 0.4, 2, 4$, and 8, from the upper to bottom panel, respectively. The quench takes place at $t = 0$ (for $t < 0$ we have $V = 0$, $\Gamma_\alpha = 0$) and for $t \to \infty$ the spectral density corresponds to the stationary case, i.e., it is characterized by two peaks localized for $E = \pm V$. These peaks for relatively small V parameter overlap each other which is visible in the upper panel (for $V = 0.4$). It results directly from Eq. (12) where for $t \to \infty$ the evolution operator matrix element for the Fermi energy $E = 0$ does not vanish, $U_{2,kL} = \frac{-V_{1,kL}}{V}$, and thus $\rho_2(E = 0, t \to \infty) \sim \frac{V_{1,kL}^2}{V^2}$. It means that the spectral density function at the Fermi level vanishes for larger V but for smaller V (for $x > 1$, i.e., for $\Gamma > 4V$) it monotonically increases after the quench (without oscillations). For larger values of V ($x < 1$) the spectral function $\rho_2(E,t)$ reveals an interesting structure as a function of time (see three bottom panels in Fig. 1). In the beginning one wide peak of $\rho_2(E,t)$ appears and for large t only two side peaks at $E = \pm V$ are observed which stand for the steady solution of the double-site system. However, as a main feature of this quench we observe interference patterns of the spectral density function between the main stationary DOS peaks. These patterns come from the evolution in time of the spectral density at both sites in the presence of the electron reservoir.

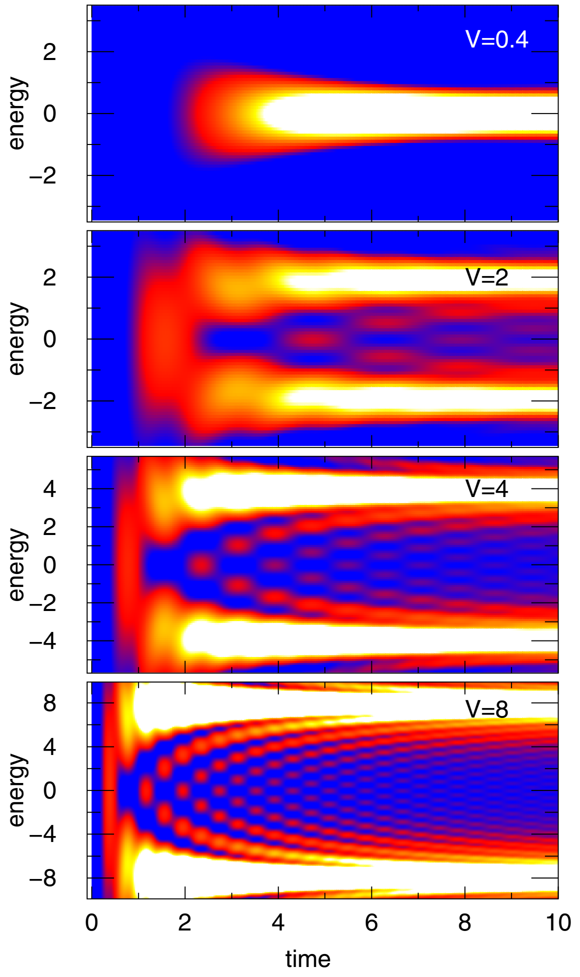

FIG. 1. Spectral density function $\rho_2(E,t)$ of the two-site system after the quench at $t=0$ (for $t<0$: $\Gamma_{L/R}=0$ and $V=0$). For $t>0$ the site-site coupling is $V=0.4$, 2, 4, and 8 (from upper to bottom panels, respectively) and $\Gamma_L=1$. The other parameters are $\Gamma_R=0$, $V_{1,kL}=4$, $V_{2,kL}=V_{1,kR}=V_{2,kR}=0$, $\varepsilon_0=0$, $U^C=0$. The units of all energies and time are $\Gamma_L=\Gamma$ and $\hbar/\Gamma$, respectively.

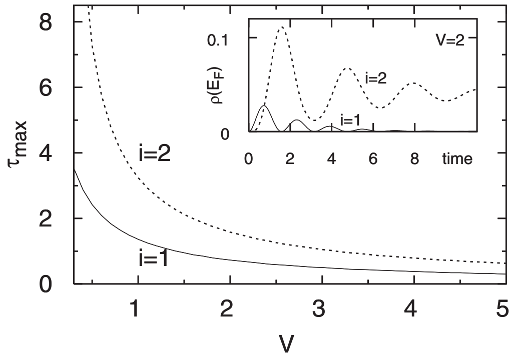

FIG. 2. Time of the first maximum in $\rho_i(E,t)$ as a function of the coupling parameter V for $i=1$ (solid curve) and $i=2$ (broken curve). The inset shows time evolution of the spectral density function at the Fermi level for $V=2$ and $i=1$ and 2, respectively. The other parameters are the same as in Fig. 1; $\tau_{\max}$ is expressed in the time units, $\hbar/\Gamma$.

Due to the coupling with the substrate just after the quench a single DOS peak at the first site appears. This information, after some time, reaches the second site, and its spectrum, $\rho_2(E,t)$, broadens leading to a single-peak DOS structure at this site—in the second panel ($V=2$) it appears for $t=1.5$. Next, the spectral density function at the second site is rebuild due to the presence of the first site and two-peaked DOS structure is observed for a moment, for $t=3.1$. However, the system is not in its equilibrium state (it is just after the quench) and still evolves in time—the spectral density peaks become narrower and this information bounces between both sites leading (for a short period of time) to appearance of a three-state spectral density function with maximal value of DOS at the Fermi level (for $t=4.7$), then four-state DOS (for $t=6.3$) and so on. This process repeats again and again and one observes M-site dynamical structure of DOS in the double-site system (see also the third and fourth bottom panels). This structure, however, vanishes with time as the system tends to the equilibrium state with two-peaked spectral density function. The substrate acts here as a dissipative electrode thus nonequilibrium oscillations vanish in time. The internal patterns of the dynamical local DOS correspond to the structure of DOS (or the conductance) of 1D stationary atomic chain, cf. Fig. 1 from Ref. [37], i.e., for a given time it is characterized by the structure of the M-site chain. Thus the two-site system after the quench has structure behavior in time, which stands for a kind of 1D transient crystal material. Of course this structure is quasiperiodic which means that it pulses/changes in time in a very regular way. Note that for the dimer decoupled from the leads such structure of the transient crystal does not appear and only regular and nonvanishing in time Rabi oscillations are observed.

It is worth mentioning that just after the quench the spectral density does not change immediately but there is some delay time until the information about continues electron states in the electrode reaches the second site. This time interval depends on the coupling between both sites and it decreases with increasing V, cf. the upper and bottom panels in Fig. 1 for $t=2.5$ and 0.25, respectively. We analyze this process in Fig. 2 where we define the delay time of the spectral density function, $\tau_{\max}$, as a time at which $\rho_{1/2}(E,t)$ reaches its first maximum. In the insight in Fig. 2 we show the time evolution of the density functions at both sites corresponding to the Fermi level ($E=E_F=0$) for $V=2$. Note that the spectral density oscillates in time with the period equals $T=\frac{\pi}{V\sqrt{1-x^2}}$ and with decreasing amplitude. For these $\rho_{1/2}(E,t)$ curves the first maximum appears for $\tau_{\max}=0.7$ (the first site) and $\tau_{\max}=1.5$ (the second site). One expects that $\tau_{\max}$ for the first site, which is directly coupled with the electrode, should not depend on the site-site coupling, V, as the information from the substrate flows only through the coupling parameter $V_{1,kL}$ (or Γ_L). Surprisingly, this conclusion is invalid and the appearance of the first maximum at this site depends on the coupling with the second site (decoupled from the electrode). It can be confirmed by analytical calculations of the spectral density functions $\rho_1(E_F,t)$ and $\rho_2(E_F,t)$. From Eq. (12) we calculate the positions of the first maxima which for $i=1$ can be expressed as: $\tau_{\max}=\frac{\ln(x+\sqrt{x^2-1})}{V\sqrt{x^2-1}}$ for $x>1$ and $\tau_{\max}=\frac{\arctan(\sqrt{1-x^2}/x)}{V\sqrt{1-x^2}}$ for $x<1$, and similar for $i=2$. These functions

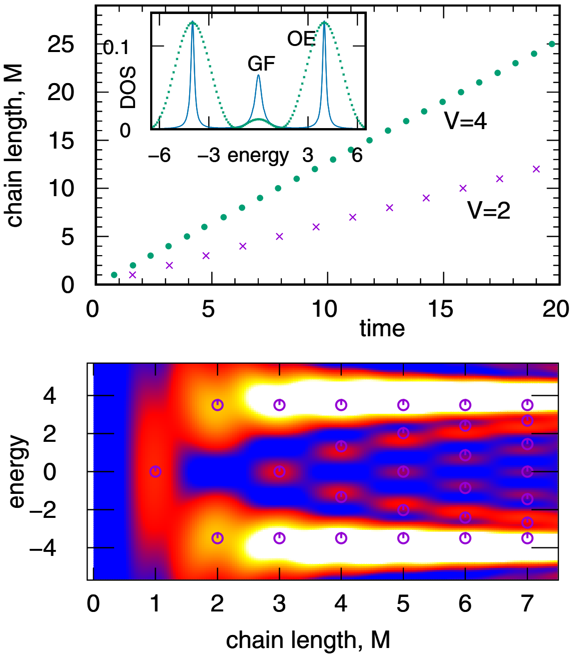

FIG. 3. (Upper panel) Effective chain length, M, as a function of time for the system described in Fig. 1 for $V = 4$ (dots) and $V = 2$ (crosses). The inset figure shows the spectral density function (normalized DOS) obtained for $M = 3$ linear sites within the Green function method with the effective coupling, $V_M = 2.83$, $\varepsilon_i = 0$ (solid curve) and for the dimer taken at time $t = 2.3$ after the quench for $V = 4$ (dotted curve). The bottom panel shows time dependent spectral density function for $V = 4$ with indicated effective chain lengths, M. The circles correspond to maxima of equilibrium DOS obtained for M-site linear chain for $V_M = V/2.3\cos(\frac{\pi}{M+1})$. The other parameters are the same as in Fig. 1.

in both cases depend on the site-site coupling parameter, V, which is visible in Fig. 2 and in general the time delay decreases monotonically with V. It is interesting that from the knowledge of $\tau_{\max}$ one can estimate the coupling parameter between the sites. Moreover, the difference in time delay between both sites $\Delta\tau$ (between the broken and solid curves in Fig. 2) is responsible for the time travel of the information between these sites. This quantity can be derived analytically and has relatively transparent form:

$$\Delta\tau = \frac{4}{\sqrt{4V^2 - \Gamma^2}}\left(\frac{\pi}{2} + \arcsin\frac{\Gamma}{4V}\right). \tag{13}$$

One can see that for large value of V, the difference $\Delta\tau$ is very small and tends to zero (two-site system stands for a strongly coupled molecule, $V > V_{1,kL}$) but for smaller V it increases rapidly. It is worth noting that this function depends nonlinearly on the site-site coupling.

The spectral density function of the double-site system reveals a regular pattern of peaks (transient crystal) which correspond to a chain of the effective length M. It is desirable to analyze how this effective chain length M changes in time after the quench in this system. To tackle this problem we study the positions of peaks of the spectral density function in time and adjust them to the effective chain length. The results are depicted in Fig. 3 (upper panel) for $V = 2$ (crosses) and $V = 4$ (dots). It is well visible that this dependence is linear for both cases. The linearity of $M(t)$ is a consequence of constant information rate which bounces between the sites. We have found that the structure of the effective chain length M appears for $t = \frac{2\pi M}{\sqrt{(2V)^2-\Gamma^2}}$ and, e.g., the local DOS corresponding to $M = 5$ chain length exists in the two-atom system for $t = 8.1$ ($V = 2$) after the quench. Moreover, for weaker couplings V the effective chain length increases much slower than for larger V (which is also visible in Fig. 1 where peaks' density changes with V). It allows us to observe M-sites structure of the double-site system even for larger times.

In the inset in Fig. 3 we compare the structure of stationary DOS obtained for $M = 3$ sites chain with the dimer spectral density function captures at time $t = 2.3$ for $V = 4$. Here the Green function (GF) method was used for the model composed of a linear chain on the substrate with the same electron energies, ε_0, and uniform effective site-site couplings, V_M. The stationary spectral density is obtained from the knowledge of the imaginary part of the site Green function, $DOS_i(E) = -\frac{1}{\pi}ImG^r_{ii}(E)$, and G^r_{ii} is found from the equation of motion for the retarded Green functions, cf., e.g., Ref. [37]. We have found that the positions of DOS peaks in the energy scale agree for both models. The differences result from the system dynamics after the quench, i.e., the intensities of the inside peaks as well as their widths for the two-site system change dynamically in time leading (for large time) to the equilibrium two-peaked structure of DOS. The general correspondence between the spectral density function of the double-site system and the M-site linear chain is shown in the bottom panel in Fig. 3. Here, on the transient crystal pattern we overplot the positions of the local DOS peaks assigned to the steady chain of the length M (circles in the bottom panel). As one can see the agreement between the dynamical structure of the two-atom system and static 1D chain DOS is quite satisfying.

IV. BEYOND THE WIDE BAND LIMIT

The transient crystal pattern appears for the two-state system after the quench in the presence of continuum electron states. In real physical systems the electron reservoir can be characterized by nontrivial band structure with peaks (van Hove singularities), gaps, or surface states. For such systems the wide band limit approximation fails and one should describe lead electrons in a more adequate way which is a nontrivial task especially for time dependent studies [21–24]. Therefore in this section we consider a more realistic model of the lead DOS as it can strongly modify the spectral density of the double-site system. We will check whether the spectral density pattern for the dimer survives in the presence of real structure of the surface DOS. In our calculations we take into consideration three different cases of the lead DOS structure shown in Fig. 4. There are: a rectangular DOS (curve A), 2D-tight binding with a single van Hove peak in the middle of the band (curve B), and DOS with two van Hove peaks with a local minimum in the middle of the band (curve C). The last two curves correspond to the 2D tight-binding rectangular and honeycomb (hexagonal) lattice which have analytical forms expressed in terms of the elliptic integrals of the first kind [38,39]. Note that in our calculations beyond the WBL one needs the time transform of DOS [as in Eq. (5) and Eq. (6)]

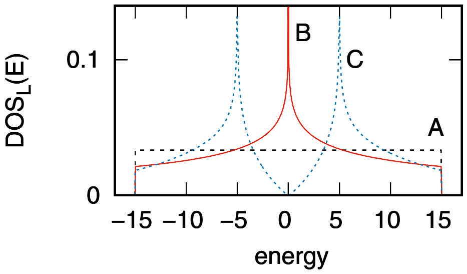

FIG. 4. Electrode density of states considered in the calculations: rectangular DOS (curve A), 2D square lattice DOS with the van Hove singularity (curve B), and 2D honeycomb (hexagonal) lattice DOS with two van Hove singularities (curve C) [38,39]. The energy unit is Γ, all curves are normalized to 1, and each DOS width is $w = 30\Gamma$.

and, e.g., for the rectangular DOS, $D(E) = \frac{\Theta(w/2-|E|)}{w}$, ($w$ is the DOS bandwidth and Θ is the Heaviside step function), the time Fourier transform has a simple analytical solution, $D(t) = \frac{\sin(tw/2)}{tw/2}$.

The spectral density function for the double-site system coupled vertically with the lead (surface electrode) described by different DOS structures is shown in Fig. 5 (A, B, and C, from the upper to bottom panels). As one can see the rectangular DOS of the electrode slightly modifies in time the spectral density pattern of the system in comparison with the results obtained within the wide band approximation, cf. Fig. 1, the third panel for $V = 4$. It results from the fact that the rectangular DOS can be well substituted by the wide band structure especially for energies lying in the middle of the band. For the surface DOS with the van Hove singularity in the middle of the band, panel B, one observes clear amplification of peaks intensities in the structure of the spectral density function. This effect results from larger values of DOS of the surface band near the Fermi level in comparison with the rectangular DOS, cf. Fig. 4. Thus the transient crystal can be observed for such DOS structure even for larger times. The situation changes for two van Hove singularities in DOS, panel C (hexagonal lattice). In this case the dimer spectral density near the Fermi level is strongly reduced due to low surface DOS at the Fermi level and the spectral density pattern is hardly visible. It is worth noting that the spectral density peaks appear at the same energies and at the same time for all considered surface DOS. Thus the surface structure does not influence the transient crystal pattern in general but can change its intensity.

V. OTHER CONFIGURATIONS

In this section we study the role of different geometries of the system on 1D transient crystal patterns. First in Fig. 6 we consider a linear change of the site-site coupling from zero to $V = 4$ within 5 time units (between $t = 10$ and $t = 15$). Thus we assume that there is a single site at the electrode and at a given time, $t = 10$, the second site is coupled with it. As one can see the evident peaked pattern of the spectral density appears with decreasing intensities. The first spectral density peak which appears just after $t = 10$ is broadened and exists longer in time than for the sudden quench. Moreover, one observes a linear change of the main DOS peaks in time (tilted white ridges) up to the time when the site-site coupling is constant. It is the reason that the structure of 1D transient crystal with DOS peaks is slightly squeezed in the energy scale and shifted in time.

Thus far we have investigated two-site systems in the vertical geometry at the surface. In real situations they can

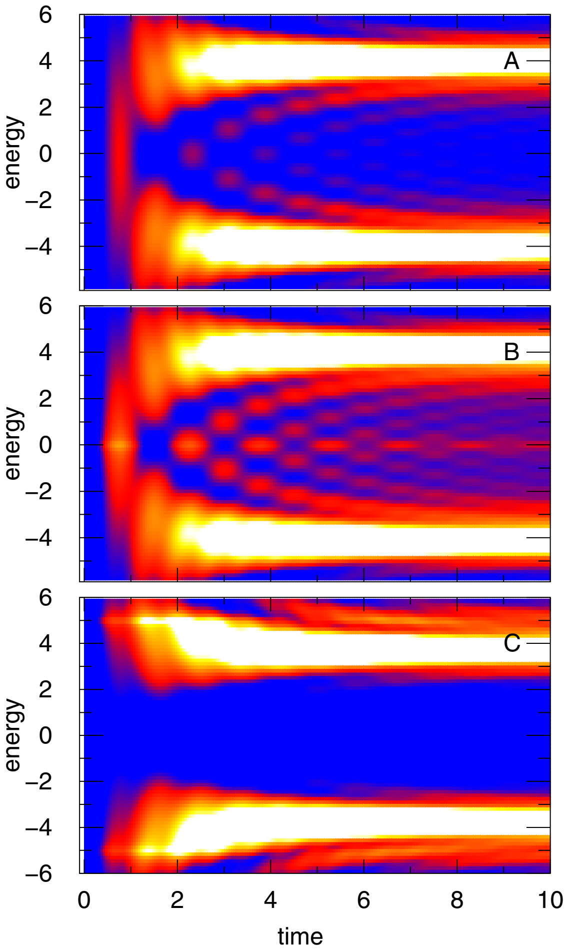

FIG. 5. Spectral density function $\rho_2(E, t)$ of the two-site system coupled vertically with the lead characterized by different DOS shown in Fig. 4, curves A, B, and C (upper, middle, and bottom panel, respectively). The other parameters are the same as in Fig. 1, $V = 4$.

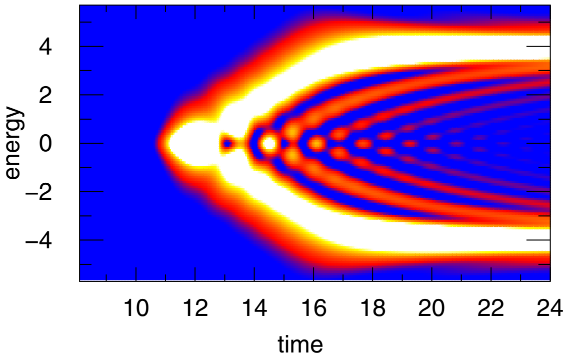

FIG. 6. Spectral density function $\rho_2(E, t)$ for linear change of V from $V = 0$ (at $t = 10$) up to $V = 4$ (for $t \geqslant 15$). The other parameters are the same as in Fig. 1.

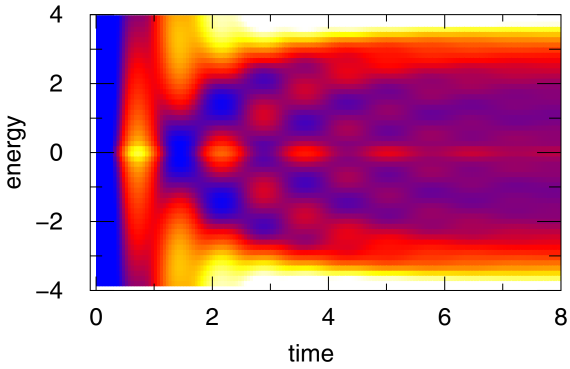

FIG. 7. Spectral density function of the two-site system in the horizontal geometry $\rho_2(E,t)=\rho_1(E,t)$ after the quench with the substrate characterized by 2D tight-binding DOS with a van Hove peak in the middle of the band. The other parameters are the same as in Fig. 1, $V=4$, $V_{1,kL}=V_{2,kR}=V_k=2.82$.

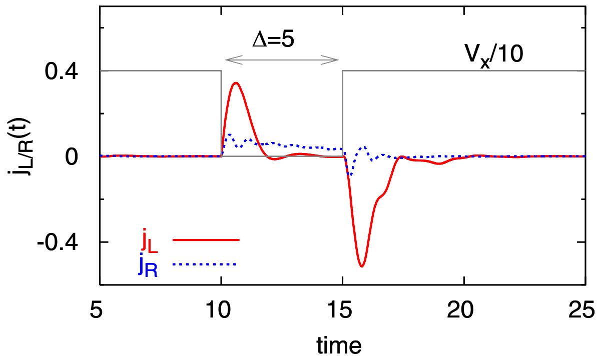

FIG. 8. Time dependent currents flowing from the left (red solid curve) and from the right (blue broken curve) electrodes for $\varepsilon_0=-2$. The coupling $V=4$ was switched off at $t=10$ for a period of $\Delta=5$ time units (black dotted line). The left (right) electrode is characterized by 2D-TB DOS with one (two) van Hove singularity (see Fig. 4), both DOS are symmetrical and their widths are $w=50$ energy units, the current unit is $e\Gamma/\hbar$.

be also coupled horizontally or can be situated between two electrodes (as for a DQD system). In this case the evolution operator matrix elements $U_{i,kL}(t)$ needed to obtain the spectral density satisfy similar equations to Eq. (8) [for this horizontal geometry in the second equation one should add the term: $-\frac{\Gamma}{2}U_{2,kL}(t)$], and for the wide band approximation and symmetrical couplings $\Gamma_L=\Gamma_R=\Gamma$ ($V_{1,kL}=V_{2,kR}=V_k$) we can obtain the Laplace transformations for the evolution operator elements: $F_1(s)=-iV_k(s+\frac{\Gamma}{2})/N$, and $F_2(s)=-VV_k/N$, where $N=[s-i(\varepsilon_0-\varepsilon_k)](s+\frac{\Gamma}{2}-iV)(s+\frac{\Gamma}{2}+iV)$. After some algebra the inverse Laplace transformations for them can be obtained as follows (for $\varepsilon_k=E_F=0$):

$$\begin{aligned}U_{1,kL}(t)&=\frac{-iV_k}{\left(\frac{\Gamma}{2}\right)^2+V^2}\\&\quad\times\left(\frac{\Gamma}{2}-e^{-\frac{\Gamma}{2}t}\frac{\Gamma}{2}\cos(Vt)+Ve^{-\frac{\Gamma}{2}t}\sin(Vt)\right)\\U_{1,kR}(t)&=\frac{V_k}{\left(\frac{\Gamma}{2}\right)^2+V^2}\\&\quad\times\left(-V-e^{-\frac{\Gamma}{2}t}\frac{\Gamma}{2}\sin(Vt)+Ve^{-\frac{\Gamma}{2}t}\cos(Vt)\right)\end{aligned}\tag{14}$$

and the spectral density function at the Fermi level (which is the same for both sites) can be written in the following form:

$$\rho_{1/2}(t)=\frac{1}{2\pi}\frac{1}{V^2+\left(\frac{\Gamma}{2}\right)^2}\left(1+e^{-\Gamma t}-2e^{-\frac{\Gamma}{2}t}\cos(Vt)\right).\tag{15}$$

It is interesting that in this case the oscillation period of $\rho_i(E,t)$ is exactly the same as for the isolated dimer system (Rabi oscillations), i.e., $T=2\pi/V$. Apparently, for the system decoupled from the substrate these oscillations do not vanish in time but here due to nonzero Γ parameter they exponentially decrease. Note that the oscillations of the spectral density in the horizontal geometry are also observed for other nonconstant surface DOS (for which analytical formulas do not exist). In Fig. 7 we show the results for the two-site horizontal system coupled with the lead (surface electrode) described by the 2D tight-binding DOS with the van Hove singularity at the Fermi level. As one can see the transient crystal pattern is well visible in this case with a larger intensity of peaks for $E\simeq 0$ related to the van Hove singularity at the Fermi level. As before, the oscillation period of $\rho_i(E,t)$ corresponds to the Rabi oscillations.

VI. MONO-PARAMETRIC PUMPING

We have shown that a two-site system coupled with the electrode reveals regular oscillations for a short period of time after the quench. During this time the system is out of equilibrium thus it can be proposed as an effective monoparametric electron pump. In doing so we consider two electron sites between unbiased leads and change nonadiabatically in time only the site-site coupling parameter, V. In Fig. 8 we analyze the left and right currents flowing through such a system for suddenly vanishing in time coupling strength V at $t=10$ and switched on again at $t=15$, as is indicated by the broken black curve. The system is space symmetrical but here we consider two different density of states of the left and right leads, i.e., with one (left lead) or two (right lead) van Hove singularities, Fig. 4. It leads to asymmetry which is crucial for the pumping effect (in the case of the same structure of the left and right DOS electrons are not pumped through the system). Before the perturbation, $t<10$, the spectral density of the two-site system is characterized by two peaks localized below and above the Fermi energy (in our case at $E=\varepsilon_0\pm V=-6,+2$) thus both sites are almost half occupied. At $t=10$ the sites are decoupled and the local DOS is transformed to a single peak DOS with the maximum at $E=\varepsilon_0=-2$ which lies below the Fermi energy. In this case the occupancies of both sites increase and the electrons flow from the leads to the sites (the currents are positive). It is evident that for the electrode with larger DOS around the Fermi energy this process occurs much faster (red curve) in comparison with the electrode with low DOS(E_F), blue curve. At $t=15$ the sites are coupled together again and their spectral density evolves

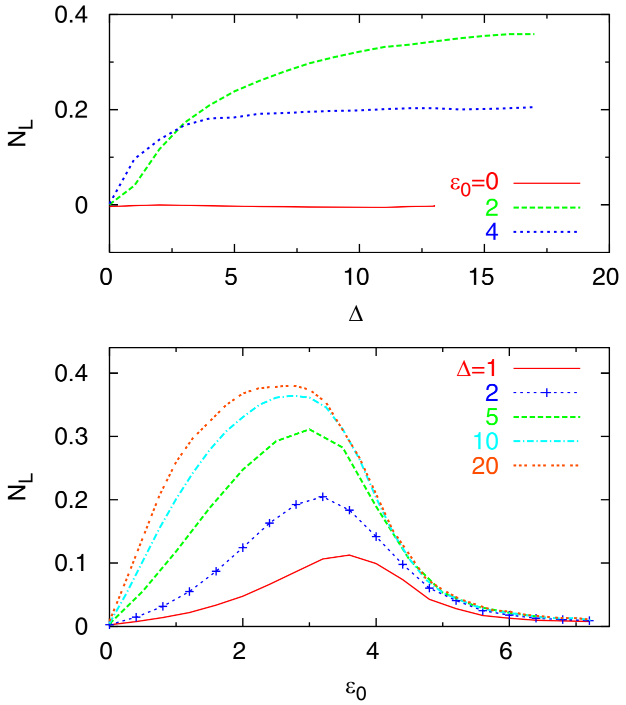

FIG. 9. Pumped charge through the two-site system between the unbiased leads during the changing of V parameter (shown in Fig. 8) as a function of Δ for $\varepsilon_0 = 0, 2, 4$ (upper panel) and as a function of ε_0 for $\Delta = 0, 2, 5, 10, 20$ (bottom panel). The unit of Δ is $\hbar/\Gamma$.

in time to the same structures as before the quench (with two peaks of DOS lying below and above the Fermi energy). This is the reason that some excess charge, related to the state below the Fermi energy, has to leave the sites and the current is negative. After about 5 time units from the quench ($t > 20$) the system reaches its steady state and the currents vanish. During this process the transient crystal pattern appears at both sites as was discussed in Fig. 7 but the left and right sites are charged/discharged with different rates, e.g., the right site is charged very slowly due to low DOS of the right lead at the Fermi energy. Thus after the quench (for $t > 15$) the excess charge flows to the right electrode (very slowly) but also to the left electrode through the first site. Nonuniform charge migration after the quench leads to electron pumping in the double-site system using only one time dependent parameter (monoparametric pumping) and it is desirable to analyze this phenomenon in more details.

The net charge flowing from the left/right electrode can be calculated by integration of the time-dependent currents, i.e., $N_{L/R} = \int j_{L/R}(t)dt$. We assume only one cycle of $V(t)$ variations shown in the upper panel in Fig. 8, and obtain the net charge, N_L, flowing from/to the left electrode (extension to periodic cycles is straightforward). Both sites are decoupled during the period of Δ and the system is in the same equilibrium state before and after the perturbation. First we are interested how Δ parameter influences the pumping charge and in Fig. 9, upper panel, we show the charge flowing from the left electrode, N_L, as a function of Δ for various onsite energies, ε_0. As one can see for $\Delta = 0$ electrons do not flow through the system (there is no quench). For nonzero Δ and symmetrical local DOS at both sites (symmetrical versus the Fermi energy) the net charge also does not flow (red line). However, in the presence of asymmetry in the local DOS ($\varepsilon_0 = 2, 4$) green and blue curves) the charge is pumped and increases for small Δ. For larger Δ it tends to some constant value which means that for this perturbation maximal charge is pumped through the system. Note also that for negative ε_0 the charge is pumped from the right to the left electrode and for positive ε_0 the current direction is opposite. Thus the gate voltage can effectively control the electron current direction in the system.

In order to reveal further the role of the onsite energies on the pumping current we analyze in the bottom panel of Fig. 9 the net charge as a function of ε_0 for different Δ parameter indicated in the legend. As before for $\varepsilon_0 = 0$ (symmetrical case) the charge is not pumped through the system independently of Δ. Also for large ε_0 electrons are not transferred between electrodes because there are no local DOS peaks at the Fermi level in both sites. Maximal pumped charge is observed for average values of ε_0 when there is asymmetry in the spectral density function and simultaneously there is nonzero DOS at the Fermi level. The pumped charge depends on the Δ parameter—for small Δ maximal N_L appears for $\varepsilon_0 \simeq V$ which corresponds to the local DOS peak at the Fermi energy but for larger Δ the system reaches its steady state after each change of V and maximal value of N_L is observed for $\varepsilon_0 = V/2$.

VII. TRANSIENT CRYSTAL PATTERN IN THE PRESENCE OF THE COULOMB REPULSION

Electron correlations in low dimensional systems can play an important role leading to, e.g., the Kondo effect, Coulomb blockade, spin-charge separation, and others. However, in many real atomic structures the correlation effects are marginal and can be omitted (like for Pb atoms on vicinal surfaces [40]) or can be described effectively as an electrostatic coupling between charged electron sites. In this section we consider the Coulomb electrostatic coupling between the sites and check whether the Coulomb repulsion influences or destroys the transient crystal pattern. In general, even for the wide-band approximation analytical solutions of Eqs. (5) and (6) do not exist. However, in the limit of small U^C, e.g., for the two-site system coupled only with one electrode, instead of the integrodifferential Volterra equations of the second kind we have the following ones:

$$\begin{aligned}\frac{dU_{1,kL}(t)}{dt} &= -iVe^{iU^C(n_2(t)-n_1(t))t}U_{2,kL}(t)\\&\quad - iV_{1,kL}e^{i(\varepsilon_0+U^Cn_2(t)-\varepsilon_{kL})t} - \frac{\Gamma}{2}U_{1,kL}(t)\\\frac{dU_{2,kL}(t)}{dt} &= -iVe^{iU^C(n_1(t)-n_2(t))t}U_{1,kL}(t)\,.\end{aligned} \tag{16}$$

Unfortunately, due to the time dependent occupations, $n_i(t)$, the Laplace transform technique cannot be applied to find analytical solutions. Further approximations, like the assumption that $n_i(t)$ does not depend on time [only in the RHS of Eq. (16)] lead to unphysical effects. Thus in the paper we consider finite values of U^C and show the results obtained numerically for small U^C and wide band approximation

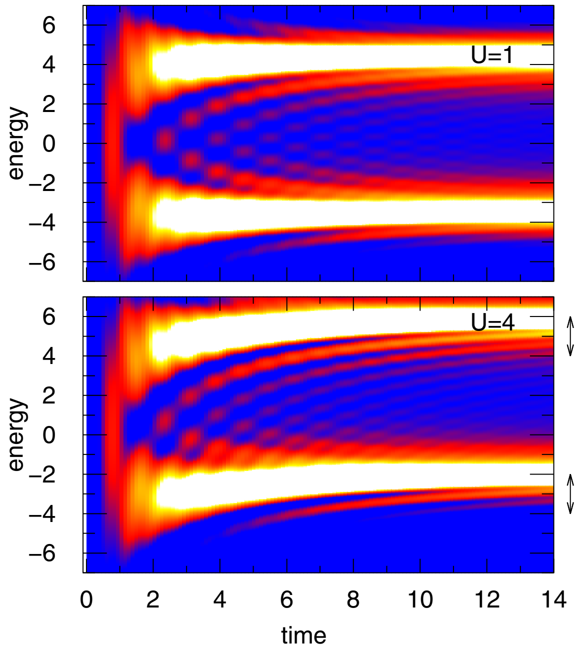

FIG. 10. Time dependent spectral density function of the two-site system after the quench at $t = 0$ for small Coulomb repulsion between sites $U^C = 1$ (upper panel) and for the stronger one, $U^C = 4$, (bottom panel). The arrows indicate the energy shifting of the stationary peaks of the local DOS due to the Coulomb repulsion. The other parameters are the same as in Fig. 1, $V = 4$.

according to Eq. (16) and for larger U^C and beyond the WBL (rectangular lead DOS) using Eq. (5) and Eq. (6).

In order to reveal the role of the Coulomb repulsion on the transient crystal pattern we analyze in Fig. 10 the spectral density function for weak electron-electron repulsion, $U^C = 1$ (upper panel), and for $U^C = 4$ (bottom panel). As one can see the structure of $\rho_2(E, t)$ for small U slightly differs from that from Fig. 1 obtained for $U^C = 0$ and for $V = 4$. However, for larger U^C we observe that the spectral density is shifted and the main DOS peaks for $t \to \infty$ appear for $E = \pm V + U^C n(t)$: The occupation number in our case tends to 0.5 thus $U^C n(t) \to 2$ which was indicated in Fig. 10 by the arrows. It leads to modifications of the spectral density pattern but the transient crystal structure of the local DOS peaks is still visible. Note that similar behavior of the conductance spectra (shifting towards higher energies) was observed for N-site linear chain in the presence of the Coulomb interactions obtained within the slave boson and mean-field techniques [41]. Here this effect holds in time for only the two-site system which additionally confirms its relation with the DOS structure behavior of 1D chains.

VIII. CONCLUSIONS

In this work we have studied the dynamical properties of a system composed of two coupled sites focusing on the time dependent spectral density function and its evolution due to quantum quenches and linear perturbations. Using the evolution operator technique and tight-binding Hamiltonian we have found that the spectral density function reveals a very regular structure of peaks in the time domain. This peaked pattern oscillates in time, and it corresponds to a quantum chain density of states with increasing chain length. Thus it stands for a new material which is characterized by the pulsed structure changing regularly in time. This transient crystal exists for nonequilibrium systems (e.g., after the quench) and vanishes as the system tends to its steady state so it cannot be classified strictly as a time crystal. We have also shown that the predicted pattern of the transient crystal could be observed for two-site systems on different electrodes with the van Hove singularities as well as for different system geometries. Additionally, we have found that in the presence of the Coulomb repulsion between sites the spectral density function is shifted towards higher energies but the transient crystal pattern is still visible in the system.

Moreover, using the series of quantum quenches we propose an effective monoparametric pump based on the transient crystal system between unbiased leads. In the presence of two different lead DOS, by changing in time only the coupling parameter between the sites, the net electron charge can be transferred in the system. In this case the transient crystal pattern appears together with the pumping current whose direction can be determined by the gate voltage potential.

It is believed that our results will bring new perspectives to a wide range of time-dependent crystals. They can be verified experimentally using time spectroscopy techniques or in photonic crystals.

ACKNOWLEDGMENTS

This work was partially supported by National Science Centre, Poland, under Grant No. 2018/31/B/ST3/02370.

---

[1] T. H. Oosterkamp, L. P. Kouwenhoven, A. E. A. Koolen, N. C. van der Vaart, and C. J. P. M. Harmans, Phys. Rev. Lett. **78**, 1536 (1997).

[2] L. P. Kouwenhoven, A. T. Johnson, N. C. van der Vaart, A. van der Enden, C. J. P. M. Harmans, and C. T. Foxon, Z. Phys. B-Condensed Matter **85**, 381 (1991).

[3] R. H. Blick, R. J. Haug, J. Weis, D. Pfannkuche, K. v. Klitzing, and K. Eberl, Phys. Rev. B **53**, 7899 (1996).

[4] S. K. Watson, R. M. Potok, C. M. Marcus, and V. Umansky, Phys. Rev. Lett. **91**, 258301 (2003).

[5] G. Platero and R. Aguado, Phys. Rep. **395**, 1 (2004).

[6] N. H. Lindner, G. Refael, and V. Galitski, Nat. Phys. **7**, 490 (2011).

[7] G. Usaj, P. M. Perez-Piskunow, L. E. F. Foa Torres, and C. A. Balseiro, Phys. Rev. B **90**, 115423 (2014).

[8] F. Wilczek, Phys. Rev. Lett. **109**, 160401 (2012).

[9] K. Sacha, Phys. Rev. A **91**, 033617 (2015).

[10] K. Sacha and J. Zakrzewski, Rep. Prog. Phys. **81**, 016401 (2017).
[11] S. Choi, J. Choi, R. Landig, G. Kucsko, H. Zhou, J. Isoya, F. Jelezko, S. Onoda, H. Sumiya, V. Khemani, C. von Keyserlingk, N. Y. Yao, E. Demler, and M. D. Lukin, Nature (London) **543**, 221 (2017).
[12] J. Zhang, P. W. Hess, A. Kyprianidis, P. Becker, A. Lee, J. Smith, G. Pagano, I.-D. Potirniche, A. C. Potter, A. Vishwanath, N. Y. Yao, and C. Monroe, Nature (London) **543**, 217 (2017).
[13] R. Taranko, T. Kwapiński, and T. Domański, Phys. Rev. B **99**, 165419 (2019).
[14] T. Fujisawa, Y. Tokura, and Y. Hirayama, Phys. Rev. B **63**, 081304(R) (2001).
[15] T. Fujisawa, D. G. Austing, Y. Tokura, Y. Hirayama, and S. Tarucha, J. Phys.: Condens. Matter **15**, R1395 (2003).
[16] T. Hayashi, T. Fujisawa, H. D. Cheong, Y. H. Jeong, and Y. Hirayama, Phys. Rev. Lett. **91**, 226804 (2003).
[17] E. Taranko, M. Wiertel, and R. Taranko, J. Appl. Phys. **111**, 023711 (2012).
[18] T. Kwapiński and R. Taranko, Physica E **63**, 241 (2014).
[19] A.-P. Jauho, N. S. Wingreen, and Y. Meir, Phys. Rev. B **50**, 5528 (1994).
[20] R. Taranko, T. Kwapiński, and E. Taranko, Phys. Rev. B **69**, 165306 (2004).
[21] Y.-Q. Zhou, R.-Q. Wang, L. Sheng, B. Wang, and D. Y. Xing, Phys. Rev. B **78**, 155327 (2008).
[22] J. Maciejko, J. Wang, and H. Guo, Phys. Rev. B **74**, 085324 (2006).
[23] Y. Zhu, J. Maciejko, T. Ji, H. Guo, and J. Wang, Phys. Rev. B **71**, 075317 (2005).
[24] T. Kwapiński, R. Taranko, and E. Taranko, Phys. Rev. B **66**, 035315 (2002).
[25] M. Switkes, C. M. Marcus, K. Campman, and A. C. Gossard, Science **283**, 1905 (1999).
[26] B. Roche, R.-P. Riwar, B. Voisin, E. Dupont-Ferrier, R. Wacquez, M. Vinet, M. Sanquer, J. Splettstoesser, and X. Jehl, Nat. Commun. **4**, 1581 (2013).
[27] L. E. F. Foa Torres, Phys. Rev. B **72**, 245339 (2005).
[28] M. G. Vavilov, L. DiCarlo, and C. M. Marcus, Phys. Rev. B **71**, 241309(R) (2005).
[29] L. DiCarlo, C. M. Marcus, and J. S. Harris, Phys. Rev. Lett. **91**, 246804 (2003).
[30] L. E. F. Foa Torres, H. L. Calvo, C. G. Rocha, and G. Cuniberti, Appl. Phys. Lett. **99**, 092102 (2011).
[31] T. Aref, V. F. Maisi, M. V. Gustafsson, P. Delsing, and J. P. Pekola, Europhys. Lett. **96**, 37008 (2011).
[32] P. San-Jose, E. Prada, S. Kohler, and H. Schomerus, Phys. Rev. B **84**, 155408 (2011).
[33] Y. Zhou and M. W. Wu, Phys. Rev. B **86**, 085406 (2012).
[34] T. Kwapiński and R. Taranko, Eur. Phys. J. B **88**, 140 (2015).
[35] S. Kohler, J. Lehmann, and P. Hänggi, Phys. Rep. **406**, 379 (2005).
[36] T. Grimley, V. Jyothi Bhasu, and K. Sebastian, Surf. Sci. **121**, 305 (1983).
[37] T. Kwapiński, J. Phys.: Condens. Matter **17**, 5849 (2005).
[38] T. C. Choy, Phys. Rev. Lett. **55**, 2915 (1985).
[39] T. Horiguchi, J. Math. Phys. **13**, 1411 (1972).
[40] M. Jałochowski, T. Kwapiński, P. Łukasik, P. Nita, and M. Kopciuszyński, J. Phys.: Condens. Matter **28**, 284003 (2016).
[41] M. Krawiec and T. Kwapiński, Surf. Sci. **600**, 1697 (2006).

applied sciences

MDPI

Article

Electron Pumping and Spectral Density Dynamics in Energy-Gapped Topological Chains

Marcin Kurzyna † and **Tomasz Kwapiński** *,†

Department of Physics, Maria Curie-Sklodowska University, PL20031 Lublin, Poland; marcin.kurzyna@live.umcs.edu.pl

* Correspondence: tomasz.kwapinski@umcs.pl

† These authors contributed equally to this work.

Abstract: Electron pumping through energy-gapped systems is restricted for vanishing local density of states at the Fermi level. In this paper, we propose a topological Su–Schrieffer–Heeger (SSH) chain between unbiased leads as an effective electron pump. We analyze the electron transport properties of topologically trivial and nontrivial systems in the presence of external time-dependent forces in the form of one-Gaussian or two-Gaussian perturbations (train impulses). We have found that the topologically trivial chain stands for much better charge pump than other normal or nontrivial chains. It is important that, during the perturbation, electrons are pumped through the mid-gap temporary states or through the induced sidebands states outside the energy gap. We also analyze the local density of states dynamics during the quench transition between different topological phases of the SSH chain. It turns out that after the quench, the edge topological states migrate through other sites and can temporarily exist in a topologically trivial part of the system. The tight-binding Hamiltonian and the evolution operator technique are used in our calculations.

Keywords: quantum dots; charge pumping; topology; atomic chains

check for updates

Citation: Kurzyna, M.; Kwapiński, T. Electron Pumping and Spectral Density Dynamics in Energy-Gapped Topological Chains. *Appl. Sci.* **2021**, *11*, 772. https://doi.org/10.3390/app11020772

Received: 7 December 2020
Accepted: 11 January 2021
Published: 15 January 2021

Publisher's Note: MDPI stays neutral with regard to jurisdictional claims in published maps and institutional affiliations.

Copyright: © 2021 by the authors. Licensee MDPI, Basel, Switzerland. This article is an open access article distributed under the terms and conditions of the Creative Commons Attribution (CC BY) license (https://creativecommons.org/licenses/by/4.0/).

1. Introduction

Atomic wires are the thinnest electrical conductors, and they can be used in plenty of applications [1–4]. Many new quantum effects were observed in such systems as spin-charge separation [5], charge-density waves [6] or Majorana topological states [7,8]. Non-equilibrium one-dimensional (1D) systems reveal much richer physics and in the presence of time-dependent perturbations the turnstile effect, photon-assisted tunneling, or coherent destruction of tunneling [9–14] can appear. Dynamical phenomena in 1D structures can also lead to novel solid-state phases such as the Floquet topological insulators [15], time crystals [16–18] or transient crystals [19].

For a quantum system between unbiased leads the electron current does not flow in the stationary case. However, in the presence of non-equilibrium phenomena (e.g., time-dependent forces or perturbations) electrons can be transferred between leads even without the source-drain voltage which leads to the electron pumping effect. This effect has been the subject of many theoretical and experimental works [18,20–25]—it was observed in single and double quantum dot (QD) systems for periodical changes of two or more device-control parameters [20,26] which were responsible for the left-right spatial symmetry breaking of the whole system. Please note that in the presence of the spatial symmetry the probability of electron tunneling from the central system to the left or to the right lead is exactly the same. The pumping current can be also generated for breaking the time-reversal symmetry in the system e.g., by adding the second harmonic to the driving potential or in the presence of time-dependent dipole-like forces [25]. In particular, single-parametric pumping or train-impulse pumps are especially interesting due to their potential applications in nanoelectronics [27–29]. For larger one-dimensional systems electron pumping effects were studied for different time-periodic perturbations (delta-like, harmonic or pulsed) [30–34], where the net electron current flows between unbiased leads. From the local electronic properties point of view this current can appear if the system is characterized by finite spectral density function (Local Density of States, LDOS) near the Fermi energy. In such a case an electron can flow from the lead to the unoccupied LDOS state of the central system and then pass to the second lead. On the other hand, the presence of an energy gap in the structure of the central system strongly restricts the pumping effect. However, this conclusion can be invalid for the new state of matter i.e., for topological insulators where energy gaps appear inside the system. These structures are also characterized by collective edge states (topological states) at the system boundaries. Please note that the quantization of particle transport in such structures were studied for Thouless pumping [35], Moire pumping [36], for quantum spin-Hall insulator [37], for twisted bilayer graphene [38], coupled fermionic chains [39], nonadiabatic Floquet structures [40] or others. Topological phases in one-dimensional chains can be obtained within a Su–Schrieffer–Heeger (SSH) model [41–43]. The model due its $\mathcal{CT}$ symmetry possesses two different topological phases: the trivial phase with an energy gap along the whole system, and the nontrivial one for which there exist spectrally isolated mid-gap states localized at the system boundaries which are protected against local perturbations [41,42,44].

In this paper, we explore the possibility of electron pumping in the SSH chain under a time-periodic driving in the form of external one-Gaussian or two-Gaussian perturbations moving along the system (so called the train impulse) which in the nonadiabatic regime can generate the pumping current between unbiased leads. Although plenty of studies in the topic of electron pumping have been performed for single or double parameter time-dependent potentials there is a lack of information in the literature about the electron pumping through topological systems affected by the train-impulse perturbations. Such a train-like impulse can drug electrons between unbiased electrodes in the same or also in the opposite direction in comparison with the impulse propagation way which makes these structures especially interesting. Thus, in this paper we consider trivial and nontrivial SSH chains and concentrate on the time dynamics of the site occupancies and the electron currents under the influence of external train perturbations. It allows us to find the net electron charge which is transferred between unbiased leads. In our studies we also analyze the spectral density dynamics during the external perturbation spreading along the system and observe time evolution of the system quasiparticles. From these studies we can find how electrons are transfer through various energy-gapped 1D systems. Moreover, we consider dynamical transition processes (sudden quenches) between two different topological phases of the SSH chain [45–47] and observe mid-gap topological states migration between the system sites. We expect that topological states do not disappear immediately after the quench, but they survive in nontopological systems for a longer time and can penetrate even middle sites of the normal or trivial chain.

It is worth noting that new experimental techniques allow one to investigate quench dynamics and different geometric configurations of such atomic systems within the scanning tunneling microscope methods. Moreover, train-like perturbations can be realized experimentally in many one-dimensional systems e.g., for a linear series of QDs with fully controlled external electrodes, for atomic chains in the mechanically controlled break junction geometry with periodical changes of the electrode position. Alternatively, one can use fully controlled 1D optical lattices or atomic chains epitaxially grown on a surface and change the atom-atom couplings using a piezoelectric substrate or laser impulses.

The paper is organized as follows. The theoretical model and the calculation methods are described in Section 2. In Section 3, the main results of the paper are discussed for electron pumping through the SSH chain. In Section 4 the spectral density dynamics for train impulses and quenches is analyzed. The last Section 5 gives a short summary.

2. Theoretical Description

The physical model consists of the SSH chain composed of N sites that may be coupled to the electron reservoir (substrate electrode) underneath or to the left and right leads via the edge sites as shown in Figure 1. This model corresponds to atomic chains on vicinal surfaces (with the insulating or conducting substrate below the chain) or to the linear series of QDs with fully controlled system parameters.

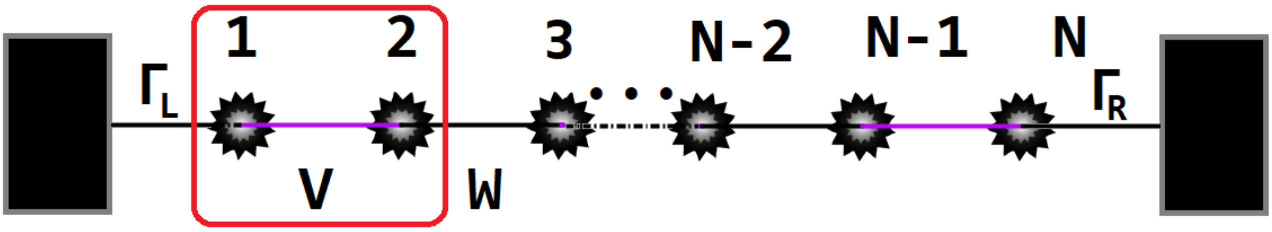

Figure 1. Model of atomic SSH chain composed of N sites on the insulating surface (which can stand for a gate electrode). The nearest-neighbor couplings between sites are denoted by V and W and the couplings with the left and right electrodes represent $\Gamma_{L/R}$ symbols.

The SSH chain is characterized by the two-site primitive cell with two different couplings between sites inside each cell and between cells—V and W parameters, respectively. The chain for $V = W$ represents nontopological normal chain without an energy gap. For the intracell couplings greater than intercell couplings we get a topological SSH chain in the nontrivial phase i.e., with topological mid-gap states at both chain ends (SSH$_1$), otherwise we obtain a chain in the trivial topological phase with an energy gap but without the edge states (SSH$_0$).

The Hamiltonian describing the SSH chain composed of N sites coupled with the electrodes can be written in terms of the second quantization notation as follows:

$$H = \sum_{i=1}^{N} \varepsilon_i a_i^\dagger a_i + \sum_{i=1}^{N} \sum_{\vec{k}_i} (\varepsilon_{\vec{k}_i} a_{\vec{k}_i}^\dagger a_{\vec{k}_i} + V_{\vec{k}_i,i} a_{\vec{k}_i}^\dagger a_i) + \sum_{i,j}^{N} V_{i,j}(t) a_i^\dagger a_j + H.c. \tag{1}$$

Here $a_i^\dagger, a_i$ are creation/annihilation operators respectively at i-th site, ε_i is the on-site energy level and $\varepsilon_{\vec{k}}$ corresponds to possible electron energies in the leads. $V_{\vec{k},i}$ stands for the coupling between electrodes and corresponding chain atom and $V_{i,j}$ is responsible for the couplings between chain sites (note that $V_{i,j} = V$ within the primitive cell and $V_{i,j} = W$ between the neighboring cells). These couplings can vary in time during the train-impulse propagation or sudden quenches. For $V_{\vec{k},i} = 0$ except for $i = 1$ and $i = N$ (i.e., for nonzero $V_{\vec{k},L}$ and $V_{\vec{k},R}$ elements) the model corresponds to that from Figure 1.

In our paper time dynamics of the system is calculated within the interaction picture using the evolution operator method for which the following equation of motion can be written ($\hbar = 1$):

$$i\frac{\partial}{\partial t} U(t,t_0) = \hat{V}(t) U(t,t_0)\,, \tag{2}$$

where $\hat{V}(t) = U_0(t,t_0)V(t)U^\dagger(t,t_0)$, $U_0(t,t_0) = \mathcal{T}\exp\left(i\int_{t_0}^{t} dt' H_0(t')\right)$ and $\mathcal{T}$ is the time ordering operator. Here $V(t)$ is the coupling part of the total Hamiltonian and $H_0(t)$ represents the on-site energy part, $H_0 = \sum_\alpha \varepsilon_\alpha a_\alpha^\dagger a_\alpha$. The physical properties of the system are expressed by the evolution operator matrix elements obtained from Equation (2). The local time-dependent charge occupancies, $n_i(t)$, can be found from the relation [48,49]:

$$n_i(t) = \sum_{j=1}^{N} n_j(t_0)|U_{i,j}(t,t_0)|^2 + \sum_{j,\vec{k}_j} n_{\vec{k}_j}(t_0)|U_{i,\vec{k}_j}(t,t_0)|^2\,, \tag{3}$$

where $n_i(t_0)$ represents the initial filling of the corresponding single-particle state. As we are not interested in the transient effects, which appear only for small t ($t \geq t_0$), we assume empty initial occupancies of all chain sites. The evolution operator elements, which are necessary to obtain the occupancies, satisfy the following set of integro-differential equations ($t_0 = 0$ is assumed):

$$\begin{aligned} i\frac{\partial U_{i,\vec{k}_j}(t)}{\partial t} &= \sum_{i'} V_{ii'}(t)e^{i(\varepsilon_{i'}-\varepsilon_i)t}U_{i',\vec{k}_j}(t) - V_{i\vec{k}_j}(t)e^{i(\varepsilon_i-\varepsilon_{\vec{k}_j})t} \\ &- |V_{i\vec{k}_j}(t)|^2 \int_0^t dt' \int d\varepsilon D_j(\varepsilon)e^{i\varepsilon(t-t')}e^{i\varepsilon_i(t-t')}U_{i,\vec{k}_j}(t')\,, \end{aligned} \tag{4}$$

where $D_j(\varepsilon)$ is the j-th lead's spectral density function.

Assuming the wide-band approximation which is justified for flat leads DOS or in the case when the lead's DOS varies slowly in the vicinity of the central system electron energies, the effective chain-electrode coupling can be expressed by $\Gamma_i(\varepsilon) = 2\pi \sum_{\vec{k}} |V_{i\vec{k}}|^2 \delta(\varepsilon - \varepsilon_{\vec{k}}) = \Gamma_i$, which is energy independent. Within this approach Equation (4) for the left electrode takes the form:

$$\frac{dU_{i,kL}(t)}{dt} = -i\sum_{i'} V_{ii'}(t)e^{i(\varepsilon_{i'}-\varepsilon_i)t}U_{i',\vec{k}_L}(t) - iV_{1,\vec{k}L}(t)e^{i(\varepsilon_1-\varepsilon_{\vec{k}L})\,t} - \frac{\Gamma_L}{2}U_{i,\vec{k}L}(t)\,, \tag{5}$$

and similar for the right lead.

The current flowing from the left electrode is obtained from the time derivative of the total number of electrons in this reservoir:

$$j_L(t) = -e\frac{d}{dt}\sum_{\vec{k}_L} n_{\vec{k}_L}(t)\,, \tag{6}$$

where the occupancies $n_{\vec{k}_L}(t)$ can be expressed similarly to Equation (3) by the corresponding evolution operator matrix elements. In this case, the spectral density function at each chain site for the zero temperature satisfies the relation:

$$\rho_i(\varepsilon, t) = \sum_{\alpha} D_\alpha(E)|U_{i,\alpha}(\varepsilon, t)|^2\,, \tag{7}$$

where $U_{i,\alpha}$ elements are calculated numerically from Equation (4) or Equation (5).

In this manuscript we use the unit of energy $\Gamma_L = \Gamma \equiv 1$, the time unit is $\hbar/\Gamma$, and the current is expressed in the units of $e\Gamma/\hbar$. Thus, for $\Gamma = 1$ meV the units of time and current are 0.66 ps and 0.25 µA, respectively. Please note that the reference energy point is the left electrode Fermi energy, $E_F = 0$.

3. Electron Pumping through SSH Chains

Topological chains seem to be very poor candidates for an effective quantum pump due to their electronic structure i.e., energy gap at the Fermi level. However, for quantum systems which are suddenly quenched the spectral density function at each site changes/evolves and it takes some time for the system to obtain its new equilibrium state. For a system with strong asymmetry in its LDOS this non-equilibrium processes can lead to the pumping effect between unbiased leads. Here we propose a 1D topological chain as an electron pump where the electron current direction can be controlled by means of the gate voltage potential. In such systems a gate electrode can be provided by external auxiliary electrodes or the substrate underneath the atomic chain. To avoid the electron leakage to the substrate we consider the chain on the insulating surface with two electron reservoirs at both chain ends ($\vec{k}_1 = \vec{k}L$ and $\vec{k}_N = \vec{k}R$). It is assumed that the external perturbation applied to the chain does not change the couplings homogeneously but there is a kind of the wire inertia which introduces the phase shift between the couplings (depending on the site position in the chain). In our investigations we consider the one-Gaussian or two-Gaussian perturbations in the form of a train-impulse spreading through the chain, see Figure 2, upper panels, where we show time-dependent perturbations, f_0, f_i and f_N which are related to the couplings, $V_{\vec{k}L}$, V_i and $V_{\vec{k}R}$, respectively and $V_i(t) = V_i f_i(t)$. The analytical relations for these perturbations can be written in the following form $f_j(t) = 1 + \exp\left(\frac{\tilde{t}^2}{\sigma}\right)$ for the one-Gaussian pulse and $f_j(t) = 1 + \exp\left(\frac{\tilde{t}^2}{\sigma}\right) - \exp\left(\frac{[\tilde{t}-t_1]^2}{\sigma}\right)$ for the two-Gaussian perturbation, where $\tilde{t} = t - (t_{00} + jt_x)$ and $j = 0, 1, 2, \cdots, N$. Here t_{00} stands for the time for the first Gaussian maximum, t_x is responsible for the time shift of the external perturbation between the nearest-neighbor couplings (for $t_x = 0$ all couplings change simultaneously in time in the same way), t_1 stands for the time shift between the Gaussian functions, and σ corresponds to the half-width of the Gaussian signal. Such train pulses locally modify the site-site couplings and can change the system topology (depending on the coupling differences between chain sites). This perturbation concerns only small part of the whole chain, but it has a huge impact on the electron current flowing through the system.

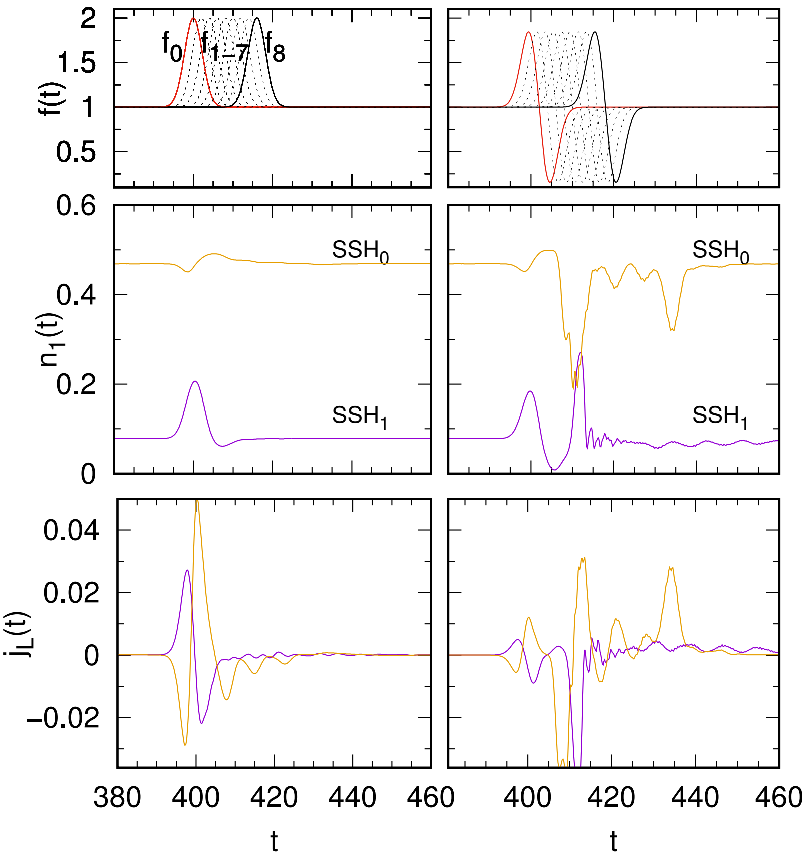

Figure 2. One-Gaussian (left panel) and two-Gaussian (right panel) perturbations of the time-dependent couplings: f_0 (between the left electrode and first wire site, red lines), f_i (between i-th and $(i+1)$-th sites, broken curves) and f_N (between the last chain site and the right electrode, back solid curves)—upper panels. Charge occupation of the first wire site (middle panels) and time-dependent current flowing from the left electrode (bottom panels) for the SSH chain in the trivial phase (yellow lines, $V = 4, W = 1$, SSH_0) and for nontrivial phase (violet lines, $V = 1, W = 4$, SSH_1). The other parameters are: $\varepsilon_0 = 3$, $t_x = 3$, $\sigma = 10$, $V_L = V_R = 4$, $t_{00} = 400$, $t_1 = 4$, $N = 8$.

The time-dependent occupancies are obtained from Equation (3) and the current flowing through the system from Equation (6), which in the wide-band approximation we calculate from the relation:

$$j_L(t) \quad = \quad -\Gamma^L f_0^2(t) n_1(t) - 2\mathrm{Im}\left\{ \sum_{\vec{k}L} n_{\vec{k}L}(0) V_{\vec{k}L} f_0(t) e^{i(\varepsilon_{\vec{k}L} - \varepsilon_0)t} U_{1,\vec{k}L}(t) \right\}, \qquad (8)$$

where the evolution operator matrix elements $U_{1,\vec{k}L}$ are obtained from Equation (5).

In the beginning in Figure 2 we analyze the time-dependent electron occupations (middle panels) and the currents flowing from the left electrode (bottom panels) for the SSH topological chain in the trivial phase (SSH$_0$, $V = 4, W = 1$, yellow curves) and nontrivial phase (SSH$_1$, $V = 1, W = 4$, violet curves) for $\varepsilon_0 = 3$. Before the train impulse starts (at $t \simeq 390$) the system is in its equilibrium state – the occupancies do not change in time and the currents do not flow between electrodes. The structure of LDOS is symmetrical with respect to ε_0 and in the first case (SSH$_0$ chain) there is an energy gap around the Fermi energy, thus the electron occupancy is almost 0.5 (middle panels) even for $\varepsilon_0 = 3$. For the one-Gaussian perturbation, in the first stage, the chain-lead coupling strength increases and some charge from the chain leaks to the lead and the chain occupation locally decreases. This is also the reason why in this case the current is negative (it flows from the chain to the left electrode). In the second stage of this train perturbation the couplings between atomic sites inside the chain increase and the lower sideband LDOS states move deeper below the Fermi energy, thus the occupancy locally increases, and the current is positive. On the other hand, in the presence of this perturbation, for the chain with topological states at both edges (nontrivial phase) the empty LDOS states spread below the Fermi level and the occupancy of the chain site increases rapidly (the current flows from the left electrode to the chain). Please note that the perturbation (train impulse) goes through the chain up to $t = 420$ units of time but the occupancies and the currents tend very fast to their equilibrium values.

The situation changes for the two-Gaussian perturbation (right panels). In this case, charge oscillations do not vanish rapidly, but they are visible also for larger t, i.e., even for times for which the perturbation has passed through the system. The reason for such long-time oscillations is very low value of the two-Gaussian perturbation for a short period of time, $f(t)$, which leads to almost vanishing site-site couplings in the system. Thus, the chain sites are almost decoupled for a moment (like in the atomic limit) and then the system needs much more time to reach the equilibrium state. Please note that after and before the perturbation, the occupancies are exactly the same and from the careful inspection of the currents flowing from the left electrode one can find the total charge pumped through the chain. For the SSH$_1$ chain and two-Gaussian impulse it is evident that most of the violet curve is negative, thus one expects the net pumping charge in the system. For the one-Gaussian impulse (left bottom panel) the currents for SSH$_0$ and SSH$_1$ chains oscillate around the zero value, but they are asymmetrical and more detailed study is required to classify these systems as electron pumps.

The total charge pumped through the chain is obtained by integrating the time-dependent currents, $N_{L/R} = \int j_{L/R}(t)dt$, where in our system the condition $N_L = -N_R$ is always satisfied. Here, positive values of $N_{L/R}$ correspond to electrons flowing from the electrode to the chain. In Figure 3 the pumped charge from the left lead is analyzed as a function of ε_0 (which corresponds to the gate voltage) for the one-Gaussian (upper panel) and two-Gaussian perturbations (bottom panel) for both SSH$_0$ (yellow curves) and SSH$_1$ (violet curves) chains. As one can see for symmetrical LDOS with respect to the Fermi energy ($\varepsilon_0 = 0$) the charge does not flow through the chain, independently on the perturbation shape and topological phase of the chain. For $\varepsilon_0 \neq 0$ the shape of the train impulse spreading through the chain plays a crucial role in the electron pumping effect in topological systems. For the one-Gaussian perturbation the couplings between sites locally increase leading to smaller difference between V_i parameters. In this case, the energy gap is not closed. It is the reason that electrons do not flow through the SSH$_0$ chain for ε_0 smaller than the energy gap width (here the gap appears for $|\varepsilon - \varepsilon_0| \leq 3$, cf. the inset in Figure 3, bottom panel). Note that also for the chain in the nontrivial phase the pumping effect does not occur for these values of ε_0 although there is a topological state at the first chain site (nonzero LDOS at the Fermi level, see the inset, violet curve). In this case, electrons which flow out from the electrode cannot be transferred through the middle part of the chain due to the energy gap at these middle sites. It means that the zero-energy edge states do not play a main role in the electron pumping through 1D systems—this problem will be discussed in more details in the next section.

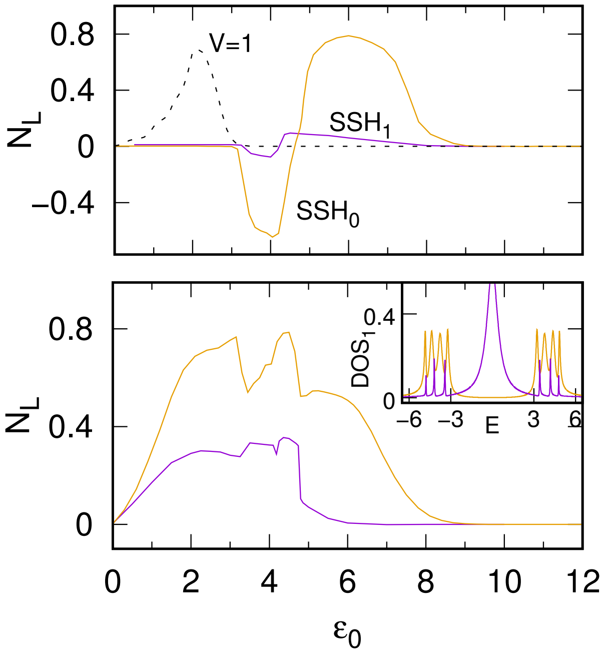

Figure 3. Charge pumped through the 8-atom SSH chain as a function of ε_0 for $t_x = 3$. The upper (lower) panel corresponds to the one-Gaussian (two-Gaussian) perturbation. The broken line corresponds to the normal chain with $V = 1$. The other parameters are the same as in Figure 2. The inset in the bottom panel shows the local DOS at the first site of the SSH chain in the trivial (SSH$_0$) and nontrivial (SSH$_1$) phases.

For larger ε_0 (beyond the energy gap) electrons are pumped in the system. In our case for $\varepsilon_0 > 3$ the bottom sideband peaks which are below the Fermi level (they are occupied) change their positions in the presence of the one-Gaussian perturbation, and thus the electron charge leaks out of the chain (the current is negative). Next, for larger ε_0 ($\varepsilon_0 \simeq 4.7$) the bottom LDOS sideband is symmetrical with respect to the Fermi energy and the current does not flow through the system (similarly as for $\varepsilon_0 = 0$). The second upper LDOS sideband lies too far from the Fermi level and does not influence the current. For $\varepsilon_0 > 4.5$ there are more LDOS peaks above the Fermi level and in the presence of the perturbation they move below the Fermi energy. In that case electrons from the electrode occupy these empty LDOS states and the current is positive. For larger and larger ε_0 there are no electron states near the Fermi level and the net charge cannot be pumped through the system. Note that for the nontrivial chain (SSH$_1$, violet curve upper panel) and the one-Gaussian impulse the pumping current almost does not flow through the system which is a consequence of relatively low LDOS in the upper and lower sidebands (cf. the violet curve in the inset), and because the sidebands are responsible for the pumping current this effect is marginal in the SSH$_1$ chain. Thus, the shape of the pumping current as a function of the gate voltage allows us to distinguish between the trivial and nontrivial phases of the topological system.

In Figure 3 the results obtained for the SSH$_0$ and SSH$_1$ chains are compared also with the normal chain of the same length (black broken curve, upper panel). There are crucial differences between topological and normal systems. First, for the normal chain the pumping current starts to flow for $\varepsilon_0 > 0$ as there is no energy gap in the system and even small asymmetry in its energetic structure leads to the electron pumping. The maximal pumping current is observed for such ε_0 for which the bottom of chain energy band corresponds to the Fermi energy (here it is for $\varepsilon_0 = 2$). For larger ε_0 the pumping current vanishes due to the lack of states at the Fermi level. It is also important that for the normal chain the pumping current is always positive (for $\varepsilon_0 > 0$) whereas in the topological chains one can control the direction of the current slightly tuning the gate voltage of the system.

The situation changes for the two-Gaussian perturbation (bottom panel) which modulates the coupling strengths along the chain in such a way that in the first stage the couplings increase but then they decrease below their initial values. It leads to smaller difference between the neighboring couplings in the chain which almost closes the energy gap at the Fermi level. Thus, electrons can flow from the electrode to the chain (like in the normal chain) even for small ε_0. However, in the second stage of the perturbation the couplings tend to zero and these electrons cannot back to the previous sites (they are pushed toward the second electrode). In this case, the pumping current is always positive and for larger and larger ε_0 it vanishes. Moreover, the system in the trivial phase, SSH$_0$, more effectively pumps electrons through the chain due to its unique energetic structure which will be analyzed in the next section. Please note that the pumping current curves are not very smooth because they reflect the peaked structure of the sidebands (see the inset figure) which for smaller couplings in the two-Gaussian mode tends to atomic limit and the peaks are much more evident.

4. Spectral Density Dynamics

To explain the nature of the pumping process in topological chains in more details we must study time-dependent LDOS along the chain during the perturbations. Please note that within the evolution operator method which we use in our calculations one can analyze simultaneously the occupancies, currents and time-dependent LDOS structures. Detailed analysis of the spectral density dynamics during the pumping process or sudden quenches allows one to observe time evolution of the system quasiparticles at a given site as well as their time-migration along the system or between chain sites.

4.1. Train Impulses

Here, we are going to explain more precisely the electron transfer process through the energy-gapped structure between unbiased leads. Thus, in Figure 4 we show the spectral density functions related to four sites of the SSH$_0$ chain during the propagation of the train impulse (one-Gaussian perturbation, panel a, or two-Gaussian impulse, panel b). As one can see the chain is characterized by the energy gap at the Fermi level, independent on the site number (the total chain length is $N = 8$). The perturbation starts at $t = 400$ and it leads to wider LDOS - the sidebands are shoved outside the Fermi energy due to larger values of the coupling parameters. After some time, all LDOS peaks return to their initial positions and the induced sideband structure follows the perturbation. When the train impulse reaches the edge site the system evolves to its previous equilibrium state. In this case, electrons are transferred through the LDOS sidebands which are outside the energy gap of the chain.

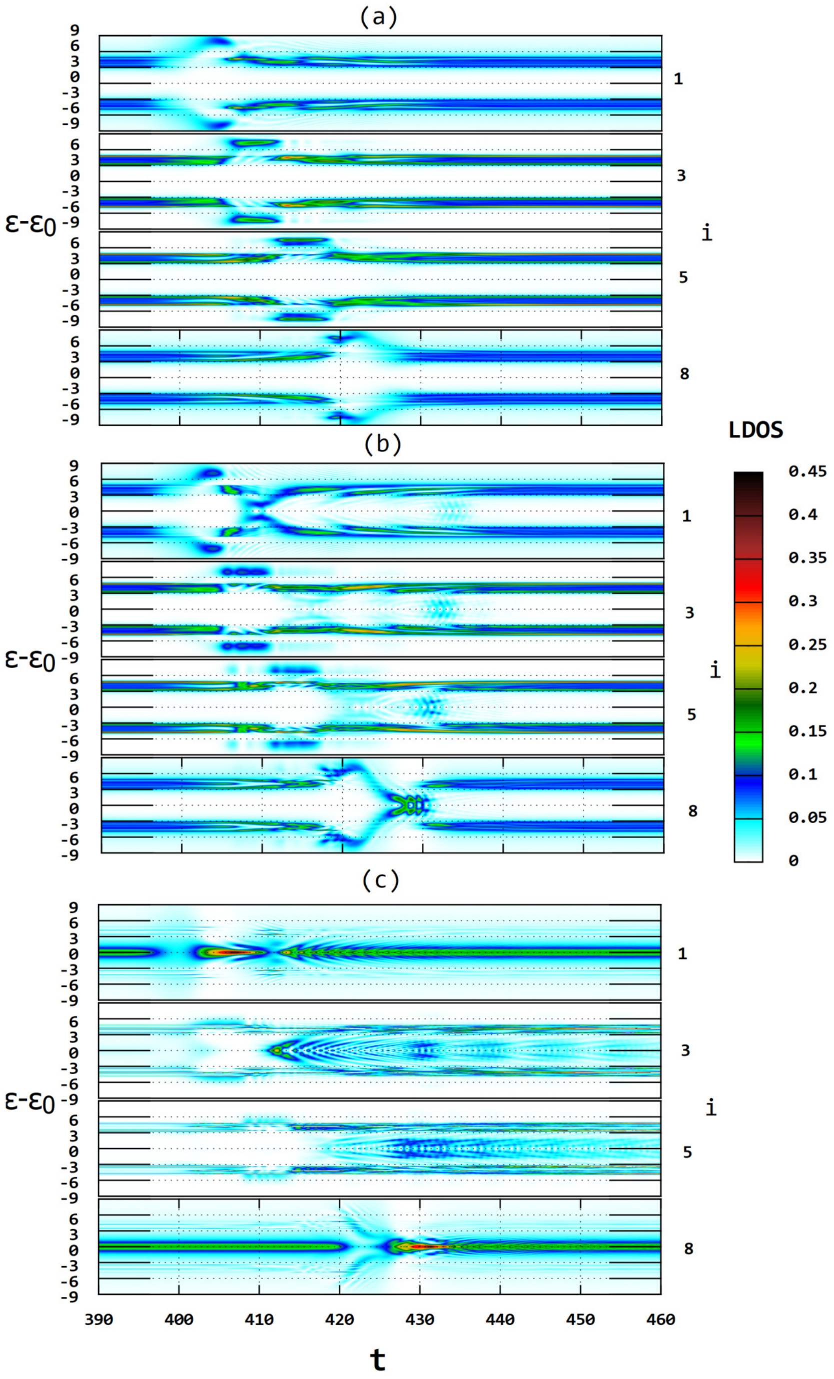

Figure 4. LDOS time evolution at $i = 1, 3, 5$ and 8 sites of the SSH trivial chain [$V = 4, W = 1$, panels (**a**,**b**)] and nontrivial chain [$V = 1, W = 4$, panel (**c**)] composed of $N = 8$ sites. Panel (**a**) represents the system disturbed by the one-Gaussian perturbation, panels (**b**,**c**) correspond to the two-Gaussian impulse, the same as in Figure 2.

The situation changes for the two-Gaussian perturbation (panel b) as now some site-site couplings decrease in time and at the same time some of them increase. It leads to the induced sidebands outside the energy gap (like in the one-Gaussian impulse) but also dynamical nonzero LDOS structure in the energy gap region is observed. Thus, for this perturbation electrons can be pumped through these temporary mid-gap states. For the nontrivial topological chain, SSH_1, the LDOS dynamics during the two-Gaussian impulse is analyzed in panel c. In this case, the sidebands outside the energy gap are slightly visible and the main pumping process is realized only inside the energy gap region. Thus, one expects lower values of the net pumping current in comparison with the trivial chain, as one can see in Figure 3. The inside structure of LDOS during the perturbation is formed from the mid-gap topological state localized at the first site—this state oscillates in time and we observe a periodic emission of this state to other chain sites. These induced states also follow the train-impulse propagation along the chain. Please note that sudden local change of the site-site couplings disturbs both topological states related to the first and the last chain sites for a moment (the difference between the nearest-neighbor couplings decreases rapidly which influences the chain periodicity) but after some time the mid-gap states are rebuilt again. It is also interesting that for the two-Gaussian pulse both topological states have very high intensity for short period of time. This results from the fact that for a moment the coupling between the first (last) chain site and its neighboring site decreases and the energetic structure of LDOS tends to the atomic limit in this case.

From the detailed studies of time-dependent LDOS characteristics we have found that electrons are transferred through the mid-gap temporary states in nontrivial topological chains or through the induced sidebands outside the energy gap region in trivial chains. The pumped current direction depends only on the relative position of the LDOS peaks and the leads Fermi energy, cf. Figure 3. We have also checked that the spectral density dynamics of the SSH chain coupled with a noninsulating surface underneath does not reveal significant differences. In that case the chain-substrate coupling is responsible for the half-width of the spectral density peaks and for larger couplings these LDOS peaks are wider and smoother. It is important from the practical point of view, because it opens more perspectives for experimental studies of such structures.

4.2. Quench Dynamics in SSH Chains

Topological chains which are characterized by an energy gap along the system can transfer electrons through the induced mid-gap states as shown in the previous section. This effect can be observed only for non-equilibrium processes such as in the presence of a train impulse moving along the chain. Alternatively, after a sudden change of the system parameters (so called the quantum quench) the system needs some time to reach its steady state which opens a new possibility for coexistence of both trivial and nontrivial phases simultaneously in the system. Thus, it is desirable to analyze the mid-gap topological states dynamics between SSH_1 and SSH_0 (or normal) chains, which takes place not just for a while (as during the train impulse) but which lasts for a long time after the quench.

Thus, in Figure 5 we analyze a segment of energy-dependent LDOS near the Fermi energy (at sites from $i = 1$ to $i = 10$) as a function of time for topological chain of the length $N = 20$. At a given time ($t = 400$) the quantum quench switches topological phase from nontrivial to the trivial one (panel a) or to the normal chain (panel b) and we can analyze the mid-gap state dynamics along the chain. As one can see before the transition the system is characterized by wide topological states at the edge sites ($i = 1$, and the same at $i = 20$) and the energy gap in all middle sites (panels a and b). For very large time after the quench, we can notice that the system reaches its steady state i.e., trivial topological state with energy-gapped LDOS (panel a) or normal nontopological chain with no energy gap (panel b).

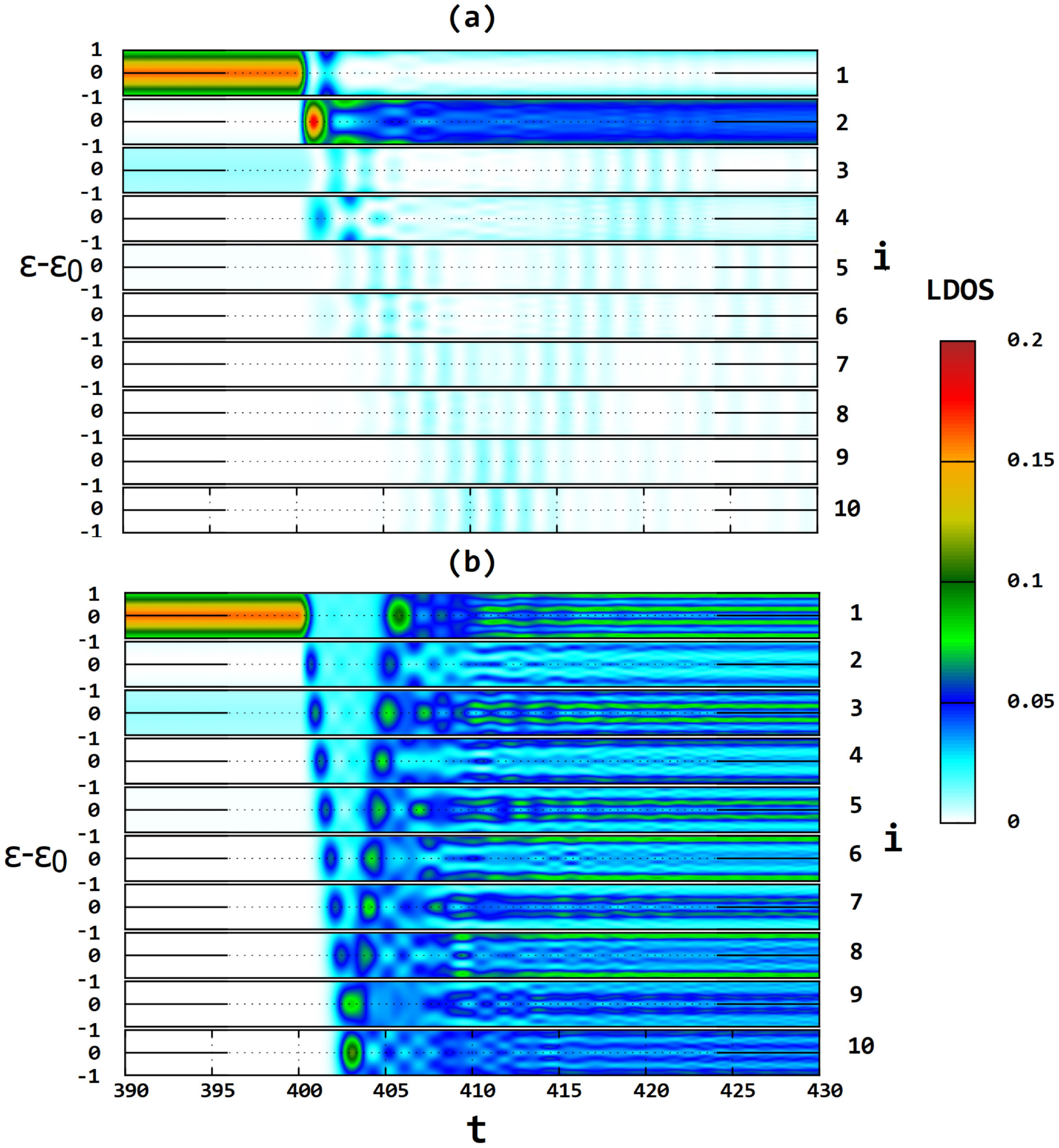

Figure 5. LDOS time evolution at first 10 sites in the topologically nontrivial chain, SSH$_1$ ($V = 0.5$, $W = 2$) quenched to the trivial chain SSH$_0$ [$V = 2, W = 0.5$, panel (a)] or to the normal chain [$V = W = 2$, panel (b)] at $t = 400$. The chain length is $N = 20$ and the on-site energies $\varepsilon_0 = 0$.

The most interesting physics happens just after the quench. Surprisingly, topological state does not disappear immediately but rather moves into middle parts of the chain. However, in the upper panel this state survives only on the first few boundary sites and then it is blurred in time, but it is visible that at $t \simeq 410$ it reaches the middle site of the chain. The same signal moves from the last chain site and they pass each other. Thus, the

X-shaped LDOS is observed and as time evolves these states balance between the edges with vanishing intensities. This process is more evident in the bottom panel where both topological states migrate after the quench through the normal chain and they also form a V-shaped LDOS dynamical structure. Note that in the normal chain the edge states travel much faster and they reach the middle chain site just at $t \simeq 403$, i.e., only 3 time units after the quench. It means that the travel speed of the mid-gap state strongly depends on the energy-gapped structure in the spectral density function and for nonzero LDOS it moves much faster along the chain. Please note that similar time evolution was observed for the absolute value of the spinor component related to the Majorana mode in 1D topological systems [50].

5. Conclusions

In this work we have studied electron transfer through the 1D topological systems which are characterized by an energy gap and are expected to be poor electron pumps. Using the evolution operator technique and the tight-binding Hamiltonian we have analyzed the occupancies, currents and time-dependent LDOS along the SSH trivial and nontrivial chains affected by external train impulses in the form of the one-Gaussian and two-Gaussian perturbations. It turns out that such systems can work as effective electron pumps and surprisingly, topological trivial chains can transfer more charge during one cycle of such external perturbation than nontrivial SSH chains. This effect is explained by strong asymmetry in the structure of LDOS for the edge sites (due to the absence of topological states) and is crucial for the pumping effect. It is also important that for the normal chain the pumping current is always positive (for positive on-site energies) whereas in topological chains one can control the direction of the pumping current slightly tuning the gate voltage of the system.

We have also analyzed how electrons are transferred through the energy-gapped topological materials and we have found that during the train perturbation electrons are pumped through the mid-gap temporary states in the nontrivial topological chains and through the induced LDOS sidebands outside the energy gap region in the trivial chains. This conclusion stands for the main result of the paper and can be useful for potential applications of such topological materials in nanoelectronics.

Additionally, we have investigated LDOS time dynamics along the chain after a sudden quench which changes topological phase of the system (from the nontrivial to the normal or to the trivial one). We have found that during this change topological states do not disappear at once, but they balance between the edges of the chain with vanishing intensities. Even more importantly, the travel speed of topological states strongly depends on the chain energetic structure such that for gapped materials the states move relatively slow and for normal materials they move much faster along the chain.

Author Contributions: Conceptualization, T.K. and M.K.; methodology, T.K.; software, T.K. and M.K.; formal analysis, T.K. and M.K.; results interpretation, T.K. and M.K.; investigation, T.K. and M.K.; resources and data curation, M.K.; writing, T.K. and M.K.; original draft preparation, T.K. and M.K.; review and editing, T.K. and M.K.; visualization, T.K. and M.K.; scientific supervision T.K. All authors have read and agreed to the published version of the manuscript.

Funding: This work was partially supported by National Science Centre, Poland, under Grant No. 2018/31/B/ST3/02370.

Institutional Review Board Statement: Not applicable.

Informed Consent Statement: Not applicable.

Data Availability Statement: It does not apply to this work.

Conflicts of Interest: The authors declare no conflict of interest. The funders had no role in the design of the study; in the collection, analyses, or interpretation of data; in the writing of the manuscript, or in the decision to publish the results.

References

1. Kopciuszyński, M.; Dyniec, P.; Krawiec, M.; Łukasik, P.; Jałochowski, M.; Zdyb, R. Pb nanoribbons on the Si(553) surface. *Phys. Rev. B* **2013**, *88*, 155431. [CrossRef]
2. Crain, J.N.; McChesney, J.L.; Zheng, F.; Gallagher, M.C.; Snijders, P.C.; Bissen, M.; Gundelach, C.; Erwin, S.C.; Himpsel, F.J. Chains of gold atoms with tailored electronic states. *Phys. Rev. B* **2004**, *69*, 125401. [CrossRef]
3. Baski, A.; Saoud, K.; Jones, K. 1-D nanostructures grown on the Si(5 5 12) surface. *Appl. Surf. Sci.* **2001**, *182*, 216–222. [CrossRef]
4. Jałochowski, M.; Kwapiński, T.; Łukasik, P.; Nita, P.; Kopciuszyński, M. Correlation between morphology, electron band structure, and resistivity of Pb atomic chains on the Si(553)-Au surface. *J. Phys. Condens. Matter* **2016**, *28*, 284003. [CrossRef]
5. Auslaender, O.M.; Steinberg, H.; Yacoby, A.; Tserkovnyak, Y.; Halperin, B.I.; Baldwin, K.W.; Pfeiffer, L.N.; West, K.W. Spin-Charge Separation and Localization in One Dimension. *Science* **2005**, *308*, 88–92. [CrossRef]
6. Shin, J.S.; Ryang, K.D.; Yeom, H.W. Finite-length charge-density waves on terminated atomic wires. *Phys. Rev. B* **2012**, *85*, 073401. [CrossRef]
7. Nadj-Perge, S.; Drozdov, I.K.; Li, J.; Chen, H.; Jeon, S.; Seo, J.; MacDonald, A.H.; Bernevig, B.A.; Yazdani, A. Observation of Majorana fermions in ferromagnetic atomic chains on a superconductor. *Science* **2014**, *346*, 602–607. [CrossRef]
8. Pawlak, R.; Kisiel, M.; Klinovaja, J.; Meier, T.; Kawai, S.; Glatzel, T.; Loss, D.; Meyer, E. Probing atomic structure and Majorana wavefunctions in mono-atomic Fe chains on superconducting Pb surface. *NPJ Quantum Inf.* **2016**, *2*, 16035. [CrossRef]
9. van der Wiel, W.G.; De Franceschi, S.; Elzerman, J.M.; Fujisawa, T.; Tarucha, S.; Kouwenhoven, L.P. Electron transport through double quantum dots. *Rev. Mod. Phys.* **2002**, *75*, 1–22. [CrossRef]
10. Fujisawa, T.; Tokura, Y.; Hirayama, Y. Transient current spectroscopy of a quantum dot in the Coulomb blockade regime. *Phys. Rev. B* **2001**, *63*, 081304. [CrossRef]
11. Hayashi, T.; Fujisawa, T.; Cheong, H.D.; Jeong, Y.H.; Hirayama, Y. Coherent Manipulation of Electronic States in a Double Quantum Dot. *Phys. Rev. Lett.* **2003**, *91*, 226804. [CrossRef]
12. Arkinstall, J.; Teimourpour, M.H.; Feng, L.; El-Ganainy, R.; Schomerus, H. Topological tight-binding models from nontrivial square roots. *Phys. Rev. B* **2017**, *95*, 165109. [CrossRef]
13. Jürß, C.; Bauer, D. High-harmonic generation in Su-Schrieffer-Heeger chains. *Phys. Rev. B* **2019**, *99*, 195428. [CrossRef]
14. Huneke, J.; Platero, G.; Kohler, S. Steady-State Coherent Transfer by Adiabatic Passage. *Phys. Rev. Lett.* **2013**, *110*, 036802. [CrossRef]
15. Lindner, N.H.; Refael, G.; Galitski, V. Floquet topological insulator in semiconductor quantum wells. *Nat. Phys.* **2011**, *7*, 490–495. [CrossRef]
16. Wilczek, F. Quantum Time Crystals. *Phys. Rev. Lett.* **2012**, *109*, 160401. [CrossRef]
17. Sacha, K. Modeling spontaneous breaking of time-translation symmetry. *Phys. Rev. A* **2015**, *91*, 033617. [CrossRef]
18. Sacha, K.; Zakrzewski, J. Time crystals: A review. *Rep. Prog. Phys.* **2017**, *81*, 016401. [CrossRef]
19. Kurzyna, M.; Kwapiński, T. Nontrivial dynamics of a two-site system: Transient crystals. *Phys. Rev. B* **2020**, *102*, 245414. [CrossRef]
20. Stefanucci, G.; Kurth, S.; Rubio, A.; Gross, E.K.U. Time-dependent approach to electron pumping in open quantum systems. *Phys. Rev. B* **2008**, *77*, 075339. [CrossRef]
21. Fuhrer, A.; Fasth, C.; Samuelson, L. Single electron pumping in InAs nanowire double quantum dots. *Appl. Phys. Lett.* **2007**, *91*, 052109. [CrossRef]
22. Low, T.; Jiang, Y.; Katsnelson, M.; Guinea, F. Electron Pumping in Graphene Mechanical Resonators. *Nano Lett.* **2012**, *12*, 850–854. [CrossRef]
23. van der Heijden, J.; Tettamanzi, G.C.; Rogge, S. Dynamics of a single-atom electron pump. *Sci. Rep.* **2017**, *7*, 44371. [CrossRef]
24. Yamahata, G.; Giblin, S.P.; Kataoka, M.; Karasawa, T.; Fujiwara, A. Gigahertz single-electron pumping in silicon with an accuracy better than 9.2 parts in 10^7. *Appl. Phys. Lett.* **2016**, *109*, 013101. [CrossRef]
25. Kohler, S.; Lehmann, J.; Hanggi, P. Driven quantum transport on the nanoscale. *Phys. Rep.* **2005**, *406*, 379–443. [CrossRef]
26. Braun, M.; Burkard, G. Nonadiabatic Two-Parameter Charge and Spin Pumping in a Quantum Dot. *Phys. Rev. Lett.* **2008**, *101*, 036802. [CrossRef]
27. Likharev, K.K. Single-electron devices and their applications. *Proc. IEEE* **1999**, *87*, 606–632. [CrossRef]
28. Ono, Y.; Takahashi, Y. Electron pump by a combined single-electron/field-effect- transistor structure. *Appl. Phys. Lett.* **2003**, *82*, 1221–1223. [CrossRef]
29. Kwapiński, T.; Taranko, R. Spin and charge pumping in a quantum wire: The role of spin-flip scattering and Zeeman splitting. *J. Phys. Condens. Matter* **2011**, *23*, 405301. [CrossRef]
30. Gasparian, V.; Altshuler, B.; Ortuño, M. Charge pumping in one-dimensional Kronig-Penney models. *Phys. Rev. B* **2005**, *72*, 195309. [CrossRef]
31. Agarwal, A.; Sen, D. Nonadiabatic charge pumping in a one-dimensional system of noninteracting electrons by an oscillating potential. *Phys. Rev. B* **2007**, *76*, 235316. [CrossRef]
32. Das, S.; Rao, S. Effects of interaction on an adiabatic quantum electron pump. *Phys. Rev. B* **2005**, *71*, 165333. [CrossRef]
33. Faizabadi, E.; Ebrahimi, F. Charge pumping in quantum wires. *J. Physics: Condens. Matter* **2004**, *16*, 1789–1802. [CrossRef]
34. Mahmoodian, M.M.; Braginsky, L.S.; Entin, M.V. One-dimensional two-barrier quantum pump with harmonically oscillating barriers: Perturbative, strong-signal, and nonadiabatic regimes. *Phys. Rev. B* **2006**, *74*, 125317. [CrossRef]

35. Thouless, D.J. Quantization of particle transport. *Phys. Rev. B* **1983**, *27*, 6083–6087. [CrossRef]
36. Fujimoto, M.; Koschke, H.; Koshino, M. Topological charge pumping by a sliding moiré pattern. *Phys. Rev. B* **2020**, *101*, 041112. [CrossRef]
37. Wang, M.J.; Wang, J.; Liu, J.F. Quantized spin pump on helical edge states of a topological insulator. *Sci. Rep.* **2019**, *9*, 3378. [CrossRef]
38. Zhang, Y.; Gao, Y.; Xiao, D. Topological charge pumping in twisted bilayer graphene. *Phys. Rev. B* **2020**, *101*, 041410. [CrossRef]
39. van Voorden, B.A.; Schoutens, K. Topological quantum pump of strongly interacting fermions in coupled chains. *New J. Phys.* **2019**, *21*, 013026. [CrossRef]
40. Deng, W.Y.; Luo, W.; Geng, H.; Chen, M.N.; Sheng, L.; Xing, D.Y. Non-adiabatic topological spin pumping. *New J. Phys.* **2015**, *17*, 103018. [CrossRef]
41. Asbóth, J.K.; Oroszlány, L.; Pályi, A. A Short Course on Topological Insulators. *Lect. Notes Phys.* **2016**, *919*, 997–1000. [CrossRef]
42. Pérez-González, B.; Bello, M.; Álvaro Gómez-León.; Platero, G. SSH model with long-range hoppings: Topology, driving and disorder. *arXiv* **2018**, arXiv:1802.03973.
43. Su, W.P.; Schrieffer, J.R.; Heeger, A.J. Solitons in Polyacetylene. *Phys. Rev. Lett.* **1979**, *42*, 1698–1701. [CrossRef]
44. Kurzyna, M.; Kwapiński, T. Non-local electron transport through normal and topological ladder-like atomic systems. *J. Appl. Phys.* **2018**, *123*, 194301. [CrossRef]
45. Cheung, C.H.; Zou, J. Tunable SSH model in ferromagnetic systems. *arXiv* **2020**, arXiv:2009.13034.
46. Yao, R.; Li, H.; Zheng, B.; An, S.; Ding, J.; Lee, C.S.; Zhang, H.; Guo, W. Electrically Tunable and Reconfigurable Topological Edge State Lasers. *arXiv* **2018**, arXiv:1804.01587.
47. Han, X.; Yan, Y.; Qi, L.; Cui, W.X.; Wang, H.F.; Zhang, S. Topological phase transition of the generalized Su-Schrieffer-Heeger model based on a frequency-modulated circuit quantum electrodynamics lattice. *Laser Phys. Lett.* **2020**, *17*, 065203. [CrossRef]
48. Kurzyna, M.; Kwapiński, T. Edge-state dynamics in coupled topological chains. *Phys. Rev. B* **2020**, *102*, 195429. [CrossRef]
49. Kwapiński, T. Conductance oscillations and charge waves in zigzag shaped quantum wires. *J. Phys. Condens. Matter* **2010**, *22*, 295303. [CrossRef]
50. Sacramento, P.D. Fate of Majorana fermions and Chern numbers after a quantum quench. *Phys. Rev. E* **2014**, *90*, 032138. [CrossRef]

materials

MDPI

Article

Topological Atomic Chains on 2D Hybrid Structure

Tomasz Kwapiński *,† **and Marcin Kurzyna** †

Department of Physics, Maria Curie-Skłodowska University, PL20031 Lublin, Poland;
marcin.kurzyna@live.umcs.edu.pl
* Correspondence: tomasz.kwapinski@umcs.pl
† These authors contributed equally to this work.

Abstract: Mid-gap 1D topological states and their electronic properties on different 2D hybrid structures are investigated using the tight binding Hamiltonian and the Green's function technique. There are considered straight armchair-edge and zig-zag Su–Schrieffer–Heeger (SSH) chains coupled with real 2D electrodes which density of states (DOS) are characterized by the van Hove singularities. In this work, it is shown that such 2D substrates substantially influence topological states end evoke strong asymmetry in their on-site energetic structures, as well as essential modifications of the spectral density function (local DOS) along the chain. In the presence of the surface singularities the SSH topological state is split, or it is strongly localized and becomes dispersionless (tends to the atomic limit). Additionally, in the vicinity of the surface DOS edges this state is asymmetrical and consists of a wide bulk part together with a sharp localized peak in its local DOS structure. Different zig-zag and armachair-edge configurations of the chain show the spatial asymmetry in the chain local DOS; thus, topological edge states at both chain ends can appear for different energies. These new effects cannot be observed for ideal wide band limit electrodes but they concern 1D topological states coupled with real 2D hybrid structures.

Keywords: atomic chain; Su-Schrieffer-Heeger model; density of states; van Hove singularities; localized states; hybrid systems

check for updates

Citation: Kwapiński, T.; Kurzyna, M. Topological Atomic Chains on 2D Hybrid Structures. *Materials* **2021**, *14*, 3289. https://doi.org/10.3390/ma14123289

Academic Editor: Gennady L. Gutsev

Received: 31 March 2021
Accepted: 10 June 2021
Published: 14 June 2021

Publisher's Note: MDPI stays neutral with regard to jurisdictional claims in published maps and institutional affiliations.

Copyright: © 2021 by the authors. Licensee MDPI, Basel, Switzerland. This article is an open access article distributed under the terms and conditions of the Creative Commons Attribution (CC BY) license (https://creativecommons.org/licenses/by/4.0/).

1. Introduction

Nowadays, one can notice a growing interest of scientists in low-dimensional structures which find almost constantly new applications in many branches of science and technology, e.g., in nanoelectronics [1,2], biotechnology, engineering [3], chemistry [4] and medicine [5]. Atomic wires as the thinnest possible electrical conductors are especially interesting objects to study mainly from practical point of view. Their electronic properties are the subject of many theoretical and experimental papers as they reveal a great deal of interesting physical phenomena which are often hard to notice in bulk materials, e.g., spin-charge separation [6,7], Majorana topological states [8,9], charge-density waves [10–12], turnstile effects, photon-assisted tunneling and pumping effects, or coherent destruction of tunneling [13–20]. In low-dimensional structures one can also observe unique solid-state phases such as time crystals [21–23], transient crystals [24] or Floquet topological insulators [25,26]. Especially interesting are hybrid systems composed of different low-dimensional structures where quantum states of one structure could penetrate to the second one leading to a kind of proximity effect which was studied, e.g., in one-dimensional (1D) coupled systems [27,28].

The main topic of interest in this work are the electrical properties of 1D topological chains which are fabricated on a flat two-dimensional (2D) electrode or which are placed between two 2D leads. Such a hybrid system can reveal constructive or destructive coexistence of 1D and 2D features of different quantum structures thus it is desirable to investigate their properties thoroughly. Topological chains are special materials where energy gaps appear inside the system and the edge states (topological states) are observed at the system boundaries. Such materials have unique electrical properties, i.e., topological states are insensitive to external perturbations, they survive for different substrates, reveal long-range conductance oscillations and can play a role of effective electron pumps [11,20]. Simple topological phases in one-dimensional chains can be obtained within a fermionic Su–Schrieffer–Heeger (SSH) model [29,30]. The model possesses two different topological phases: the trivial phase with an energy gap along the whole system, and the nontrivial one with spectrally isolated mid-gap states at the system boundaries.

In this paper we analyse modified SSH chains (straight, zig-zag and armchair edge geometries) in contact with different types of 2D electrodes which play a role of electron reservoirs. The leads can be characterized by a flat band structure or can possess van Hove singularities in their density of states (DOS). Such singularities (peaks or dips in DOS) are commonly found in real 2D structures like graphene, silicene, antimonene or other atomic layers that could be fabricated and modified to obtain fully functional materials [2,31,32]. Although topological insulators, as well as topological 1D structures have been intensively investigated in last years the influence of low-dimensional electrodes on topological states in hybrid systems has been often overlooked. The main objective of this work is to find how topological SSH states are influenced by the DOS singularities of 2D substrates. It is crucial to verify if these states are robust to these singularities and if the space and energetic symmetries of 1D edge states (which are responsible for the particle-hole symmetry) survive in the presence of 2D substrates. Moreover, the question if the SSH topological states can appear outside the electrode's DOS (beyond the band) is going to be answered in this paper.

2. Model and Theoretical Description

Hybrid systems under consideration are shown in Figure 1. In the simplest case there is a straight SSH chain on 2D electrode (panel a). The surface is described by the tight-binding Hamiltonian for a regular atomic lattice (e.g., rectangular or hexagonal) which leads to the effective surface DOS with the van Hove singularities (see Appendix A). The hybrid systems (Hybrid1 and Hybrid2) are depicted in panels (b) and (c) in Figure 1, where a zig-zag (or armchair edge) SSH chain is placed between two 2D electrodes. In this case, the electronic structure of the chain is influenced by two different electron reservoirs (hybrid structures) which is the central point of studies prested in this paper.

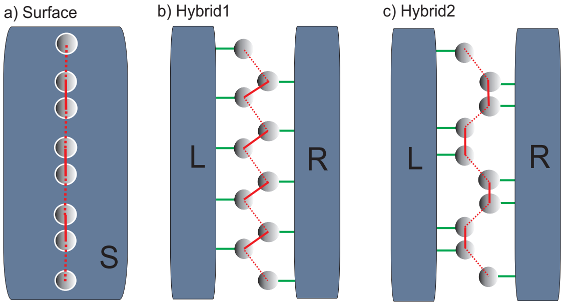

Figure 1. Schematic view of the SSH atomic chain for different geometries: (**a**) straight chain on 2D electrode, (**b**,**c**) zig-zag and armchair edge chains between two 2D electrodes called here Hybrid1 and Hybrid2, respectively. The broken and solid red lines represent different couplings between the nearest-neighbour atomic sites in the SSH chain.

Such systems can be realized experimentally using modified vicinal surfaces where a single or double chains as well as atomic ribbons can be easily fabricated within the epitaxy method. These structures can be investigated by means of the STM (Scanning Tunneling Microscope) technique which measures current-voltage characteristics or the conductance that is proportional to the local DOS. Detailed analysis of this quantity allows one to distinguish different topological phases of the SSH chains [33,34]. Among many experimental fabrication methods of 1D systems one can find atomic chains grown epitaxially on silicon surfaces, such as Si(335), Si(557) [35–37], 1D chains with gate-defined quantum dot in 2D electron gas or chains of dopant atoms in silicon [38,39]. Alternatively, the SSH topology was found in chlorine vacancies on Cu(100) surfaces [34,40]. In such systems, the role of 2D substrate electrodes can play the surface atomic reconstruction (like Si(111)-(6 × 6)Au surface) or atomically flat graphene, silicene, antimonene or other layers which nowadays can be easily fabricated [2,31,32,41,42]. It is also possible to combine one-dimensional SSH chains between two 2D substrates (hybrid geometry). In such a case, the chain localized at the step of the surface is coupled with both nearest terraces (they stand for 2D structures with different DOS). Alternatively, one can use precisely controlled quantum dot chain coupled with different electrodes characterized by the van Hove peaks.

The tight-binding model Hamiltonian in the standard second-quantized notation for the system shown in Figure 1, can be written as follows: $H = H_0 + H_{coup}$, where:

$$H_0 \quad = \quad \sum_{i=1}^{N} \varepsilon_i a_i^\dagger a_i + \sum_{\alpha} \sum_{\vec{k}} \varepsilon_{\vec{k}\alpha} a_{\vec{k}\alpha}^\dagger a_{\vec{k}\alpha} \tag{1}$$

describes the on-site electron energies in the atomic chain, ε_i, and in the α electrode, $\varepsilon_{\vec{k}\alpha}$, with the wave vectors $\vec{k}$ ($\alpha = S$ corresponds to only one surface electrode (Figure 1, panel a), and $\alpha = L, R$ corresponds to the hybrid geometries shown in Figure 1, panels b and c). The operators $a_i(a_i^\dagger)$ annihilate(create) an electron at i-th site of the chain ($i = 1, ..., N$) and $a_{\vec{k}\alpha}(a_{\vec{k}\alpha}^\dagger)$ are the according leads annihilation(creation) operators. In calculations both spin directions are independent of each other and the spin index in operators is suppressed. As we are interested in the SSH topological state modifications, in the first step it is assumed that the electron correlation effects do not play an important role. This assumption is reasonably well satisfied, e.g., for lead or gold chains on vicinal silicon surfaces. For small electron-electron correlation it can be captured by an effective shift of the chain onsite energies [43–45]. The electron transitions along the chain and between the surface and chain sites are described by the coupling Hamiltonian in the following form:

$$H_{coup} \quad = \quad \sum_{i=1}^{N-1} V_{i,i+1} a_i^\dagger a_{i+1} + \sum_{i=1}^{N} \sum_{\vec{k}\alpha} V_{i,\vec{k}\alpha} a_{\vec{k}\alpha}^\dagger a_i + H.c. \tag{2}$$

The first part of this Hamiltonian consists of the tunneling matrix elements $V_{i,i+1}$ which describe the couplings between the neighboring sites in the chain. Note that for different every second couplings $V_{i,i+1}$ ($V_{i,i+1} = V, V_{i+1,i+2} = W$ such that $V \neq W$) the system corresponds to the topological SSH chain [46–48] and for equally coupled sites ($V = W$) the system is in the normal state. By taking $V < W$ one gets a topological chain in the nontrivial phase (called here SSH$_1$), i.e., with topological mid-gap states at both chain ends. When one applies $V > W$ it is obtained a chain in the trivial topological phase without end states (SSH$_0$). The second part of Equation (2) describes the chain-substrate coupling where electron transitions between the i-th chain state and the surface states are established by $V_{i,\vec{k}\alpha}$ matrix elements (hybridization terms).

In this paper the topic of interest is the spectral density function at atomic sites in the chain (local DOS) which can be obtained from the knowledge of the corresponding diagonal matrix elements of the retarded Green's operator at a given site: [49,50]

$$LDOS_i(E) = -\frac{1}{\pi} \mathtt{Im}(G_{ii}^r(E^+))\,, \tag{3}$$

where $E^+ = E + i\varepsilon$ (ε is positive infinitesimal number which tends to zero) and $G_{ii}^r(E)$ for the time-independent Hamiltonian satisfies the following equation of motion:

$$EG_{ij}^r(E) = \langle [a_i, a_j^\dagger]_+ \rangle + \langle\langle [a_i, H]_-; a_j^\dagger \rangle\rangle_E, \tag{4}$$

where the bracket $\langle\langle ... \rangle\rangle_E$ corresponds to new energy-dependent Green's function which includes $\vec{k}\alpha$ states due to the total Hamiltonian in the above equation. For N-site system the total Green's function could be obtained by solving N coupled linear equations which can be written in the matrix notation: $\hat{G}^r \cdot \hat{A} = \mathbb{I}$, where $\mathbb{I}$ is the identity matrix. The matrix $\hat{G}^r$ stands for $N \times N$ array of the appropriate Green's functions and $\hat{A}$ is a square $N \times N$ complex array which can be found from Equation (4) and it takes the following form:

$$A_{i,j}^{N\times N}(E) \quad = \quad (E-\varepsilon_i)\delta_{i,j} - V_{i,j+1}(\delta_{i,j+1}+\delta_{i+1,j}) + \Sigma_{i,j}(E), \tag{5}$$

where $\Sigma_{i,j}(E) = \sum_{\vec{k}\alpha} \frac{V^*_{i,\vec{k}\alpha} V_{j,\vec{k}\alpha}}{E^+ - \varepsilon_{\vec{k}\alpha}}$. The off-diagonal elements of the matrix $\hat{\Sigma}(E)$ depend exponentially on i-th and j-th atomic distance [45,51] so they rapidly vanish and in the paper are negligible. It allows one to consider the electrode as a set of equivalent leads such that each chain site is coupled with its own electrode. Thus, assuming that only diagonal terms of the matrix $\hat{\Sigma}(E)$ play an important role (and they are the same for all chain sites, $\Sigma_{i,j}(E) = \delta_{ij}\Sigma(E)$) one can express this function by the real and imaginary complex forms as $\Sigma(E) = \Lambda(E) - i\Gamma(E)/2$. Here $\Gamma(E) = 2\pi|V_{\vec{k}\alpha}|^2 \sum_{\vec{k}\alpha} \delta(E-\varepsilon_{\vec{k}\alpha}) = 2\pi|V_{\vec{k}\alpha}|^2 DOS_\alpha(E)$, where $DOS_\alpha(E)$ stands for energy dependent α lead (surface) DOS. Both functions $\Lambda(E)$ and $\Gamma(E)$ are not independent, see Appendix B, and they are responsible for the localized states in the system which appear for some values of the chain on-site energies. For a flat and $\vec{k}$-independent surface DOS, i.e., within the wide band approximation one has: $\Lambda(E) = 0$ and $\Gamma(E) = \Gamma$ which is constant and energy independent [44,45,49,51]. On the other hand, assuming a specific surface DOS like for 2D materials (see Appendix A for the 2D van Hove DOS) one can find $\Gamma(E)$ function and then using the Hilbert transform can obtain the second $\Lambda(E)$ function. It allows one to write explicitly all matrix elements of $\hat{A}$, Equation (5), and the retarded Green's functions can be obtained by inversion of this matrix, i.e.,

$$G^r_{ii}(\varepsilon) = (\hat{A}^{-1})_{ii} = \frac{\mathtt{cof}\,\hat{A}_{ii}}{\det \hat{A}}\,, \tag{6}$$

where $\mathtt{cof}\,\hat{A}$ and $\det \hat{A}$ mean the cofactor (algebraic complement) and determinant of the matrix $\hat{A}$. For a regular chain with the same atom-atom couplings and homogenous on-site energies these functions can be expressed analytically by means of the Chebyshev polynomials of the second kind [45,52]. In general case, for topological SSH chains analytical solutions are also possible but they have no simple transparent forms. Thus, we obtains here the local DOS along the chain for a given leads DOS numerically (using Java and Fortran codes) and compare the results for different system geometries.

In the calculations homogenous on-site energies for all chain sites are considered, $\varepsilon_i = \varepsilon_0$ and there is used the zero temperature limit. The energies are expressed in units of $\Gamma = 1$ where Γ is defined as usually for a flat, $\vec{k}$-independent lead DOS of the width w as follows: $\Gamma = 2\pi|V_{\vec{k}}|^2/w$ (which is related to the wide band limit approximation). The energy reference point is the chemical potentials of the leads, $E_F = 0$. For experimentally available values of $\Gamma \simeq 0.5$eV the typical coupling units between atomic sites would be $0.5 - 2$eV.

3. Results and Discussions

3.1. Straight SSH Atomic Chain

The first system under consideration is a straight SSH chain on 2D electrode (see Figure 1, panel a). In Figure 2 we analyze the local DOS of the chain for different surfaces. In particular it is assumed a flat rectangular surface DOS (panels a and d), surface DOS with one van Hove singularity in the middle of the band (panels b and e), and the surface DOS with two van Hove singularities with vanishing value in the middle of the band (panels c and f). These functions are shown in Figure 2 (dashed black curves) and they correspond to the wide-band approximation, 2D rectangular lattice, and 2D honeycomb lattice, respectively. The surface DOS can be obtained exactly for different regular atomic latices [53–56] and their analytical forms are shown in the Appendix A. Note that such atomic lattices are fabricated in many experiments e.g., Pb atomic films form a hexagonal close-packed structure on Al(111) substrate, Sn atoms on Al(100) or Al(111) are found to form square-like structures [57,58] similarly, Sb films form square-like structures on Rh(111) [59]. In addition, on vicinal surfaces one can obtain multiple Pb chains which form regular atomic nanoribbons on each terrace of Si(553)-Au substrate [43]. We are interested in the local DOS of the chain at the edge site (where the mid-gap topological state appears, $i = 1$, dashed blue curves) and also at one inner site with no topological states (here $i = 2$, red solid curves). Additionally, both symmetrical and asymmetrical cases, i.e., $\varepsilon_0 = E_F = 0$ (left panels) and $\varepsilon_0 = 4$ (right panels) are considered.

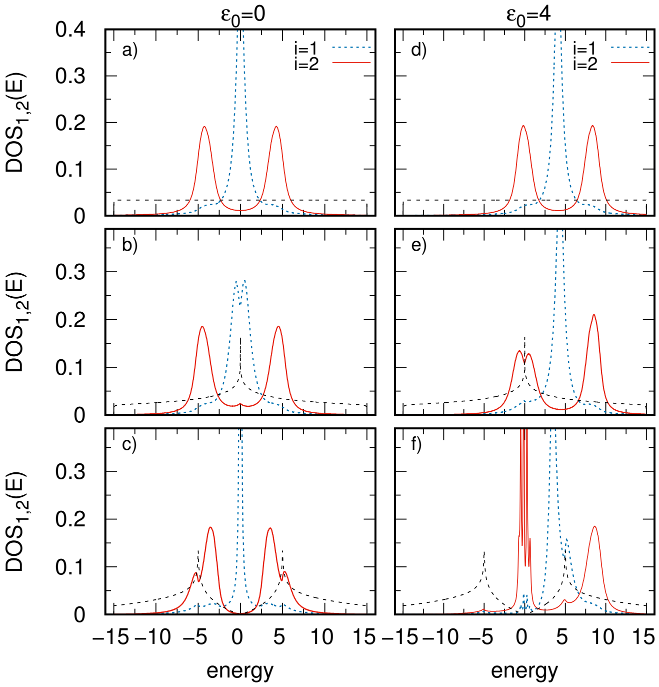

Figure 2. Local DOS at two sites of the straight SSH chain (see panel a in Figure 1), $i = 1$ (blue broken curves) and $i = 2$ (red solid curves) as a function of energy, and for different surface DOS shown by the dashed black curves: rectangular DOS (panels **a** and **d**), 2D-DOS with one van Hove singularity (panels **b** and **e**) and for 2D-DOS with two van Hove peaks (panels **c** and **f**). The left (right) panels correspond to $\varepsilon_0 = 0$ ($\varepsilon_0 = 4$). The chain length is $N = 12$ sites, the couplings are $V = 1$, $W = 4$, and the surface DOS width is $w = 30$ (all energies are expressed in Γ units).

For the SSH$_1$ chain on the surface with rectangular DOS (panels a and d) the electronic structure of the chain is characterized by two sideband peaks (bulk bands) with the energy gap between them for the interior sites (e.g., for $i = 2$) and the mid-gap state localized at $E = \varepsilon_0$ for the edge site ($i = 1$ and $i = N$). In this case, the surface DOS is flat (energy independent) and can be effectively described within the wide-band limit approximation. Thus, the surface described within this approximation does not influence the chain topological states which is in agreement with the literature results [60]. The situation changes for realistic 2D square lattice substrate with the van Hove singularity in the middle of the band (panels b and e). This van Hove peak can be considered as a kind of sharp atomic state which is coupled with the mid-gap edge state of the SSH chain. It is the reason that the topological SSH state splits for $E = 0$ (panel b) and it is not robust against the surface states. In addition, for the asymmetrical case (panel e, $\varepsilon_0 = 4$) the energy of the van Hove peak corresponds to the energy of the lower (left) sideband in the chain and there is a small local minimum in the structure of this band at $E = 0$. For other energies, i.e., beyond the van Hove singularity the substrate spectral density is relatively flat and thus the chain DOS is almost the same as for the rectangular case (see the upper panels). The most interesting case one can observe for the honeycomb lattice underneath the chain (panels c and f). Now, the substrate DOS is characterized by two van Hove peaks at $E = \pm 5$ and a local minimum in the middle of the band. As before these peaks are responsible for the local minima in the chain DOS, i.e., in both sidebands (panel c) or in the mid-gap state (panel f). However, for very low values of the substrate DOS (near $E = 0$) the chain-surface effective coupling $\Gamma(E)$ tends to zero which leads to the atomic limit for this energy span. Thus, for the symmetrical case the mid-gap topological state is very narrow (and almost disperssionless) than for non-zero surface DOS (shown in panels a and b). One can see that 2D substrates essentially modify topological states and change effectively their shape. For the asymmetrical case (panel f) low values of the substrate DOS correspond to the left sideband of the chain DOS. The sidebands consist of many bulk states (due to the surface coupling they form relatively smooth function of the energy) but in this case the lower one reveals an atomic structure around the zero energy and has many sharp peaks. At the same time the second (upper) sideband of the chain DOS (around $E = 9$) remains in the form of the bulk shape. As a consequence, very regular structure of the chain DOS can drastically change in the presence of the van Hove singularity or energy dips in the substrate DOS. Note that for $\varepsilon_0 = 0$ (left panels) all local DOS functions are symmetrical in the energy scale which results from symmetrical structures of the surface DOS with respect to the Fermi energy and the particle-hole symmetry is not broken in this case. For different value of ε_0 this symmetry still exists for a plane surface DOS (right upper panel) but it is broken for real 2D lattice DOS (panels e and f). Thus, strong asymmetry in the local DOS of atomic system can come from the peaked structure of the surface DOS which was not reported before and it leads to breaking of the system particle-hole symmetry.

3.2. *Boundary Effects in Chain DOS*

It was shown that local dips in the structure of the substrate DOS strongly modify electronic properties of the SSH chain for symmetrical as well as asymmetrical cases (i.e for different positions of the chain on-site energies, ε_0). However, for larger ε_0 or for relatively narrow surface band the chain on-site energies can lie in the vicinity of the substrate DOS boundaries or even beyond the band. In such a case one expects localized states in the system (like for an adatom on the surface [50]) and significant changes in the chain DOS structure can appear. Thus, it is desirable to study this effect for topologically trivial and nontrivial SSH chains on a surface. The corresponding results are depicted in Figure 3 for both chains, SSH_0 (upper panel) and SSH_1 (bottom panel) in the form of heatmaps of the local DOS along the whole chain, i.e., at each chain site, $i = 1, ..., 12$. The position of ε_0 is very close to the surface DOS boundary, $\varepsilon_0 = 14$, such that the bottom sideband of the SSH chain lies inside the surface DOS and the second one is outside this band. For the trivial SSH chain (upper panel) the boundary of the surface DOS ($E = 15$) corresponds to the chain energy gap and there are still two sidebands of the chain DOS (inside and outside the surface band). The lower sideband is quite smooth (like the sidebands in Figure 2, upper panels) as its energy lies inside the surface band. On the other hand, the outside sideband is characterized by very sharp and high DOS peaks as in this case there are no corresponding energy states in the substrate and the effective coupling $\Gamma(E) = 0$ for $E > 15$. Thus, outside the substrate band the chain states tend to atomic limit and strong asymmetry of the local DOS appears (as a function of the energy). For nontrivial SSH_1 chain (bottom panel) both chain sidebands are also nonsymmetrical and they behave in the same way as for the SSH_0 chain. However, at both edge sites, $i = 1$ and $i = N$, there exist topological states and as one can see for $E > 15$ (outside the substrate band) these states suddenly disappear and no extra states are observed above this energy. In this case, the structure of topological state becomes asymmetrical and this interesting effect is going to be studied in more details.

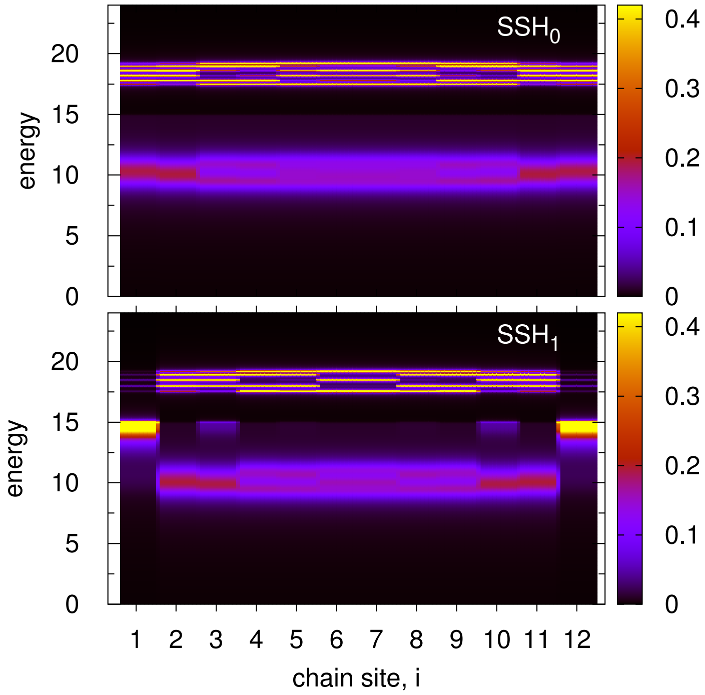

Figure 3. Heatmap plots of the energy and site dependent local DOS along the whole chain, $N = 12$, for the same system as in Figure 2 for the rectangular surface DOS and for $\varepsilon_0 = 14$ (in the vicinity of the edge surface DOS). The upper (bottom) panel corresponds to the SSH$_0$ chain with $V = 4$, $W = 1$ (SSH$_1$ chain with $V = 1$, $W = 4$).

In order to analyze the SSH mid-gap states near the surface DOS boundary there were performed additional studies which are described in Figure 4. Here it is considered the local DOS at $i = 1$ for different on-site energies in the chain, around $\varepsilon_0 \simeq 15$, as it is depicted in the legend. Note that the surface is described by a rectangular DOS with nozero constant value for $|E| \leq 15$, thus the chain on-site energies correspond to the surface band edge. For $\varepsilon_0 = 12$ the whole mid-gap state lies inside the surface DOS region and its shape is almost the same as for smaller ε_0 (see Figure 2, upper panels) or as for the surface DOS obtained within the wide band limit. Here, the maximum of this state is somewhat shifted from $\varepsilon_0 = 12$ towards higher energies due to nonzero $\Lambda(E)$ function which effectively shifts the on-site energies (see Appendix B). Note that for small value of ε_0 (in the middle of the band) the local DOS peak at the edge site appears for $E \simeq \varepsilon_0$ because $\Lambda(E)$ tends to zero for $E = 0$ as was shown in Figure A1 in the Appendix. However, for larger value of ε_0 this function increases thus the local DOS maximum is slightly shifted and appears for $E = 12.4$ in this case ($\varepsilon_0 = 12$). For $\varepsilon_0 = 14$ the state lies closer to the band edge (red curve) and the structure of topological state drastically changes. As before there is no maximum of this state at $E = \varepsilon_0 = 14$ but it is shifted towards higher energies. However, outside the surface band only dispersionless localized states can be observed (a very high and narrow peak appears for the energy near the surface DOS edge). Its position is determined by the cross of $E - \varepsilon_0$ linear function with $\Lambda(E)$, as was shown in the Appendix B. In consequence the mid-gap topological state assumes asymmetrical structure which consists of a wide part together with strongly localized peak (red curve). Such a shape of the edge topological state in 1D chain has not been reported before and it cannot appear in a system described by the wide band approximation. For further values of ε_0, beyond the surface band, one can observe only sharp dispersionless states of the chain local DOS ($\varepsilon_0 = 16, 18$) but also some small DOS spikes are visible for $E > 15$. These small peaks are related to the sideband structure of the local DOS in the chain. It is worth mentioning that for the SSH$_0$ chain the local DOS at the edge sites has only two sidebands structure and for the SSH$_1$ chain this structure still exists together with the mid-gap states.

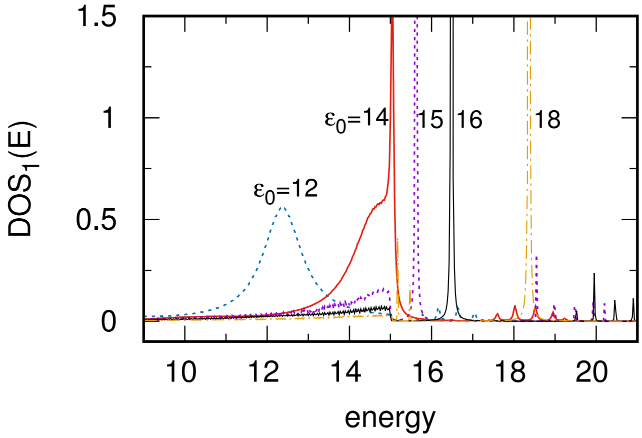

Figure 4. Local DOS at the first site of the SSH$_1$ chain on a surface described by a rectangular DOS (the same as in Figure 2, upper panels) for different values of the chain on-site energy, $\varepsilon_0 = 12, 14, 15, 16$ and 18, respectively. The SSH$_1$ couplings are $V = 1$, $W = 4$.

3.3. Zig-Zag and Armchair-Edge Chains between 2D Systems

Thus far, there was investigated a straight SSH chain on different 2D substrates. Now the objects of study will be more complex hybrid systems composed of a chain between two 2D electrodes which are schematically shown in Figure 1 (panels b and c). We consider a simple zig-zag geometry of the SSH chain, as well as an armchair edge chain structure which can be fabricated on various vicinal surfaces. For the same lattice structure of both (left and right) leads the results are similar to those discussed in the previous sections, thus in this part there is considered two different surface leads composed of a square or hexagonal 2D atomic lattices which are characterized by the van Hove singularities.

Let us first assume a simple zig-zag SSH chain which sites are coupled alternately with the left or right electrodes (so called Hybrid1 system, Figure 1, panel b). It is analysed the energy dependent local DOS at each chain site along the whole chain ($N = 20$) for the symmetrical case (Figure 5, upper panel) and for $\varepsilon_0 = 4$ (Figure 5, bottom panel). In this system every odd chain site is coupled with an electrode characterized by a single van Hove peak in the middle of the band. Thus, for the first atomic chain the nontrivial state is relatively wide with small local minimum appearing for $E = 0$ - the same effect was discussed in Figure 2 panel b. On the other hand, every even number of atom in the chain is coupled with a honeycomb lattice electrode characterized by two van Hove peaks and minimum value of DOS in the middle of the band, thus the edge topological state at the last site, $i = 20$, becomes narrower and higher (as was discussed in Figure 2, panel c). However, this state has some effective dispersion as it is coupled via the last but one site (and also other sites) with the left electrode for which there is a finite value of DOS at the Fermi level. It is also interesting that every second site in the SSH$_1$ chain is characterized by small but nonzero DOS in the energy gap region. This effect is known in the SSH chains where topological states appear mainly at both chain ends but they also symmetrically leak inside the chain with decreasing intensities [29,46]. Here one can observe asymmetrical values of DOS along the chain. It is a consequence of much higher topological state at the last site $i = 20$ in comparison with the first site DOS, which allows for deeper penetration of this state into the chain. As an unexpected result it was found that nonzero local DOS at the Fermi level in the chain is observed for these sites which are directly coupled with the right electrode (which has no states at the Fermi energy).

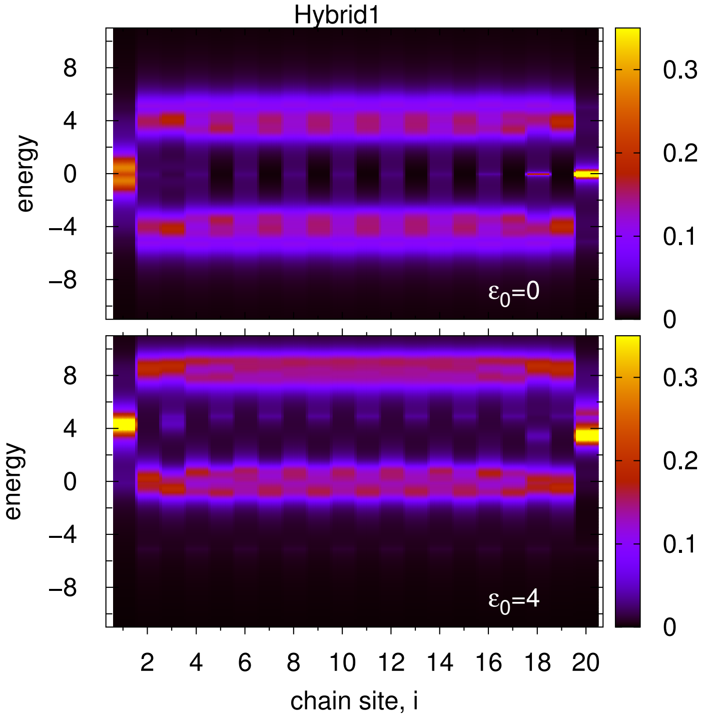

Figure 5. Heatmap plots of the energy and site dependent local DOS along the whole zig-zag chain for the Hybrid1 system (see panel b in Figure 1) for the on-site energies $\varepsilon_0 = 0$ (upper panel) and for $\varepsilon_0 = 4$ (bottom panel). The left (right) 2D electrode is described by DOS with one van Hove (two van Hove) singularity and the chain length is $N = 20$ sites, $V = 1$, $W = 4$.

For the non-symmetrical case ($\varepsilon_0 = 4$, bottom panel) both topological states in the chain are coupled with nonzero DOS of the leads and their energy dispersions are similar to each other. However, the local DOS along the chain is not symmetrical and the maxima of both topological states appear for slightly different energies (the left one for $E \simeq 4.2$ and the right one for $E \simeq 3.5$). It results from the fact that the last chain site (and also every even site in the chain) is coupled with the lead characterized by two van Hove singularities (they appear for $E = \pm 5$). Thus, the edge state for $i = 20$ is split (cf. also Figure 2, panel f), and the topological peak becomes asymmetrical with shifted maximum. This effect shows that maxima of topological edge states in the SSH chain can appear at both edges for slightly different energies in 2D hybrid systems which is a new feature of topological states. It is interesting that the edge state at the first site is symmetrical (as it is coupled to the plain lead DOS around $E = 4$) and it much more effectively spreads over the chain in comparison with the last site topological state which is strongly suppressed inside the chain due to the splitting effect. Moreover, the upper and bottom sideband structures of the local DOS are non-symmetrical in this case-the upper one is relatively smooth but the bottom one reveals periodical oscillations from site to site along the chain depending on the lead band structures. In general, the bottom sideband maxima for this system should appear near $E = 0$ but for this energy the left lead possesses a single van Hove peak and the right lead is characterized by a local dip in DOS. Taking into account that the sites are coupled directly with only one electrode and non-directly with the second one (via the neighbouring sites), one observes mixed effects from both leads-split states with shifted maxima at every second chain site.

In the last study of this paper there is considered armchair edge geometry of the SSH chain (Hybrid2 system), i.e., every atomic dimer of the chain (two sites) is coupled alternatively with the left or right electrodes (see Figure 1, panel c). As before it is plotted energy and site dependent local DOS for two positions of the chain on-site energies $\varepsilon_0 = 0$ and $\varepsilon_0 = 4$, Figure 6, upper and bottom panels, respectively. Note that in our case the chain length is $N = 20$, thus the first and last sites are coupled to the same left electrode which leads to fully symmetrical structure of the local DOS along the chain (they are the same for i-th and $(N - i + 1)$-th sites). This armchair edge geometry is also reflected in the results depicted in both panels in Figure 6. In the upper panel the edge topological states are split and have local minimum at the Fermi energy due to the coupling with the van Hove singularity of the left lead. Two next sites are coupled to the right lead with the singularities localized at $E = \pm 5$, and for these energies one observes local minima in the upper and bottom sidebands. It is the reason that the sideband maxima appear below $|E| = 4$. The further two sites are coupled again to the left lead with relatively flat DOS around the chain sideband energy so the maxima of these sidebands are for $E = \pm 5$. Note that beside the space symmetry of the local DOS along the chain there is also full energy symmetry of DOS at each atomic site with respect to the Fermi energy.

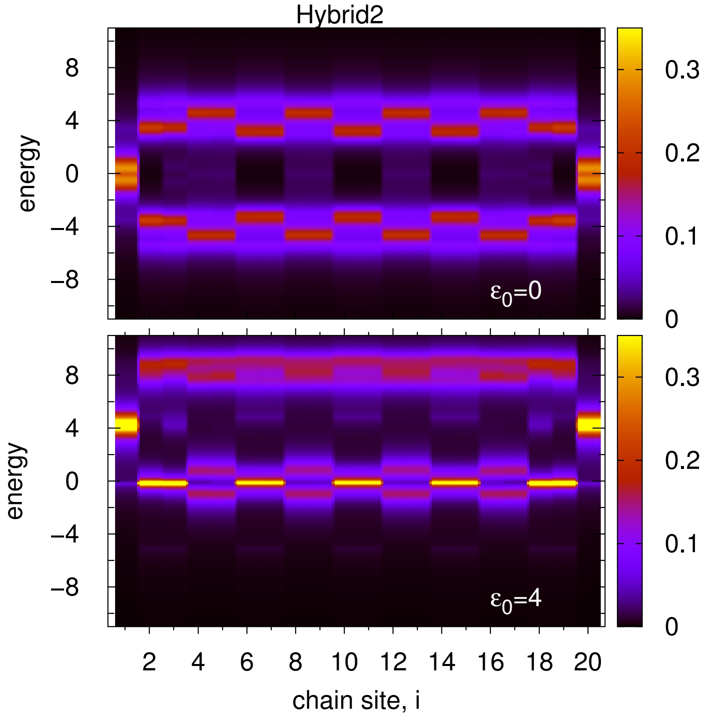

Figure 6. The same as in Figure 5 but for the armchair edge SSH_1 chain (Hybrid2 geometry-see panel c in Figure 1). All parameters are the same as in Figure 5.

This symmetry is broken for nonzero value of the on-site energies, $\varepsilon_0 = 4$ (bottom panel). Now, the edge topological states at $i = 1$ and $i = N$ are described by almost symmetrical local DOS with respect to $E = \varepsilon_0$ but at the rest chain sites this function is non-symmetrical. The upper sideband energy lies beyond the singularities of the lead DOS and for this energy the sideband structure is relatively simple with a local maximum at $E = 8$ (see also the right panels in Figure 2). On the other hand, the bottom sideband corresponds to the Fermi energy of the system where there are extrema of the lead band. In particular, the right lead for the zero energy has no states (local minimum in DOS); thus, the corresponding chain states tend to the atomic limit which is well visible for every two sites of the chain coupled with this electrode (light narrow peaks for $E = 0$). The other chain sites are coupled with the left lead characterized by a single van Hove peak at the Fermi level. In this case, the bottom sideband is split leading to a local minimum in the chain DOS for this energy. In consequence, the local DOS function is asymmetrical with respect to the energy and it reveals double-site periodical oscillations in space (along the chain).

To conclude, for non-linear chain in 2D hybrid configurations one observes interesting periodical in space structures of the local DOS which reflect topological nature of the chain and singularities of both leads. In consequence, one can obtain modified topological chain with asymmetrical sideband structures and split edge states. Such a behavior makes these structures very attractive to potential applications in nanoelectronics. In the next step, it could be interesting to consider superconducting electrodes which can lead to the Majorana states in the chain and analyze time dynamics and proximity effect with topological states in 2D hybrid structures.

4. Conclusions

In this paper, the electronic properties of different hybrid systems composed of the SSH topological chain coupled with 2D electrodes were investigated. In particular, the mid-gap state modifications due to real structures of the surface characterized by the van Hove singularities were analysed. For rectangular or hexagonal 2D atomic lattices, such singularities in DOS often appear (like in graphene or silicene). The calculations were performed within the tight binding Hamiltonian and the Green's function technique. The main conclusions of this work are as follows:

1. Surface with singularities in DOS essentially influences the spectral density function (local DOS) along the chain and is responsible for strong asymmetry in the topological chain energetic structure. It leads to the particle-hole symmetry breaking in the system.
2. The surface van Hove singularities can split the SSH topological state of the chain. On the other hand dips in the surface DOS lead to dispersionless strongly localized states (topological or normal) in the chain.
3. There was also discovered that topological mid-gap states can exist outside the surface band boundaries. It is important that when the chain on-site energies lie near the surface DOS edges topological state reveals partially localized behaviour with both wide dispersion due to continuous band states and sharp localized peak which comes from the surface band boundaries.
4. Different geometries of the SSH atomic chain between two 2D electrodes systems show spatial and energetic asymmetry in the structure of chain DOS which leads to different energies of both topological edge states at the chain ends.

The above findings can be verified experimentally for self-assembling or STM-manipulated atomic chains in the SSH geometries fabricated on different 2D materials (in particular on vicinal substrates).

Author Contributions: Conceptualization, T.K. and M.K.; methodology, T.K.; software, T.K. and M.K.; formal analysis, T.K. and M.K.; results interpretation, T.K. and M.K.; investigation, T.K. and M.K.; resources and data curation, M.K.; writing, T.K. and M.K.; original draft preparation, T.K. and M.K.; review and editing, T.K. and M.K.; visualization, T.K. and M.K.; scientific supervision T.K. All authors have read and agreed to the published version of the manuscript.

Funding: This work was partially supported by National Science Centre, Poland, under Grant No. 2018/31/B/ST3/02370.

Institutional Review Board Statement: Not applicable.

Informed Consent Statement: Not applicable.

Data Availability Statement: It does not apply to this work.

Acknowledgments: Not applicable.

Conflicts of Interest: The authors declare no conflict of interest. The funders had no role in the design of the study; in the collection, analyses, or interpretation of data; in the writing of the manuscript, or in the decision to publish the results.

Appendix A

The energy-band dispersion, $DOS_s(E)$, for the surface described by a regular tight-binding Hamiltonian can be expressed analytically by the relation:

$$DOS_s(E) = \sum_n \int \frac{d\vec{k}}{(2\pi)^2} \delta[E - \varepsilon_n(\vec{k})] \,, \tag{A1}$$

where the summation over n concerns the energy bands in the Brillouin zone with the energy dispersion, $\varepsilon_n(\vec{k})$. In 2D tight-binding models e.g., for square, triangle, honeycomb, graphene-like, Lieb, Kagome and other lattices the energy dispersion is derived analytically and can be expressed by means of the elliptic integrals [53–56]. In particular for 2D rectangular lattice one has:

$$DOS_s(E) = \frac{4}{\pi^2 w} K\left(\sqrt{1 - \left(\frac{2E}{w}\right)^2}\right) \Theta\left(\frac{w^2}{4} - E\right), \tag{A2}$$

where $K(x) = \int_0^{\pi/2} \left(1 - x \sin^2 \varphi\right)^{-1/2} d\varphi$, and w is the bandwidth of DOS. This relation is characterized by a van Hove logarithmic singularity in the middle of the band as it is shown in Figure 2 (dashed black curve, panel b). For the honeycomb lattice the structure of DOS is described by the following formulae:

$$DOS_s(E) = \frac{2|E|}{\pi^2 t^2} \begin{cases} \frac{1}{\sqrt{f(|E|/t)}} K\left(\frac{4|E|/t}{f(|E|/t)}\right), & for \quad 0 < |E| < t \\ \frac{1}{\sqrt{4|E|/t}} K\left(\frac{f(|E|/t)}{4|E|/t}\right), & for \quad t < |E| < 3t \end{cases} \tag{A3}$$

where $f(x) = (1 + x)^2 - (1 - x^2)^2/4$, and $t = w/6$. In this case, the structure of DOS has two van Hove singularities localized at $E = \pm t$ with a local minimum in the middle of the band, which is shown in Figure 2 (dashed black curve, panel c). It is worth noting that in three dimensions a simple cubic lattice is characterized by a flat dispersion of DOS in the middle of the band thus a rectangular DOS (or even wide band limit approximation) relatively well describes this structure.

Appendix B

Localized states which can appear at the chain sites are related with the Green's function determinant in the form $E - \varepsilon_0 - \Sigma(E)$, where $\Sigma(E)$ is expressed by the relation below Equation (5) and satisfies the relation: $\Sigma(E) = \Lambda(E) - i\Gamma(E)/2$. These functions, $\Lambda(E)$, $\Gamma(E)$, are related through the Hilbert transform:

$$\Lambda(E) = \frac{1}{2\pi} \int_{-\infty}^{\infty} \frac{\Gamma(E')}{E - E'} dE', \tag{A4}$$

thus the knowledge of $\Gamma(E)$ which depends in the substrate DOS structure allows one to determine all other functions. Moreover, it is also possible to predict the appearance of localized states in the system. These states are observed for vanishing $\Gamma(E)$ (outside the surface band) and they appear for minimal value of $E - \varepsilon_0 - \Lambda(E)$, i.e., for $E - \varepsilon_0 = \Lambda(E)$. In this case, $\Lambda(E)$ function renormalizes the on-site energy position leading to the localized state outside the substrate DOS. It can be shown graphically in Figure A1, where $\Lambda(E)$, $\Gamma(E)$ and $E - \varepsilon_0$ functions for a rectangular lead DOS are analysed.

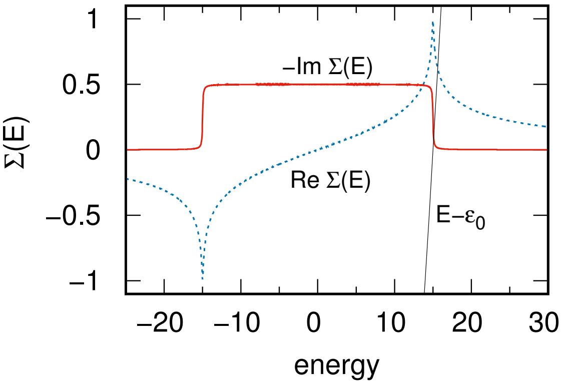

Figure A1. Real and imaginary parts of the $\Sigma(E)$ function, $\mathtt{Re}\Sigma(E) = \Lambda(E)$ and $\mathtt{Im}\Sigma(E) = -\Gamma(E)/2$, respectively, for a rectangular lead DOS of the width $w = 30$. The cross point of $E - \varepsilon_0$ and $\Lambda(E)$ indicates a localized state in the system, here it is set $\varepsilon_0 = 15$.

As one can see $\Gamma(E)$ function (red solid curve) is strictly related to the lead DOS. Its Hilbert transform, $\mathtt{Im}\Sigma(E) = \Lambda(E)$ (broken blue curve), is nonzero even for vanishing $\Gamma(E)$, and the localized state appears for the crossing point of $E - \varepsilon_0$ and $\Lambda(E)$ functions.

References

1. Yu, B. Graphene nanoelectronics: Overview from post-silicon perspective. In Proceedings of the 2012 IEEE 11th International Conference on Solid-State and Integrated Circuit Technology, Xi'an, China, 29 October–1 November 2012; pp. 1–2. doi:10.1109/ICSICT.2012.6467685.
2. Shore, K.A. Introduction to Graphene-Based Nanomaterials: From Electronic Structure to Quantum Transport, by Luis E.F. Foa Torres, Stephan Roche and Jean-Christophe Charlier. *Contemp. Phys.* **2014**, *55*, 344–345, doi:10.1080/00107514.2014.933267.
3. Li, D.; Liu, T.; Yu, X.; Wu, D.; Su, Z. Fabrication of graphene–biomacromolecule hybrid materials for tissue engineering application. *Polym. Chem.* **2017**, *8*, 4309–4321. doi:10.1039/C7PY00935F.
4. Lieber, C.M. One-dimensional nanostructures: Chemistry, physics and applications. *Solid State Commun.* **1998**, *107*, 607–616. doi:10.1016/S0038-1098(98)00209-9.
5. Saxena, S.K.; Nyodu, R.; Kumar, S.; Maurya, V.K., Current Advances in Nanotechnology and Medicine. In *NanoBioMedicine*; Saxena, S.K., Khurana, S.M.P., Eds.; Springer: Singapore, 2020; pp. 3–16. doi:10.1007/978-981-32-9898-9_1.
6. Auslaender, O.M.; Steinberg, H.; Yacoby, A.; Tserkovnyak, Y.; Halperin, B.I.; Baldwin, K.W.; Pfeiffer, L.N.; West, K.W. Spin-Charge Separation and Localization in One Dimension. *Science* **2005**, *308*, 88–92, doi:10.1126/science.1107821.
7. Kwapiński, T.; Taranko, R. Spin and charge pumping in a quantum wire: The role of spin-flip scattering and Zeeman splitting. *J. Physics: Condens. Matter* **2011**, *23*, 405301. doi:10.1088/0953-8984/23/40/405301.
8. Nadj-Perge, S.; Drozdov, I.K.; Li, J.; Chen, H.; Jeon, S.; Seo, J.; MacDonald, A.H.; Bernevig, B.A.; Yazdani, A. Observation of Majorana fermions in ferromagnetic atomic chains on a superconductor. *Science* **2014**, *346*, 602–607. doi:10.1126/science.1259327.
9. Pawlak, R.; Kisiel, M.; Klinovaja, J.; Meier, T.; Kawai, S.; Glatzel, T.; Loss, D.; Meyer, E. Probing atomic structure and Majorana wavefunctions in mono-atomic Fe chains on superconducting Pb surface. *NPJ Quantum Inf.* **2016**, *2*, 16035. doi:10.1038/npjqi.2016.35.
10. Shin, J.S.; Ryang, K.D.; Yeom, H.W. Finite-length charge-density waves on terminated atomic wires. *Phys. Rev. B* **2012**, *85*, 073401. doi:10.1103/PhysRevB.85.073401.
11. Kurzyna, M.; Kwapiński, T. Non-local electron transport through normal and topological ladder-like atomic systems. *J. Appl. Phys.* **2018**, *123*, 194301, doi:10.1063/1.5028571.
12. Kwapiński, T. Conductance oscillations and charge waves in zigzag shaped quantum wires. *J. Phys. Condens. Matter* **2010**, *22*, 295303. doi:10.1088/0953-8984/22/29/295303.
13. van der Wiel, W.G.; De Franceschi, S.; Elzerman, J.M.; Fujisawa, T.; Tarucha, S.; Kouwenhoven, L.P. Electron transport through double quantum dots. *Rev. Mod. Phys.* **2002**, *75*, 1–22. doi:10.1103/RevModPhys.75.1.
14. Fujisawa, T.; Tokura, Y.; Hirayama, Y. Transient current spectroscopy of a quantum dot in the Coulomb blockade regime. *Phys. Rev. B* **2001**, *63*, 081304. doi:10.1103/PhysRevB.63.081304.
15. Hayashi, T.; Fujisawa, T.; Cheong, H.D.; Jeong, Y.H.; Hirayama, Y. Coherent Manipulation of Electronic States in a Double Quantum Dot. *Phys. Rev. Lett.* **2003**, *91*, 226804. doi:10.1103/PhysRevLett.91.226804.
16. Arkinstall, J.; Teimourpour, M.H.; Feng, L.; El-Ganainy, R.; Schomerus, H. Topological tight-binding models from nontrivial square roots. *Phys. Rev. B* **2017**, *95*. doi:10.1103/physrevb.95.165109.
17. Jürß, C.; Bauer, D. High-harmonic generation in Su-Schrieffer-Heeger chains. *Phys. Rev. B* **2019**, *99*. doi:10.1103/physrevb.99.195428.

18. Huneke, J.; Platero, G.; Kohler, S. Steady-State Coherent Transfer by Adiabatic Passage. *Phys. Rev. Lett.* **2013**, *110*. doi:10.1103/physrevlett.110.036802.
19. Kohler, S.; Lehmann, J.; Hänggi, P. Driven quantum transport on the nanoscale. *Phys. Rep.* **2005**, *406*, 379–443. doi:https://doi.org/10.1016/j.physrep.2004.11.002.
20. Kurzyna, M.; Kwapiński, T. Electron Pumping and Spectral Density Dynamics in Energy-Gapped Topological Chains. *Appl. Sci.* **2021**, *11*. doi:10.3390/app11020772.
21. Wilczek, F. Quantum Time Crystals. *Phys. Rev. Lett.* **2012**, *109*, 160401. doi:10.1103/PhysRevLett.109.160401.
22. Sacha, K. Modeling spontaneous breaking of time-translation symmetry. *Phys. Rev. A* **2015**, *91*, 033617. doi:10.1103/PhysRevA.91.033617.
23. Sacha, K.; Zakrzewski, J. Time crystals: A review. *Rep. Prog. Phys.* **2017**, *81*, 016401. doi:10.1088/1361-6633/aa8b38.
24. Kurzyna, M.; Kwapiński, T. Nontrivial dynamics of a two-site system: Transient crystals. *Phys. Rev. B* **2020**, *102*, 245414. doi:10.1103/PhysRevB.102.245414.
25. Lindner, N.H.; Refael, G.; Galitski, V. Floquet topological insulator in semiconductor quantum wells. *Nat. Phys.* **2011**, *7*, 490–495. doi:10.1038/nphys1926.
26. Perez-Piskunow, P.M.; Usaj, G.; Balseiro, C.A.; Torres, L.E.F.F. Floquet chiral edge states in graphene. *Phys. Rev. B* **2014**, *89*. doi:10.1103/physrevb.89.121401.
27. Kraus, C.V.; Dalmonte, M.; Baranov, M.A.; Läuchli, A.M.; Zoller, P. Majorana Edge States in Atomic Wires Coupled by Pair Hopping. *Phys. Rev. Lett.* **2013**, *111*, 173004. doi:10.1103/PhysRevLett.111.173004.
28. Kurzyna, M.; Kwapiński, T. Edge-state dynamics in coupled topological chains. *Phys. Rev. B* **2020**, *102*, 195429. doi:10.1103/PhysRevB.102.195429.
29. Pérez-González, B.; Bello, M.; Álvaro Gómez-León.; Platero, G. SSH model with long-range hoppings: Topology, driving and disorder. *arXiv* **2018**, arXiv:1802.03973.
30. Su, W.P.; Schrieffer, J.R.; Heeger, A.J. Solitons in Polyacetylene. *Phys Rev. Lett.* **1979**, *42*, 1698–1701. doi:10.1103/PhysRevLett.42.1698.
31. Jałochowski, M.; Krawiec, M. Antimonene on Pb quantum wells. *2D Mater.* **2019**, *6*, 045028. doi:10.1088/2053-1583/ab33ba.
32. Stpniak-Dybala, A.; Dyniec, P.; Kopciuszyski, M.; Zdyb, R.; Jałochowski, M.; Krawiec, M. Planar Silicene: A New Silicon Allotrope Epitaxially Grown by Segregation. *Adv. Funct. Mater.* **2019**, *29*, 1906053, doi:https://doi.org/10.1002/adfm.201906053.
33. Drost, R.; Ojanen, T.; Harju, A.; Liljeroth, P. Topological states in engineered atomic lattices. *Nat. Phys.* **2017**, *13*, 668–671.
34. Le, N.H.; Fisher, A.J.; Curson, N.J.; Ginossar, E. Topological phases of a dimerized Fermi–Hubbard model for semiconductor nano-lattices. *NPJ Quantum Inf.* **2020**, *6*, 24. doi:10.1038/s41534-020-0253-9.
35. Crain, J.N.; McChesney, J.L.; Zheng, F.; Gallagher, M.C.; Snijders, P.C.; Bissen, M.; Gundelach, C.; Erwin, S.C.; Himpsel, F.J. Chains of gold atoms with tailored electronic states. *Phys. Rev. B* **2004**, *69*, 125401. doi:10.1103/PhysRevB.69.125401.
36. Kopciuszyński, M.; Dyniec, P.; Krawiec, M.; Łukasik, P.; Jałochowski, M.; Zdyb, R. Pb nanoribbons on the Si(553) surface. *Phys. Rev. B* **2013**, *88*, 155431. doi:10.1103/PhysRevB.88.155431.
37. Baski, A.; Saoud, K.; Jones, K. 1-D nanostructures grown on the Si(5 5 12) surface. *Appl. Surf. Sci.* **2001**, *182*, 216–222. doi:10.1016/S0169-4332(01)00412-3.
38. Hensgens, T.; Fujita, T.; Janssen, L.; Li, X.; Van Diepen, C.J.; Reichl, C.; Wegscheider, W.; Das Sarma, S.; Vandersypen, L.M.K. Quantum simulation of a Fermi–Hubbard model using a semiconductor quantum dot array. *Nature* **2017**, *548*, 70–73. doi:10.1038/nature23022.
39. Zwanenburg, F.A.; Dzurak, A.S.; Morello, A.; Simmons, M.Y.; Hollenberg, L.C.L.; Klimeck, G.; Rogge, S.; Coppersmith, S.N.; Eriksson, M.A. Silicon quantum electronics. *Rev. Mod. Phys.* **2013**, *85*, 961–1019. doi:10.1103/revmodphys.85.961.
40. Huda, M.N.; Kezilebieke, S.; Ojanen, T.; Drost, R.; Liljeroth, P. Tuneable topological domain wall states in engineered atomic chains. *NPJ Quantum Mater.* **2020**, *5*, 17. doi:10.1038/s41535-020-0219-3.
41. Ji, J.; Song, X.; Liu, J.; Yan, Z.; Huo, C.; Zhang, S.; Su, M.; Liao, L.; Wang, W.; Ni, Z.; et al. Two-dimensional antimonene single crystals grown by van der Waals epitaxy. *Nat. Commun.* **2016**, *7*, 13352.
42. Sun, X.; Song, Z.; Liu, S.; Wang, Y.; Li, Y.; Wang, W.; Lu, J. Sub-5 nm Monolayer Arsenene and Antimonene Transistors. *ACS Appl. Mater. Interfaces* **2018**, *10*, 22363–22371, doi:10.1021/acsami.8b03840.
43. Jałochowski, M.; Kwapinski, T.; Łukasik, P.; Nita, P.; Kopciuszyński, M. Correlation between morphology, electron band structure, and resistivity of Pb atomic chains on the Si(553)-Au surface. *J. Phys. Condens. Matter* **2016**, *28*, 284003. doi:10.1088/0953-8984/28/28/284003.
44. Krawiec, M.; Kwapiński, T.; Jałochowski, M. Double nonequivalent chain structure on a vicinal Si(557)-Au surface. *Phys. Rev. B* **2006**, *73*, 075415. doi:10.1103/PhysRevB.73.075415.
45. Kwapiński, T.; Kohler, S.; Hänggi, P. Electron transport across a quantum wire in the presence of electron leakage to a substrate. *Eur. Phys. J. B* **2010**, *78*, 75–81. doi:10.1140/epjb/e2010-10452-x.
46. Asboth, J.K.; Oroszlany, L.; Palyi, A. *A Short Course on Topological Insulators*; Springer: Cham, Switzerland, 2016.
47. Li, L.; Yang, C.; Chen, S. Winding numbers of phase transition points for one-dimensional topological systems. *EPL* **2015**, *112*, 10004. doi:10.1209/0295-5075/112/10004.
48. Li, L.; Xu, Z.; Chen, S. Topological phases of generalized Su-Schrieffer-Heeger models. *Phys. Rev. B* **2014**, *89*, 085111. doi:10.1103/PhysRevB.89.085111.

49. Datta, S. *Electronic Transport in Mesoscopic Systems*; Cambridge Studies in Semiconductor Physics and Microelectronic Engineering; Cambridge University Press: Cambridge, UK, 1995. doi:10.1017/CBO9780511805776.
50. Podloucky, R. M. C. Desjonquères and D. Spanjaard: Concepts in surface physics, 2nd edition, Springer Verlag, Berlin Heidelberg, **1996**, ISBN 978-3-540-58622-7.
51. Newns, D.; Read, N. Mean-field theory of intermediate valence/heavy fermion systems. *Adv. Phys.* **1987**, *36*, 799–849, doi:10.1080/00018738700101082.
52. Kwapiński, T. Conductance oscillations of a quantum wire disturbed by an adatom. *J. Phys. Condens. Matter* **2007**, *19*, 176218. doi:10.1088/0953-8984/19/17/176218.
53. Choy, T.C. Density of states for a two-dimensional Penrose lattice: Evidence of a strong Van-Hove singularity. *Phys. Rev. Lett.* **1985**, *55*, 2915–2918. doi:10.1103/PhysRevLett.55.2915.
54. Horiguchi, T. Lattice Green's Functions for the Triangular and Honeycomb Lattices. *J. Math. Phys.* **1972**, *13*, 1411–1419, doi:10.1063/1.1666155.
55. Katsnelson, M.I. *Graphene: Carbon in Two Dimensions*; Cambridge University Press: Cambridge, UK, 2012. doi:10.1017/CBO9781139031080.
56. Kogan, E.; Gumbs, G. Green's Functions and DOS for Some 2D Lattices. *Graphene* **2021**, *10*, 1–12. doi:10.4236/graphene.2021.101001.
57. Yuhara, J.; Shichida, Y. Epitaxial growth of two-dimensional Pb and Sn films on Al(111). *Thin Solid Film.* **2016**, *616*, 618–623. doi:10.1016/j.tsf.2016.09.028.
58. Feng, H.; Liu, C.; Zhou, S.; Gao, N.; Gao, Q.; Zhuang, J.; Xu, X.; Hu, Z.; Wang, J.; Chen, L.; et al. Experimental Realization of Two-Dimensional Buckled Lieb Lattice. *Nano Lett.* **2020**, *20*, 2537–2543, doi:10.1021/acs.nanolett.9b05316.
59. Yuhara, J.; Schmid, M.; Varga, P. Two-dimensional alloy of immiscible metals: Single and binary monolayer films of Pb and Sn on Rh(111). *Phys. Rev. B* **2003**, *67*, 195407. doi:10.1103/PhysRevB.67.195407.
60. Kurzyna, M.; Kwapiński, T. Electronic properties of atomic ribbons with spin-orbit couplings on different substrates. *J. Appl. Phys.* **2019**, *125*, 144301, doi:10.1063/1.5080651.

FEATURE ARTICLE

Braid Plot—A Mixed Palette Plotting Method as an Extension of Contour Plot

Marcin Kurzyna and Tomasz Kwapiński, *Maria Curie-Sklodowska University, 20-031 Lublin, Poland*

In this article, we propose a new method of three-dimensional data plotting based on the use of mixed hue palettes, which makes it possible to distinguish simultaneously both huge and subtle changes in the value of the presented quantity at the same plot. This method called "braid plot" is based on the alternating use of multiple palettes of colors (a kind of interlacing), which greatly increases the sharpness of the graph and allows us to define areas of equal values more accurately than using traditional graphs with a single palette or contour plot. We present here an algorithm of preparing braid plot composed of any number of initial color sets. As a result of using this type of plot, it was possible to detect, e.g., weak perturbation effects or subtle oscillations of the spectral density function, which is very hard to observe using classical plots.

In scientific work, we often face the need to work with 2-D, 3-D, or even multidimensional sets of data. The most common visualization technique of 3-D data is based on associating values of studied quantity with colors.[1,2,3] It enables mapping 3-D data into 2-D plane. Rainbow color plots, though regarded as not always the best way of visualization,[4,5] are very intuitive. Warm colors (red, yellow) are received as the colors representing high values in contrast to cold colors (blue, cyan). We are able to imagine a lot of examples of such representations in an instant, even based on real-life experiences: temperature maps in a forecast, altitude maps in a geographic atlas, pressure maps, etc. There are many areas of science where such representation helps to analyze large sets of data and sometimes it is the only way to get appropriate interpretation of results. In past years, much effort was made to improve techniques of visualization of often highly varied data in vast fields of scientific disciplines, e.g., oceanography,[6] meteorology,[7] or network visualization.[2] In the aforementioned altitude maps, except color palette, the technique of drawing contours is used. Such an approach makes it much easier to distinguish the terrain of the same height. It is especially important when planning, for example, a bicycle or scooter trip. The use of a contour plot, however, has its drawbacks. Namely, we have reduced the possibility of precisely assigning a specific value to points on the map. Instead, we have to be content with a discrete set of values as opposed to the traditional chart where hue transitions (and their corresponding values) take place continuously. To see the difference, let us first take a look at Figure 1 in which graphs of two-variable, arbitrarily selected function

$$f(x,y) = \sin 1.1\mathrm{x}\cos\mathrm{y} + \sin 2\mathrm{y}\cos 0.9\mathrm{x} + \cos 0.3\mathrm{xy} \quad (1)$$

are presented. The top panel shows the use of a continuous color palette. We can see that this chart shows many details of the function in a very good resolution. It is easy to describe properties of the function like, for example, smoothness, extrema, monotony, etc. On the other hand, it is more difficult to define areas of the same value on this graph due to its continuity and the imperfection of our organ of vision. It is hard to distinguish at which point the function is almost zero as this area appears to be blurry. The contour plot, presented on the lower panel of Figure 1, is different. Here, the ease of data reading is much greater, because we have a countable set of values (in the lower panel, the set of values has been divided into 20 equal segments, which the skilled eye of the observer can easily distinguish). In this kind of plot, it is very easy to see regions of equal values, but one

---

0272-1716 © 2021 IEEE
Digital Object Identifier 10.1109/MCG.2021.3057924
Date of publication 9 February 2021; date of current version 26 January 2022.

Authorized licensed use limited to: Eileen McGuinness. Downloaded on January 26,2022 at 22:03:24 UTC from IEEE Xplore. Restrictions apply.

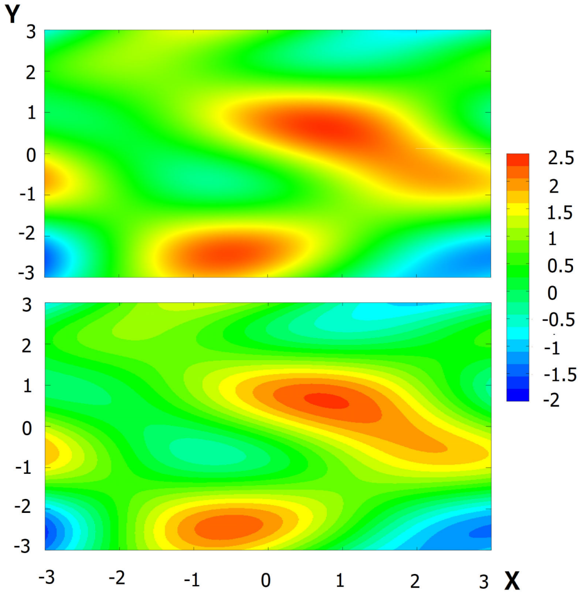

FIGURE 1. Graph of a function $f(x, y) = \sin 1.1x \cos y + \sin 2y \cos 0.9x + \cos 0.3xy$ made in two different ways. (a) Continuous (upper panel). (b) Discrete palette (lower panel).

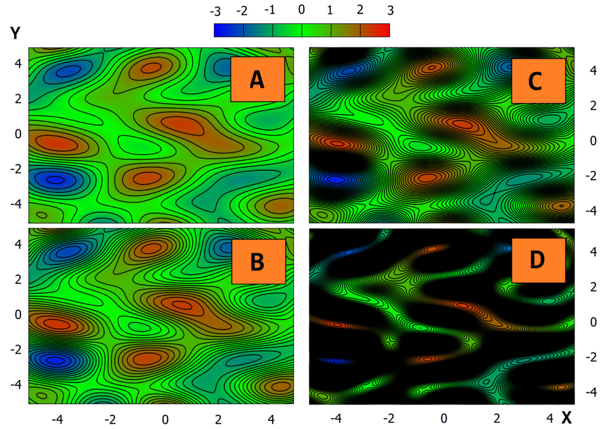

FIGURE 2. Graphs of an arbitrary selected function $f(x, y) = \sin 1.1x \cos y + \sin 2y \cos 0.9x + \cos 0.3xy$ prepared with isolines of different density. In panel A, isolines are drawn every $\Delta f = 0.5$ starting from $f_{\text{MIN}} = -3$. In panel B, $\Delta f = 0.25$, in panel C, $\Delta f = 0.125$, and in panel D, $\Delta f = 0.05$.

must be content that this benefit comes at the expense of accuracy.

So do we have to face a choice? The answer is **no**! We can gain profits of both styles by introducing isolines—curves along which the function has a constant value, such that each curve joins points of equal value.[8] Thanks to this approach, we gain the ease of data reading, while maintaining the continuity (high resolution of details) of the chart. In Figure 2, we can see the graphs with isolines of the function described by (1). Each panel, A, B, C, and D, represents different density of isolines. Isolines are drawn for such points for which the value of the function $f(x, y)$ is equal to $f_{\text{MIN}} + \Delta f$. All panels share the same minimal value of the function $f_{\text{MIN}} = -3$. In panel A, we have $\Delta f = 0.5$; in panel B, isolines are drawn two times denser $\Delta f = 0.25$; in panel C, four times $\Delta f = 0.125$, and in panel D, 10 times denser $\Delta f = 0.05$. As we can see, isolines separate regions of different function values keeping smoothness of the hue transition. However, if we want to increase density of drawing isolines to reach better accuracy, we have to face another problem. Isolines have nonzero thickness. Therefore, increasing their amount covers a bigger amount of the plot. In panels A and B of Figure 2, we can see that the bigger amount of isolines brings a positive result. Panel B reveals much more detail than panel A, so one can think "the more, the better." However, increasing the amount of isolines brings benefits only to a certain critical point. In panels C and D of Figure 2, higher density of isolines at some areas starts to decrease readability instead of improving it. In panel D, we see whole black regions, which arise from overlapping isolines. It makes such a graph completely useless.

Are we doomed to fail then? The results of scientific work are rarely analytical and most often we have to analyze numerical results and some information (subtle physical phenomena, terrain topology) can be lost by smoothness and approximations of 3-D charts. In the most popular computer programs that allow one to create 3-D plots, we cannot find a type of chart that would make it possible to distinguish minor changes from large.[9,10] In the field of programming languages there exist a vast number of graphical libraries allowing one to perform high-quality plots. In the Java language, an effective library named JFreeChart is available, which mainly supports 2-D charts. A more interesting comprehensive library for creating static, animated, and interactive visualizations in Python is Matplotlib.[11] We can find there a variety of different color pallets including periodic color maps, like prism and flag plots (which can be also found in MATLAB[1]). This kind of color map greatly enhances the amount of information available in the plot, but completely loses any metric information-one cannot distinguish values and magnitude order of the perturbations, which is a major disadvantage of such methods.

The comparison of the classical approach with flag and prism plots is shown in Figure 3, where an

Authorized licensed use limited to: Eileen McGuinness. Downloaded on January 26,2022 at 22:03:24 UTC from IEEE Xplore. Restrictions apply.

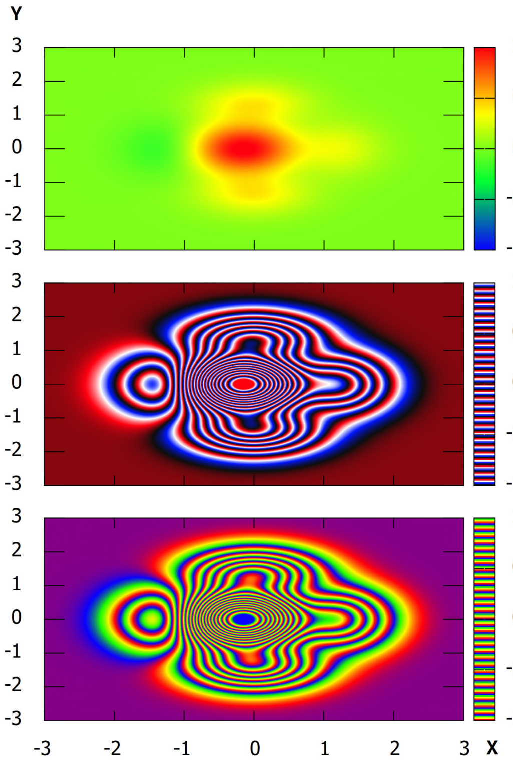

FIGURE 3. Plots of an arbitrary selected function of two variables $f(x,y)=(1-\frac{x}{2}+x^5+y^6)\exp(-\frac{\pi}{2}(x^2+y^2))$ prepared with different types of color maps. Upper panel represents classical plot, middle and bottom panels represent flag and prism plot, respectively.

arbitrary selected function of two variables, given by the following formula

$$f(x,y)=\left(1-\frac{x}{2}+x^5+y^6\right)e^{-\frac{\pi}{2}(x^2+y^2)} \qquad (2)$$

is drawn. Upper, middle, and bottom panels correspond to classical, flag, and prism plots, respectively. As we can see, flag and prism plots reveal many details of the function invisible in the upper panel. However, their accuracy is not as good as one can suspect. This type of plot has another big disadvantage concerning the plot resolution, which we discuss in the "Results" section.

Unfortunately, there is a lack of methods that combine the benefits of value reading ease (continuous, contour plots) with high quality of detail (prism, flag plots). Using both techniques separately and comparing the results is difficult, time-consuming, and requires big effort to properly interpret data of high-complexity in which simultaneously small perturbations and big changes appear. However, in this article, we give a remedy for this problem.

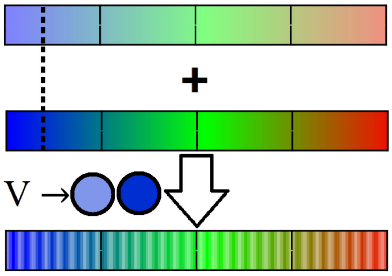

FIGURE 4. Model of a mixed hue palette created by interweaving two palettes with different hue saturation.

MODEL, DESCRIPTION, AND ALGORITHM

In this section, we introduce a new type of 3-D plot based on a combination of multiple color palettes. We present an algorithm of creating mixed palettes and give few examples of its use.

As one can see in Figure 4, every numerical value V is associated with more than one color (upper palettes). Colors assigned to any value are similar (in this figure, V is represented by blue colors of different saturation) but fully distinguishable by the human eye. What is the most interesting, our idea of both color sets combination (presented in the bottom mixed palette) brings surprising benefits. Overlapped colors play a similar role as isolines. They allow one to determine regions of equal value, but they have the advantage that high overlapping frequency does not reduce the readability of the chart. In this article, graphs created with mixed palette are called **braid plots**. Similarly, as in the case of a braid where several hair strands are interlaced with each other to create a hairstyle, our technique requires interweaving of several color palettes to create a plot. The recipe for creating the mixed palette of density D (color compaction factor) composed of M initial palettes (each composed of N initial colors) is described by the following algorithm.

1) Choose the number N of initial colors, which are represented by red, green, and blue components $[r,g,b]$. Define M arrays (M is a number of component palettes) of size N and freely pick colors for each array:

   palette^0

   color$_0^0 = [r_0^0, g_0^0, b_0^0]$,

   color$_1^0 = [r_1^0, g_1^0, b_1^0]$,

   ...

   color$_{N-1}^0 = [r_{N-1}^0, g_{N-1}^0, b_{N-1}^0]$

Authorized licensed use limited to: Eileen McGuinness. Downloaded on January 26,2022 at 22:03:24 UTC from IEEE Xplore. Restrictions apply.

palette^1
color$_0^1 = [r_0^1, g_0^1, b_0^1]$,
color$_1^1 = [r_1^1, g_1^1, b_1^1]$,
...
color$_{N-1}^1 [r_{N-1}, g_{N-1}, b_{N-1}]$

...

palette^{M-1}
color$_0^{M-1} = [r_0^{M-1}, g_0^{M-1}, b_0^{M-1}]$,
color$_1^{M-1} = [r_1^{M-1}, g_1^{M-1}, b_1^{M-1}]$,
...
color$_{N-1}^{M-1} = [r_{N-1}^{M-1}, g_{N-1}^{M-1}, b_{N-1}^{M-1}]$.

2) For every array palette^i find differences between all neighboring colors:

$$\Delta_{0,1}^i = [\Delta r_{0,1}^i, \Delta g_{0,1}^i, \Delta b_{0,1}^i] = [r_1^i - r_0^i, g_1^i - g_0^i, b_1^i - b_0^i]$$
$$\Delta_{1,2}^i = [\Delta r_{1,2}^i, \Delta g_{1,2}^i, \Delta b_{1,2}^i] = [r_2^i - r_1^i, g_2^i - g_1^i, b_2^i - b_1^i]$$
...

Define density of output braid plot D. Divide each difference Δ^i by D rounding to integers:

$$\delta_{0,1}^i = [\delta r_{0,1}^i, \delta g_{0,1}^i, \delta b_{0,1}^i] = \left[\frac{\Delta r_{0,1}^i}{D}, \frac{\Delta g_{0,1}^i}{D}, \frac{\Delta b_{0,1}^i}{D}\right]$$

$$\delta_{1,2}^i = [\delta r_{1,2}^i, \delta g_{1,2}^i, \delta b_{1,2}^i] = \left[\frac{\Delta r_{1,2}^i}{D}, \frac{\Delta g_{1,2}^i}{D}, \frac{\Delta b_{1,2}^i}{D}\right]$$
...

3) Add to every color $(D-1)$ times the $\delta_{j,j+1}^i$ element. Store each result in one of M temporary arrays temp^i of size $N \times D$:

temp$_{j+k}^i$ = color$_j^i + k\delta_{j,j+1}^i$, where $0 \leq k < D$.

4) Define the **weaving number** w, which determines how many colors from a given palette should be taken during each iteration. Create output array by taking alternately w elements from each temporary array temp^i and place them into final array.

To better understand the algorithm in Figure 5, we give an example of creating the mixed color palette shown in Figure 4. This palette was created with two arrays of colors ($M = 2$). Each palette has $N = 3$ initial colors: palette^0 : ([128, 128, 255], [128, 255, 128], [255, 128, 128]) palette^1 : ([0, 0255], [0255, 0], [255, 0, 0]). Density of braid plot $D = 5$ and weaving number $w = 2$. An implementation of the algorithm written in Java is available in the Appendix.

RESULTS

In this section, we will demonstrate examples of graphs prepared with a mixed palette plotting technique and compare them to traditional plots.

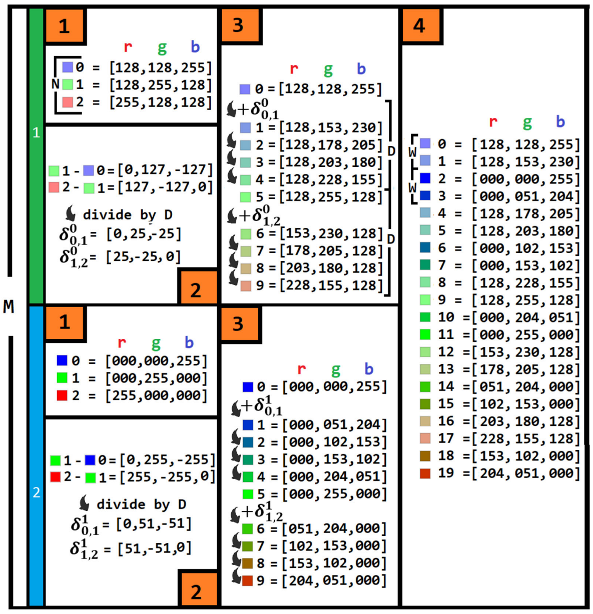
M
1
2
1
r g b
N
0 = [128,128,255]
1 = [128,255,128]
2 = [255,128,128]
1 - 0 = [0,127,-127]
2 - 1 = [127,-127,0]
divide by D
$\delta^0_{0,1}$ = [0,25,-25]
$\delta^0_{1,2}$ = [25,-25,0]
2
3
r g b
0 = [128,128,255]
$+\delta^0_{0,1}$
1 = [128,153,230]
2 = [128,178,205]
3 = [128,203,180]
4 = [128,228,155]
5 = [128,255,128]
D
$+\delta^0_{1,2}$
6 = [153,230,128]
7 = [178,205,128]
8 = [203,180,128]
9 = [228,155,128]
D
4
r g b
W
W
0 = [128,128,255]
1 = [128,153,230]
2 = [000,000,255]
3 = [000,051,204]
4 = [128,178,205]
5 = [128,203,180]
6 = [000,102,153]
7 = [000,153,102]
8 = [128,228,155]
9 = [128,255,128]
10 =[000,204,051]
11 =[000,255,000]
12 =[153,230,128]
13 =[178,205,128]
14 =[051,204,000]
15 =[102,153,000]
16 =[203,180,128]
17 =[228,155,128]
18 =[153,102,000]
19 =[204,051,000]
1
r g b
0 = [000,000,255]
1 = [000,255,000]
2 = [255,000,000]
1 - 0 = [0,255,-255]
2 - 1 = [255,-255,0]
divide by D
$\delta^1_{0,1}$ = [0,51,-51]
$\delta^1_{1,2}$ = [51,-51,0]
2
3
r g b
0 = [000,000,255]
$+\delta^1_{0,1}$
1 = [000,051,204]
2 = [000,102,153]
3 = [000,153,102]
4 = [000,204,051]
5 = [000,255,000]
$+\delta^1_{1,2}$
6 = [051,204,000]
7 = [102,153,000]
8 = [153,102,000]
9 = [204,051,000]

FIGURE 5. Preparation example of mixed color palette of density $D = 5$ and weaving number $w = 2$ composed of two color sets ($M = 2$) with three initial colors ($N = 3$) each.

Braid Plots of Simple Functions

As a first example, we consider, shown in Figure 6, a graph of a freely selected positive function of two variables:

$$f(x,y) = \left(\sin x \cos y + \sin 2y \cos x + \cos \frac{xy}{2}\right)^2. \quad (3)$$

For easier understating, the graph of the function $f(x, y)$ could be compared to an archipelago. Blue can be associated with water, while green, yellow, and red resemble terrain. Looking at panel A and using this analogy, we can notice differences in the terrain construction, we can easily find height changes there. On the other hand, the water gives an impression of a static area. So we can get a false impression that this is one great set of constant values and nothing interesting happens there. The reason for that observation is caused by the fact that the altitude differences at sea are several orders of magnitude smaller than the terrain height differences. This chart cannot capture such subtle changes. In panel B, which is made with isolines drawn with density $\Delta f = 0.5$, one has a greater possibility to notice areas of constant height on the islands, but still is not able to capture changes taking place at sea. In panel C, in which the isolines have been more concentrated $\Delta f = 0.1$, we finally notice differences in water levels. Unfortunately, this happens at the expense of the readability of the data on

Authorized licensed use limited to: Eileen McGuinness. Downloaded on January 26,2022 at 22:03:24 UTC from IEEE Xplore. Restrictions apply.

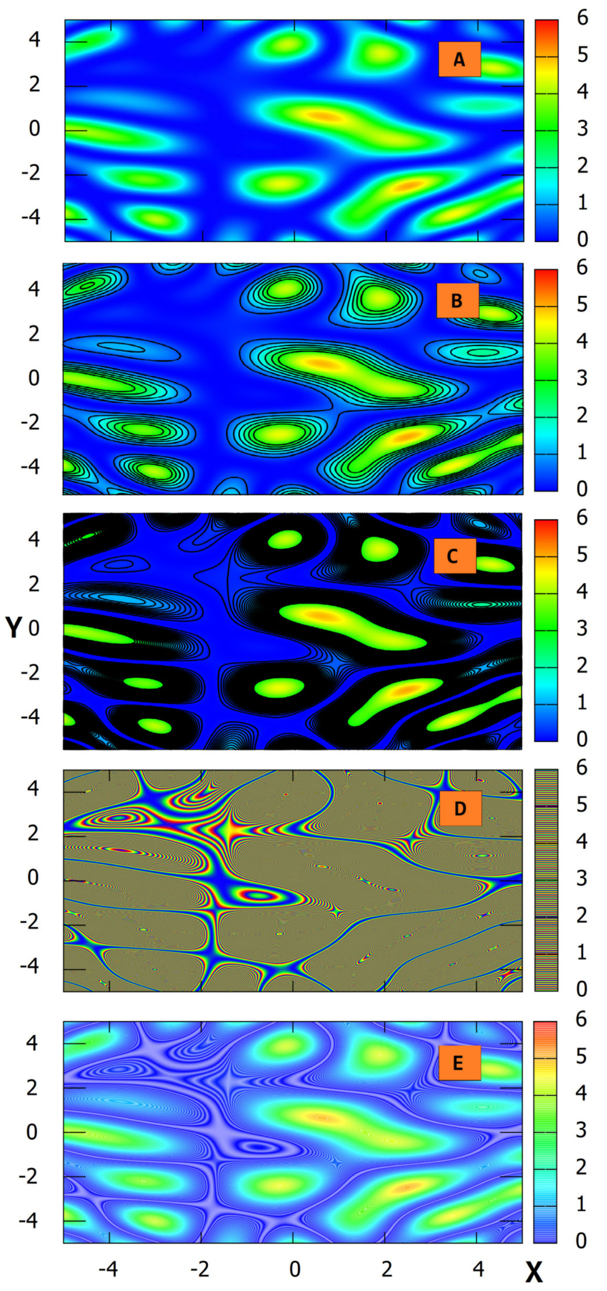

FIGURE 6. Comparison of four plotting styles for arbitrary function $f(x, y) = (\sin x \cos y + \sin 2y \cos x + \cos \frac{xy}{2})^2$. In panel A, the plot is generated with classical color palette. In middle panels, we see the contour plots with different isoline densities: $\Delta f = 0.5$-panel B, $\Delta f = 0.1$-panel C. Panel D represents prism plot in which different colors are used every $\Delta f = 0.015$. Panel E represents a braid plot created with two mixed color palettes of the same hue change frequency as in panel D.

the islands, which disqualifies this type of chart. In panel D, we can see a prism plot of high resolution $\Delta f = 0.015$ (rate of color change). As we could see in Figure 3, despite the inability to read values, this type of plot is very useful in detecting small perturbations. Panel D, however, reveals to us another major drawback of a prism plot. Increasing the resolution of the plot and, hence, the accuracy of small effects comes at the expense of the possibility of distinguishing big changes like in panel C. On the other hand, if we decrease a color change rate, we cannot observe subtle perturbations anymore (like in panel B). Therefore, we must be very careful in interpreting this type of chart, because often a wrongly chosen scale may lead to false conclusions. Finally, in panel E, which was made using our hue layering technique, not only do we see changes taking place on land in good resolution, but also we have a full view of small changes at sea level. One can see that this is not a static area as we used to suppose looking at panel A. The changes that occur there are small, but very dynamic, which would be important if we wanted to cross our water by boat. Thanks to this technique, we can notice channels of constant values along the coasts (calm sea) and vortexes further from the mainland that we would certainly like to avoid. Comparing panels D and E, we can see that in both cases details of small perturbations are very well visible. Nonetheless, in case of bigger values, only the braid plot keeps all details of the land, which are almost completely illegible in panel D. In Figure 6, we do not show a flag plot, because it shares the same properties as a prism plot and reveals the same issues. In this example, the analogy with the terrain construction is not accidental. We hope that analyzing topography with our method can be very useful in Solar System exploration missions. We think that braid plots could help to find the most optimal diameter of rovers' wheels and will allow one to adjust the appropriate speed to the surface conditions of the terrestrial planets or the moons of the Gas Giants.

To visualize benefits of the braid plot even more in the upper panel of Figure 7, we analyze a Gaussian curve given by the following analytical expression:

$$f(x, y) = e^{-(x^2+y^2)}. \tag{4}$$

The function takes values from 0 to 1 and has its maximum at point (0,0). Another Gaussian-like function we consider is shown in the second panel of Figure 7. It is given by the following formula:

$$g(x, y) = \frac{1}{100} e^{-((x-3)^2+(y+1)^2)}. \tag{5}$$

As we can see in the two upper panels of Figure 7, $g(x, y)$ is a scaled and shifted version of $f(x, y)$ with the scaling

Authorized licensed use limited to: Eileen McGuinness. Downloaded on January 26,2022 at 22:03:24 UTC from IEEE Xplore. Restrictions apply.

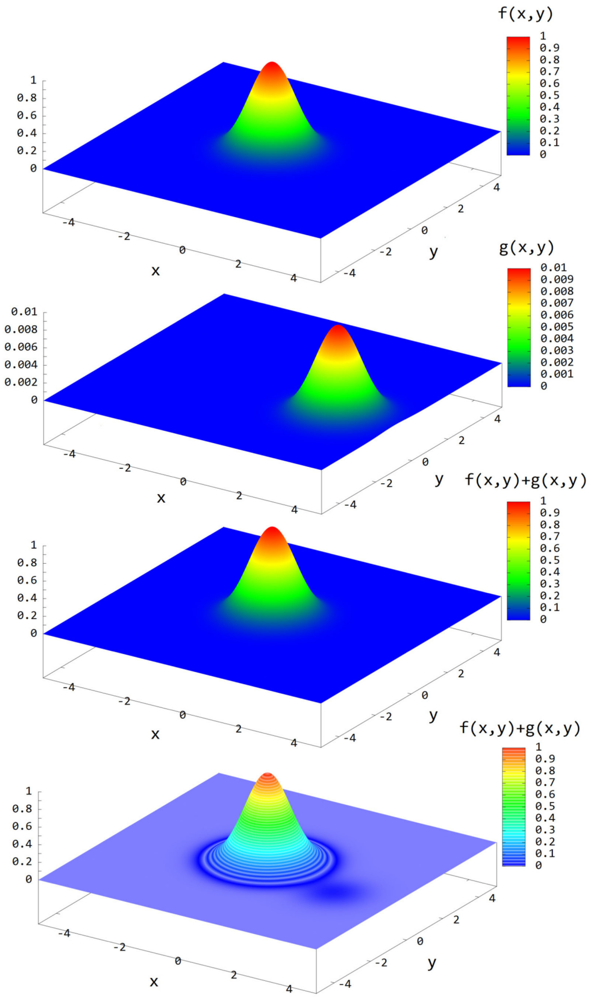

FIGURE 7. Plots of two-variable functions made using standard technique: $f(x,y)=e^{-(x^2+y^2)}$ (upper panel), $g(x,y)=\frac{1}{100}e^{-((x-3)^2+(y+1)^2)}$ (middle panel), and their sum ($f(x,y)+g(x,y)$) (last but one panel). Bottom panel represents plot of $f(x,y)+g(x,y)$ made with the mixed palette (braid plot) method ($M=2, N=5, D=10, w=1$).

factor $A=\frac{1}{100}$ and the translation vector $\vec{t}=[3,-1]$. The two bottom panels show a sum of both Gaussian curves $f(x,y)+g(x,y)$. As one can see, the traditional method (last but one panel) completely covers up the existence of small perturbations. This disqualifies the applicability of the traditional coloring methods in tasks requiring capturing external disruptions. This simple example can play a role of representing small impurities that are present in many experimental studies on the background of collected data. We can imagine that $f(x,y)$ represents distribution of measured physical quantity like, e.g., quasi-particle spectrum energy or velocity and $g(x,y)$ is an external interruption. Lack of awareness of environmental disturbances existence is a crucial issue in many studies, which require high accuracy. We believe that our technique of drawing will allow one to avoid such problems. The important thing is that although we do not see full details of $g(x,y)$, we are aware of its existence!

Method Limitations and Discussion

As almost every method, braid plot has, unfortunately, its disadvantages and limitations. The main disadvantage of this method is the fact that in the case of rapidly changing functions (high gradient) in certain areas, the interweaving of colors can appear. For the human eye, the colors in these areas merge to form a more uniform hue. In the critical case of an extremely high growth rate, this phenomenon can lead to a similar effect as in the case of a traditional chart, which uses a single color palette. One could observe such an effect looking at local maxima (terrain) shown in panel E of Figure 6, where the big change rate of the function makes it difficult to spot smaller perturbations with the same ease as it was in the "sea level." However, this issue could be improved by using more contrasting colors and increasing the number of mixed palettes. The braid plot is not limited to a single set of hues and can be used for arbitrarily selected colors, which can significantly improve the quality of the plots.

Figure 8 is an example of braid plots prepared with different sets of colors. It represents the plots of the same function as in Figure 6. Panel A corresponds to a braid plot created by mixing four palettes of colors. Black and dark gray colors associated with the minimal value are in a big contrast with brighter hues representing greater values. Such a selection of colors makes the differences between the subtle perturbations and big changes more apparent. Additionally, increasing the amount of initial palettes increases the quality of details in structures representing big values. Panel B represents a braid plot composed of two diverging color maps.[2] Although a smaller amount of initial colors ($N=3$) decreases the possibility of precise assignment of specific numbers to colors, this set of hues strongly increases readability of the plot as suggested by Borland and Taylor II.[4] As we can see, properly selected sets of colors allow us to notice more details on the "terrain" level, which were less evident in previous graphics. The human eye can more easily notice differences at high-valued regions of the graph.

Another disadvantage of braid plots is the fact that they are not applicable for drawing data of a very low number of samples, which in the case of a classical plot is not an obstacle. We must be aware that setting

Authorized licensed use limited to: Eileen McGuinness. Downloaded on January 26,2022 at 22:03:24 UTC from IEEE Xplore. Restrictions apply.

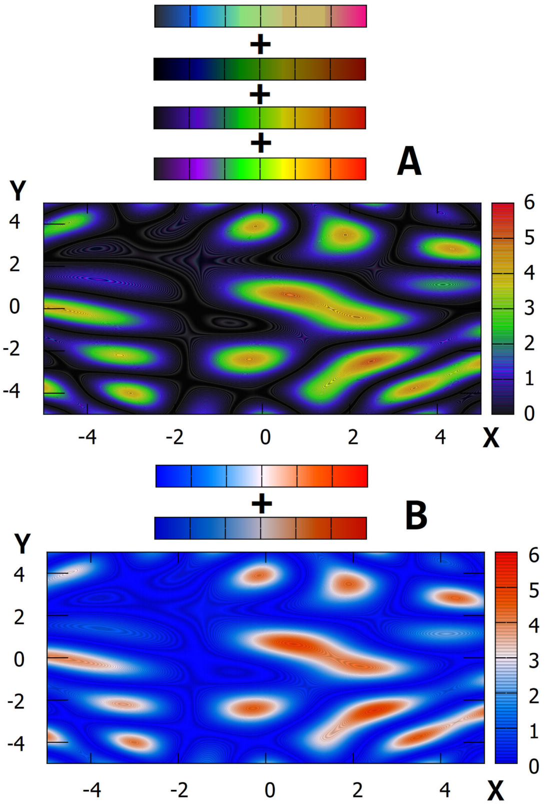

FIGURE 8. Braid plots of the function $f(x,y) = (\sin \mathrm{x} \cos \mathrm{y} + \sin 2\mathrm{y} \cos \mathrm{x} + \cos \frac{\mathrm{xy}}{2})^2$ prepared by mixing four initial palettes of colors $(N = 5, D = 10, w = 1)$-panel A and by mixing two diverging color sets $(N = 3, D = 15, w = 1)$-panel B.

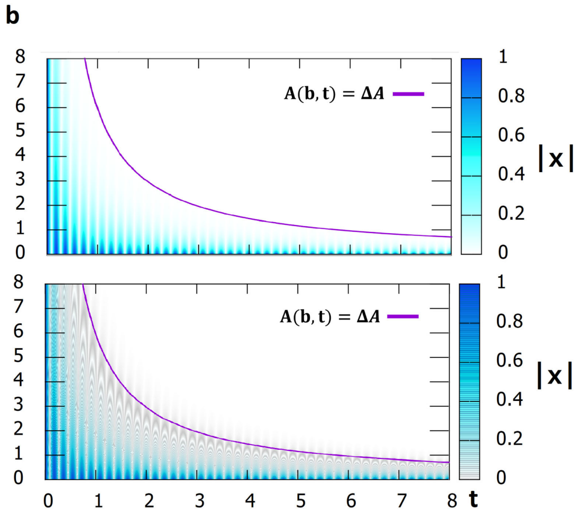

FIGURE 9. Graph of harmonic oscillator's distance from the point of equilibrium $|x|$, where x denotes oscillator's position, which is a function of damping factor b and time t. Oscillator's position is given by the equation $x(b,t) = A_0 \exp(-\frac{bt}{2\,m}) \cos(\omega \mathrm{t})$, where $A_0 = 1$ m is an initial amplitude, $m = 0.5$ kg denotes mass of a physical object, $\omega = (\frac{k}{m} - \frac{b^2}{4\,m^2})^{1/2}$ is damped oscillation frequency, and $k = 150$ Nm^{-1} represents harmonic constant. Upper plot is made with traditional method, lower panel with mixed palette technique $(M = 2, N = 3, D = 50, w = 1)$. Purple curves, given by the equation $b(t) = -\frac{2\,m}{t} \ln \frac{\Delta A}{A_0}$, connect all the points (b,t) for which damped amplitude $A(b,t)$ is equal $\Delta A = 5$ mm.

too big mixing density D will not always improve the quality of the chart if we do not have accurate enough data. However, this problem concerns all 3-D methods.

The last minor disadvantage of the braid plot technique is a higher computational complexity. Preparing braid plots requires more time than classical plots due the mixing algorithm, which should be executed earlier. What is important, the difference is almost indistinguishable for braid plots made with up to 10 palettes and density counted in the hundreds. However, we need to notice that modern computers have high technical parameters, which make the execution of the algorithm not a problematic task. Additionally, we can always save the mixing algorithm output in a file if we want to use one style of a braid plot multiple times.

Applications in Physics

A mixed palette plotting method has found practical usage in physics, where one can find dozens of subtle phenomena that can be often overlooked when appropriate magnification of plot is not used.

Damped Harmonic Oscillator

The first practical example we consider is a simple model of damped harmonic oscillator, which is a type of oscillator where the vibrations (more precisely the amplitude of vibrations) are weakened due to the action of external forces (e.g., friction). The solution of harmonic oscillator is given by the formula

$$x(b,t) = A(b,t) \cos(\omega \mathrm{t}) \tag{6}$$

where x is a position of physical object, t-time, b-damping factor, $\omega = \sqrt{\frac{k}{m} - \frac{b^2}{4\,m^2}}$ is damped oscillation frequency with harmonic (e.g., spring) constant k for physical object of mass m. The damped amplitude $A(b,t)$ is expressed by the following relation:

$$A(b,t) = A_0 e^{-\frac{bt}{2\,m}} \tag{7}$$

where A_0 is an initial amplitude of vibrations.

In Figure 9, we can see two plots of harmonic oscillator's distance from the point of equilibrium-$|x|$ as a function of time t and damping factor b. The upper

Authorized licensed use limited to: Eileen McGuinness. Downloaded on January 26,2022 at 22:03:24 UTC from IEEE Xplore. Restrictions apply.

panel, made with the classical method, reveals that the damping factor strongly decreases the oscillation amplitude of the physical object. We can see that starting from $b = 2$, the system reaches its equilibrium position (i.e., does not oscillate) for $t \simeq 1.8$. Our conclusions are different when we take a look at the braid plot made by mixing two color palettes (lower panel). Here, the oscillations last much longer, and for $b = 2$, we can see that system needs almost twice as much time to be stabilized than we initially thought. Subtle phenomena detection is very important from a practical point of view. It could help, e.g., to estimate the minimum time that must elapse between two consecutive attempts of a given experiment so that these attempts have no effect on each other, which is hard to do looking at a classical plot where the boundary between the excited and stable state is more blurred. In this example, the colorbox in the lower panel is divided into $n = M \times (N-1) \times D = 200$ segments of equal width. That gives us a possibility to detect vibrations to $\Delta A = \frac{A_0}{n} = 5$ mm. It means that changing parameters of the braid plot allows experimenters to set the desired vibration detection scale in advance!

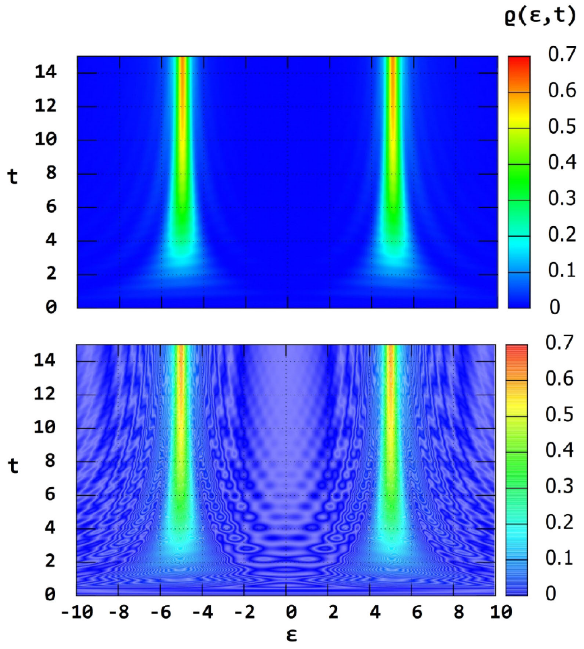

FIGURE 10. Graph of the spectral density function [$\rho(\varepsilon, t)$, where ε denotes energy and t time] of the first site of system composed of two quantum dots and electrode made using traditional color palette-upper panel and with mixed palette method-lower panel ($M = 2, N = 5, D = 10, w = 1$).

To verify the last statement, let us find an equation of the curve along which vibrations are equal $A(b,t) = \Delta A = \text{const}$. To do so, let us transform (7) by taking $A(b,t) = \Delta A$

$$\Delta A = A_0 e^{-\frac{bt}{2\,m}} // \div A_0 \tag{8}$$

$$\frac{\Delta A}{A_0} = e^{-\frac{bt}{2\,m}} // \ln() \tag{9}$$

$$\ln\frac{\Delta A}{A_0} = -\frac{bt}{2\,m} // \div \frac{-t}{2\,m} \tag{10}$$

$$b(t) = -\frac{2\,m}{t}\ln\frac{\Delta A}{A_0}. \tag{11}$$

In both panels of Figure 9, except $|x|$, we can also see curves, given by (11), along which $A(b,t) = \Delta A$. As we can see, there is no correlation between the graph shown in the upper panel and the curve. In the bottom panel, we can see that the readability limit of the braid plot follows the curve precisely.

Two Atom System

Thanks to the benefits of our new plotting method, an interesting phenomenon in the field of condensed matter physics has been detected in our studies. The effect manifests itself in slight oscillations of the electron density of states ρ in the system composed of two interconnected quantum dots, one of which is coupled to an electrode. We are interested in the time evolution of the spectral density function. This function describes the amount of states that are to be occupied by electrons from the lead. Its maxima correspond to quasi-particles, which can change dynamically in the system. To calculate ρ at given energy (ε) and time (t), we use commonly known in quantum physics evolution operator technique, which often gives long, hard for interpretation formulas.[12] Therefore, a more reasonable way of analysis is to calculate equations numerically and draw a plot of quantity to study its properties in detail. The electron density at first dot (ρ_1) evolves in time and for large t it has a shape of two Lorentzian curves as it is shown in the upper panel of Figure 10. Looking at the plot, which is created with the traditional coloring method, we can predict that after some time the system is in its equilibrium state (after around 12 time units) and after that time ρ_1 does not change in time. We also notice that region between spectral density peaks is quite smooth and flat.

However, if we apply our method of drawing graphs, we come to different conclusions. Looking at the bottom panel of Figure 10, we see that time evolution of the quantum dot system is much richer (dynamical) than the results depicted in the upper panel. However, the oscillation/perturbation magnitude

Authorized licensed use limited to: Eileen McGuinness. Downloaded on January 26,2022 at 22:03:24 UTC from IEEE Xplore. Restrictions apply.

is much smaller than the value of ρ at the main peaks, which makes it a very subtle phenomenon. We can notice subtle structure which shows the quantum nature of electrons after the quench and reveals interesting dynamic oscillations which take the form of geometrical shapes called transient crystals.[12] We also see that regions outside Lorentzians are highly perturbed and even for a long time the system is definitely not yet in its equilibrium state. It is highly important if we think about the potential applications of these systems in nanoelectronics or quantum computing.

CONCLUSIONS

In conclusion, this work presents a new alternative method of 3-D data visualization based on the use of multiple hue palettes that reveals essential/significant advantage over traditional methods, contour, and periodic-color plots. It can lead to a significant increase in the possibility of interpreting the presented results by specifying areas characterized by the constant value in the chart without need of drawing solid lines.

We hope that this method will find many applications in physics, mathematics, geography, and other areas of science. We believe that it will allow one to notice phenomena that have often been overlooked due to their almost imperceptible, subtle nature. We believe it will influence new discoveries through a new look at usual things.

APPENDIX

Here, we show an implementation example of the algorithm presented in the “Model, Description, and Algorithm” section. The code is written in Java language and represents three methods responsible for data reading, creating temporary arrays, and mixing palettes. Running all three methods will allow one to create a mixed palette of any density, number of colors, number of component palettes, and weaving number.

Listing 1 represents a method of reading data. Input parameters are N-number of initial colors in each array, M-number of arrays. The method reads the RGB components of each color from the standard input and puts them to the output array of palettes. This method represents the first step of the algorithm.

In Listing 2, we can see a Java method, which is responsible for creating a temporary array that stores base and transitional colors. In this method, we have two input parameters D-braid plot density and array of colors representing one of the M component color palettes. As a result, the method returns an array of initial and transitional colors of given density. This method represents steps 2 and 3 from the algorithm.

```java
static ArrayList<ArrayList<Color>> readData(int N, int M)
            throws java.io.IOException{

        ArrayList<ArrayList<Color>> outputArray = new ArrayList<>();
        BufferedReader reader =
            new BufferedReader(new InputStreamReader(System.in));
            for (int j = 0; j < M; j++) {
                // 0 <= j < M - palettes counter
                ArrayList<Color> palette = new ArrayList<>();
                println("palette_"+j);
                for (int i = 0; i < N; i ++) {
                    // 0 <= i < N - colors counter
                    int r, g, b;
                    println("Insert␣color_"+i+"␣RGB␣components");
                    r = Integer.parseInt(reader.readLine());
                    g = Integer.parseInt(reader.readLine());
                    b = Integer.parseInt(reader.readLine());
                    palette.add(new Color(r,g,b));
                }
                outputArray.add(palette);
            }
        return outputArray;
    }
```

LISTING 1. Data reading method implementation example. The method reads from the standard input M palettes composed of N colors each. The user enters the colors by specifying red, green, and blue components of each color.

```java
    static ArrayList<Color> createTemporaryPalette
                (int D, ArrayList<Color> pallete){

            ArrayList<Color> result = new ArrayList<>();
            int N = pallete.size();
            // N - nuber of colors in array
            int [][] differences = new int[N -1][3];
    // differences is an array storing δ elements

    //step 2: finding differences
    for (int i = 0; i < N - 1; i++){
        // 0 <= i < N - color counter
        differences[i][0] =
                ((pallete.get(i + 1) .getRed()) -
                        (pallete.get(i) .getRed()))/D;
        differences[i][1] =
                ((pallete.get(i + 1) .getGreen()) -
                        (pallete.get(i) .getGreen()))/D;
        differences[i][2] =
                ((pallete.get(i + 1) .getBlue()) -
                        (pallete.get(i) .getBlue()))/D;
    }

    //step 3: adding δ elements to colors
    for (int n = 0; n < differences.length; n++)
    {
        for(int i = 0; i <= D; i++){
            int r = (pallete.get(n) .getRed()
                    + differences[n][0]*i);
            int g = (pallete.get(n) .getGreen()
                    + differences[n][1]*i);
            int b = (pallete.get(n) .getBlue()
                    + differences[n][2]*i);
            result.add(new Color(r,g,b));
        }
    }
    return result;
}
```

LISTING 2. A Java method representing creating temporary array of colors of density D from initial set of colors chosen by the user in method shown in Listing 1.

Authorized licensed use limited to: Eileen McGuinness. Downloaded on January 26,2022 at 22:03:24 UTC from IEEE Xplore. Restrictions apply.

```
static ArrayList<Color> mixPalettes(
            ArrayList<ArrayList<Color>> palletes,//list of palettes
            int w, int N){
        //step 4: mixing palettes
        ArrayList<Color> mixedPalette = new ArrayList<>();
        // mixedPalette - output palette
        int M = palletes.size();
        for (int i = 0; i < N; i += w) {
            // 0 <= i < N - colors counter
            for (int j = 0; j < M; j++) {
                // 0 <= j < M - palettes counter
                for(int k = 0; k < w; k++){
                    // 0 <= k < w - weaving number counter
                    mixedPalette.add(palletes.get(j).get(i + k));
                }
            }
        }
        return mixedPalette;
    }
```

LISTING 3. Implementation example of a method which intertwines M arrays and puts results in mixed palette of colors.

Listing 3 represents a method of mixing palettes received by using function from Listing 2. This method intertwines colors from each palette and puts results in final output mixed palette. Here, input parameters are list of palettes, number of initial colors in each palette N, and the weaving number w. The method corresponds to step 4 in the algorithm.

ACKNOWLEDGMENTS

This work was supported in part by the National Science Centre, Poland, under Grant 2018/31/B/ST3/02370.

REFERENCES

1. S. Bianco, G. Francesca, and S. Raimondo, “Color coding for data visualization,” *Encyclopedia of Information Science and Technology*, M. Khosrow-Pour, Ed., 3rd ed. Hershey, PA, USA: IGI Global, 2015, pp. 1682–1691, 2015. [Online]. Available: http://doi:10.4018/978-1-4666-5888-2.ch161
2. R. M. Karim,O.-H. Kwon, C. Park, and K. A. Lee, “Study of colormaps in network visualization,” *Appl. Sci.*, vol. 9, no. 20, 2019, Art. no. 4228.
3. D. A. Szafir, “Modeling color difference for visualization design,” *IEEE Trans. Vis. Comput. Graph.*, vol. 24, no. 1, pp. 392–401, Jan. 2018.
4. D. Borland and R. M. Taylor II, “Rainbow color map (still) considered harmful,” *IEEE Comput. Graph. Appl.*, vol. 27, no. 2, pp. 14–17, Mar./Apr. 2007.
5. R. Bujack, T. L. Turton, F. Samsel, C. Ware, D. H. Rogers, and J. Ahrens, “The good, the bad, and the ugly: A theoretical framework for the assessment of continuous colormaps,” *IEEE Trans. Vis. Comput. Graph.*, vol. 24, no. 1, pp. 923–933, Jan. 2018.
6. K. Thyng, C. A. Greene, R. D. Hetland, H. M. Zimmerle, and S. F. DiMarco, “True colors of oceanography: Guidelines for effective and accurate colormap selection,” *Oceanography*, vol. 29, no. 3, pp. 9–13.
7. K. Potter *et al.*, “Ensemble-Vis: A framework for the statistical visualization of ensemble data,” in *IEEE Int. Conf. Data Mining Workshops*, 2009, pp. 233–240, doi: 10.1109/ICDMW.2009.55.
8. D. Hughes-Hallett, W. McCallum, and A. M. Gleason, *Calculus: Single and Multivariable*, 6 ed. Hoboken, NJ, USA: Wiley, 2013.
9. K. P. Janert, *Gnuplot in Action: Understanding Data With Graphs*. Shelter Island, NY, USA: Manning Publications Co., 2009.
10. Plot3D-Wolfram Language Documentation. [Online]. Available: https://reference.wolfram.com/language/ref/Plot3D.htm. Accessed: Aug. 8, 2020.
11. J. D. Hunter, “Matplotlib: A 2D graphics environment,” *Comput. Sci. Eng.*, vol. 9, no. 3, pp. 90–95, May/Jun. 2007.
12. M. Kurzyna and T. Kwapiński, “Nontrivial dynamics of two-site system: Transient crystals,” *Phys. Rev. B*, vol. 102, no. 24, 2020, Art. no. 245414.

MARCIN KURZYNA is currently working toward the Ph.D. degree in physics with Maria Curie-Skłodowska University (MCSU), Lublin, Poland. His research interests include solid-state physics, nanotechnology, quantum information, numerical methods, physical phenomena modeling, and programming languages. His professional career is also associated with software development for medical facilities. He has graduated in theoretical physics in MCSU and computer science from the Lublin University of Technology (LUT), Lublin, Poland. He is the corresponding author of this article. Contact him at marcin.kurzyna@live.umcs.edu.pl.

TOMASZ KWAPIŃSKI is currently an Assistant Professor with the Department of Surface Physics and Nanotechnology, Institute of Physics, Maria Curie-Skłodowska University, Lublin, Poland. His research interests include quantum dots, quantum chains, stationary and time-dependent electron transport through low-dimensional systems, charge waves, quantum and spin pumps, STM conductance, and topological chains. He is a Fellow of the Foundation for Polish Science and the Alexander von Humboldt Foundation. Contact him at tomasz.kwapinski@umcs.pl.

Authorized licensed use limited to: Eileen McGuinness. Downloaded on January 26,2022 at 22:03:24 UTC from IEEE Xplore. Restrictions apply.